Higher Dimensional Time-Energy Entanglement

Daniel Lampert Richart

München 2014

Higher Dimensional Time-Energy Entanglement

Daniel Lampert Richart

Dissertation
an der Fakultät für Physik
der Ludwig–Maximilians–Universität
München

vorgelegt von
Daniel Lampert Richart

München, den 20.05.2014

Erstgutachter: Prof. Harald Weinfurter
Zweitgutachter: Prof. Jan von Delft
Tag der mündlichen Prüfung: 08.07.2014

ZUSAMMENFASSUNG/SUMMARY

ZUSAMMENFASSUNG

Es ist in den letzten Jahren immer deutlicher geworden, dass weitere Forschung zur Untersuchung von quantenmechanischen Systemen durchgeführt werden muss um die wachsenden Probleme in der heutigen Informationstechnologie zu adressieren. Insbesondere sticht hier die exponentiell wachsende Nachfrage nach Computerressourcen und nach sicheren Kommunikationsprotokollen mit hoher Bandbreite hervor, um der weiter wachsenden Datengenerationsrate standzuhalten. Dies stösst auf fundamentale Grenzen, wie die erforderliche Miniaturisierung von Prozessorstrukturen (CPUs) auf atomare Dimensionen demonstriert.
Von dieser Perspektive her ist es erforderlich weitere Forschung zur Kontrolle und Manipulation von Quantenzuständen durchzuführen, wie sie zum Beispiel im Feld der Quanteninformation erfolgt ist. Diese Strategie ermöglicht von weiteren Eigenschaften der Quantenmechanik, wie zum Beispiel der Präparation von Superpositionszuständen, Gebrauch zu machen. Dies ist insbesondere relevant, da es ermöglicht NP harte Probleme zu lösen, die durch klassische Computer nicht effizient gelöst werden können. Allerdings sind bisher experimentell realisierte quantenmechanische Systeme noch nicht skalierbar genug um den Anforderungen der klassischen Technologie gerecht zu werden. Ähnlichen Argumenten folgend sind Quantenkommunikationssysteme, die die Sicherheit von Kommunikationsprotokolle zertifizieren können, noch nicht in der Lage angemessene Bandbreiten zu gewährleisten.
Diese Doktorarbeit gliedert sich diesen Forschungsprojekten an, mit dem Ziel die Skalierbarkeit von quantenmechanischen Systemen zu vergrössern und entsprechend den genannten Anforderungen gerecht zu machen. Die Strategie die hier verfolgt wird basiert auf die Kodierung von Quantenzuständen in Photonenpaare, die durch den Prozess der Spontanen Parametrischen Down-conversion (SPDC) erzeugt werden. Dieses Verfahren bringt allerdings eine limitierte Skalierbarkeit der Quantensysteme mit sich, da die Detektionseffizienz von kommerziell erhältlichen Einzelphotonendetektoren limitiert ist. Dieses Problem wird in dieser Arbeit umgangen indem die Quantenzustände in höher dimensionale Hilberträume eines Zweiphotonenzustands kodiert werden, was einen deutlichen Vorteil gegenüber der Kodierung in einen Mehrphotonenzustand darstellt. Darüber hinaus ermöglicht die Kodierung der Quantenzustände in den Emissionszeit Freiheitsgrad der Photonen intrinsische Vorteile bei ihrer Anwendung auf die Quantenkommunikation. Hier ist insbesondere der Vorteil gegenüber der Kodierung in den Impuls- und Polarisationsfreiheitsgrad gemeint, die durch deutliche Einschränkungen bei der Transmission über lange Strecken gekennzeichnet sind.
Mit einem Augenmerk auf diese Ziele wird in dieser Arbeit die experimentelle Umsetzbarkeit des beschriebenen Schemas gezeigt. Dies wurde durch die Anwendung von geeigneten Maßen wie die Verschränkung, Dimension und Präparationsfidelity auf die generierten Zustände quantifiziert. Insbesondere bei der Abschätzung der Fidelity wurde von Forschungsergebnissen rund um Compressed Sensing Gebrauch gemacht und weiter mit

einem adaptiven Messschema kombiniert, um die effektive Betriebszeit dieser Systeme zu verringern. Dies ist für die weitere skalierbare Anwendung zur Quanteninformationsverarbeitung von Vorteil. Die Ergebnisse verdeutlichen, dass eine Skalierbarkeit der Dimension des Systems auf grösser als $2x8$ Dimensionen, äquivalent zur Dimension eines 6-Qubit Zustands, in der Reichweite einer experimentellen Umsetzung liegt.

SUMMARY

Judging by the compelling number of innovations based on taming quantum mechanical effects, such as the development of transistors and lasers, further research in this field promises to tackle further technological challenges in the years to come. This statement gains even more importance in the information processing scenario. Here, the growing data generation and the correspondingly higher need for more efficient computational resources and secure high bandwidth networks are central problems which need to be tackled. In this sense, the required CPU minituarization makes the design of structures at atomic levels inevitable, as foreseen by Moore's law.

From these perspectives, it is necessary to concentrate further research efforts into controlling and manipulating quantum mechanical systems. This enables for example to encode quantum superposition states to tackle problems which are computationally NP hard and which therefore cannot be solved efficiently by classical computers. The only limitation affecting these solutions is the low scalability of existing quantum systems. Similarly, quantum communication schemes are devised to certify the secure transmission of quantum information, but are still limited by a low transmission bandwidth.

This thesis follows the guideline defined by these research projects and aims to further increase the scalability of the quantum mechanical systems required to perform these tasks. The method used here is to encode quantum states into photons generated by spontaneous parametric down-conversion (SPDC). An intrinsic limitation of photons is that the scalability of quantum information schemes employing them is limited by the low detection efficiency of commercial single photon detectors. This is addressed by encoding higher dimensional quantum states into two photons, increasing the scalability of the scheme in comparison to multi-photon states. Further on, the encoding of quantum information into the emission-time degree of freedom improves its applicability to long distance quantum communication schemes. By doing that, the intrinsic limitations of other schemes based on the encoding into the momentum and polarization degree of freedom are overcome.

This work presents results on a scalable experimental implementation of time-energy encoded higher dimensional states, demonstrating the feasibility of the scheme. Further tools are defined and used to characterize the properties of the prepared quantum states, such as their entanglement, their dimension and their preparation fidelity. Finally, the method of quantum state tomography is used to fully determine the underlying quantum states at the cost of an increased measurement effort and thus operation time. It is at this point that results obtained from the research field of compressed sensing help to decrease the necessary number of measurements. This scheme is compared with an adaptive tomography scheme designed to offer an additional reconstruction speedup. These results display the scalability of the scheme to bipartite dimensions higher than $2x8$, equivalent to the encoding of quantum information into more than 6 qubits.

CONTENTS

Part I

TIME-ENERGY ENCODING OF QU*D*IT ENTANGLED STATES

1

INTRODUCTION

The work presented in this thesis wouldn't have been possible without the significant advances in the control and manipulation of quantum mechanical properties of light and matter witnessed during the 20th century. These advances motivated by a first treatment and taming of quantum mechanical properties [42]: The development of the theoretical foundations for describing black-body radiation and the photoelectric effect enabled to tackle the interaction of light and matter, and to apply them to giving rise to well established technologies in today's economy such as transistors and lasers. With more relevance to this work, the improvement in the precision of these measurements has enabled to tame further quantum mechanical properties such as entanglement [149], which are about to further enhance the capabilities of information technologies or to even implement new ones [125]: Within the ongoing research, the fields of quantum cryptography [58] and quantum computation [124] have emerged as the most promising candidates. As most notable applications, the first field has made the secure distribution of keys [45] possible and the implementation of communication protocols outperforming classical schemes [24]. In similar terms, quantum computers were proposed which could in principle outperform the decryption speed of secret keys of classical computers [154] (Shor's algorithm) as well as the best possible classical search algorithm [61] (Grover's algorithm).
Closely related to these research fields is the field of quantum metrology [56, 57], promising to improve the shot-noise limited resolution in precision measurements. Here, the entanglement of photons enables high-precision interferometric phase measurements [5].
Several quantum information carriers suited for these tasks have been proposed and experimentally tested with regard to their scalability and susceptibility to decoherence: Superconducting qubits [111], trapped ions [35, 67, 66], atoms trapped in optical lattices [17, 33], quantum dots [105], nuclear spin (NMR) [172], nitrogen vacancy centers in diamonds [102, 123], electrons [69] and finally, and with more relevance to this work, single photons [84, 85, 137]. First results regarding the successfull implementation of quantum computation tasks were based on trapped ions [64], or on photonic states encoded into higher Hilbert space dimensions, where the number 21 was factorized via the Shor algorithm [112]. In general, the intrinsic limitation of these systems is given by the high number of independent information carriers whose encoded quantum states are to be efficiently controlled, manipulated and, further on, transmitted. For example, for photonic and ionic based systems the number of entangled qubits is currently limited to 8 and 17 respectively [186, 66, 119], to 12 for spin encoded qubits based on molecules [122] and to 3 for superconducting qubits [121].
It will be the purpose of this thesis to enhance the complexity of the entangled quantum states prepared to use them for more complex quantum information processing tasks, designed to increase the information band-

width of quantum information processing and the capabilities of quantum computation schemes. The approach chosen here consists in increasing the Hilbert space dimension of the states encoded into a particle from 2, defining a qubit, to an arbitrary dimension d, generally denoted as a qu$d$it. This approach is particularly advantageous as it allows to increase the security thresholds for example for the distribution of keys encoded in qu$d$its [46, 176]. Additionally, qu$d$its were shown to enhance the quantum information bandwidth per single particle [7]. From yet another perspective qu$d$its are advantageous with respect to other schemes used to enhance the complexity of quantum information tasks, such as photon based multi-qubit entangled states [82]. Here, the detection efficiency of photonic based entangled 2-qu$d$it states is orders of magnitude higher than for multi-qubit entangled states. Yet, from another perspective, it could be shown that qu$d$its enable to lower the requirements for closing the detection loophole in Bell-type experiments as the critical detection efficiency is reduced with respect to qubits[174, 114].
Encoding qu$d$its into photons is motivated in part by their intrinsically low susceptibility to decohere, what makes them more suitable for quantum communication applications. This is best exemplified by long distances over which entanglement can be preserved [170, 110]. Nevertheless, due to their limited ability to interact with each other without much nonlinear coupling they were not suitable for quantum computation schemes. This could be shown to be no stringent limitation when considering the one-way quantum computation scheme applied on a set of entangled photons [84]. Several experimental demonstrations based either on multi-photon entangled [137] or higher dimensional bipartite qu$d$it [171] states encoded into photons revealed the suitability of this scheme.
This work presents important steps towards the generation and development of reliable entanglement and dimension detection schemes for states encoded in higher dimensional spaces higher than 8. For that purpose, an efficient scheme for the generation and analysis of bipartite qu$d$it entanglement based on the encoding of photon pairs into the time-energy degree of freedom [52] will be presented. As will be shown, it is scalable to high dimensions [81] and well suited for facilitating long distance quantum communication [110] (see chapter **2** for a theoretical description and chapter **3** for an experimental implementation, as well as the publication **P1**). In order to make these schemes suitable for further applications a high degree of entanglement as well as a high preparation fidelity has to be ensured, relying on the efficient determination of corresponding figures of merit. The entanglement detection schemes employed here will concentrate only on the detection of bipartite 2xd dimensional entanglement [38, 48, 39] (see chapter **4** and publication draft P4) based on a test of 2xd dimensional Bell-type inequalities [38]. Further on, this work will present a complete tomographic characterization of the generated emission time encoded states (see chapter **5**). This is a scheme which, even at the cost of an increased experimental effort, is to be favored as it offers a complete characterization of the generated quantum states [75, 181, 82] by providing an estimate of corresponding measures of the entanglement quality. An important question adressed in this work is whether the corresponding measurement effort in the range of several hours for full state tomography can be reduced such as to leverage the requirements for practical quantum information processing tasks. This can be adressed by using compressed sensing based reconstruction schemes [29]

combined with convex optimization algorithms [22, 151]. This is a method already successful in a vast range of signal processing applications requiring a speedup in the signal acquisition without reducing the reconstruction fidelity [108, 1, 76]. Here, it allows the tomographic measurement effort to scale only logarithmically instead of exponentially with the dimensions of the encoded quantum states [60]. Further on, this work will study how other fundamental symmetries of quantum theory, such as correlation complementarity (studied in more detail in publications P2 and P3), can be used to achieve an even higher reduction of the acquisition time than with compressed sensing based schemes. The work presented here will have as a figure of merit the achieved reconstruction fidelity. Special discussion will be given here on the reduction of the fidelity due to an intrinsic bias associated to the estimators used to reconstruct the states (see related publication **P5**).
The suitability of the encoded states for quantum information tasks making use of a higher complexity of the encoded states relies on the knowledge of the dimension of the entangled states. This motivates to apply reliable measures on the number of entangled modes for the experimentally generated states in the last chapter **6**.
This work is designed to adress some of the open questions limiting the widescale applicability of quantum computation and communication schemes regarding the scalability of the required system sizes.

2

TIME-ENERGY ENCODED QUDIT ENTANGLED STATES

This chapter has as the major aim to provide the theoretical foundations for the following chapters. It will start with a general description of quantum states (see 2.1.1) and particularly focus on their representation in higher dimensional Hilbert spaces (see 2.1.2). Here, explaining in detail the notions of separability and entanglement will be central to this work (2.1.3). Further on, a special focus will be put on describing the encoding of entangled states into the time-energy degree of freedom as used in this work (2.3). Finally, methods suited to expand the Hilbert space dimensionality of quantum states encoded in the time-energy (2.4) or time-bin (2.4.2) degree of freedom will be discussed.

2.1 ELEMENTS OF QUANTUM THEORY

2.1.1 *Quantum States*

> Hilbert space is a big place
> – Carlton Caves

A central element of quantum theory is that any (pure) quantum state Ψ can be represented as a vector. In Dirac's notation a state is denoted as $|\Psi\rangle \in \mathcal{H}$ (ket) with corresponding dual vector $\langle\Psi|$ (bra), defined in the vector space commonly referred to as Hilbert space $\mathcal{H}$ [124]. The basic properties of this vector space are based on the fulfillment of the inner product function $(\cdot,\cdot)$ projecting the two vectors $|\Psi\rangle$ and $|\Phi\rangle$ from $\mathcal{H}\times\mathcal{H}$ to the complex numbers $\mathbb{C}$. It allows to define the following basic properties of quantum states:

1. Positive semidefiniteness: $(|\Psi\rangle,|\Psi\rangle) \geq 0$: The inner product of $|\Psi\rangle$ with itself is positive definite.

2. Hermiticity: $(|\Psi\rangle,|\Phi\rangle) = (|\Phi\rangle,|\Psi\rangle)^*$.

3. Sesquilinearity: $(|\Psi\rangle,\sum_i \lambda_i|\Phi\rangle_i) = \sum_i \lambda_i(|\Psi\rangle,|\Phi\rangle_i)$: The inner product is linear in the second and semilinear in the first vector.

They allow to define other fundamental properties of quantum theory. One of these properties, the requirement that the probability distribution of any quantum state $|\Psi\rangle$ is normalized to 1, is met by defining the norm of a state as $|||\Psi\rangle|| = \sqrt{\langle\Psi|\Psi\rangle}$. Correspondingly, the state is described in the normalized form as $|\Psi\rangle/|||\Psi\rangle||$. Two states $|\Psi\rangle$ and $|\Phi\rangle$ are orthogonal in their Hilbert spaces if $\langle\Psi|\Phi\rangle = 0$ holds.
Note that requirement (3) allows to define the fundamental axiom of quantum theory, the superposition principle:

- If $|\Psi_1\rangle$ and $|\Psi_2\rangle$ are two states of the Hilbert space $\mathcal{H}$, the superposition of both states $\alpha|\Psi_1\rangle + \beta|\Psi_2\rangle$ is a valid state defined in the same space $\mathcal{H}$ (with $|\alpha|^2 + |\beta|^2 = 1$).

For a 2 dimensional Hilbert space $\mathcal{H} = \mathbb{C}^2$ a qubit state can be defined by using the basis $|0\rangle = (1,0)$ and $|1\rangle = (0,1)$. Here, a superposition state can be expressed as $|\Psi\rangle = \alpha|0\rangle + \beta|1\rangle$. A generalization of the scheme is to define states in Hilbert spaces $\mathcal{H} = \mathbb{C}^d$ of arbitrary dimension $dim(\mathcal{H}) = d$. These states, commonly denoted as qu*d*it states, are superpositions of d dimensional basis states $|0\rangle = (1,0,...,0)$, $|1\rangle = (0,1,...,0)$,...,$|d-1\rangle = (0,0,...,1)$

$$|\Psi_d\rangle = \sum_{k=0}^{d-1} c_k|k\rangle, \tag{1}$$

with a normalization of the coefficients according to $\sum_k^{d-1} |c_k|^2 = 1$.
It is the aim of this work to study the properties of qu*d*it states in more detail, by applying appropriate measurements on states embedded in d dimensional Hilbert spaces $\mathcal{H}_d$. To do so, a generalized framework for describing the measurement process as an interaction between a macroscopic measurement device and a quantum system has to be considered. Here, a central postulate in quantum mechanics, the **measurement postulate** (here presented in its simplified form for projection measurements), addresses this problem by stating:

- A quantum measurement can be represented by a projection operator $P_k = P_k^2$ which is used to acquire the knowledge about the probability distribution of a given state $|\Psi\rangle$ according to $p_k = \langle\Psi|P_k|\Psi\rangle = |c_k|^2$.
- A measurement P_k projects the state $|\Psi\rangle$ to $|\Psi\rangle_k = P_k|\Psi\rangle / \sqrt{p_k}$
- The projectors P_k fulfill the completeness relation $\sum_k P_k = \mathbb{I}$ if P_k corresponds to a (tomographically) complete set.

A straightforward way to describe a general set of projection operators $\{P_k\}$ defined on $\mathcal{H}_d$ is by decomposing it in the eigenstates $\{|k\rangle\}$ it projects to. For example, as a projector $P_k = |k\rangle\langle k|$ onto the eigenstate $|k\rangle$ where $|k\rangle\langle k|$ denotes the outer product of $|k\rangle$. Similarly, any operator on $\mathcal{H}_\lceil$ can be represented by a linear combination $\hat{O} = \sum_k c_k P_k$ with c_k corresponding to the eigenvalues of the decomposition.
The projector formalism describes another fundamental property of quantum physics: The measurement outcomes associated to a specific observable applied on a given quantum state $|\Psi\rangle$ are distributed according to a discrete probability distribution $p_k = |c_k|^2$: For finite dimensional Hilbert spaces, such as the ones considered in this work, the finite number of basis states defines the number of discrete modes contributing to $|\Psi\rangle$. It allows to describe a state by a classical continuum of modes only in the case of an infinite dimensional Hilbert space.
A set of commonly used projection measurements can be represented by using projectors defined by using the Pauli-spin basis, which for didactical purposes are described as

$$\begin{aligned} \sigma_x &= |0\rangle\langle 1| + |1\rangle\langle 0| \\ \sigma_y &= |0\rangle\langle 1| - i|1\rangle\langle 0| \\ \sigma_z &= |0\rangle\langle 0| - |1\rangle\langle 1| \end{aligned} \tag{2}$$

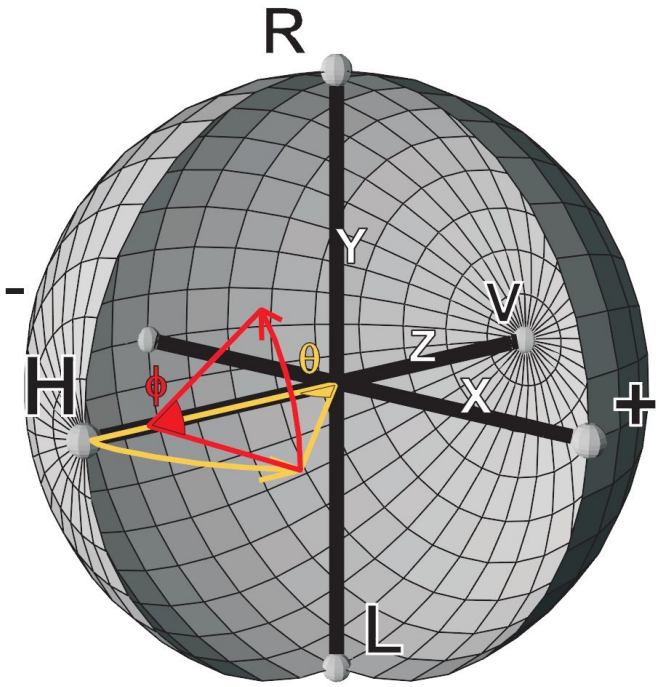

Figure 1: Representation of the Bloch sphere with a pure state described as a vector pointing to its surface (from [82]). It is useful to parameterize each vector in the eigenbases $|0\rangle/|1\rangle$ of σ_z, $|+\rangle/|-\rangle$ of σ_x and $|R\rangle/|L\rangle$ of σ_y.

At this point the Bloch representation of pure states (see Fig. 1) demonstrates to be useful as any point on the sphere corresponds to the pure state $|\Psi\rangle$ and can be described in the two dimensional basis $|0\rangle/|1\rangle$ which is the eigenbasis of the σ_z operator, $|+\rangle = 1/\sqrt{2}(|0\rangle + |1\rangle)/|-\rangle = 1/\sqrt{2}(|0\rangle - |1\rangle)$, the eigenbasis of σ_x and $|R\rangle = 1/\sqrt{2}(|0\rangle + i|1\rangle)/|L\rangle = 1/\sqrt{2}(|0\rangle - i|1\rangle)$ the eigenbasis of σ_y.

The determination of the probabilities p_k requires the measurement over many identically prepared states and identical projection measurements. The observed frequencies f_k correspond exactly to the probabilities only in the limit of an infinite number of repetitions (Born's rule [179]), and correspond in average to $p_k = \langle\Psi|P_k|\Psi\rangle = \langle\Psi|P_k^2|\Psi\rangle = ||P_k|\Psi\rangle||^2$ for a projection measurement P_k applied on $|\Psi\rangle$.

So far, quantum states and the measurements applied on them have been described by using the vector formalism: A state is described as a point on a unit Bloch sphere, in the case that the states are **pure**, while a state defined as a point within the sphere is denoted as **mixed**.

In order to further clarify the distinction between pure and mixed states the concept of a density matrix ρ is introduced. Using a set of pure states $|\Psi_k\rangle$ prepared with probabilities p_k the density matrix is defined as

$$\rho = |\Psi\rangle\langle\Psi| = \sum_k p_k |\Psi_k\rangle\langle\Psi_k|. \tag{3}$$

Here, a mixed state is in the state $|\Psi_k\rangle$ with probability p_k, while for a pure state the state can be decomposed into only one component $\rho = |\Psi\rangle\langle\Psi|$ with

probability 1.
An important property of a density operator is that for any ensemble of states and probabilities $\{P_k, |\Psi_k\rangle\}$ it fulfills the **trace condition** $tr(\rho) = 1$. This formalizes the requirement that the state $|\Psi\rangle$ is completely determined by the probability distribution p_k. Further on, the **positivity condition** $rho \geq 0$ has to hold, stating that all probabilities are positive.
Making use of the definition of a projection measurement, it is easy to observe that any (projection) measurement operator P_k acting on $|\Psi\rangle$ can be described as a matrix. In this picture, the probability to observe the state $|\Psi\rangle$ in the state projected on by P_k simplifies to the evaluation of the trace $p_k = Tr(P_k|\Psi\rangle) = \langle\Psi|P_k|\Psi\rangle$.
In the case of the Pauli spin operator

$$\sigma_z = \begin{pmatrix} 1|0\rangle\langle 0| & 0|0\rangle\langle 1| \\ 0|1\rangle\langle 0| & -1|1\rangle\langle 1| \end{pmatrix} \tag{4}$$

the projector on the eigenvector $|0\rangle$ with eigenvalue $+1$ is given by $(\mathbb{1} + \sigma_z)/2$. That definition can be generalized to any particular Pauli spin direction by defining a projector as

$$|\Pi\rangle = \frac{1}{2}(\mathbb{1} \pm \vec{n} \cdot \vec{\sigma}) \tag{5}$$

along an arbitrary direction $\vec{n}$ with $|\vec{n}| = 1$.
Using this notation allows to simplify the calculation of the probability that the state $|\Psi\rangle = 1/\sqrt{2}(|0\rangle + |1\rangle)$ is projected onto $|0\rangle$ as

$$P_{|0\rangle} = Tr(\rho 0\rangle\langle 0|) = Tr(|\Psi\rangle\langle\Psi|0\rangle\langle 0|) = \frac{1}{2} \tag{6}$$

$$\tag{7}$$

The usefulness of the density matrix formalism comes into play again as the density matrix ρ of any qubit state can be defined as a linear combination of a complete set of basis operators (see section 5.1 for a detailed desciption). One such basis is the Pauli basis, allowing to decompose a one-qubit state ρ according to

$$\rho = (\mathbb{1} + \sum_{i=x,y,z} r_i\sigma_i)/2 = (\mathbb{1} + \vec{r}\vec{\sigma})/2 \tag{8}$$

with suited coefficients r_i.

Again, in order to generalize the scheme to d dimensional Hilbert spaces a pure density matrix ρ is described by a $d \times d$ dimensional matrix generated by the outer product $|\Psi_d\rangle\langle\Psi_d|$ of a d dimensional state $|\Psi_d\rangle$. Operators acting on these states will be described in the next section. Concrete examples of density matrices for qu*d*it states will be presented in 5.1.

2.1.2 *Bases for d dimensional Hilbert spaces*

In order to find a generalized form of operators acting on d dimensional Hilbert spaces it is useful to consider the Pauli spin operators described before as the generators of the special unitary Lie algebra $\mathcal{SU}(d)$ in the case of $d = 2$. For arbitrary dimension d, general properties of the group are that the d^2 generators it consists of fulfill the commutator relation $[\hat{G_{ij}}, \hat{G_{kl}}] = \delta_{jk}\hat{G_{il}} - \delta_{il}\hat{G_{kj}}$. Similarly, the condition $\hat{N} = \sum_i^d G_{ii}$ fulfilling $[\hat{N}, \hat{G_{ij}}] = 0$

allows to reduce the number of independent generators to $d^2 - 1$. A prominent example of generators are the 8 Gell-Mann generators for 3 dimensional states [54].
Nonetheless, this work will make use of operators whose eigenstates form maximally unbiased bases (MUB) [183, 184, 185]. Here, the terminology of unbiased bases refers to the property that any eigenvector $|v_i\rangle$ of a basis has a minimal overlap with any other vector $|u_j\rangle$ of another basis. This corresponds to the extreme case in which projectors defined in these bases project onto states which don't share the other eigenbasis. In the mathematical formalism this can be expressed by the fact that they correspond to complementary measurements, for which no simultaneous measurement results can be obtained [156]. Concretely, the overlap for maximally unbiased bases is $|\langle v_i|u_j\rangle| = 1/\sqrt{d}$.
Formally, for $d > 2$ the basis vectors are defined as

$$|j_m\rangle = \frac{1}{\sqrt{d}} \sum_{s=0}^{d-1} e^{i2\pi/d(js+s^2)} |s\rangle \tag{9}$$

and it can be shown that for a given space of dimension d there exist maximally up to $d+1$ mutually unbiased bases.
The usefulness of choosing MUBs comes into play for the tomographic reconstruction of a quantum state ρ [3], for the application of quantum key distribution schemes [32] or for the observation of higher dimensional EPR-Bell correlations [188].

It will be shown that the d dimensional states prepared in this work can be analyzed by using these bases (see 4.2).
The decomposition of a density matrix ρ in MUB operators is possible. In a similar fashion as in the 2 dimensional case (8), any complete operator basis defined in a d dimensional Hilbert space can be used for that purpose. It is for example uniquely defined by the full set of $d + 1$ MUBs, by expanding the density matrix ρ in terms of the corresponding MUB operators $\hat{O}_i$. Similar representations in an operator basis spanned by MUBs defined in a 2 dimensional Hilbert space will be used in this work (see 5.1).

2.1.3 *Composite systems and entanglement*

Several features of quantum mechanics, displaying the most striking departure from classical physics, come into play when considering composite quantum systems. Here, a bipartite maximally entangled state consisting of two qu*d*its defined in a 2x*d* dimensional Hilbert space $\mathcal{H}_1^d \otimes \mathcal{H}_2^d$ can be given by

$$|\Psi_d\rangle = \frac{1}{d} \sum_{k=0}^{d-1} |k\rangle_A |k\rangle_B. \tag{10}$$

In this notation, $|k\rangle_A$ and $|k\rangle_B$ corresponds to bases in the d dimensional Hilbert spaces $mathcal H_A^d$ and $mathcal H_B^d$ corresponding to the two states distributed to the two parties, Alice and Bob. Then, entanglement refers to the fact that the composite state $|\Psi_d\rangle \in \mathcal{H}_A^d \otimes \mathcal{H}_B^d$ cannot be written as

$$|\Psi_d\rangle \neq |\Psi_A\rangle \otimes |\Psi_B\rangle, \tag{11}$$

while, in contrast, a separable state can be decomposed according to $|\Psi_d\rangle = |\Psi_A\rangle \otimes |\Psi_B\rangle$.
This property is generalized for mixed states, i.e. a state ρ is entangled if

$$\rho \neq \sum_i p_i \rho_{A,i} \otimes \rho_{B,i}, \tag{12}$$

i.e the composite state cannot be described as the tensor product of both states it is composed of [178].
It is possible to quantify the entanglement using the von Neumann entropy of the reduced state ρ_A:

$$S = -Tr\rho_A log\rho_A = -\sum_n p_{A,n} log_2 p_{A,n}. \tag{13}$$

Here, for a probability distribution $p_{A,n}$ with only one term being equal to 1, i.e the subsystem A is a pure state, the reduced entropy is 0. The state is fully determined. Similarly, maximal entanglement refers to the case in which the reduced density matrices of the states are maximally mixed, i.e. the probabilities have the same value $p_{A/B,n} = 1/d$. Equivalently the entropy of the reduced states is maximal $S_{A/B} = log(d)$ if the entangled state $|\Psi_d\rangle$ is pure.
At this point, the striking features of quantum entanglement already lead to intrepretations not possible to reconcile with a classical description of a the world:
The results obtained from the von Neumann entropy lead to the interpretation that, prior to the measurement only the composite maximally entangled state encoded in d dimensions is determined. In contrast, the reduced states $|\Psi_A\rangle$ and $|\Psi_B\rangle$ are maximally undetermined. Making use again of the measurement postulate of quantum mechanics, a projection measurement on Alice's state $|k\rangle$ will project the bipartite state $|\Psi\rangle$ onto $|\Psi_k\rangle = |k\rangle_A |k\rangle_B$. This corresponds to the projection onto a pure state with full knowledge about Alice's and Bob's respective locally defined states. A usual interpretation of this mathematical property of quantum mechanics is based on the collapse of the two-photon wavefunction describing the two-particle state [20].
That a measurement performed on the first subystem's state would allow to determine the state of the second party, independently of the distance between both systems has propelled the research on this striking feature called entanglement.

2.1.4 *EPR paradox, Bell inequality and entanglement*

It was Einstein, together with Podolski and Rosen [44] who conceived a fundamental discrepancy between the properties of composite quantum states and of classical systems (denoted as the EPR paradoxon). They devised a Gedankenexperiment with two particles sharing the same entangled quantum state and each particle distributed to two distinct parties. Further, they devised that these parties can perform a measurement on the momentum and the position of their respective particles. Due to momentum conservation, it is possible for each party to predict the momentum of the other party. It is here, that a discrepancy between the prediction of a classical theory and quantum theory was devised. This arises once the observed measurement outcomes are to be described by an *element of reality* allowing to predict

them with full certainty. Nevertheless, this requirement is in contradiction to the postulates of quantum mechanics such as the Heisenberg uncertainty relation applied on non-commuting observables, such as the position and momentum. If, for example the position of a particle can be determined exactly, its corresponding non-commuting observable, the momentum, will be maximally undetermined, i.e. both properties are assumed to have no simultaneous reality. In this scenario, they devised a paradoxon between two assertions made by quantum theory: That the underlying wavefunction offers a complete description of the state and that two physical results corresponding to non-commuting observables cannot have simultaneous reality. Concretely, in the example of a two-particle state, the first assumption would lead to the determination of the second particles position (momentum) once the position (momentum) of the first particle was determined precisely. Both observables would have simultaneous reality, a contradiction with the statements of quantum theory.
It was 30 years later that this question of declared philosophical relevance could be be put under experimental scrutiny. It was the seminal work by J.S. Bell which allowed to devise experiments able to discard specific models describing the properties of quantum systems cited previously [13]. Concretely, he devised an inequality, in literature coined as *Bell inequality*, able to determine the bounds any local and realistic theory can fulfill. These are theories where measurement outcomes obtained at space-like separated distances from each other are determined by hidden variables. The requirement of locality was needed to be in accordance with the predictions of special relativity: A measurement outcome observed at one site should be independent of the transformations applied at the other site. Bell showed that these predictions were in contradiction with the ones given when observing entangled states. In this case a violation of the inequality would be possible and would allow to disvalidate local hidden variable theories to explain the physical phenomena associated to these states. The balance was finally inclined towards quantum theory, as demonstrated first by Freedman et al. [53] and later on by Aspect et al. [9, 10] based on Bell inequalities developed by Clauser et al. [37, 36]. In consequence, many fundamental epistemological questions were raised about nature [116, 14].
The main source for these interpretational problems lies in the definition of the wavefunction describing entangled states. Concretely, the wavefunction is required to have a correspondence to a physical quantity as specified by a realistic theory: The measurement of the respective photon's state will instantly determine the state of the paired photon, apparently violating the condition of locality. This seemingly unsolvable paradox has lead to different interpretations. To mention only the most prominent ones, the Copenhagen version rejects the realistic interpretation of the wavefunction, in favor of a local description. In full contrast to this program, the theory presented by Bohm aims at offering a realistic interpretation of the wavefunction, while explicitly stating that quantum theory is required to be intrinsically nonlocal [18, 19].

2.2 ENCODING OF ENTANGLEMENT INTO DIFFERENT PHOTONIC DEGREES OF FREEDOM

A photon can be described as a wave packet with a transverse oscillation direction $\vec{p}$ (polarization), wave vector $\vec{k}$ (momentum) and frequency ν (en-

ergy). Futhermore, it is a necessary condition for preparing photonic entangled states that at least two photons are created and that the quantities corresponding to these degrees of freedom are conserved during the two-photon emission process. The process of spontaneous parametric downconversion (SPDC) [168] has proven to be a reliable and efficient source for the emission of correlated (multi-) photonic states: Momentum and energy conservation warrants that during the nonlinear conversion of n photons, the created $2n$ photons are intrinsically correlated in these degrees of freedom. And, with more relevance for this work, also in the respective emission times.

For the purpose of encoding quantum states in high dimensional Hilbert spaces one can make use of the spatial distribution of the photon's momentum, concretely the orbital angular momentum (OAM) [48, 133, 109] or the linear momentum of SPDC photon pairs [31].
In general, the encoding of quantum states in several degrees of freedom allowed to prepare photon pairs in higher dimensional product Hilbert spaces denoted as hyperentangled [12]: Here, the state space is composed of the tensor product of entangled states encoded in the different degrees of freedom. Furthermore, it is possible to entangle the states between the degrees of freedom by suited entangling operations [31].
Nevertheless, it could be shown that practical implementations of these states in the field of quantum cryptography were restricted. Particularly, when they require the transmission of the physical information carriers over large distances. For a free space transmission the encoded quantum states could be affected by variations in the refractive index of the air [135, 170]. Active compensation schemes for a rotation of the quantum states encoded in the polarization or angular momentum degree of freedom are required when the free space transmission is chosen. Similar limitations apply to the transmission over optical fibers, for which the transmission of only one spatial mode makes it unsuitable for OAM states.

2.3 TIME-ENERGY ENTANGLEMENT

Franson experiment— A suitable alternative not affected by the limitations listed previously is to encode quantum states into the emission time degree of freedom of photon pairs: This scheme was originally proposed by Franson [52] by using the properties of atomic cascade sources emitting emission time correlated photons, i.e. photons emitted within the emission time uncertainty defined by the linewidth of an atomic transition. The properties required for the generation of these states are fulfilled by SPDC processes (see 3.1 for a detailed description): The simultaneous emission of both photons of a pair guarantees the photons to be correlated in their emission times.
As pointed out by Franson, it is now possible to devise the situation in which the emission times of the two-photon pairs are undetermined up to an uncertainty Δt predicted by the (Heisenberg uncertainty)relation $\Delta E \cdot \Delta t \geq \hbar/2$ [1]. This emission time uncertainty Δt is large in the case the energy uncertainty ΔE of the incoming pump photon is small.
The emission time uncertainty Δt can be described in terms of the coherence

1 It is to note that no operator can be associated to the time variable, therefore the uncertainty relation cannot be derived from the commutation relation neither associate a time eigenstate to it. Furthermore, the uncertainty is motivated by phenomological observations regarding the linewidth limited emission time uncertainty for an atomic process.

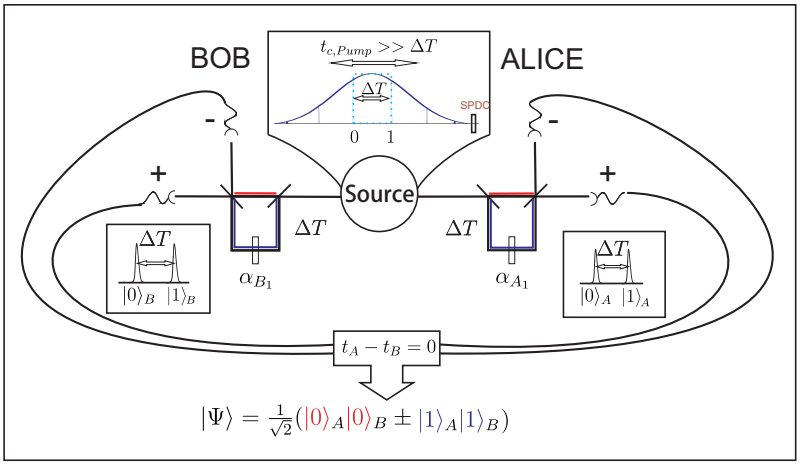

Figure 2: Scheme for the setup encoding 2 time-energy entangled qubits. The emission of a time-energy correlated photon pair is possible at any of two emission times 0 and 1 separated by a time delay ΔT. The choice of a time delay orders of magnitude smaller than the coherence time of the pump process allows to ensure the coherence of the photon pairs emitted. Next, each photon of a pair is distributed to one of the two separated interferometers at the disposal of both parties, Alice and Bob. They are used to project each photon's state onto the interferometer eigenstates $|0\rangle_A + e^{i\alpha_A}|1\rangle_A$ and $|0\rangle_B + e^{i\beta_B}|1\rangle_B$. Subsequently, a coincidence measurement (at time delay 0) allows them to analyze the time-energy entangled Bell state $|\Psi\rangle = 1/\sqrt{2}(|0\rangle_A|0\rangle_B + e^{i(\alpha_A+\beta_B)}|1\rangle_A|1\rangle_B)$.

time $t_{c,Pump}$ of a light source (see inset of Fig. 2), which is a measure on the time the different spectral components of a wave still remain in phase. Using a monochromatic light source, with a tight distribution of the incoming frequency modes [103], a large emission time uncertainty is achieved, as described by the large coherence time $t_{c,Pump}$.

Under these conditions and by resorting to a suited two-photon source, a continuous range of two-photon modes can be coherently emitted, i.e. photon pairs emitted at different times $|t\rangle$, superposing to the state

$$|\Psi\rangle_S \propto \int_{-\infty}^{\infty} c(t)|t\rangle_A|t\rangle_B dt \tag{14}$$

with the weights described by the emission time distribution function $c(t)$.

Time-energy Entanglement between photon pairs— First, as described in Fig. 2, a pump photon can undergo the process of spontaneous parametric downconversion (described in further detail in 3.1), such that a pair of entangled photons is emitted at any of the emission times constrained within the coherence time $t_{c,Pump}$ of the source. The two photons are now distributed to 2 different parties, Alice and Bob.

Each party is provided with appropriate analysis devices measuring the coherence between photon pairs emitted at only 2 emission time modes 0 and 1 (denoted by times t_0 and $t_0 + \Delta T$ with a time difference of ΔT) selected out of the full range of emission time modes prepared in the source. The coherence between them can be tested if each party applies a delay

ΔT on each photon, respectively. For that purpose, they analyze each photon's state in the interferometer mode eigenbasis of two unbalanced two-path interferometers: $|0\rangle_{A/B} = |0\Delta T\rangle_{A/B}$ for the undelayed and $|1\rangle_{A/B} = |1\Delta T\rangle_{A/B}$ for the delayed path in units of the time delay ΔT present between the two emitted two-photon fields. For a 50/50 splitting ratio configuration of the interferometer beamsplitters, the photons will be projected to the superposition states $(|0\rangle_A + e^{i\alpha_A}|1\rangle_A)/\sqrt{2}$ and $(|0\rangle_B + e^{i\beta_B}|1\rangle_B)/\sqrt{2}$ (see Fig. 2). These have well defined relative phases α_A and β_B acquired between the delayed and undelayed paths. Additionally, each party projects the respective photon onto the interferometer output modes $|+\rangle$ and $|-\rangle$ depending on the interferometer output the photon has chosen, where finally the photons are detected.
It is important to choose a time delay ΔT orders of magnitude larger than the coherence times of the SPDC photons as this will allow to sort out first order interference effects: Both parties would observe a variation of their single photon detection rates as measured at the outputs of the interferometers depending on the relative phases α_{A_1} or β_{B_1} acquired between the single photon fields taking the short and long interferometer path.
Next, both parties are required to measure the detection times of the photons at the outputs of their interferometers. If additionally a coincidence analysis is performed (for the moment only a coincidence detection at output modes $|+\rangle_A|+\rangle_B$ will be considered) the state is projected onto the a superposition state spanned by the two-photon eigenbasis $|0\rangle_A|0\rangle_B$, $|0\rangle_A|1\rangle_B$, $|1\rangle_A|0\rangle_B$ and $|1\rangle_A|1\rangle_B$ states:

$$(|0\rangle_A + e^{i\alpha_A}|1\rangle_A) \otimes (|0\rangle_B + e^{i\beta_B}|1\rangle_B) =$$
$$\frac{1}{2}(|0\rangle_A|0\rangle_B + e^{i\beta_B}|0\rangle_A|1\rangle_B + e^{i\alpha_A}|1\rangle_A|0\rangle_B + e^{i(\alpha_A+\beta_B)}|1\rangle_A|1\rangle_B) \tag{15}$$

In (15) 3 states can be discriminated by the relative delay in the detection: For a coincidence measurement at delay ΔT the emitted two-photon state is projected onto $|1\rangle_A|0\rangle_B$, for a delay of $-\Delta T$ to $|0\rangle_A|1\rangle_B$. More interestingly, for a delay of 0 the terms $|0\rangle_A|0\rangle_B$ attributed to both shortest arms and $|1\rangle_A|1\rangle_B$ corresponding to the long arms in the respective interferometers superpose to

$$|\Psi\rangle = \frac{1}{\sqrt{2}}(|0\rangle_A|0\rangle_B + e^{i(\alpha_A+\beta_B)}|1\rangle_A|1\rangle_B). \tag{16}$$

Here, the coherence between only two two-photon states delayed (i.e. taking the respective paths $|0\rangle_A|0\rangle_B$ and undelayed (i.e. taking the respective paths $|1\rangle_A|1\rangle_B$ with respect to each other, is tested.
Different approaches exist in order to avoid the required postselection of two-photon coincidence probabilities, either by the transformation of the contributing time modes into polarization modes [160] or by using a setup allowing to detect Alice's delayed (undelayed) photon together with Bob's undelayed (delayed) photon in the same detector, perfoming the postselection of unwanted events already locally [104]. The significance of the postselection procedure regarding the question if any local realistic model can describe the correlations observed will be discussed in section 4.2.2.

Coincidence function and visibility— If both parties agree to measure only in the detection time window $\Delta T = 0$, a variation of their coincidence count rates as a function of the respective phase settings α_A and β_B will be

observed.In order to evaluate the concrete coincidence function, it is necessary to resort again to describing the distribution of the incoming entangled emission time modes.
For the used analysis only the coherence between 2 emission-time modes with mode amplitudes $c(t_0)$ and $c(t_0 + \Delta T)$ at the respective emission times t_0 and $t_0 + \Delta T$ is tested. The coincidence probability is now evaluated as

$$P(\alpha_A, \beta_B) = |\langle \Psi | \Psi_S \rangle|^2 \propto (1 + V \cos(\alpha_A + \beta_B)). \tag{17}$$

Alice and Bob observe a variation of the coincidence count rates with the two-photon interference visibility V. Here, it is useful to choose the interferometric visibility as a figure of merit. For that purpose the two-photon intensities of either delayed $I_{|0\rangle_A|0\rangle_B} = |c(t_0)|^2$ and undelayed $I_{|1\rangle_A|1\rangle_B} = |c(t_0 + \Delta T)|^2$ probability amplitudes enter via

$$V = 2\frac{\sqrt{I_{|0\rangle_A|0\rangle_B} I_{|1\rangle_A|1\rangle_B}}}{I_{|0\rangle_A|0\rangle_B} + I_{|1\rangle_A|1\rangle_B}}. \tag{18}$$

As will be shown in 4.1.2 the visibility can be used to describe the generated entanglement quality. For maximally entangled states as aimed to be prepared in this work, the visibility is maximal for an equal amplitude of the respective two-photon fields.
Note, that the entanglement quality of the postselected state (Eq. 16) depends on the precision at setting the time delays $\Delta T = \Delta T_A = \Delta T_B$ chosen by each party. If they differ, the additional which-path information would enable both parties to distinguish between both superposing two-photon states $|0\rangle_A|0\rangle_B$ and $|1\rangle_A|1\rangle_B$.
Both parties can as well detect their respective photons at other outputs of their interferometers. For example for a detection at the $|+\rangle_A|+\rangle_B$ and $|-\rangle_A|-\rangle_B$ the state is projected into $|\Psi\rangle_{+,+} = |\Psi\rangle_{-,-} = \frac{1}{\sqrt{2}}(|0\rangle_A|0\rangle_B + e^{i(\alpha_A+\beta_B)}|1\rangle_A|1\rangle_B)$ while for different outputs $|+\rangle_A|-\rangle_B$ and $|-\rangle_A|+\rangle_B$ it is projected to $|\Psi\rangle_{+,-} = |\Psi\rangle_{-,+} = \frac{1}{\sqrt{2}}(|0\rangle_A|0\rangle_B - e^{i(\alpha_A+\beta_B)}|1\rangle_A|1\rangle_B)$. Here, the sign change -1 is attributed to the phase a two-photon state acquires by the reflection at the output beamsplitters of their respective interferometers: $(e^{i\pi/2})^2 = -1$.
Correlation measurements— For a choice $\alpha_A = \beta_B = 0$, the two-photon observables (after postselection) project onto the eigenstates of the $\sigma_x \otimes \sigma_x$ basis $\{1/\sqrt{2}(|0\rangle + |1\rangle); 1/\sqrt{2}(|0\rangle - |1\rangle)\}$. For a choice of $\alpha_A = \beta_B = \pi/4$ the eigenstates correspond to the ones defined for the σ_y basis $\{1/\sqrt{2}(|0\rangle + i|1\rangle); 1/\sqrt{2}(|0\rangle - i|1\rangle)\}$. Accordingly, it is possible to describe the projection measurements performed by both parties in the operator basis, as measurements constrained along the plane spanned by the σ_x and σ_y operators (in analogy for Bob's operator):

$$\frac{1}{2}(|0\rangle + e^{i\alpha_A}|1\rangle)(\langle 0| + e^{i\alpha_A}\langle 1|) = \frac{1}{2}(\mathbb{1} + \cos\alpha_A \sigma_x + \sin\alpha_A \sigma_y) = \frac{1}{2}(\mathbb{1} + \sigma(\alpha_A)). \tag{19}$$

This description is useful as it will enable to describe the correlations observed between both parties as a measurement [82] of

$$C(\alpha_A, \beta_B) = Tr[(\sigma(\alpha_A) \otimes \sigma(\beta_B))|\Psi\rangle_S\langle\Psi_S|] = \cos(\alpha_A + \beta_B). \tag{20}$$

As will be shown in 5.1, the evaluation of correlations enables to reconstruct tomographically the underlying quantum states.

2.4 TIME-ENERGY ENTANGLEMENT IN HIGH DIMENSIONAL HILBERT SPACES

Proposals for analyzing high dimensional emission time entangled states— It is the aim of this work to enhance the number of entangled two-photon modes, and, correspondingly, the dimension of the Hilbert space spanned by the quantum states. For this purpose, time-energy encoded states offer an intrinsic potential: Theoretical simulations could show that a high number of time-energy modes are available in typical SPDC sources (up to $\approx 10^6$) [7]. The task to prepare entangled qu*d*it states with an as high as possible number of modes is therefore reduced to the problem of finding a suited interferometric system. This is required to test the coherence of the emitted time modes with respect to each other.

Different approaches for making use of this scheme have been proposed. One of them is based on the scheme of multiport interferometers allowing to encode d dimensional maximally entangled states by using couplers equally distributing the incoming d modes into d output modes. Nevertheless, their scalability is restricted to low dimensional systems as each of the d interferometer arms needs to be interferometrically stable [163].

The scheme offers the advantage that the quantum states are directly prepared in d dimensional MUB bases (see 2.1.2) as the output state is defined according to $|\Psi'\rangle = \sum_{j=0}^{d-1} c_j|j\rangle$ with coefficients $c_j = \sum_k 1/\sqrt{d}e^{i2\pi jk/d}b_k$ (compare with the MUB bases of Eq. (9) for a d-mode input state $|\Psi\rangle = \sum_{k=0}^{d-1} b_k|k\rangle$ [188, 23].

Scheme of this work— In this work an alternative approach offering a better scaling of the dimensionality of the quantum states analyzed with the number of interferometer arms is presented and experimentally demonstrated (See Fig. 3).

Concretely, an interferometer scheme is used for exponentially, instead of linearly (as for the multiport scheme), multiplexing the number of time modes analyzed with the number of each additional interferometer arm. It is based on the consecutive application of 2x2 interferometer arm transformations onto the incoming d time modes. The resulting analyzed state is embedded within a Hilbert space which is increased by a factor of 2 with each additional interferometer arm. For the choice of up to 3 interferometer arms as performed in this work, the interferometers analyze up to 8 modes $|0\rangle, |1\rangle, ..., |7\rangle$ ($log_2(8) = 3$ bits). The states spanned by each interferometer arm can be described as $1/\sqrt{2}(|0\rangle_i + e^{\alpha_i}|1\rangle_i)$ with α_i corresponding to the relative phases acquired between the respective undelayed $|0\rangle_i$ and delayed $|1\rangle_i$ paths. The consecutive application of these transformations lead to the encoding of an 8 dimensional state

$$
\begin{aligned}
|\Psi^8\rangle = \frac{1}{\sqrt{2}}(|0\rangle_1 + e^{\alpha_1}|1\rangle_1) \otimes \frac{1}{\sqrt{2}}(|0\rangle_2 + e^{\alpha_2}|1\rangle_2) \otimes \frac{1}{\sqrt{2}}(|0\rangle_3 + e^{\alpha_3}|1\rangle_3) = \\
\frac{1}{2\sqrt{2}}(|0\rangle_1|0\rangle_2|0\rangle_3 + e^{\alpha_1}|1\rangle_1|0\rangle_2|0\rangle_3 + e^{\alpha_2}|0\rangle_1|1\rangle_2|0\rangle_3 + \\
e^{(\alpha_1+\alpha_2)}|0\rangle_1|1\rangle_2|0\rangle_3 + ... + e^{(\alpha_1+\alpha_2+\alpha_3)}|1\rangle_1|1\rangle_2|1\rangle_3) = \\
\frac{1}{2\sqrt{2}}(|0\rangle + e^{\alpha_1}|1\rangle + \\
e^{\alpha_2}|2\rangle + e^{(\alpha_1+\alpha_2)}|3\rangle + ... + e^{(\alpha_1+\alpha_2+\alpha_3)}|7\rangle). \quad (21)
\end{aligned}
$$

For simplification, at the last step the notation describing the 8 dimensional eigenstates has been abbreviated by the total number of delays acquired by a photon after traversing the corresponding interferometer paths. As the respective states $|0\rangle$,$|1\rangle$,...$|7\rangle$ are required to correspond to different modes, the time delays chosen for each interferometer arm have to be different by at least the coherence time of each photon. Only in this case single photon interference of the incoming photons can be avoided. Furthermore, the time delays have to be chosen such that they are multiples of a minimum time delay ΔT in order to enable the experimental discrimination of the encoded two-photon states (see 3.2). Interferometer arms are chosen here with time delays subsequently doubling the time delays acquired at the previous interferometers: ΔT, $2\Delta T$ and $4\Delta T$.
Alice and Bob are provided each with one multiarm interferometer used to analyze an 2x8 dimensional emission time entangled state. In order to ensure the coherence of the emitted two-photon modes, the coherence time of the pump source is chosen such that it surpasses the maximal time delay of $7\Delta T$ present between the 8 analyzed modes by many orders of magnitude.
If both parties use the interferometer systems they project the generated emission time correlated states onto $|\Psi^8\rangle_A \otimes |\Psi^8\rangle_B$, a superposition of up to 64 two-photon states. As these two-photon states are distinguishable by their relative detection times, Alice and Bob can detect entanglement if they project the 64 possible two-photon emission probabilities into 15 different time windows, defined for a specific relative delay between Alice's and Bob's detection times (see Fig. 4). The time delay associated to these detection time windows ranges from $-7\Delta T$ to $7\Delta T$.
For example for a choice of a time delay of $\Delta T = 0$ (and for a detection of the coincidence count rates at the $+_A+_B$ interferometer outputs corresponding to a projection onto $|+\rangle_A|+\rangle_B$) they will project their entangled two-photon state $\Psi_S\rangle$ defined in Eq.(2.3) into the 2x8 dimensional state

$$|\Psi_8\rangle_{+,+} = \frac{1}{2\sqrt{2}}(|0\rangle_A|0\rangle_B + e^{(\alpha_{A_1}+\beta_{B_1})}|1\rangle_A|1\rangle_B + e^{(\alpha_{A_2}+\beta_{B_2})}|2\rangle_A|2\rangle_B + e^{(\alpha_{A_1}+\beta_{B_1}+\alpha_{A_2}+\beta_{B_2})}|3\rangle_A|3\rangle_B + ... + e^{(\alpha_{A_1}+\beta_{B_1}+\alpha_{A_2}+\beta_{B_2}+\alpha_{A_3}+\beta_{B_3})}|7\rangle_A|7\rangle_B). \quad (22)$$

Evaluation of coincidence probability— The coincidence probability is evaluated for a projection onto the interferometer output modes $|+\rangle_A|+\rangle_B$ and $|-\rangle_A|-\rangle_B$. It varies as a function of the 6 phase settings acquired by both photons according to

$$P(\alpha_{A_1},\alpha_{A_2},\alpha_{A_3},\beta_{B_1},\beta_{B_2},\beta_{B_3})_{+,+} = |\langle\Psi_S|\Psi_8\rangle_{+,+}|^2 = |\langle\Psi_C|\Psi_8\rangle_{-,-}|^2 = \cos\frac{(\alpha_{A_1}+\beta_{B_1})}{2}^2 \cos\frac{(\alpha_{A_2}+\beta_{A_2})}{2}^2 \cos\frac{(\alpha_{A_3}+\beta_{B_3})}{2}^2. \quad (23)$$

For a detection at the output combinations $|+\rangle_A|-\rangle_B$ and $|-\rangle_A|+\rangle_B$ this results into an additional phase shift of π in the last term:

$$C(\alpha_{A_1},\alpha_{A_2},\alpha_{A_3},\beta_{B_1},\beta_{B_2},\beta_{B_3})_{+,-;-,+} = \cos\frac{(\alpha_{A_1}+\beta_{B_1})}{2}^2 \cos\frac{(\alpha_{A_2}+\beta_{A_2})}{2}^2 \sin\frac{(\alpha_{A_3}+\beta_{B_3})}{2}^2, \quad (24)$$

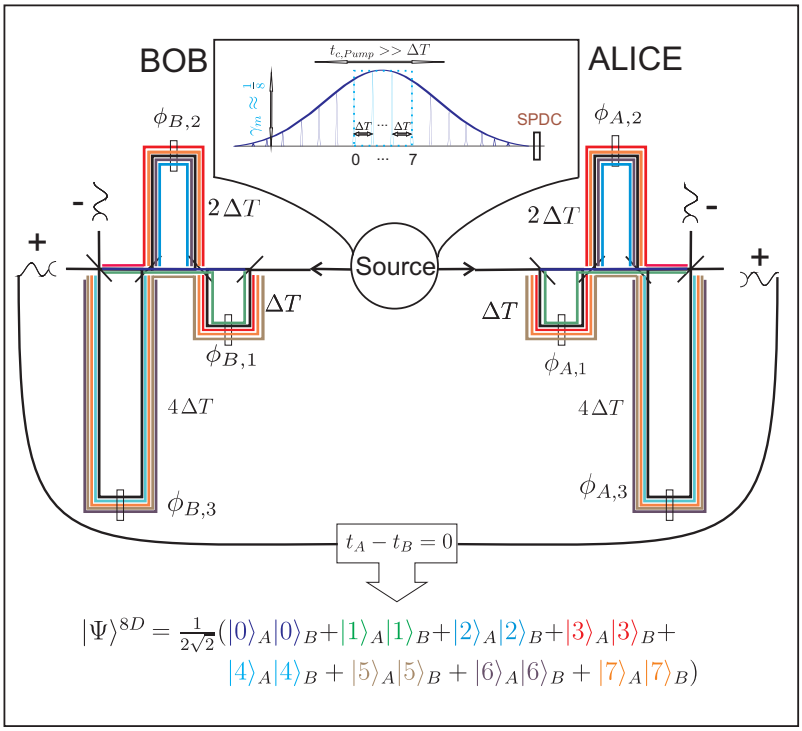

Figure 3: Scheme for the setup analyzing up to 2x8 dimensional time-energy entangled qu*d*its. The setup can be used to test the coherence between up to 8 different two-photon emission time modes present within the continuous range of two-photon emission times. They are coherent as long as the maximal time delay between them doesn't surpass the coherence time $t_{c,Pump}$ of the pump source. Under these conditions, both parties, Alice and Bob can make use of a 3 arm interferometer setup analyzing each photon of a pair in the 8 dimensional computational basis $|0\rangle$,$|1\rangle$,...$|7\rangle$ in units of the time delay ΔT acquired at any of the different paths through their respective interferometers. Finally, a measurement of coincidence count rates at time delay 0 allows both parties to analyze a 2x8 dimensional two-photon state $|\Psi_S\rangle = \sum_{k=0}^{7} |k\rangle|k\rangle$.

Here, the dichotomic measurements onto two different interferometer outputs $|+\rangle$ and $|-\rangle$ correspond only to 2 different projections of the 8 dimensional photon state encoded into each party's photon. This number of projections is insufficient to provide the full analysis of a 2x*d* dimensional two-photon state as this requires the projection of each photon onto at least 8 different basis states (see 2.1.2). Different approaches suited for overcoming this limitation will be described in 4.2.
A major advantage of the scheme is that it is possible to analyze the encoded states in specific subspaces spanned by the 2x8 dimensional full computational basis defined by the analysis. For that purpose it is necessary to resort to coincidence detections at time delays different than 0, as will be shown subsequently.

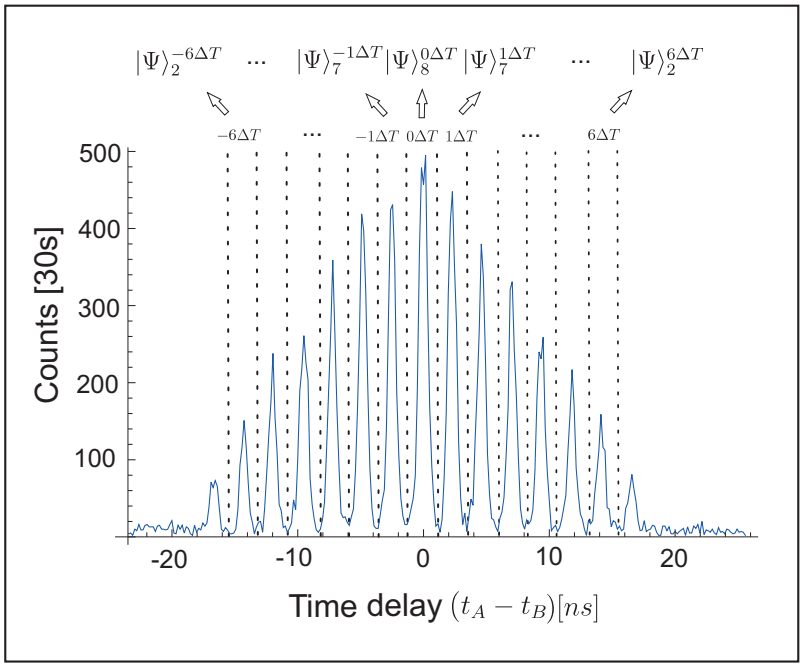

Figure 4: Typical coincidence time distribution observed for a 2x8 dimensional analysis of a two-photon time-energy entangled photon pair. The coincidences are distributed along 15 different time windows, allowing the analysis of time-energy entangled states with a dimensionality of up to 2x8.

2.4.1 *Time-energy entanglement in d<8 dimensional Hilbert spaces*

It is possible to discriminate between up to 15 coincidence time distributions for the 2x8 dimensional analysis chosen by both parties as depicted for a typical measurement run in Fig. 4.

The coincidences are probabilistically distributed by the interferometer setup used by both parties such that the number of contributing two-photon amplitudes varies between 1 to 8 for time delays ranging from $\pm 7\Delta T$ to $0\Delta T$. The time separation between coincidences distributed between different windows corresponds to the time delay ΔT. The measurement of coincidence count rates at different time delays equals to the projection of the emitted two-photon pairs onto lower dimensional states. These correspond to states with dimensions ranging from 2x1 to 2x8 encoded within the computational basis spanned by the 2x8 dimensional two-photon analysis. Concretely, for time delays ΔT (the discussion for negative time delays is equivalent) a 2x7 dimensional state is encoded as

$$|\Psi\rangle_7^{1\Delta T} = \frac{1}{\sqrt{7}}(e^{\alpha_{A_1}}|1\rangle_A|0\rangle_B + e^{(\alpha_{A_2}+\beta_{B_1})}|2\rangle_A|1\rangle_B + e^{(\alpha_{A_1}+\alpha_{A_2}+\beta_{B_2}+\pi)}|3\rangle_A|2\rangle_B + e^{(\alpha_{A_3}+\beta_{B_1}+\beta_{B_2})}|4\rangle_A|3\rangle_B + ... + e^{(\alpha_{A_1}+\alpha_{A_2}+\alpha_{A_3}+\beta_{B_2}+\beta_{B_3}+\pi)}|7\rangle_A|6\rangle_B). \quad (25)$$

In comparison, for delays $2\Delta T$ and $3\Delta T$ the analysis projects onto the 2x6 and 2x5 dimensional states

$$|\Psi\rangle_6^{2\Delta T} = \frac{1}{\sqrt{6}}(e^{\alpha_{A_2}}|2\rangle_A|0\rangle_B + e^{(\alpha_{A_1}+\alpha_{A_2}+\beta_{B_1}+\pi)}|3\rangle_A|1\rangle_B + e^{(\alpha_{A_3}+\beta_{B_2})}|4\rangle_A|2\rangle_B + e^{(\alpha_{A_1}+\alpha_{A_3}+\beta_{B_1}+\beta_{B_2}+\pi)}|5\rangle_A|3\rangle_B + ... + e^{(\alpha_{A_1}+\alpha_{A_2}+\alpha_{A_3}+\beta_{B_1}+\beta_{B_3})}|7\rangle_A|5\rangle_B) \quad (26)$$

and

$$|\Psi\rangle_5^{2\Delta T} = \frac{1}{\sqrt{5}}(e^{(\alpha_{A_1}+\alpha_{A_2}+\pi)}|3\rangle_A|0\rangle_B + e^{(\alpha_{A_3}+\beta_{B_1})}|4\rangle_A|1\rangle_B + e^{(\alpha_{A_1}+\alpha_{A_3}+\beta_{B_2}+\pi)}|5\rangle_A|2\rangle_B + e^{(\alpha_{A_1}+\alpha_{A_3}+\beta_{B_1}+\beta_{B_2}+\pi)}|6\rangle_A|3\rangle_B + e^{(\alpha_{A_1}+\alpha_{A_2}+\alpha_{A_3}+\beta_{B_3}+\pi)}|7\rangle_A|4\rangle_B. \quad (27)$$

For 4 contributing two-photon modes, as registered for a time delay of $4\Delta T$ the analyzed 2x4d state is

$$|\Psi\rangle_4^{4\Delta T} = \frac{1}{2}e^{(\alpha_{A_3}+\beta_{B_3})}(|4\rangle_A|0\rangle_B + e^{(\alpha_{A_1}+\beta_{B_1})}|5\rangle_A|1\rangle_B + e^{(\alpha_{A_2}+\beta_{B_2}+\pi)}|6\rangle_A|2\rangle_B + e^{(\alpha_{A_1}+\alpha_{A_2}+\beta_{B_1}+\beta_{B_2}+\pi)}|7\rangle_A|3\rangle_B) \quad (28)$$

where a change in the phase α_{A_3} performed on Alice's 3rd interferometer arm doesn't influence the analysis. This is also the case for the 2x3 dimensional state analyzed at a delay of $5\Delta T$:

$$|\Psi\rangle_3^{5\Delta T} = \frac{1}{\sqrt{3}}e^{\alpha_{A_3}}(e^{\alpha_{A_1}}|5\rangle_A|0\rangle_B + e^{(\alpha_{A_2}+\beta_{B_1}+\pi)}|6\rangle_A|1\rangle_B + e^{(\alpha_{A_2}+\beta_{B_2}+\pi)}|7\rangle_A|2\rangle_B). \quad (29)$$

Finally, the 2x2d dimensional state analysis is restricted to measurements performed on Alice's and Bob's 1st interferometer arms:

$$|\Psi\rangle_2^{6\Delta T} = \frac{1}{\sqrt{2}}e^{(\alpha_{A_2}+\alpha_{A_3})}(|6\rangle_A|0\rangle_B + e^{(\alpha_{A_1}+\beta_{B_1})}|7\rangle_A|1\rangle_B). \quad (30)$$

The 2x1 dimensional state postselected at a time delay of $7\Delta T$ is of no interest here, as it is intrinsically separable: $|\Psi\rangle_1^{7\Delta T} = \frac{1}{\sqrt{2}}e^{(\alpha_{A_1}+\alpha_{A_2}+\alpha_{A_3})}|7\rangle_A \otimes |0\rangle_B$.

The presented scheme for encoding qu*d*it states offers a simple procedure to increase the complexity of the encoded quantum states. Only by agreeing on a different delay between their registered coincidence count rates, Alice and Bob can apply a projection measurement on states of varying dimensionality ranging up to 2x8.

2.4.2 *Time bin entanglement of Qudits*

Full analysis of qudit states— Of crucial importance for the optimal detection of entanglement is that the analysis described in the previous section is

able to access the full Hilbert space of the prepared emission time entangled modes. For example, for the analysis of the 2x8 dimensional state of Eq.(22) each party is provided with 3 independent relative phase settings, inferior to the number of 8 emission time modes between which the coherence is tested. For example, the 2x8 dimensional state can be analyzed fully if the analysis projects it onto

$$|\Psi\rangle_8 = \sum_{k=0}^{7} e^{i(\alpha_{A_k}+\beta_{B_k})}\lambda_k|k\rangle_A|k\rangle_B \tag{31}$$

with the 7 independent phase settings α_{A_k} and β_{B_k}.
Further on, the present setup doesn't allow to arbitrarily manipulate the coupling coefficients $\gamma_k = |\lambda_{A_k}|^2 = |\lambda_{B_k}|^2$. These are given by the respective weights λ_{A_k} and λ_{B_k} describing the weights with which the different emission time modes are superposed to each other. Here, a change in the coupling strength would require the beamsplitters building up the interferometers to provide variable splitting ratios.
A manipulation of all qu*d*it states amplitudes and phases can be achieved by making use of time-bin entanglement based on pulsed sources:
Time bin entanglement— Following similar arguments as the ones used to describe time-energy correlated states, it is experimentally challenging to analyze time-energy entanglement for pulsed instead of continuous wave sources: The coherence time of the emission process is intrinsically restricted to the pulse duration t_P, limiting the time delays of the interferometers to lie within t_P. This is a challenging task in view of the limited timing resolution of typical photonic detection devices.
An alternative has been devised by resorting to additional interferometer systems placed before the two-photon source. These allow to prepare a pump pulse emitted by the source in a coherent superposition of two or more pulses [110]. In the concrete case of an 2x8 dimensional state analysis as described in the previous section, the coherent preparation of up to 8 pulses pumping a SPDC source is required (Fig. 5).

A more elaborate treatment for this process is given in [142] and restricted here to the example of 2x8 dimensional systems:
For the purpose of preparing time bin correlated states it is possible to use unbalanced interferometer systems with the same construction as used for the analysis of 2x8 dimensional time-energy entangled states. A pump pulse is split into 8 pump pulses delayed by ΔT with respect to each other by making use of the interferometer system depicted in Fig. 5. They are used the prepare a pump photon state in the eigenbasis $|0\rangle_P$, $|1\rangle_P$,...,$|7\rangle_P$ as a function of the time delays t_k acquired:

$$|\Psi\rangle_8^P = \frac{1}{2\sqrt{2}}\sum_{k=0}^{7}|t_k\rangle_P \tag{32}$$

Any of the 8 resulting pulses can trigger the downconversion of a pump pulse photon into a photon pair. As the process maintains the coherence present before a time bin entangled two-photon state is emitted:

$$|\Psi\rangle_8^{AB} = \frac{1}{2\sqrt{2}}\sum_{k=0}^{7}|t_k\rangle_A|t_{k'}\rangle_B. \tag{33}$$

In contrast to a source with a coherence time surpassing the total time delay acquired between all 8 two-photon emission time modes, no correlations

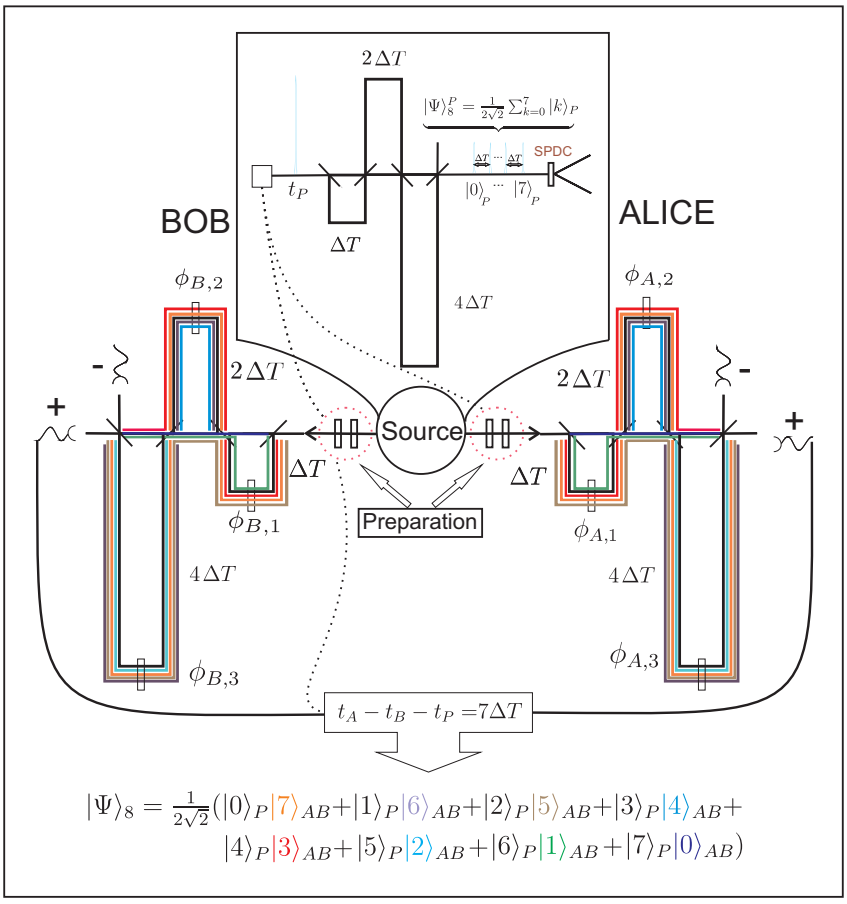

Figure 5: Scheme for the preparation of time-bin entangled two-photon states in dimensions up to 2x8. The source consists of a series of up to 8 pump laser pulses described by $|\Psi\rangle_8^P = 1/\sqrt{8}\sum_{k=0}^{7}|k\rangle_P$ into which the pump pulse is split up by making use of a series of unbalanced interferometer arms. Each pulse can be used to prepare a SPDC photon pair, which is analyzed by sending each photon to two parties, Alice and Bob, provided with an interferometer system used to analyze each photon separately. In order to obtain an entangled state in 2x8 dimensions, both parties are required to trigger their respective coincidence count rates to the emission time of a pump pulse and to further on discriminate photons with a relative time delay of 0. The resulting time bin state is described in terms of the paths a pump photon has traversed through the pump interferometer and, subsequently, the paths a photon pair has traversed through the analysis according to $|\Psi\rangle_8^{P,A/B} = \sum_{k=0}^{7}|d-1-k\rangle_P|k\rangle_A|k\rangle_B$.

can be observed between detectors placed at their respective outputs when each photon is distributed to each party's 8 path interferometer systems: The two-photon states registered within any coincidence time window can be distinguished with respect to the relative detection time between Alice's and Bob's detectors t_A and t_B. This violates the condition for the observation of interference as stated by the quantum superposition principle.
They can resolve this problem by additionally triggering their registered coincidences to the emission time t_P of the pump pulse. Concretely, triggering the total acquired time delay on $7\Delta T$ will lead to a projection onto the two-photon state

$$|\Psi\rangle_8 = \frac{1}{2\sqrt{2}}(e^{i(\alpha_{A_1}+\beta_{B_1})}|0\rangle_P|7\rangle_{AB} + e^{i(\alpha_{A_2}+\beta_{B_2})}|1\rangle_P|6\rangle_{AB} + e^{i(\alpha_{A_3}+\beta_{B_3})}|2\rangle_P|5\rangle_{AB} + e^{i(\alpha_{A_4}+\beta_{B_4})}|3\rangle_P|4\rangle_{AB} + e^{i(\alpha_{A_5}+\beta_{B_5})}|4\rangle_P|3\rangle_{AB} + e^{i(\alpha_{A_6}+\beta_{B_6})}|5\rangle_P|2\rangle_{AB} + e^{i(\alpha_{A_7}+\beta_{B_7})}|6\rangle_P|1\rangle_{AB} + |7\rangle_P|0\rangle_{AB}). \quad (34)$$

Here, the respective two-photon states of each photon traversing a specific path in the respective analysis interferometers is represented as $|k\rangle_{AB} = |k\rangle_A|k\rangle_B$ with $k = 0,..,7$.
The state Eq.(34) onto which the prepared time bin entangled state is projected to is the superposition of all two-photon states defined by the possible paths an emitted photon pair could have traversed before being detected.
Relevant for the preceding discussions is the fact that the emission time of each photon pair state $|k\rangle_A|k\rangle_B$ is well defined. This allows to trigger fast phase and amplitude devices placed before the analysis. They enable to manipulate the independent phase and amplitude settings necessary to prepare the states $|k\rangle_A$ and $|k\rangle_B$ in different bases.

3

EXPERIMENTAL IMPLEMENTATION OF QUDIT STATES

Quantum phenomena do not occur in a Hilbert space, they occur in a laboratory— Asher Peres

This chapter will present a detailed description of the experimental setup used for analyzing entangled two-photon states of up to 2x8 dimensions in the emission time degree of freedom. It will start with a description of the source based on spontaneous parametric downconversion (SPDC) employed to generate the entangled photon pairs (3.1). The setup used to analyze the created time-energy correlated qu*d*it states will be described in detail in (3.2). Special emphasis will be put on describing the used stabilization scheme warranting the stability of the setup (3.3) and it will be complemented by further details about the adjustment and calibration of the setup (3.4). The suitability of the experimental scheme for analyzing entangled states in high dimensional Hilbert spaces will be tested in the last section 3.5.

3.1 SPONTANEOUS PARAMETRIC DOWNCONVERSION SOURCE

Photon sources— The main requirement when performing quantum information tasks is to rely on a stable source of particles into which quantum states are encoded. Desirable for implementations of for example photonic based quantum computation tasks is the possibility to emit photons deterministically [84]. Solid state based sources such as nitrogen vacancy centers in nanodiamonds [90], molecules [106] and quantum dots [118] stand up to this demand. Nevertheless, they still suffer from low emission rates and the intrinsic limitations for their experimental implementation, such as their operation at cryogenic temperatures.

Spontaneous parametric downconversion process— For the purpose of generating qu*d*it entangled states with a high emission efficiency it is sufficient to use sources emitting photons probabilistically like the ones based on spontaneous parametric downconversion. Here, the nonlinear χ^2coupling process in the medium of non inversion-symmetric crystals is responsible for the coupling of n high energy photons to $2n$ low energy photons. This phenomenon is best described by the induced polarization in the medium of the crystal when it is traversed by the electric field $\mathbf{E}$ of an incoming photon (See [168]).

The crystals used are required to have a high as well as an anisotropic dielectric susceptibility, i.e their susceptibility is described as a (symmetric) tensor. In this case, the induced polarizations can be described independently in all three spatial orientations $i, j, k, l \in x, y, z$ [144, 180] as

$$P_i(E) = \epsilon_0(\sum_j \chi_i^{1,j} E_j^1 + \sum_{j,k} \chi_i^{2,j,k} E_j^1 E_k^2 + \sum_{j,k,l} \chi_i^{3,j,k,l} E_j^1 E_k^2 E_l^3 + ...). \qquad (35)$$

Here, the higher order coupling strengths to the photon fields E_j^1, E_k^2 and E_l^3 are described via the nonlinear susceptibilities χ_i^2 and χ_i^3 with an order limited by 3. These are tensors, describing the coupling strength between the contributing fields in dependence of their orientations with respect to the optical axes of the crystal. For this work only the second order term χ_i^2 will be relevant as it describes the three-wave mixing between one pump field and two downconversion photon fields denoted as the spontaneous parametric downconversion process (SPDC). It can as well be used to describe the reverse process of upconversion of two photons of low energy into one high energy photon (e.g. second harmonic frequency generation [51]). The term coupling to χ_i^3 describes the process described in literature as the Spontaneous Four Wave Mixing (SFWM) of 4 different electrical fields [161].
Typical coupling strengths of up to $\chi_2 \approx 10^{-6}$ [47] suffice to generate photon pairs with an efficiency high enough to implement tasks in quantum cryptography and computation [177]. The high relevance for further applications in quantum information processing [126] and quantum metrology [56] lies in the exploitation of multiple emission processes described by a multiple coupling of pump fields with 2 SPDC fields with χ^2, respectively.
Phase matching— In the process of downconversion [168, 180] momentum and energy of the involved waves have to be conserved. Thus the relations

$$\hbar\vec{k}_p = \hbar\vec{k}_s + \hbar\vec{k}_i \tag{36}$$

$$\hbar\omega_p = \hbar\omega_s + \hbar\omega_i \tag{37}$$

hold between the pump (p) and the emitted signal (s) and idler (i) waves. Here, the frequencies are described by $\omega_{p,s,i}$ and the wave vectors by $\vec{k}_{p,s,i}$ with absolute values $|\vec{k}_{p,s,i}| = \omega_{p,s,i} n(\omega_{p,s,i})/c$ depending on the refractive index $n(\omega_{p,s,i})$ of the respective photons in the optical medium of the crystal. The fact that the exchanged momentum depends on the respective refractive indices $n(\omega_{p,s,i})$ of the different waves and that this depends linearly on the frequency of the corresponding photons, makes it difficult to achieve phase matching in most materials: The lower energy downconverted photons would observe a lower refractive index and correspondingly the sum of their momenta would be lower than for the photon which emitted them. For that reason, birefringent optical materials have to be used in order to fulfill the phase matching conditions.
Studies on the birefringence of a crystal will be restricted here on uniaxial crystals, i.e. crystals for which the refractive index is equal for 2 spatial directions and different to these along the 3rd direction. The refractive index can be represented by its spatial distribution along the surface of an ellipsoid, where the major axis is commonly denoted as the optical axis. In this scenario, input light polarized along the plane containing the optical axis and the input vector $\vec{k}$ is denoted as extraordinarily polarized with refractive index n_e, while if it is polarized perpendicular to the plane it is called ordinarily polarized with refractive index n_o.
The phase matching condition (36) can now be fulfilled if the polarizations of the input and output waves fulfill specific conditions. For example, for negative uniaxial crystals as used here, i.e. crystals for which $n_e < n_o$ holds, the pump photon is required to have the polarization with the lower refractive index. It is therefore required to be extraordinarily polarized, while at

least one of the downconverted photons has to be orthogonally polarized. Two different types of phase matching fulfilling this condition, denoted in literature as Type I and Type II are defined. The first one describes the case where both signal and idler photons are ordinarily polarized, while the second one describes the situation where the signal photon is ordinarily and the idler photon extraordinarily polarized.
In order to tune the refractive indices to fulfill these phase matching conditions, it is useful to define the relative angle between the input wave vector $\vec{k_p}$ and the optical axis θ. While for ordinarily polarized light its refractive index is independent of θ, the refractive index of an extraordinarily polarized wave shows a dependency $n_e(\theta)$. It is this last relation which allows to fulfill the phase matching condition by changing the angle θ for a given input wave $\vec{k_p}$, as at least one wave traversing the crystal is extraordinarily polarized.
Further on, a variation of the same angle θ can be used to vary the relative orientation of the respective wave vectors of the different photons in the downconversion process. In the type I configuration the photons are emitted along cones which are concentric to each other, with ring radii depending on θ, while in the type II case the cones are additionally symmetrically shifted with respect to each other with a variation of θ [168]. One can differentiate between the collinear and the non-collinear configuration, where the first case describes that all wave vectors $\vec{k}_p, \vec{k}_s, \vec{k}_i$ are parallel while in the second case, these are oriented along arbitrary directions fulfilling the phase matching conditions. Further on, depending on the energies of the emitted photons one distinguishes the degenerate, where both energies are equal, and the non-degenerate case, where these are different to each other.
Generation of entangled photon pairs and limitations— The process of SPDC offers high potential for the generation of entangled photon pairs. Polarization entangled states have both been implemented by using type II [94] and type I [95] phase matching, while in this work they are used to emit photon pairs entangled in their emission times [166]. Common to all these schemes is that the generation of photon pairs with a high entanglement quality relies on their spectral, spatial and timing indistinguishability. Particularly for pulsed type II downconversion where the central frequencies of the emitted photons differ from each other, spectral filtering offers the best solution for reducing their spectral distinguishability. The second requirement can be met by coupling the signal and idler photons into single mode fibers, such that both photons share the same TEM_{00} mode distribution. Nevertheless, with increasing crystal length, ensuring the second and third condition is difficulted by an increasing transversal and longitudinal walkoff between the emitted photons:
The different refractive indices in the birefringent material of the crystal lead to different group velocity distributions associated to different polarizations of the wave packets. In analogy, the different emission direction of the extraordinarily polarized photon leads to a transverse shift with respect to the ordinarily polarized photon. Unless compensation schemes based on letting the photons traverse additional birefringent crystals, the effective crystal length L and correspondingly the efficiency with which entangled photon pairs can be emitted is limited for these sources [168].
Similar limitations concerning the photon pair emission efficiency of conventional nonlinear crystals such as BBO ($\beta - Ba_2B_2O_4$) are based on the following property: The fulfillment of the phase matching conditions using

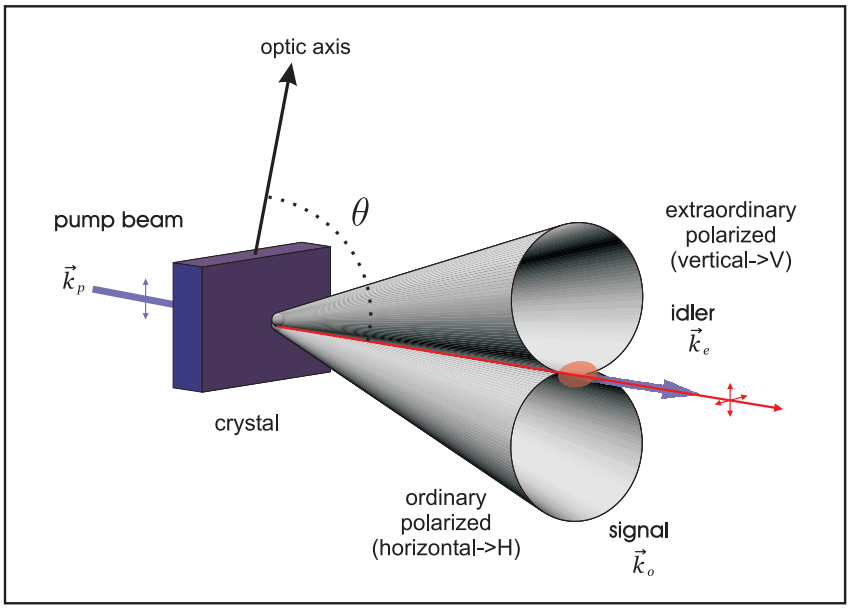

Figure 6: Schematic description of the emission directions of a pump photon into a signal and idler photon in the type II crystal configuration by using the spontaneous parameteric downconversion process (SPDC) [82]. Here, an extraordinarily polarized pump photon is downconverted in a suited crystal offering a high second order susceptibility $\chi^2_{i,j}$ with $i,j \in x,y,z$. Each photon's wavevector $\vec{k}_o$ for an ordinarily polarized signal photon and $\vec{k}_e$ for an extraordinarily polarized idler photon is oriented on the surface of a cone, which can be made to intersect at one point (collinear case) as depicted here. This corresponds to the type of source used in this work, where the generated photon pairs are coupled into the same spatial mode and separated by making use of a polarization beamsplitter.

only the birefringence of the material restricts the coupling waves to couple with a strength defined only by some specific components of the electric susceptibility tensor $\chi^2_{i,j}$ with $i,j \in x,y,z$. These are not necessarily the maximal achievable for the specified material. Therefore, alternative schemes based on using periodically poled crystals, have been developed:

3.1.1 *Photon pair source based on periodically poled crystal*

Quasi-phasematching— An alternative backed by recent successful implementations of high efficiency down-conversion sources [47, 157, 128] is to use quasi-phasematching in a crystal medium whose effective nonlinearity is periodically inverted. Here, the periodic poling leads to the addition of a term allowing to fulfill the phase matching conditions for a new combination of pump $\vec{k}_p$, signal $\vec{k}_s$ and idler $\vec{k}_i$ wave vectors according to

$$\vec{k}_p(\omega_p, n(\omega_p)) = \vec{k}_s(\omega_s, n(\omega_s)) + \vec{k}_i(\omega_i, n(\omega_i)) + \frac{2\pi}{\Lambda(T)} \tag{38}$$

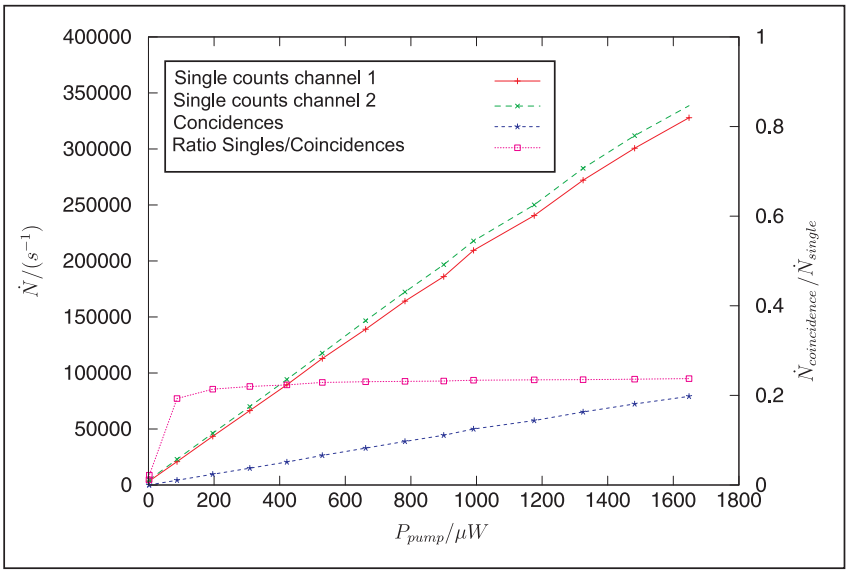

Figure 7: Single and coincidence counts as a function of the input pump power (from [49]). A linear increase in both single (red and green curve) and coincidence (blue curve) count rates (per second) is observed, leading to maximal coincidence count rates of $6 \cdot 10^5 \cdot s^{-1}$. The two-photon emission efficiency of the source is evaluated as the ratio of the coincidence count rates per mW of pump power, which remains at a constant value of $\approx 4.9 \cdot 10^4 (s \cdot mW)^{-1}$ for a broad range of pump powers. The observed single to coincidence count ratio remains nearly constant at a value of $\approx 24\%$.

with the temperature dependent poling period $\Lambda(T)$.

A major advantage of these sources, is that the tuning of the temperature by the coupling term $\Lambda(T)$ effectively warrants the phase matching of the emitted photon pairs over a broader range of directions $i, j \in x, y, z$, even for those directions for which the susceptibility tensor elements are maximal. This allows to increase the efficiency ($\approx 10^{-6}$ for periodically poled lithium niobate materials [157]) of these sources by $4 - 5$ orders of magnitude with respect to bulk crystal sources [180]. Similarly, the periodic poling allows to offer an intrinsic compensation of the transverse walk off observed for type II crystals, as the sign of the shift is reversed with each subsequent period, allowing to increase the crystal lengths L to more than 3cm. In comparison, for bulk crystals such as BBO the effects are noticeable already for lengths larger than 1mm.

Application to this work— It is for these reasons that a periodically poled potassium titanyl phosphate (PPKTP) crystal [1] fulfilling the type II phase matching criteria is used [128]. Type II crystals are chosen as the spectral bandwidth of the emitted photons is lower than for the type I case, avoiding the usage of filters. These would be required in order to effectively diminish dispersion effects at the optical components. Here, the collinear configuration simplifies the experimental effort by coupling the emitted H and V photons into the same single mode fiber.

In this work an external grating stabilized laser diode with a wavelength of 402.8 ± 0.4nm is used as the pump source. Residual light emitted in the

1 Produced by Raicol

near infrared wavelength regime is filtered before coupling the laser intensity into a single mode fiber. The spatial distribution of the outcoupled intensity is a symmetric Gaussian well suited to match the spatial mode distribution of the emitted photons with the single mode of the fiber collecting the photons. The laser intensity is focused onto a spot with a FWHM beam waist size of $w_p \approx 25\mu m$, delivering the highest photon pair collection efficiencies in close correspondence to similar studies [47]. Calculations show that for the chosen poling period of $9.675\mu m$ and for a length of 1cm degenerate phase matching can be achieved for a temperature of 45.75° set up at the used oven [2]. Nevertheless, measurements show that the degenerate phase matching temperature is $26.0 \pm 0.2^\circ$ corresponding to a poling period of $9.724\mu m$ [49]. The expected value for the non-degeneracy wavelength of $805.6 \pm 0.4nm$ is close to the experimentally evaluated value of 805.9 ± 1.1nm. Here, the measured bandwidth is limited by the resolution of 1.1nm of the single photon spectrometer employed [49]. Reasons for the deviation from the predicted degeneracy temperature can be attributed to the fact that the poling period was ensured with a fabrication accuracy of $0.25\mu m$.

3.1.2 *Photon pair generation efficiency*

To characterize the efficiency of the source, the detected single count rates observed at the respective outputs of the polarizing beamsplitter are plotted together with the coincidence count rates as a function of the CW pump intensity present at the crystal. The efficiency of the source is characterized by the coincidence count rate normalized to the incoming pump power and remains constant at $\approx 4.9 \cdot 10^4 (s \cdot mW)^{-1}$ for a broad range of input powers (see 7). Maximal count rates of up to $6 \cdot 10^5 \cdot s^{-1}$ are observed for the maximal laser output power for which a stable operation of the laser is observed. The observed ratio in the range of $\approx 24\%$ between the single count rates and the coincidence count rates is lower than identity, what can be attributed to the limited detection efficiency in the range of $\approx 60\%$ of the single photon detectors used [3] at a wavelength of $\approx 800nm$. In this measurement, residual reflection losses at the (non-antireflection coated) end faces of the used single mode fiber contribute to an additional decrease in the efficiency in the range of up to $\approx 8\%$, while residual losses on the rest of the optical components is conservatively assumed to lie in the range of $\approx 3\%$. These factors reduces the maximal observable ratio to the range of $\approx 0.49^2 = 0.24$, corresponding to the experimentally observed values. Here, the quadratic scaling with the efficiency is due to the fact that the loss of one of the photons will lead to not registering a corresponding coincidence event for the respective paired photon, too.
Similar sources based on a type I configuration of two crossed PPKTP crystals [158] have been used to improve the emission efficiency to a regime of up to $0.64 \cdot 10^6 \cdot (s \cdot mW)^{-1}$, an increase of the efficiency by a factor of more than 10 as compared to the source used here. Nevertheless, the increased spectral bandwidth makes them less suitable for the dispersive optical materials used in this setup.
High photon emission efficiencies are relevant for the detection of entanglement in the time degree of freedom with a high signal to noise ratio. Here, the analysis of these modes is provided by an interferometer system, prob-

2 Oven by GWU Lasertechnik
3 Perkin Elmer SPCM-AQ4C

abilistically distributing the different emission time modes into different coincidence time windows, what reduces the effective rates of coincidences observed within them. Similarly, accidental coincidences, resulting either from photon pair emission processes for which one of the photons was lost and from a detector dark count, contribute to a constant background count rate. This rate is required to remain low with respect to the true coincidence count rate in order to detect a high entanglement quality.

3.2 EXPERIMENTAL SETUP

This section's purpose is to clarify from the standpoint of current technological limitations why and how the following experimental setup was chosen for the task of increasing the complexity of the encoded quantum states. Further details will be presented regarding the particular design of the interferometer arms used to analyze the correlations between the different emission times. The motivation for choosing this setup will be based on the actual technological constraints limiting the scalability of the scheme to arbitrarily high dimensional systems:

- *High preparation efficiency* (section 3.2.1)— Applications for quantum communication schemes require a sufficiently high emission and detection rate of the photons.
- *Detection time resolution* (3.2.2)— A crucial requirement for demonstrating the entanglement of a high number of two-photon emission times is the detector timing resolution enabling to distinguish between different time modes.
- *High fidelity* (3.2.3)— The interferometer systems used are required to test the coherence between different emission time modes. For that purpose the acquired which-path information due to polarization and frequency mode dispersion and due to spatial mode mismatch are to be compensated.
- *Stability* (3.3)— In order to enable the analysis of the prepared states and further application for quantum information processing tasks, a reliable stabilization scheme has to be applied over the required measurement times.

3.2.1 *High preparation efficiency*

Several schemes were proposed and experimentally realized in order to enhance the Hilbert space dimension of the quantum states encoded into a set of photons. Here, the encoding of qu*d*it states into two photons offers a significant advantage with respect to the encoding of qubits into multiple photon pairs [82, 181, 186]: For a probabilistic detection scheme, the latter schemes requires a high single photon detection efficiency in order to detect the encoded multi-qubit states with high count rates.
This disadvantage is closely related to current technical limitations on the detection of photons: The direct detection of multiphoton events by resorting to detectors sensitive to a multiphoton absorption process are still in the experimental testbed [6]. Schemes based on the probabilistic distribution of the photons using a linear state analysis [181] and the posterior detection

of the photons at separate single photon detectors suffer from the limited detection efficiency of current state of the art Si-based detectors. Here, quantum efficiencies of commercially available detectors of up to $\eta = 70\%$ [55] in the visible wavelength regime severely limits the state detection efficiency of a N qubit state as count rates are reduced by a factor $\propto \eta^N$. In order to overcome these limitations high power sources in the UV wavelength regime can be applied [88]. Conversely, this scheme suffers from the admixture of higher order multi-photon events due to the generation of multiple pairs of photons.
An important alternative to these schemes, based on superconducting nanowire detectors [143, 129] with reported detection efficiencies $> 91\%$ still suffers from the important drawback to require cooling below 1K.
These problems are circumvented when distributing quantum states embedded within the Hilbert space of N qubits equally to two parties, as done for the states prepared in this and similar [31] work. Here, the limited detection efficiency contributes to a decrease of the count rates only proportional to η^2, as only two detectors are required. Overall observed count rates of up to $1kc/s$ (within a time window of 1.64ns) for 2x8 dimensional states for pump powers in the mW pump power regime are sufficient to ensure the manipulation and analysis of the generated states with high statistical relevance.

3.2.2 *Detection time resolution*

The detection time resolution puts a lower limit on the time delays ΔT implemented by the interferometer systems used to test the coherence between a high number of emission time modes. This is so as a low resolution disables to discriminate between coincidences distributed between different coincidence windows (2.3). In this work detectors with a single photon detection resolution of $\approx$ 500ps are chosen due to their higher single photon detection efficiency of up to 50%in the infrared wavelength regime of 800nm. Further reductions down to 40ps [159] in the timing resolution of CMOS based detector circuits could be achieved, with recent research aimed at increasing the detection efficiency[4].
For the detectors used in this setup a typically observed value for a two-photon coincidence time resolution is $\Delta T_{res} \approx 2ns$ (determined at the background level). This leads to a choice of the interferometer time delays of $\Delta T > 2.4ns$ surpassing the observed resolution, corresponding to typical path length differences of $\Delta L \approx 0.72m$.
Similarly, an upper bound restricting the maximum number of delays introduced is the coherence time of the laser source. This is so as it has to be longer than the maximal time delay between all two-photon emission times. In order to ensure a high coherence of the pump laser a diffraction grating stabilization scheme [139] is applied on a blue laser diode emitting at 402.8nm. The enhancement in the coherence time allows to surpass the required specifications by many orders of magnitude: $2.58\mu s >> \Delta T$ (methods described in detail in [142]). The choice of a laser diode at this wavelength enables to emit SPDC photon pairs at 806nm, which is still within the high efficiency detection range of the used single photon detectors.

4 Micro Photonic Devices

3.2.3 *High fidelity*

Bulk/Fibred configuration— The timing constraints described before impose limitations regarding the design of the interferometers. Specially for a large unbalance of the two arms, usual Mach-Zehnder interferometer configurations based on bulk optics suffer from a limited spatial mode overlap of the two superposed modes at the output beamsplitters. Thus fused fiber couplers have been used for which the spatial mode distribution of the two modes is exactly the same at their overlap.
Still, an important drawback for this implementation, specially for unbalanced interferometers, is the frequency mode dispersion in the silica based core material of optical fibers (see Chapter 2.6. in [142]): A photon with FWHM frequency bandwidth $\Delta\nu$ encoded in the $|0\rangle$ and $|1\rangle$ eigenbasis of a two-path interferometer, will acquire a frequency mode spread proportional to the time delay implemented: A photon transmitted through the long interferometer arm implementing a time delay ΔT will acquire a spread of its photon time distribution higher than the one of the shorter path. This path dependent delay can be parameterized as

$$\Delta t_{S,L}^{Max} = t_{\lambda_0+\frac{\Delta\lambda}{2}} - t_{\lambda_0-\frac{\Delta\lambda}{2}} = \Delta L\left(\frac{1}{v_{\lambda_0+\frac{\Delta\lambda}{2}}} - \frac{1}{v_{\lambda_0-\frac{\Delta\lambda}{2}}}\right) \tag{39}$$

leading to a FWHM time delay between the frequency modes for the short and long path of $|\Delta t_S^{Max}| = 0.1951$ps and $|\Delta t_L^{Max}| = 0.3902$ps, respectively. These values are calculated for a FWHM wavelength bandwidth of 3nm and a path length difference of $\Delta L = 0.6m$. The resulting difference in the maximal frequency mode spread of $\Delta t_L^{Max} - \Delta t_S^{Max} = 195$fs is comparable to typical coherence times of SPDC photons. The associated increased which-path information effectively leads to a reduction in the interference quality.
Additionally, interferometers based on full fibred paths have the important drawback that thermal drifts at the fibers can arbitrarily change the phase encoded. Closely related to this problem, they induce a transformation of the polarization mode detrimental for warranting a good indistinguishability of the interfering modes. These factors require a high temperature stability for similar applications [165] or, when renouncing to maintain a constant temperature, even to the inability to analyze the encoded states for longer measurement times [138].
Interferometer configuration used here— A compromise between the advantages of a bulk interferometer setup and a fibred configuration is achieved here by constructing an interferometer consisting of both systems (see 9 describing the scheme). This system is particularly suited to construct unbalanced interferometers, with an interferometer arm being orders of magnitude longer than the other one. For this configuration it is advantageous to use fused fibre couplers to split and further on to overlap both interfering modes as this ensures their high spatial mode overlap. Here, it is important to choose the optical path length of the fibers to be equal along both interferometer arms and to introduce the required delay by transmitting one mode through an additional free space path. In this case, the frequency mode dispersion acquired by a photon traversing any of both paths is equalized. Residual dispersion effects at the other optical components placed at the interferometers path are negligible here.
The time delay is introduced into each interferometer loop by coupling the

light out of the single mode fibers[5] and transmitting them over a free space path. A retro reflection of the light at a 90° prism[6] allows to couple the light back into the input fiber of the next fused fiber coupler. In addition, for longer interferometer paths, an optical delay line consisting of two 50.4mm mirrors allows to introduce an additional path difference of $12cm$ with each reflection. This doubles and quadruples the time delays implemented by the 2 longer interferometer arms. Here, stainless steel is chosen as the material of the cylindrical structure holding both mirrors together at the required distance, as the material offers reduced thermal expansion coefficients with regards to other metals. In order to construct the undelayed interferometer arms, the other output fibers of each fiber coupler are directly coupled to the input fibers of the next fiber coupler.
Using the hybrid interferometer configuration losses in the range of up to 8% have been observed for the longest interferometer paths (limited mainly by mode deformations by the reflections in the optical delay lines and residual reflection losses of $1-2\%$ at the AR coated fiber ends). These are only slightly higher than the losses accumulated at the short arms of $4-5\%$. In order to compensate for the difference in the losses, enabling to equalize the interferometer mode strengths, it is possible to increase the losses in the short paths of the respective arms. This is achieved by reducing the coupling between the fibers of subsequent fiber couplers.
An advantage of the scheme is that the interferometer delay can be precisely adjusted by placing the retro-reflection prisms on translation stages provided with piezo actuators driven by a proportional-integral feedback loop (see 3.3). These allow to control the interferometer delays with a nm precision and up to an overall translation of up to $\approx 6\mu m$.

Alternative experimental implementations— The most promising alternative to employing bulk and fibre optics, as implemented in the current experimental setup, is to resort to integrated optics circuits, as they offer intrinsic advantages with respect to their stability. A reason for this is that they warrant a high preparation fidelity as already demonstrated experimentally [147, 132].
However, for the encoding of time-energy emission modes in high dimensional states, these schemes are still limited by current detection time resolutions in the range of down to 40ps for CMOS based avalanche photodetectors (APDs) corresponding to path lengths of $\approx 1.5cm$ [159]. These are well above typical structure sizes of integrated optics waveguides in the range of $200\mu m$. An interesting alternative to overcome these limitations can be based on the usage of upconversion photodetectors: As the name indicates, they are based on applying a frequency upconversion process on the two-photons emitted by a downconversion source [92]. As an upconversion process is possible only if both photons are detected with a time delay restricted by each photon's coherence time, it is possible to detect the conversion of a photon pair very precisely. A major drawback of the method is the inefficiency of the process, requiring higher pump powers in the W regime in order to compensate for the low generation rates of the photons.

5 Fiber couplers made by Schäfter Kirchhoff
6 Bernhard Halle

3.3 STABILIZATION SETUP

The interaction of the created quantum states with the environment will lead to a reduction in the reconstruction fidelity of the prepared states. Effectively, this diminishes the ability of both parties, Alice and Bob, to use the prepared quantum states for further applications. A major limitation to be faced with when designing unbalanced interferometers is their increased sensitivity to drifts in the refractive index of air and of the used fibers with a change in the ambient temperature. Additionally, mechanical vibrations with an amplitude exceeding the photon wavelength cannot be suppressed completely even for ideal laboratory conditions.
Fluctuations in the pump laser frequency of $\Delta\nu_p$ contribute to a variation in the photon's phase acquired in the interferometer. This is enhanced by the factor N corresponding to the difference in the number of wavelengths fitting in the short and in the long interferometer arm: $\Delta\phi \propto \pi\Delta L/\lambda \cdot \Delta\nu_p/\nu_p = \pi N \cdot \Delta\nu_p/\nu_p$. In order to reduce this contribution it is necessary to reduce the pump laser frequency fluctuation $\Delta\nu_p$ as much as possible [142, 140].

3.3.1 *Polarization multiplexing scheme*

Current stabilization techniques— Standard interferometer stabilization techniques designed for stabilizing the phase acquired by single photons require the use of an additional reference laser. This laser is used to extract sufficient information on the phase fluctuations acquired in the respective interferometer arm.
An optimal compensation can be achieved for interferometer configurations for which the downconversion photons and the stabilization laser share the same spatial mode distribution and correspondingly acquire almost identical phase shifts (the difference is dependent only on the different refractive indices for the two different wavelengths). This is an inherent property of the used hybrid interferometers, for which both wavelengths are guided through the same single mode fibers. Similarly, the wavelengths have to be chosen to allow the spectral discrimination between them by using standard filters (bandwidth typically limited to $\approx$ 1nm). Their difference has to remain within definite boundaries defined by the fiber cutoff wavelength, as otherwise no single mode transmission for both wavelengths could be warranted. It is for these reasons that a grating stabilized stabilization laser at 781.6nm is used, a wavelength differing sufficiently from the 805.9nm photon wavelengths. The particular wavelength can be very well referenced to extensively studied atomic transitions in Rubidium [11] or to modes of commercially available frequency comb lasers [70], as used in this work (see 3.3.3).
Standard stabilization schemes are based on extracting a suitable error signal ideally depending only on the relative interferometer phase ϕ to be stabilized. These are the basic recipients required to design a feedback loop compensating for the deviation $\Delta\phi$ the error signal is proportional to. The deviation is compensated by driving a piezoactuator with an amplitude of exactly the opposite sign and the same frequency bandwidth as the deviation [77]. For this purpose, standard proportional- integral feedback electronics coupled to piezoactuators offering a sub-nm accuracy in the frequency range of up to 100 Hz are sufficient for compensating for mechanical vibrations and

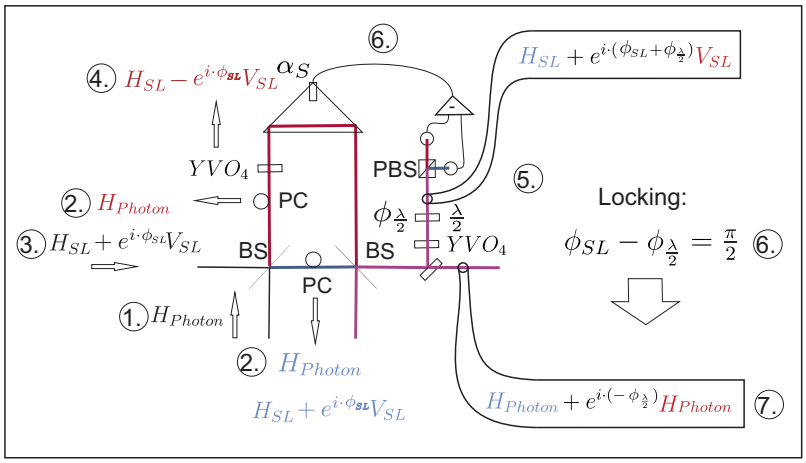

Figure 8: Polarization multiplexing technique used for stabilizing an interferometer arm. The phase acquired by the photons coupled into all interferometer arms is stabilized and controlled over arbitrary periods. In order to achieve this, a reference laser polarized along the R/L and P/M plane is rotated to two orthogonal polarizations during the traversal through both arms and fully analyzed at the output in the polarization degree of freedom. The signals measured at the outputs of the polarization analyzer can be used to extract the required error signal, used to drive a piezoactuator compensating for the acquired fluctuations in the phase ϕ_{SL}. Further on, the stabilized phase can be arbitrarily manipulated by rotating the polarization before the polarization analysis by $\phi_{\frac{\lambda}{2}}$.

temperature drifts. For the used devices, the bandwidth suffices as well to offer a proper compensation of low time scale fluctuations due to changes in the refractive indices of air and the optical fibers used.
The method for extracting a suitable error signal is based on fringe locking [150]. Here, the intensities $I_{|a\rangle} \propto (1 + V\cos(\phi + \Delta\phi)/2)$ and $I_{|b\rangle} \propto (1 + V\sin(\phi + \Delta\phi)/2)$ of a reference laser with a coherence length surpassing the path length difference are measured at both output modes $|a\rangle$ and $|b\rangle$. Under this condition it is possible to observe interference fringes with a sufficiently high visibility $V = 2\sqrt{I_{|a\rangle} I_{|b\rangle}}/(I_{|a\rangle} + I_{|b\rangle})$ as a function of the encoded phase ϕ and the additional phase fluctuation $\Delta\phi$. Finally, the difference of both signals $I_{|a\rangle} - I_{|b\rangle} \propto V\cos(\phi + \Delta\phi)$ offers the required characteristics of the searched error signal with a sign change at $\phi + \Delta\phi = \pi/2$.
Stabilization scheme used in this work— The previously described scheme cannot be directly applied to a construction of interferometer arms as pursued in this work, as each interferometer output is coupled into the next interferometer arm. This doesn't allow to extract the stabilization laser intensities at both outputs of the respective interferometers (See Fig. 8). For that purpose it is more appropriate to consider a scheme based on polarization multiplexing, as illustrated in Fig. 8:

Birefringence of the optical fibers of the fused fiber couplers leads to the fact that the polarization rotation in both arms is different, even if the input polarization for both arms is the same, in this case H (step 1 in Fig. 8). Nevertheless, one can make use of polarization controllers at both arms to rotate the polarization of the incoming H polarized photon such as to remain H

polarized in the short and long interferometer arm by using fiber polarization controllers (step 2). This requirement has to be met in order to reduce the which path-information of the transmitted single photons.
In order to extract a suitable error signal from the intensity of the stabilization laser, the following scheme is followed: Making use of the other input fiber of the fused fiber coupler, the intensity of the stabilization laser is inserted into the interferometer (step 3). Here, it is made sure that the intensity is polarized along $1/\sqrt{2}(H_{SL} + e^{i\phi_{SL}} V_{SL})$ as this simplifies the adjustments required. Subsequently, it has to made sure that the rotation of the stabilization laser is different in each arm, ideally that they are polarized orthogonally at their overlap. In the example considered here, the polarization transformation in the short arm rotates the polarization state by an unknown phase ϕ_{SL} along the P/M and R/L plane ($1/\sqrt{2}(H_{SL} + e^{i\phi_{SL}} V_{SL})$). In order to ensure a rotation of the polarization with phase $-\phi_{SL}$ along the long arm a birefringent crystal, such as Yttrium Vanadate YVO_4, is used (step 4). It allows to rotate the phase in the long arm such that the polarization state reads as $1/\sqrt{2}(H_{SL} - e^{i\phi_{SL}} V_{SL})$. It is to note that the optical axis of the crystal is oriented in parallel to H, in order to ensure that the polarization of the H polarized photons at 806nm are not rotated, while allowing the rotation of the phase of the laser polarization. This is possible as the polarization of the stabilization laser is oriented along the P/M and R/L basis with respect to the crystal axis.
After exiting the output fibers the actual analysis of the phase acquired by the stabilization laser is made (step 5). Here, the stabilization laser intensity at the output of the interferometer is rotated by an additional YVO_4 crystal ensuring it to be linearly polarized as the output fibers perform an additional transformation of the polarization. Further on, the polarization is rotated by using a $\lambda/2$ waveplate with a phase $\phi_{\lambda/2}$. Finally, splitting up the intensities on a polarizing beamsplitter allows to compare the intensities for H and V polarized light measured at two photodiodes. The difference of both intensities are now used to extract a suitable error signal E. The error signal extracted is suitable for applying a stabilization scheme as it depends on the relative phase ϕ_{SL} acquired in the interferometer and on the additional polarization rotation $\phi_{\lambda/2}$: $E(\phi_{SL}, \phi_{\lambda/2}) \propto \cos(\phi_{SL} + \phi_{\lambda/2})$.
Finally, a P-I feedback loop coupled to the piezoactuatoris applied to change the path length of the long interferometer arm and allows to lock the phase $\phi_{SL} + \phi_{\lambda/2}$ to a constant value of $\pi/2$ (step 6). The residual variations in the phase are normally distributed with a standard distribution in the range of $\Delta\phi_{SD} \leq 0.03\pi$ during closed loop operation. This value cannot be interpreted as the actual residual phase fluctuations in the interferometer, as fluctuations in the amplitude of the stabilization intensity and a non-optimal compensation of all fluctuations can contribute to it as well. Therefore the observed fluctuation $\Delta\phi_{SD} = 0.025\pi$ can be only used as a rough upper bound describing the fluctuations.
A major advantage of the scheme is that during closed loop operation any change in the phase $\phi_{\lambda/2}$ performed by rotating the $\lambda/2$ waveplate mounted on a motor[7] is compensated by introducing a relative phase shift with with opposite phase $-\phi_{\lambda/2}$ while ensuring the phase to be stable. This effectively leads to a manipulation of the relative phase acquired by the photons. In contrast to similar schemes as used in [150], allowing to apply fringe stabilization only for a limited number of periods, the phase can be manipulated

7 OWIS DRTM 40 rotation motor

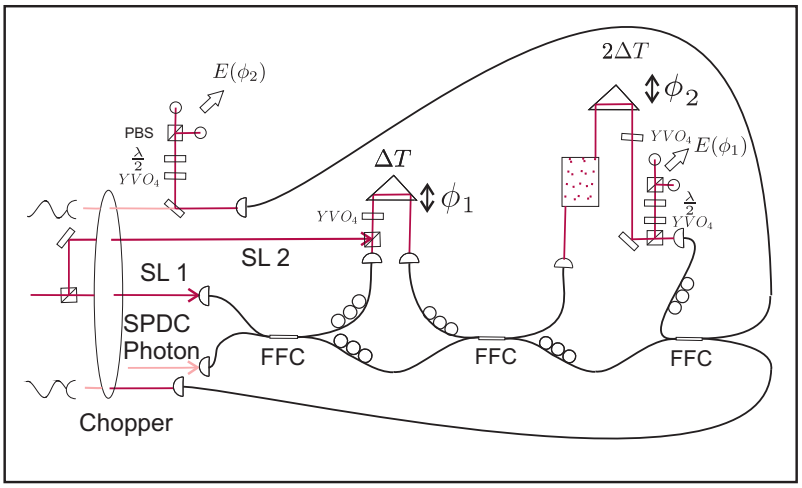

Figure 9: Time multiplexing and demultiplexing of the stabilization laser intensities allowing to stabilize each arm of a two-path interferometer configuration independently. The scheme is straightforwardly expanded to 3, as used in this work, or more interferometer arms. An optical chopper is used to time-multiplex the stabilization signals introduced into each interferometer arm into 3 different time windows. The signals are extracted at the respective interferometer output of each arm and electronically time-demultiplexed such as to gain the error signals corresponding to each interferometer arm.

arbitrarily with a speed limited only by the actuation time intrinsic to the actuators used of about *ms*. More significantly, no optical component applying these transformations is required to be placed within the interferometer, minimizing the influence of potential additional noise sources, while avoiding additional losses in the photon transmission.
This will be the method chosen to control and manipulate each of the different phase settings at each interferometer loop. Nevertheless, the reliability and independence of these adjustments can only be warranted if the stabilization intensities associated to each interferometer arm can be effectively distinguished from each other. A spatial discrimination is not possible, as the SPDC photons and the stabilization laser share the same spatial modes over all arms. Besides spectral multiplexing of the signals time multiplexing offers an effective strategy for this purpose:

3.3.2 *Time multiplexing scheme*

For the purpose of stabilizing and manipulating all 3 different interferometer loops of an interferometer system independently, the hybrid interferometer configuration offers an advantage: The required laser light for the stabilization of the longer interferometer loops are coupled into the free space path of the previous arms with the help of dichroic beamsplitters. These are designed with a polarization independent transmission/reflection ratio of 70%/30% for 780nm and a transmission $>$ 98% for 806nm (see 9). Here, the choice of an asymmetric splitting ratio is necessary as the laser light introduced in the previous arm is required to be transmitted with enough

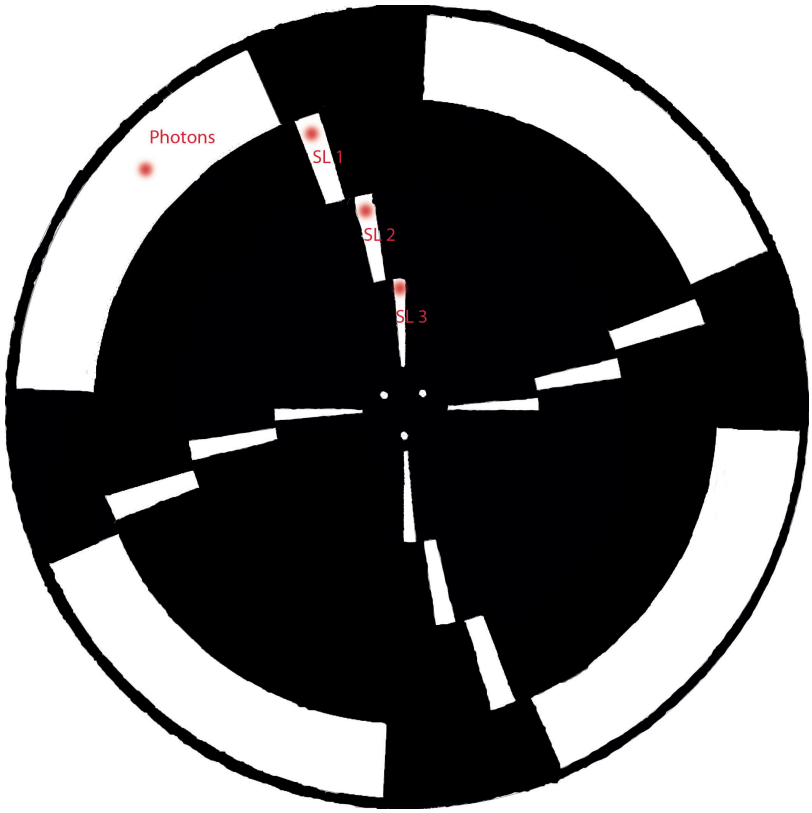

Figure 10: Design of the chopper blades used to time-modulate the stabilization laser intensities. The notation "O" denotes an open, while "B" denotes a closed surface of the chopper blades. The different stabilization laser modes are transmitted through the open chopper blades, such that they share $\approx 25\%$ of the total measurement time. In parallel, the SPDC photons are transmitted through the outer open blades over $\approx 75\%$ of the time. The spatial locations of the different stabilization laser modes (SL 1, SL 2 and SL 3) and of the photons are depicted in the same figure.

efficiency to interfere with the short arm laser light. Losses in the regime of 30% are low enough for a sufficiently high visibility above 90%. This enables a reliable stabilization as the difference between maxima and minima of the error signal is well above the range of the electronic device's noise (provided that the total signal amplitude is orders of magnitude higher than the noise amplitude). A further reduction of the noise can be achieved by serially connecting the photodiode resistance with a suited capacitance. This implements a low pass filter (<kHz regime) on higher frequent noise with a cut-off frequency well above the noise frequencies to be compensated.

As the laser light coupled into each short and long interferometer arms share the same spatial mode, it can, in the worst case, interfere and lead to the dependence of the extracted error signals on all interferometer phases acquired at each loop. In order to overcome this problem the laser light is split up into three spatial modes and time multiplexed with respect to each other by transmitting them through the (inner) alternating blades of an optical chopper (See Fig. 10 for the design of the blades used). The inner blades are distributed to offer an equivalent transmission time for each stabiliza-

tion laser. Additionally, these alternate with outer blades through which the SPDC photons are transmitted after traversing the whole interferometer system. This enables to detect the photons at times for which the stabilization laser is not coupled into the interferometers. Otherwise the stabilization laser would lead to additional photon count rates difficult to be completely suppressed by optical filtering. The openings of the outer blades are chosen to correspond to $\approx 75\%$, while the inner blades used for the stabilization laser share $\approx 25\%$. This allows a compromise between photon loss and a higher integration time available for the stabilization.
The respective intensities of the stabilization laser are analyzed at the output of each interferometer arm according to the polarization multiplexing scheme described before. Here it is ensured that the polarization along the short arm is in the P/M and R/L plane. The polarization state along the long arm can be independently addressed by an YVO_4 crystal. Another crystal placed at the output of each interferometer loop adjusts the overall polarization transformation of both modes before being analyzed at the respective polarization analysis, used to apply the polarization multiplexing scheme described in 3.3.1. The time demultiplexing of the required laser signals is performed electronically by additional sample-and-hold circuits in front of the P-I-stabilization setup. This allows to trigger a closed feedback loop only at the times for which the corresponding laser intensities are detected. This enables to stabilize the interferometers referencing them only on the respective error signals $E(\phi_{SL,i}, \phi_{\lambda/2,i}) \propto \cos(\phi_{SL,i} + 2\phi_{\lambda/2,i})$. These depend only on the respective phases $\phi_{SL,i}$ acquired by the stabilization laser and on the phases $\phi_{\lambda/2,i}$ manipulated at each arm ($i = 1, 2, 3$). Closing the feedback loop on the time-demultiplexed signal separately allows to stabilize the respective phases $\phi_{SL,i} + 2\phi_{\lambda/2,i}$ to 0 and set each relative phase acquired by a SPDC photon to the chosen value of $-2\phi_{\lambda/2,i}$.
The stabilization scheme is scalable to more interferometer systems, as for each subsequent arm the polarization state along each short and long arm can be adjusted to be orthogonal. In addition, the time multiplexing scheme only requires a proper design of chopper blades enabling to time-multiplex more stabilization laser intensities.

3.3.3 *Laser frequency stabilization*

Standard path length stabilization techniques— Instabilities in the pump and stabilization laser frequencies can lead to an additional fluctuation of the interferometer phases and therefore they have to be compensated over long measurement times as well.
These phase shifts can clearly surpass a full period for typical frequency variations $\Delta\nu_p$ in the range of several hundreds of MHz and for total path length differences ΔL of up to 4.9m (corresponding to the longest path along the 3 interferometer arms) as implemented in this work. For example, in order to achieve phase fluctuations down to $\Delta\phi \leq 0.03\pi$, a typical laser frequency stability of down to $\Delta\nu_p < 5Mhz$ is required.
The same requirements have to hold for the stabilization laser diode, which serves as a reference for each independent interferometer arm phase. During closed loop operation the phase drifts associated to a change in the stabilization laser frequency $\Delta\nu_s$ would be also compensated even if these fluctuations are independent of the intrinsic interferometer noise for which the stabilization scheme was applied.

This problem can be routinely addressed by standard stabilization techniques, allowing to achieve absolute frequency stabilizations down to $\approx 1Hz$ in the laser bandwidth. For example, by using current technology based on the coupling of the laser mode to an ultrastable cavity mode [8].
Alternatively, it is sufficient to use stable cavity systems based on materials not standing up to the high precision requirements described before. For example, by stabilizing its resonance frequency to a stable reference, such like a stable frequency reference.

Frequency Comb Stabilization— Besides references based on atomic transition frequencies, frequency combs have risen in the last 10 years as one reliable source of reference frequencies with an absolute precision down to 10^{-16} [136, 187]. A frequency comb consists of a pulsed mode train of equally distributed frequencies, which can be fully characterized by the repetition frequency f_{Rep} and the carrier envelope offset frequency f_{CEO}. Only recent developments in the spectral broadening of ultrashort pulses by using photonic crystal fibers have allowed to preserve the coherence of the pulses[8]. These advances have been central for enabling the referencing of both frequencies f_{CEO} and f_{Rep} to a stable source in the microwave regime (Hydrogen Maser). This, in summary, enabling to transfer the precision to be achieved for microwave references to the regime of optical frequencies.
The method used to transfer the optical frequency comb stability onto one laser mode as in this work, is as follows:
A maser referenced frequency comb centered at a wavelength of 780nm [9] with a repetition rate of $250Mhz$ is used to stabilize the laser frequency of the laser diode mode centered at $\lambda = 781.6 \pm 0.4$nm. The laser mode bandwidth is narrowed to $\leq 400kHz$ by a diffraction grating [139] (grating with 1800 lines/mm by Edmond Optics and laser diode by Thorlabs model DL7140-201S). Furthermore, this method allows to manipulate and stabilize the central frequency to the desired frequency by tilting the grating.
In order to stabilize its frequency, a portion of the laser light is split up and overlapped with the frequency comb light at a beamsplitter with balanced splitting ratio at 780nm. The overlap between both modes is maximized with respect to their polarization state and spatial mode distribution such that the beat note frequency $\nu = \nu_s - \nu_{FC}$ between the laser ν_s and one frequency comb frequency ν_{FC} can be detected at a Si PIN photodiode. No strict requirements for the photodiode bandwidth have to be met, as a low pass filter with cutoff frequency of 10MHz[10] is used to electronically filter out only one possible beat note frequency at frequencies below 10MHz. It is placed between two amplifiers[11] used to enhance the beat note signal with an amplitude in the μV to the mV regime as required to drive a PLL comparator. Finally, this device delivers an output signal with an amplitude depending on the phase difference between the beat note frequency and an external reference frequency in the MHz regime. The PLL comparator output signal drives a piezoelectric actuator placed at the external cavity grating of the stabilization laser diode. If it is operated in a closed loop configuration, the laser can be locked to a stable frequency. Here, the figure of merit is that the observed beat note frequency has a FWHM bandwidth of 255.03 ± 10.55kHz centered at 7.43 ± 0.05MHz. This offset frequency is given by a signal generator (see Fig. 11). The maximally achievable preci-

8 Considered were PCFs manufactured by Crystal Fibre
9 Menlo Systems
10 Mini Circuits BLP10+
11 Mini Circuits ZFL-500-LN 0.1-500MHz

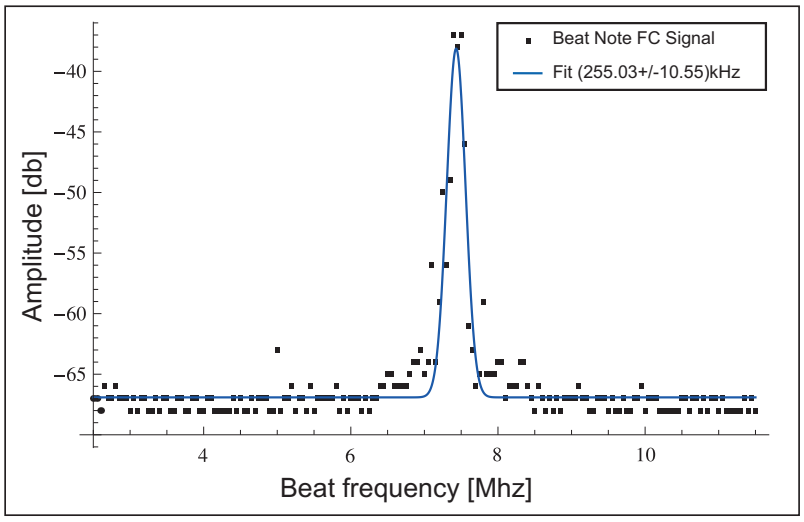

Figure 11: Measured beat note frequency between the stabilization laser and one frequency comb mode during closed loop operation and referenced to a stable frequency signal generated by a signal generator. A Gaussian fit allows to determine the beat note central frequency at 7.43 ± 0.05MHz with a FWHM bandwidth of 255.03 ± 10.55kHz characterizing the achieved stability.

sion is limited by the linewidth of the frequency comb and of the laser diode mode. Higher frequent technical noise in the kHz regime affecting the laser diode mode is not actively compensated, as the observed frequency stability fulfills the requirements for this work. Previous passive compensation of a portion of the technical noise is achieved by electronically filtering these frequency components from the laser diode driving current (leading otherwise to a significant broadening of the observed beat note bandwidth up to the MHz regime).

Referencing of the Pump Laser Frequency— The application of similar stabilization schemes for the pump laser frequency at 402.8nm is limited by the fact that no frequency combs at a wavelength regime of 400nm are commercially available. Before resorting to atomic transitions in Potassium providing a stable clock at this wavelength regime [65] it is experimentally less demanding to stabilize it on a transfer cavity whose resonance frequency is stabilized to the referenced 781.6nm laser diode. The Hänsch Couillaud locking scheme is used for that purpose. Finally, the blue laser diode frequency mode can be referenced to the transfer cavity by making use of the same stabilization technique. In this way, effectively the pump laser and stabilization laser central frequency is synchronized. This permits to stabilize the pump laser with the same precision as for the stabilization laser, too.
Concave mirrors (r=-200mm) specified with a polarization independent reflectivity of up to $> 98\%$ for wavelengths between $395 - 410$nm and between $770 - 800$nm are used for a confocal cavity configuration with a 200mm mirror separation. In order to offer a passive reduction of mechanical vibration both mirrors are placed at the end of a cylindrical aluminium structure.
In order to apply the stabilization scheme, a portion of the blue 402.8nm and infrared laser 781.6nm diode light are polarized at 45° and overlapped at a beamsplitter with 50/50 splitting ratio. The intensities in one output mode

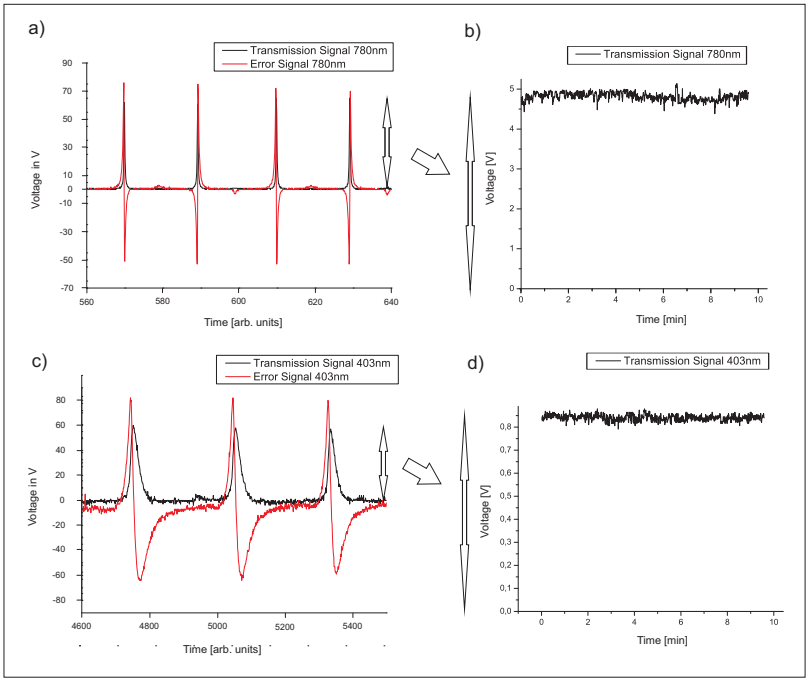

Figure 12: The Hänsch Couillaud locking scheme is used to extract a suitable error signal both for the stabilization laser at 781.6nm (a)) and for the pump laser at 402.8nm (c)) when coupled onto a Fabry-Perot cavity. These signals are displayed together with the transmission signals observed at the output of the cavity for a periodic variation of the cavity length. During closed loop operation the resonance frequency of the cavity is adjusted to observe maximal transmission for the IR light (b)). At the same time, the frequency of the blue laser diode mode is adjusted to be in resonance with the same cavity (d)), as depicted for typical measurement times of up to 10 minutes.

are coupled into the input of the confocal Fabry-Perot cavity and detected at its output after dichroically splitting up the intensities and distributing them into two separate photodiodes. A glass plate is placed at the centre of the cavity at the Brewster angle to enable the suppression of the vertical polarization components for both wavelengths (due to slightly different optimal angles for both wavelengths, the setting is optimized for the blue laser light, which suffer from an intrinsic higher absorption loss at the glass plate).

$$I_H - I_V = \frac{I_0 T_1 R \sin\phi}{(1-R)^2 4R \sin\phi/2^2}. \tag{40}$$

The light reflected at the input of the cavity is overlapped with the horizontal polarization component coming out of the cavity. It carries the phase information acquired during the traversal of the optical cavity. In order to extract that phase information, the laser light is split up dichroically and analyzed by a $\lambda/4$ waveplate allowing to project the resulting circularly polarized light into linear polarized components to be analyzed at two polarization beamsplitters designed for the different wavelengths.
Comparing the output intensities for H and V polarized light at an opera-

tion amplifier allows to extract the error signal
Here, T_1 denotes the transmission of the input mirror and R the reflectivity of the mirrors, while ϕ corresponds to the phase acquired in the cavity. The experimentally observed error functions for both wavelengths are plotted during a periodic scan of the cavity using a piezoactuator onto which one of the cavity mirrors is mounted (Figs. 12 a) and c)) together with the transmission signals observed at the output. A closed feedback loop between the cavity piezoactuator and the error signal is driven for the IR light. Similarly, another closed loop between a piezo driving the external diffraction grating of the blue laser diode and the corresponding error signal for blue light (Figs. 12 b) and d)) is operated. Both closed loops can be maintained stable over measurement times of up to several days.

3.4 ADJUSTMENTS AND CALIBRATION OF THE SETUP

The stabilization enables to run the experiment reliably over the required measurement times. Nevertheless, in order to ensure the high fidelity detection of entangled states, the equalization of the respective interferometer path length differences to each other is required. Similarly, the analysis of the entangled states requires to apply a reliable calibration scheme of the phase settings set at the respective interferometer arms.

3.4.1 *Adjustment of polarization and time delay*

Compensation of polarization rotations— The photons transmitted along the short and long interferometer arms of each interferometer are required to be indistinguishable with respect to the polarization degree of freedom. Here, it is necessary to compensate for a polarization rotation due to the birefringence of the optical fibers. Moreover, as only H or V polarized downconversion photons are fed into each interferometer system, the transformation applied along the fibre paths of the interferometers are compensated by manual polarization controllers such that at the outputs the photons are H and V polarized. No simultaneous compensation of the photon polarization along the P/M basis is required, as no input photon is polarized along that direction. All short and long interferometer arms of both partie's interferometers are adjusted such as to apply the same polarization transformation on the transmitted photons. Thus, a photon pair detected at the output of the interferometers cannot be distinguished by its polarization.
Adjustment of path length differences— A last requirement to be met in order to observe the time-energy entanglement of the created photons is that the time delays implemented by one parties interferometer arms matches the time delays of the other partie's interferometers. First, the equalization of the longer paths $|1\rangle_{A_1}$ and $|1\rangle_{B_1}$ of the first interferometer arms at Alice's and Bob's side is undertaken. For that purpose both interferometers are connected serially to each other and the intensity of a pulsed laser is coupled through them (here, a 780nm pulsed fs-laser signal with repetition rate of 82MHz). Measuring the output signal on a high speed photodiode coupled to a $10GHz$ resolution oscilloscope allows to determine the time delay up to a precision of down to $\approx$ 100ps corresponding to $\approx$ 3cm. A fine adjustment of the time delay is performed by coupling downconversion photons at 806nm into the same system and scanning the path length difference of one interferometer with a change in the retroreflection prism

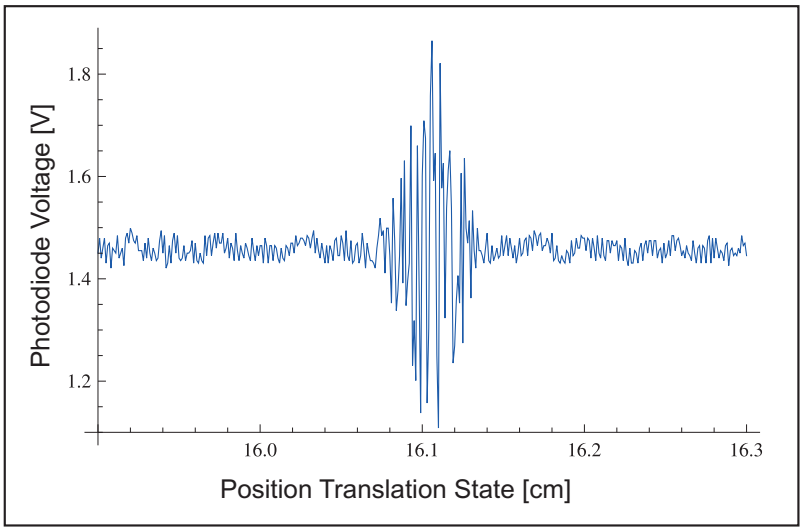

Figure 13: Observed variation of the photodiode signal of a pulsed laser signal at 780nm measured at the output of a serial interferometer construction consisting of Alice's first interferometer arm with delay ΔT and Bob's first and second interferometer arms with delays ΔT and $2\Delta T$, respectively. The intensity fluctuations due to the interference between photons traversing the short interferometer arms contributes to a small additional modulation of the signal. In contrast, the interference between the path combinations of Alice's and Bob's first interferometers and the path of Bob's second interferometer leads to maximal interference fringes for a translation stage position of 16.15mm. Setting the translation stage to this position allows to adjust the time delay 2Δ of Bob's second arm to be exactly the double as for his first arm.

position (see Fig. 9). Choosing directly SPDC photons allows to discard possible mismatches from the adjustments made at 781.6nm due to the different refractive indices observed at both wavelengths. Here, we make use of the reduced SPDC photon coherence length bounded from below as $\geq$ 1.79mm as evaluated from the (measurement resolution limited) photon bandwidth of below $\Delta\lambda \leq$ 1nm:
Only for an overlap of both time delays within the specified coherence length, interference of both traversed path configurations $|1\rangle_{A_1}|0\rangle_{B_1}$ (Alice's long arm of first IF and Bob's short arm of his first IF) and $|0\rangle_{A_1}|1\rangle_{B_1}$ (Alice's short arm of first IF and Bob's long arm of his first IF) will lead to the observation of an interference pattern. Here, the maximal interference visibility to be observed is limited to 50% due to the contribution of the terms $|0\rangle_{A_1}|0\rangle_{B_1}$ and $|1\rangle_{A_1}|1\rangle_{B_1}$ which cannot interfere with each other. Even for unequal polarization transformations in both paths, interference fringes are detected with a sufficiently high visibility to be clearly discriminated from the background noise. The motorized scan over many periods leads to the observation of interference fringes at arbitrary phases over the range defined by the coherence length. Finally, choosing the translation stage position at which a maximum interference signal was observed allows to equalize both interferometer arms.

The same procedure can be applied to adjust Bob's $2\Delta T$ arm to the double time delay as acquired by his shorter arm with delay ΔT. For that purpose, the short interferometers at Alice's and Bob's site are further serially connected with Bob's $2\Delta T$ interferometer arm. A time delay measurement with the pulsed laser allows to perform rough readjustments in the time delay of this arm. The additional difficulty at the next step is to discriminate between interference fringes resulting from an interference between both shorter interferometer paths $|0\rangle_{A_1}|1\rangle_{B_1}|0\rangle_{B_2}$ and $|1\rangle_{A_1}|0\rangle_{B_1}|0\rangle_{B_2}$ and the fringes between the paths encoded by $|0\rangle_{A_1}|0\rangle_{B_1}|1\rangle_{B_2}$ and $|1\rangle_{A_1}|1\rangle_{B_1}|0\rangle_{B_2}$. Only interference fringes obtained for the second case will be useful for adjusting Bob's long interferometer arm. This problem can be solved by ensuring that the polarization transformations for the paths $|0\rangle_{A_1}|1\rangle_{B_1}$ and $|1\rangle_{A_1}|0\rangle_{B_1}$ are orthogonal to each other, disabling them to interfere. For this configuration a fine adjustment of the path length for $|1\rangle_{B_2}$ allows again to find the optimal position (see Fig. 13 for an adjustment performed with the pulsed laser).
Subsequently, the time delay for $|1\rangle_{B_2}$ is equalized to the corresponding delay for $|1\rangle_{A_2}$ by resorting to the same method as used for balancing $|1\rangle_{A_1}$ and $|1\rangle_{B_1}$. Finally, the path $|1\rangle_{B_3}$ is adjusted to perform exactly the double time delay of $|1\rangle_{A_2}$ and $|1\rangle_{B_2}$, by applying the same method as described before for adjusting Bob's $2\Delta T$ interferometer arm to have the double path length difference as $|1\rangle_{A_1}$ and $|1\rangle_{B_1}$. Finally, the length difference encoded in $|1\rangle_{B_3}$ is equalized to $|1\rangle_{A_3}$.

3.4.2 *Calibration of the interferometer phases*

Calibration requirements— As a final step before performing further measurements it is required to calibrate the relative phase settings implemented in the respective arms. Ideally, the calibration should be performed locally, in order to allow each party to adjust their relative analyzer directions in scenarios where both analysis devices are situated at long distances from each other.
A direct measurement of the relative phases by an external high coherence laser source sharing the central wavelength as the SPDC photons can be used for that purpose: The resulting interference fringes can be used to determine the actually encoded relative phases. But this would require a different design of the chopper blades used to implement the time-multiplexing scheme: The laser intensity would have to be coupled through an additional time slot different from the ones chosen for the SPDC downconversion photons (see 3.3.2). This would avoid the saturation of the detectors.
The method chosen in this work is based on their direct adjustment by referencing on the coincidence count rates detected at the different time windows:
Calibration scheme used in this work— Here, the calibration scheme starts with a closer look at the coincidence functions associated to the 2x2, 2x3 and 2x4 dimensional states encoded in the $6\Delta T$, $5\Delta T$ and $4\Delta T$ time windows of Eqs. (30),(29) and (28) as registered at the detector outputs $+_A+_B$ (the same calibration procedure can as well be applied when using coincidence functions at other coincidence time windows with negative time delays and for the detection at other output modes):

$$C(\alpha_{A_1}, \beta_{B_1})^{2d}_{+,+} = \sin \frac{(\alpha_{A_1} + \beta_{B_1})^2}{2} \tag{41}$$

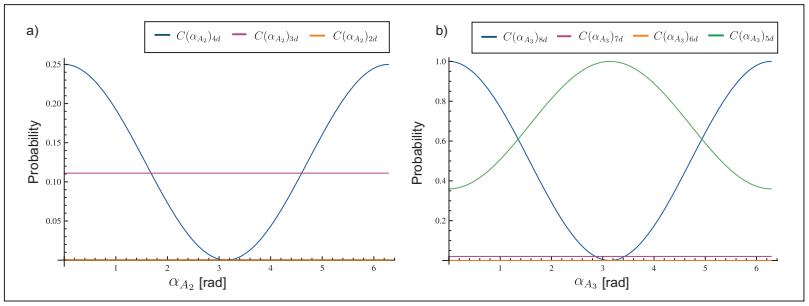

Figure 14: Theoretical coincidence probabilities corresponding to the 2x2, 2x3 and 2x4 dimensional states for a variation of the phase α_{A_2} at Alice's second (a)) and to the 2x5, 2x6, 2x7 and 2x8 dimensional states as a function of the α_{A_3} phase (b)) at Alice's third interferometer arm. The observation of coincidence count rates with the depicted behavior can be used to calibrate the respective phases α_{A_i} and β_{B_j} encoded in each parties 3 interferometer arms denoted with $i, j = 1, 2, 3$. The variation observed corresponds to the case in which the phases not being scanned are calibrated to a constant value of $\alpha_{A_i} = \beta_{B_j} = 0$.

$$C(\alpha_{A_1}, \alpha_{A_2}, \beta_{B_1}, \beta_{B_2})^{3d}_{+,+} = \frac{1}{9}(3 + 2\cos(\alpha_{A_1} - \alpha_{A_2} - \beta_{B_1}) - 2\cos(\alpha_{A_2} + \beta_{B_2}) - 2\cos(\alpha_{A_1} - \beta_{B_1} + \beta_{B_2})) \tag{42}$$

$$C(\alpha_{A_1}, \alpha_{A_2}, \beta_{B_1}, \beta_{B_2})^{4d}_{+,+} = \cos\frac{(\alpha_{A_1} + \beta_{B_1})^2}{2} \sin\frac{(\alpha_{A_2} + \beta_{B_2})^2}{2} \tag{43}$$

Detecting a minimum in the 2d coincidence function can be attributed to any combination of phases α_{A_1} and β_{B_1} satisfying the condition $\alpha_{A_1} + \beta_{B_1} = 0$, i.e. each phase can either be 0 or have the same absolute value with opposite sign.
In order to set these phases to zero it is necessary to register the 3d coincidence count rates as a function of α_{A_2} (see Fig. 14 (a))). This phase can be changed by $\phi_{\lambda/2}$ by rotating the $\lambda/2$ waveplate used at the polarization analysis of the corresponding stabilization setup. Here, if $\alpha_{A_1} = \beta_{B_1} = 0$ is filfilled the coincidence count rate remains constant at $1/9$ of the maximal observed amplitude, and varies sinusoidially if this condition is not fulfilled. For that purpose α_{A_1} and β_{A_1} are alternatingly varied during a scan of α_{A_2} until a minimum interference visibility is observed.
As a function of α_{A_2} and for the adjusted phase settings $\alpha_{A_1} = \beta_{B_1} = 0$ a variation of the coincidence count rates for the 4d state is observed with maximal visibility. If a minimum in the coincidence probability is observed the condition $\alpha_{A_2} + \beta_{B_2} = 0$ has to hold, again not excluding the possibility that both phases are equal but with the opposite sign.

A further calibration step is required in order to fulfill the condition $\alpha_{A_2} = \beta_{B_2} = 0$. For that purpose, one has to take a closer look at the coincidence functions for the 2x5d, 2x6d and 2x7d state:

$$C(\alpha_{A_1},\alpha_{A_2},\alpha_{A_3},\beta_{B_1},\beta_{B_2},\beta_{B_3})^{5d}_{+,+} = \frac{1}{25}(5 + 2\cos(\alpha_{A_1} - \alpha_{A_2} - \beta_{B_1}) - 2\cos(\alpha_{A_1} + \alpha_{A_2} - \alpha_{A_3} - \beta_{B_1}) - 2\cos(\alpha_{A_2} - \alpha_{A_3} - \beta_{B_2}) - 2\cos(\alpha_{A_1} - \alpha_{A_3} - \beta_{B_1} - \beta_{B_2}) + 2\cos(\alpha_{A_2} + \beta_{B_2}) + 2\cos(\alpha_{A_1} - \beta_{B_1} + \beta_{B_2}) - 2\cos(\alpha_{A_3} + \beta_{B_3}) + 2\cos(\alpha_{A_1} + \alpha_{A_2} - \beta_{B_1} + \beta_{B_3}) + 2\cos(\alpha_{A_2} - \beta_{B_2} + \beta_{B_3}) + 2\cos(\alpha_{A_1} - \beta_{B_1} - \beta_{B_2} + \beta_{B_3})) \quad (44)$$

$$C(\alpha_{A_1},\alpha_{A_2},\alpha_{A_3},\beta_{B_1},\beta_{B_2},\beta_{B_3})^{6d}_{+,+} = \frac{1}{9}(3 - 2\cos(\alpha_{A_2} - \alpha_{A_3} - \beta_{B_2}) - 2\cos(\alpha_{A_3} + \beta_{B_3}) + 2\cos(\alpha_{A_2} - \beta_{B_2} + \beta_{B_3}) \cdot \sin(\alpha_{A_1} + \beta_{B_1})^2 \quad (45)$$

$$C(\alpha_{A_1},\alpha_{A_2},\alpha_{A_3},\beta_{B_1},\beta_{B_2},\beta_{B_3})^{7d}_{+,+} = \frac{1}{49}(7 - 2\cos(\alpha_{A_1} + \alpha_{A_2} - \alpha_{A_3} - \beta_{B_1}) + 2\cos(\alpha_{A_2} - \alpha_{A_3} - \beta_{B_2}) + 2\cos(\alpha_{A_1} - \alpha_{A_3} - \beta_{B_1} - \beta_{B_2}) - 4\cos(\alpha_{A_2} + \beta_{B_2}) + 2\cos(\alpha_{A_1} - \alpha_{A_2} - \alpha_{A_3} + \beta_{B_2} - \beta_{B_3}) + 2\cos(\alpha_{A_2} - \alpha_{A_3} + \beta_{B_2} - \beta_{B_3}) - 2\cos(\alpha_{A_1} - \alpha_{A_3} + \beta_{B_1} + \beta_{B_2} - \beta_{B_3}) + 2\cos(\alpha_{A_3} + \beta_{B_3}) + 2\cos(\alpha_{A_1} + \alpha_{A_2} - \beta_{B_1} + \beta_{B_3}) + 2\cos(\alpha_{A_1} - \alpha_{A_2} + \alpha_{A_3} - \beta_{B_1} + \beta_{B_3}) + 2\cos(\alpha_{A_2} - \beta_{B_2} + \beta_{B_3}) + 2\cos(\alpha_{A_1} - \beta_{B_1} - \beta_{B_2} + \beta_{B_3}) - 2\cos(\alpha_{A_2} + \alpha_{A_3} + \beta_{B_2} + \beta_{B_3}) - 2\cos(\alpha_{A_1} + \alpha_{A_3} - \beta_{B_1} + \beta_{B_2} + \beta_{B_3})) \quad (46)$$

Here, scanning the relative phase adjusted at Alice's third interferometer arm α_{A_3} leads to a variation of the predicted coincidence count rates for the different states as depicted in Fig. 14 b). It suffices to take a closer look at the coincidence function for the 2x7d state and iteratively adjust the phases $\alpha_{A,2}$ and $\beta_{B,2}$ until the coincidence count rates remain constant, while the coincidences for the 2x5d state vary with maximal visibility. Only in this case, the condition $\alpha_{A,2} = \beta_{B,2} = \alpha_{A,3} = 0$ is fulfilled. Subsequently, the phase β_{B_3} is scanned until the coincidence count rate corresponding to the 2x8 dimensional state

$$C(\alpha_{A_1},\alpha_{A_2},\alpha_{A_3},\beta_{B_1},\beta_{B_2},\beta_{B_3})^{8d}_{+,+} = \cos\left(\frac{\alpha_{A_1} + \beta_{B_1}}{2}\right)^2 \cos\left(\frac{\alpha_{A_2} + \beta_{B_2}}{2}\right)^2 \cos\left(\frac{\alpha_{A_3} + \beta_{B_3}}{2}\right)^2 \quad (47)$$

reaches a maximal value. In this case the condition $\alpha_{A_3} = \beta_{B_3} = 0$ is fulfilled.

In order to implement the calibration scheme on experimentally observed coincidence count rates typical integration times of up to 3s suffice to apply a fitting scheme on the observed coincidence curves and from these to extract the corresponding motor position for which the corresponding phase is set to 0.

After applying this calibration method a first characterization of the performance of the used experimental setup for analyzing qu*d*it entangled states is made.

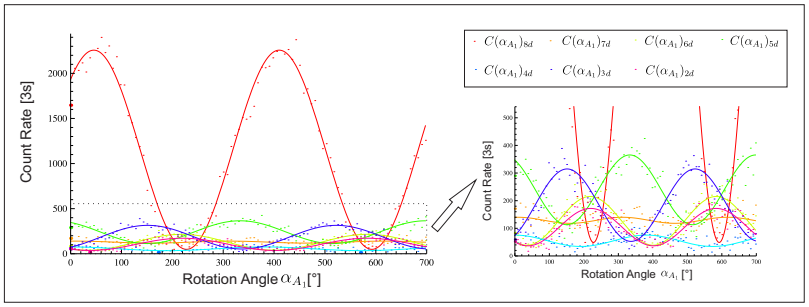

Figure 15: Variation of the coincidence count rates detected within the time windows associated to the encoded 2x8 to 2x2 dimensional states as a function of the rotation angle of the $\lambda/2$ waveplate at Alice's first interferometer arm. For each coincidence curve a sinusoidal function $f(\phi) = A(1 + V\cos 2\pi(\phi - \phi_0)/\lambda)$ is fitted, defined by the visibility V, the amplitude A, the rotation angle offset phi_0 and by the period of the fringes λ.

3.5 PERFORMANCE OF EXPERIMENTAL SCHEME

The ability of both parties to detect entanglement and to further use this resource for its application on quantum information tasks can be characterized by the interference visibility observed and the reproducibility of the results. For that purpose a scan of the respective interferometer phases will lead to the observation of interference fringes displaying intrinsic properties of the state studied: The measured interference visibilities for different states will be the figures of merit for the characterization of the quality of the generated entanglement.

Interference visibility— For a scan of the phase α_{A_1} at Alice's first interferometer arm the interference fringes vary sinusoidially as depicted in Fig. 15 for a coincidence time window of 1.15ns and an integration time for each data point of 3s. The phases are calibrated to fulfill the conditions $\alpha_{A_2} + \beta_{B_2} = 0$ and $\alpha_{A_3} + \beta_{B_3} = 0$ ensuring to observe maximal coincidence counts for the 2x8d, 2x4d and 2x2d dimensional states (Eq. 47). Here, observing maximal interference visibilities doesn't depend on the concrete values of α_{A_2}, β_{B_2}, α_{A_3} and α_{B_3} and are thus explicitly chosen to not being equal to 0. This enables to observe interference fringes for states with dimensions 2x7, 2x6, 2x5 and 2x3 simultaneously, too. Otherwise some of these count rates would remain constant as a function of the scanned phase, as described in the calibration section (See 3.4.2).

A fitting algorithm is applied on the observed coincidence counts with a function parameterized by $f(\phi) = A(1 + V\cos 2\pi(\phi - \phi_0)/\lambda)$ with V denoting the interference visibility, A the amplitude, ϕ_0 the phase offset and λ the period of the fringes. For this parameterization, the data for the 2x8 dimensional state corresponds to a (two-photon) interference visibility of $V_{8d}^{A_1} = 0.958 \pm 0.017$. For lower dimensional states such as $7d$, $6d$, $5d$ and 3d the visibilities cannot simultaneously approach unity due to the different dependence on the scanned phases (see Eqs.(46), (45), (44) and (42)). This, in a simplified picture, is due to the fact, that observing maximal interference fringes as a function of a specific phase requires the remaining phases to acquire specific multiples of $2\pi/d$ with d denoting the specific dimension of the state. Accordingly, the coincidence functions offer reduced visibili-

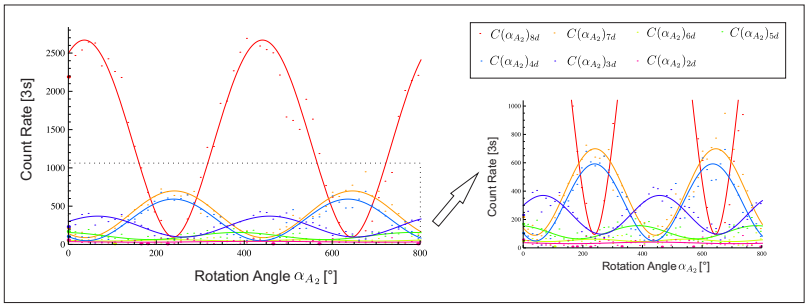

Figure 16: Variation of the coincidence count rates associated to each state of different dimensionality between 2x8 to 2x2 as a function of the rotation angle of the $\lambda/2$ waveplate at Alice's second interferometer. Each coincidence count rate is plotted together with the corresponding optimal fitted curve.

ties. That these are high enough for further applications is directly tested by applying the corresponding entanglement (see 4.2.1) and dimension entanglement schemes (see 6.1).
Negligible interference fringes are observed for the 2x4d state, as predicted for the condition $\alpha_{A_2} + \beta_{B_2} = 0$ (Eq. 43). Finally the interference visibility for the 2x2 state is only limited by the decreasing signal to noise ratio intrinsic to the probabilistic splitting of the coincidences into different time windows: Only 2 out of the possible terms contributing to a coincidence are distributed to this time window. Here, the typically observed value is in the range of $V_{2d}^{A_1} = 0.751 \pm 0.036$ (Eq. 41). This parameter can be further increased by choosing a smaller coincidence time window and therefore a better signal to noise ratio as for the coincidence curves depicted in Fig. 18.
As predicted by theory, the coincidence count rates of the 2x8 dimensional state vary proportional to $\cos^2(\alpha_{A_1} + \beta_{B_1})/2$. In contrast, this functional dependence is described as $\sin^2(\alpha_{A_1} + \beta_{B_1})/2$ for the 2x2 state. A shift in the rotation angle, corresponding closely to a phase shift of π of $0.949 \pm 0.055 \cdot \pi$ is observed, close to the predicted value of π between both curves.
In contrast, as a function of α_{A_2} and for fixed phase relations $\alpha_{A_1} + \beta_{B_1} = 0$ and $\alpha_{A_3} + \beta_{B_3} = 0$ (again, with the values for each individual phase unequal 0) one can observe different interference visibilities for the different states. A similar high visibility of $V_{8d}^{A_2} = 0.961 \pm 0.029$ is observed. The coincidence count rates for the 2x6d as well as for the 2x2d state are minimal as predicted for a phase relation $\alpha_{A_1} + \beta_{B_1} = 0$, while for the 2x7, 2x5 2x4 states now the interference visibilities are higher: $V_{7d}^{A_2} = 0.774 \pm 0.020$, $V_{5d} = 0.585 \pm 0.021$ and $V_{4d}^{A_2} = 0.847 \pm 0.024$.
Here, the phase relation between the 8d and 4d coincidence count rates corresponds closely to $1.064 \pm 0.075 \cdot \pi$. This is expected for a variation of the 8d count rates $\propto \cos^2(\alpha_{A_2} + \beta_{B_2})/2$, while for the 4d state these are predicted to vary $\propto \sin^2(\alpha_{A_2} + \beta_{B_2})/2$, i.e. with a π phase shift between each other.

Finally, a scan of the coincidence count rates as a function of α_{A_3} is presented in Fig. 17, here for a fixed phase relationship $\alpha_{A_1} + \beta_{B_1} = 0$ and $\alpha_{A_2} + \beta_{B_2} = 0$. As expected, no variation of the coincidence count rates are observed for the 4, 3 and 2 dimensional states, whose coincidence count rates show no dependence on the phase α_{A_3} nor on α_{B_3}. In contrast, the 8d

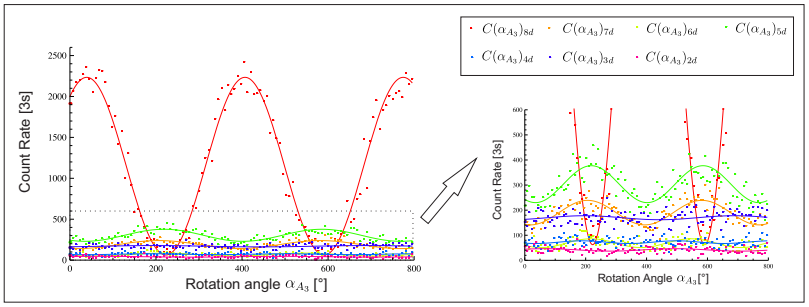

Figure 17: Variation of the coincidence count rates associated to each state of different dimensionality between 2x8 to 2x2 as a function of the rotation angle of the $\lambda/2$ waveplate at Alice's longest interferometer. Each coincidence count rate is plotted together with the corresponding optimal fitting curve.

state presents interference fringes with a visibility of $V_{8d}^{A_3} = 0.945 \pm 0.021$, while again those for the 7 to 5 dimensional states are low for the individual choice of the other phases.

For a scan of the phases as described here, the observed period of the fringes deviates within the standard deviation by up to $\lambda/\lambda_0 = (375.12°/360° \pm 11.34°/360°) = 1.042 \pm 0.032$ from the expected range of $\eta \approx 805.9/781.6 = 1.031$ (with $\lambda_{Photon} = 805.9$nm and $\lambda_{SL} = 781.6$nm corresponding to the wavelengths of the photons and the stabilization laser, respectively). The last value is given by the quotient of the SPDC photon to the stabilization laser wavelength. This factor is expected as the phase at each interferometer loop is varied over optical path lengths multiple of the stabilization laser wavelength. It differs by this factor from the optical path lengths observed by the SPDC photons: A phase change of 360° as determined from the variation of the stabilization laser signal corresponds to a phase change of $360° \cdot \eta$ for the SPDC photons (in Figs. 15,16,17 only the actual motor rotation angles multiplied by 2 are depicted. Thus the actual phase scanned by the photons can be approximated by making the described conversion.)

Reduction of the width of the coincidence time window— The observed signal to noise ratio can be further improved by reducing the width of the coincidence time windows over which the coincidence count rates are integrated. This can be attributed to the fact that the coincidence count rates are typically distributed according to a Gaussian distribution as a function of the integration time window δt_{int}. In contrast, the detected background count rates increase linearly with the time window. Calculations reveal that the signal to noise ratio decreases to a first approximation according to $\propto 1/\delta t_{int}$ as a function of the time window width δt_{int}. This leads effectively to observing the best signal to noise ratios for the minimal timing resolution, in this work of $\approx$ 164 ps specified for the used time-to-digital converter [12]. As the coincidence time distributions detected are spread over time windows with a FWHM distribution of typically $\approx$ 1ns, effectively coincidence count rates are discarded by reducing the time window.

For the reduced time window of $\approx 164ps$ the coincidence count rates observed for the 2x8, 2x4 and 2x8 dimensional states (Fig. 18) are again pre-

12 The resolution of the Acam TDC GPX is specified to be 82ps, but coincidence count rates have to be averaged over two subsequent time bins in order to reduce additional time scattering intrinsic to the card electronics.

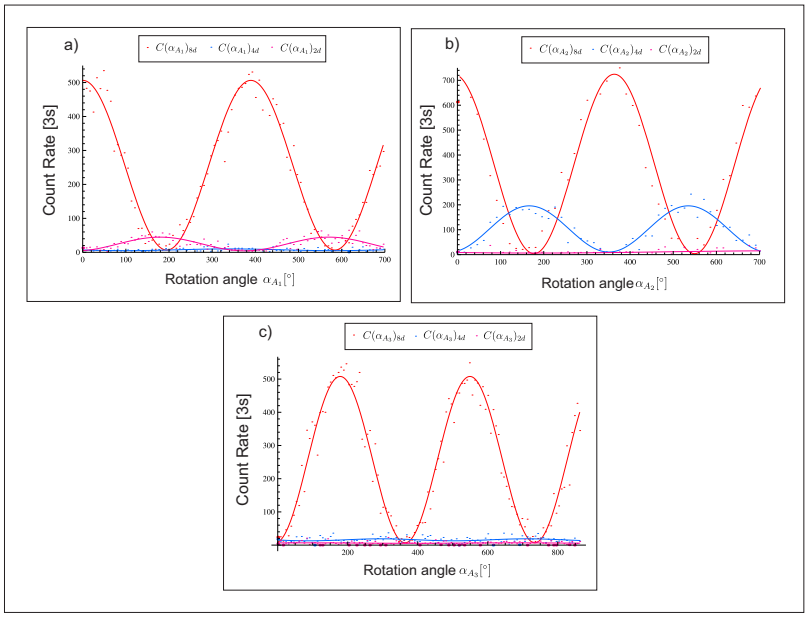

Figure 18: Observation of coincidence count rates for the 2x8, 2x4 and 2x2 dimensional states as a function of α_{A_1} (a)), α_{A_2} (b)) and α_{A_3} (c)) for a reduction of the coincidence time window down to 164ps. The improved signal to noise ratio leads to an improvement of the observed two-photon interference visibilities of the 2x8 dimensional states to $V > 97\%$: $V_{8d,A_1} = 0.973 \pm 0.012$ (a)), $V_{8d,A_2} = 0.989 \pm 0.029$ (b)) and $V_{8d,A_3} = 0.974 \pm 0.013$ (c)). Similar improvements in the visibilities are observed for the 2x4 and 2x2 dimensional states. Here, a visibility of up to $V_{4d}^{A_2} = 0.962 \pm 0.037$ and $V_{2d,A_1} = 0.822 \pm 0.042$ as a function of α_{A_1} are reached.

sented as a function of the respective phases α_{A_1}, α_{A_2} and α_{A_3} of Alice's first to third interferometer arm, while constraining the other phases not being scanned to $\alpha_{A_i} + \beta_{B_i} = 0$. The fitted visibilities for the 8 dimensional states are $V_{8d}^{A_1} = 0.973 \pm 0.012$ (a)), $V_{8d}^{A_2} = 0.989 \pm 0.029$ (b)) and $V_{8d}^{A_3} = 0.974 \pm 0.013$ (c)). Again, for a variation of α_{A_2} and respectively α_{A_1} the 2 and 4 dimensional states display a variation of the coincidence count rates with visibilities $V_{4d}^{A_2} = 0.962 \pm 0.037$ (b)) and $V_{2d}^{A_1} = 0.822 \pm 0.042$ (a)). Similarly, for the phase relation $\alpha_{A_1} + \beta_{B_1} = \pi$, the coincidence count rates for the 4d state display interference fringes with $V_{4d}^{A_1} = 0.945 \pm 0.039$ as a function of α_{A_1} (Not plotted). The observed visibilities serve as a figure of merit to characterize the capability of the analysis to detect entanglement in higher dimensional states. As will be seen in the next chapter, these are above the critical visibilities required for the observation of entanglement.

Part II

EXPERIMENTAL VERIFICATION OF ENTANGLEMENT AND SUITABILITY FOR FURTHER QUANTUM INFORMATION TASKS

4

QU*D*IT ENTANGLEMENT DETECTION

In this chapter the basic foundations for the detection and finally the experimental demonstration of entanglement for the prepared qu*d*it entangled states will be presented. Here, a general review of the entanglement criteria suited for detecting the entanglement present in qu*d*it entangled states is presented (see sections 4.1 and 4.3). These criteria enable the detection of bipartite qu*d*it entangled states based on the evaluation of Bell type inequalities (section 4.1.2), the analysis of the created states in mutually unbiased bases (section 4.3.2), on the determination of their Schmidt number (section 4.3.1) and finally on the evaluation of an entanglement witness (section 4.3.3). Finally, we present the experimental results on the evaluation of a Bell-type inequality (section 4.2) suited for detecting the entanglement of the emission time correlated two-photon qu*d*it states generated in this work.

Out of the broad range of entanglement criteria [62, 72], we will concentrate here only on the ones suited for the entanglement detection of qu*d*it entangled states as prepared in this work.

4.1 BELL-TYPE INEQUALITIES

Since the first proposal of a Bell-type inequality [13] able to describe the incompatibility of quantum theory with a local realistic theory, a broad range of inequalities have been developed:

4.1.1 *CHSH inequality*

As introduced in 2.1.4, theories satisfying both axioms of **realism** and **locality** are called **local realistic hidden variable theories**. Based on this theory a Bell inequality could be derived [13], used for showing that quantum theory cannot be reconciled with both axioms of realism and locality at the same time. A reformulation of the inequality lead to the derivation of the Clauser-Horne (CH) [37] and Clauser-Horne-Shimony-Holt (CHSH) [36] inequalities. Out of these, the second one is most widely used for the experimental verification of two-qubit entanglement of a quantum state encoded into two particles. It considers a scenario in which both particles are distributed to two parties, Alice and Bob, whose analysis devices are described by observables $A(a,\lambda)$ and $B(b,\lambda)$. The observables are dichotomic, defining that for any measurement settings a and b only two possible results $+1$ and -1 are to be observed. These depend on hidden variables λ determining the correlation between the outcomes based on the description by a hidden variable distribution function $p(\lambda)$ according to

$$E(\vec{a},\vec{b}) = \int p(\lambda)A(a,\lambda)B(b,\lambda)d\lambda, \tag{48}$$

where $\int_{-\infty}^{\infty} p(\lambda)d\lambda = 1$.
The locality condition is ensured if the measurement setting and outcome on the observable $A(a,\lambda)$ on the first particle cannot be communicated at maximum with the speed of light to the local analyzer where the observable $B(b,\lambda)$ is applied on the second particle.
Finally, the CHSH inequality is based on the measurement of 4 correlation values leading to the bound

$$I_{CHSH}^{LR} = |E(\vec{a},\vec{b}) - E(\vec{a},\vec{b'}) + E(\vec{a'},\vec{b}) + E(\vec{a'},\vec{b'})| \leq 2 \tag{49}$$

with each correlation measurement E for 4 different settings $\{a,b\}$, $\{a,b'\}$, $\{a',b\}$ and $\{a',b'\}$.
Two-qubit entangled states encoded into a pair or particles could be used to violate the Bell inequality experimentally (first by Freedman et al. [53] and followed by Aspect et al. [9, 10]) with values for the Bell inequality parameter close to the maximal expected value of $I_{CHSH,QM} = 2\sqrt{2} > 2$. These results clearly displayed that quantum states do not fulfill the description given by a local realistic hidden variable model (LHVT).
The violation of a Bell inequality can be used to detect entanglement, as, in contrast, no separable state can be used as a resource for violating it. This will be used in this work, with special emphasis put onto the application of Bell-type inequalities suited to determine the entanglement of bipartite qu$d$it entangled states.

4.1.2 *CGLMP inequality*

Entanglement detection schemes, suited to be applied on bipartite d dimensional states can be based on Bell-type inequalities such as the one derived by Collins, Gisin, Linden, Massar and Popescu (CGLMP) [38]. Bell-type inequalities on quantum states encoded in higher dimensions could be shown to display a higher violation of local realism [80, 78, 79]. As this inequality will be applied on quantum states as prepared in this work (see 4.1.2), a short derivation will be given based on [155]. It starts with the definition of a bipartite qu$d$it state with each qu$d$it state embedded in a d dimensional Hilbert space $\mathcal{H}^A = \mathcal{C}^d$ and $\mathcal{H}^B = \mathcal{C}^d$. Each party, Alice and Bob, has at its disposal an analysis device with which it can obtain up to d different results for the qu$d$it local state they are analyzing. The main requirement of a realistic theory is that the coincidence probabilities are distributed according to a well defined probability function

$$P(A_1 = j, A_2 = k, B_1 = l, B_2 = m) \tag{50}$$

to be obtained for the different measurement results $j,k,l,m \in \{0,1,...,d-1\}$. In full equivalence to the 2 dimensional case defined by the CHSH inequality, both parties can choose between two different analysis settings A_1/A_2 and B_1/B_2.
Here, the probabilities obtained for the different measurement outcomes to add up to unity according to

$$\sum_{j,k,l,m} P(A_1 = j, A_2 = k, B_1 = l, B_2 = m) = 1. \tag{51}$$

In order to simplify the notation, the probability notation is simplified according to

$$P(A_a = B_b + k) = \sum_{j=0}^{d-1} P(A_a = (j+k) mod(d), B_b = j), \tag{52}$$

describing the situation in which the measurement outcome on Alice's analysis device differs from the one obtained on Bob's state by k.
Under these constraints, an inequality can be derived with the following general form for an arbitrary dimension of each qu$d$it:

$$\begin{aligned} I_d = \sum_{k=0}^{mod[d/2]-1} (1 - \frac{2k}{d-1}) \\ \{[P(A_1 = B_1 + k) + P(B_1 = A_2 + k + 1) + P(A_2 = B_2 + k) + \\ P(B_2 = A_1 + k)] - \\ [P(A_1 = B_1 - k - 1) + P(B_1 = A_2 - k) + P(A_2 = B_2 - k - 1) + \\ P(B_2 = A_1 - k - 1)]\}. \end{aligned} \tag{53}$$

For the purpose of detecting entanglement the bound $I_d = 2$, valid for arbitrary dimensions d, has to be surpassed as it restricts the studied states to be described by a local realistic model. Accordingly, a violation of these bounds can be used to detect entanglement.
Indeed, a violation of the inequality can be calculated for example for the maximally entangled states of arbitrary dimension d

$$|\Psi\rangle_d = \frac{1}{\sqrt{d}} \sum_{k=0}^{d-1} |k\rangle_A |k\rangle_B. \tag{54}$$

Both parties define their analysis as a projection on

$$|k\rangle_{A_a} = \frac{1}{\sqrt{d}} \sum_{k=0}^{d-1} e^{(\frac{2\pi i}{d} s(k+\alpha_a))} |s\rangle_A \tag{55}$$

and

$$|l\rangle_{B_b} = \frac{1}{\sqrt{d}} \sum_{k=0}^{d-1} e^{(\frac{2\pi i}{d} s(-l+\beta_b))} |s\rangle_B, \tag{56}$$

where the analyzer phase settings are α_a and β_b.
Here, an optimal choice of the analyzer phase settings of $\alpha_1 = 0$, $\alpha_2 = 1/2$, $\beta_1 = 1/4$ and $\beta_2 = -1/4$ will lead to variation of the coincidence probabilities according to

$$\begin{aligned} P(A_a = k, B_b = l) = Tr(|\Psi\rangle_d \langle\Psi|_d |k\rangle_{A_a} \langle k|_{A_a} \otimes |l\rangle_{B_b} \langle l|_{B_b}) = \\ \frac{1}{2d^3 \sin^2(\pi(k - l + \alpha_a + \beta_b)/d)}. \end{aligned} \tag{57}$$

Inserted into the inequality this leads to its generalized form:

$$I_d = \frac{2}{d^2} \sum_{k=0}^{mod[d/2]-1} (1 - \frac{2k}{d-1}) (\frac{1}{\sin^2(\frac{\pi}{d}(k + \frac{1}{4}))} - \frac{1}{\sin^2(\frac{-\pi}{d}(k + \frac{3}{4}))}). \tag{58}$$

The evaluation of the CGLMP inequality terms for the set of maximally entangled states introduced before enables to observe an increase of the violation with increasing dimension, leading to a maximal parameter of $I_\infty = 2.9698 > 2$ for infinite dimensional maximally entangled states. This value is higher than the violation $I_2 = 2.8284$ to be obtained when testing the CHSH inequality (equivalent to CGLMP for $d = 2$) on a bipartite 2 dimensional state. It is useful to characterize the higher violation of local realism for high dimensional states by an admixture of (white) noise α. A state is parameterized here as $|\Psi\rangle = \alpha 1/\sqrt{d}\sum_{k=0}^{d-1}|k\rangle|k\rangle + (1-\alpha)\mathbb{1}/d$. For a state defined in a $d \to \infty$ dimensional Hilbert space the critical noise admixture still allowing to detect entanglement is decreased from $\alpha_{crit}^2 = 0.707$ to $\alpha_{crit}^{d\to\infty} = 0.6734$ [155].
The violation of CGLMP inequalities can be shown to be **necessary** and **sufficient** conditions for the observation of entanglement [113].

4.2 APPLICATION OF CGLMP INEQUALITY ON THE PREPARED STATES

In order to apply the CGLMP inequalities on the states studied in this work, a suitable measurement basis consisting of up to d projection measurements is required in order to obtain d different results for each qu$d$it analyzed by the respective parties Alice and Bob. For that purpose, the analysis performed by both partie's interferometer systems is described in more detail.
Definition of projection measurements— At this point we want to take a closer look at the observables required for testing a 2 dimensional CGLMP inequality (equivalent to CHSH) on a 2x2 dimensional entangled state. Here, two dichotomic measurements on each qubit encoded into a different particle are made. For example, for polarization entangled states encoded into a pair of photons these would correspond to projections onto the two orthogonal states $|H\rangle$ and $V\rangle$.
For this experimental configuration, the dichotomic measurements can be either performed by choosing devices, such as $\lambda/2$ waveplates combined with polarization beamsplitters, allowing to project the incoming state onto both states $|H\rangle$ and $|V\rangle$ or as polarizers, transmitting only one linear polarization component. In the second case, H or V polarized light is transmitted by setting appropriate settings of the polarizer itself. In order to apply the former scheme for the analysis of d dimensional time-energy encoded states multiport beamsplitters are suited [188]. In this case each qu$d$it is projected into d different orthogonal states at each of the d different output modes, in equivalence to the projection onto 2 modes for a polarization beamsplitter. It is not possible to use this scheme in this experiment, as due to the series configuration of the interferometers only dichotomic projection measurements can be performed at the output modes of the last interferometer arm. This is due to the fact that the output modes of each interferometer arm are directly fed into the input modes of the subsequent arm. This last interferometer arm applies 2 orthogonal projections on the studied state, either a projection onto the $+$ or on the $-$ output of the interferometer. It is therefore necessary to use additional (offset) phases to set the required d different projection measurements, in full analogy to choosing 2 polarizer settings as required for the 2 dimensional case:
These can be defined by appropriate choices of the respective phase settings $\alpha_{A_i}^{O,s}$ and $\beta_{B_j}^{O,t}$ encoded in each interferometer arm with indices $i,j = 1,2,3$. Here, the notation s and t refers to the full set of offset phases required

to span a basis using Alice's and Bob's interferometer phases. Further on, both parties are required to choose between two different analysis settings A_1/A_2 and B_1/B_2.
Nevertheless, each interferometer arm is able to manipulate only one phase $\alpha'^{k}_{A_i}$ and $\beta'^{l}_{B_j}$ for indices $k,l = 1,2$ and $i,j = 1,2,3$. Therefore, it is useful to decompose the phases set at the respective interferometer arms by choosing the decomposition into analysis and measurement phases according to $\alpha'^{k,s}_{A_i} = \alpha^{k}_{A_i} + \alpha^{O,s}_{A_i}$ and $\beta'^{l,t}_{B_j} = \beta^{l}_{B_j} + \beta^{O,t}_{B_j}$. In this picture, a general projection measurement is defined for each party according to

$$|a^s\rangle_A = \frac{1}{\sqrt{d}} \sum_{m=0}^{d-1} e^{i(\alpha^{k}_{A_i} + \alpha^{O,s}_{A_i})} |m\rangle_A \tag{59}$$

$$|b^t\rangle_B = \frac{1}{\sqrt{d}} \sum_{n=0}^{d-1} e^{i(\beta^{l}_{B_j} + \beta^{O,t}_{B_j})} |n\rangle_B. \tag{60}$$

Finally, the expectation value for a coincidence measurement can be expressed as

$$P_{k,l,s,t} = Tr[\rho(|a^s\rangle \otimes |b^t\rangle)(\langle a^s| \otimes \langle b^t|)] \tag{61}$$

for the states $\rho = |\Psi_d\rangle\langle\Psi_d|$. Here, $|\Psi_d\rangle = 1/\sqrt{d} \sum_{k=0,k'=m}^{d-1} |k\rangle|k'\rangle$ corresponds to the states obtained by postselection of the analyzed states at time delays $(k - k') = m\Delta T$ in units of ΔT. Correspondingly, the number of two-photon emission time modes analyzed is varied as a function of the time delays both parties agree to place their postselection window on.
Accordingly, the phase settings required for analyzing the different states of different dimension vary. As described in sect. 3.4.2, for a 2 dimensional state postselected at a time delay $\pm 6\Delta T$, only phases $\alpha^{k}_{A_1}$ and $\beta^{l}_{A_1}$ are required such as to analyze the state. Additional phase settings $\alpha^{k}_{A_2}$ and $\beta^{l}_{A_2}$ are required to analyze the 2x4 dimensional states postselected at delays $\pm 4\Delta T$, as well as the 2x3 dimensional states at $\pm 5\Delta T$. In contrast, the analysis of the bipartite 8, 7, 6 and 5 dimensional states depends on all 6 phases available to both parties.

Choice of optimal measurement basis based on MUBs— In order to evaluate the maximal possible value for I_d for the respective state analysis used, the coincidence probability functions described in full detail in 3.4.2 are used with each phase replaced according to $\alpha_{A_i} \rightarrow \alpha^{k}_{A_i} + \alpha^{O,s}_{A_i}$ and $\beta_{B_j} \rightarrow \beta^{l}_{B_j} + \beta^{O,t}_{B_j}$. Here, $k,l = 1,2$ denotes the analysis settings and the index $i,j = 1,2,3$ denotes the relative phase settings manipulated at each of Alice's and Bob's interferometer arms.
Starting from the definition of Eq. 62 and choosing $d = 2$, it is necessary to parameterize Alice's measurement basis (and correspondingly Bob's basis)

$$\frac{1}{\sqrt{2}}(|0\rangle + e^{i\alpha^{O,s}_{A_1}}|1\rangle) \tag{62}$$

as a function of the offset phase $\alpha^{O,s}_{A_1}$ in order to define a 2d basis at appropriate phase settings. For a 4d analysis it is expressed as

$$\frac{1}{2}(|0\rangle + e^{i\alpha^{O,s}_{A_1}}|1\rangle + e^{i\alpha^{O,s}_{A_2}}|2\rangle + e^{i(\alpha^{O,s}_{A_1} + \alpha^{O,s}_{A_2})}|3\rangle) \tag{63}$$

and for a 8d analysis as

$$\frac{1}{2\sqrt{2}}(|0\rangle + e^{i\alpha_{A_1}^{O,s}}|1\rangle + e^{i\alpha_{A_2}^{O,s}}|2\rangle + e^{i(\alpha_{A_1}^{O,s}+\alpha_{A_2}^{O,s})}|3\rangle + e^{i\alpha_{A_3}^{O,s}}|4\rangle + e^{i(\alpha_{A_1}^{O,s}+\alpha_{A_3}^{O,s})}|5\rangle + e^{i(\alpha_{A_2}^{O,s}+\alpha_{A_3}^{O,s})}|6\rangle + e^{i(\alpha_{A_1}^{O,s}+\alpha_{A_2}^{O,s}+\alpha_{A_3}^{O,s})}|7\rangle) \tag{64}$$

A measurement basis can be defined now by choosing concrete values of the (offset) phase settings set at the respective interferometer arms. For example, it is advantageous to make use of bases encoded in mutually unbiased bases (see 2.1.2 and appendix of [183]) for that purpose, as they allow to optimally span the respective d dimensional Hilbert spaces. In the case of 2x2, 2x4 and 2x8 dimensional states the following product bases

$$MUB^2 = \frac{1}{\sqrt{2}}\begin{pmatrix}(|0\rangle + |1\rangle)\\(|0\rangle - |1\rangle)\end{pmatrix} \tag{65}$$

$$MUB^4 = \frac{1}{2}\begin{pmatrix}(|0\rangle + |1\rangle + |2\rangle + |3\rangle)\\(|0\rangle - |1\rangle + |2\rangle - |3\rangle)\\(|0\rangle + |1\rangle - |2\rangle - |3\rangle)\\(|0\rangle - |1\rangle - |2\rangle + |3\rangle)\end{pmatrix} \tag{66}$$

$$MUB^8 = \frac{1}{2\sqrt{2}}\begin{pmatrix}(|0\rangle + |1\rangle + |2\rangle + |3\rangle + |4\rangle + |5\rangle + |6\rangle + |7\rangle)\\(|0\rangle - |1\rangle + |2\rangle - |3\rangle + |4\rangle - |5\rangle + |6\rangle - |7\rangle)\\(|0\rangle + |1\rangle - |2\rangle - |3\rangle + |4\rangle + |5\rangle - |6\rangle - |7\rangle)\\(|0\rangle + |1\rangle + |2\rangle + |3\rangle - |4\rangle - |5\rangle - |6\rangle - |7\rangle)\\(|0\rangle - |1\rangle - |2\rangle + |3\rangle + |4\rangle - |5\rangle - |6\rangle + |7\rangle)\\(|0\rangle - |1\rangle + |2\rangle - |3\rangle - |4\rangle + |5\rangle - |6\rangle + |7\rangle)\\(|0\rangle + |1\rangle - |2\rangle - |3\rangle - |4\rangle - |5\rangle + |6\rangle + |7\rangle)\\(|0\rangle - |1\rangle - |2\rangle + |3\rangle - |4\rangle + |5\rangle + |6\rangle - |7\rangle)\end{pmatrix} \tag{67}$$

can be used. Here, for example choosing different values for the (offset) phase settings $\alpha_{A_1}^{O,s}, \alpha_{A_2}^{O,s}, \alpha_{A_3}^{O,s} \in [0, \pi/2]$, enables to define the measurements in MUB bases.
A similar description is used for the definition of the 3, 5 and 7 dimensional measurement bases

$$MUB^3 = \frac{1}{\sqrt{3}}\begin{pmatrix}(|0\rangle + |1\rangle + |2\rangle)\\(|0\rangle + e^{i2\pi/3}|1\rangle + e^{i4\pi/3}|2\rangle)\\(|0\rangle + e^{i4\pi/3}|1\rangle + e^{i2\pi/3}|2\rangle)\end{pmatrix}, \tag{68}$$

$$MUB^5 = \frac{1}{\sqrt{5}}\begin{pmatrix}(|0\rangle + |1\rangle + |2\rangle + |3\rangle + |4\rangle)\\(|0\rangle + e^{i2\pi/5}|1\rangle + e^{i4\pi/5}|2\rangle + e^{i6\pi/5}|3\rangle + e^{i8\pi/5}|4\rangle)\\(|0\rangle + e^{i4\pi/5}|1\rangle + e^{i8\pi/5}|2\rangle + e^{i2\pi/5}|3\rangle + e^{i6\pi/5}|4\rangle)\\(|0\rangle + e^{i6\pi/5}|1\rangle + e^{i2\pi/5}|2\rangle + e^{i8\pi/5}|3\rangle + e^{i4\pi/5}|4\rangle)\\(|0\rangle + e^{i8\pi/5}|1\rangle + e^{i6\pi/5}|2\rangle + e^{i4\pi/5}|3\rangle + e^{i2\pi/5}|4\rangle)\end{pmatrix} \tag{69}$$

and

$$MUB_8^7 = \frac{1}{\sqrt{7}} \begin{pmatrix} 1 & 1 & 1 & 1 & 1 & 1 & 1 & 1 \\ 1 & e^{-i2\pi/7} & e^{-i4\pi/7} & e^{-i6\pi/7} & e^{i6\pi/7} & e^{i4\pi/7} & e^{i2\pi/7} & 1 \\ 1 & e^{-i4\pi/7} & e^{i6\pi/7} & e^{i2\pi/7} & e^{-i2\pi/7} & e^{-i6\pi/7} & e^{i4\pi/7} & 1 \\ 1 & e^{-i6\pi/7} & e^{i2\pi/7} & e^{-i4\pi/7} & e^{i4\pi/7} & e^{-i2\pi/7} & e^{i6\pi/7} & 1 \\ 1 & e^{i6\pi/7} & e^{-i2\pi/7} & e^{i4\pi/7} & e^{-i4\pi/7} & e^{i2\pi/7} & e^{-i6\pi/7} & 1 \\ 1 & e^{i4\pi/7} & e^{-i6\pi/7} & e^{-i2\pi/7} & e^{i2\pi/7} & e^{i6\pi/7} & e^{-i4\pi/7} & 1 \\ 1 & e^{i2\pi/7} & e^{i4\pi/7} & e^{i6\pi/7} & e^{-i6\pi/7} & e^{-i4\pi/7} & e^{-i2\pi/7} & 1 \\ 1 & 1 & 1 & 1 & 1 & 1 & 1 & 1 \end{pmatrix} \begin{pmatrix} |0\rangle \\ |1\rangle \\ |2\rangle \\ |3\rangle \\ |4\rangle \\ |5\rangle \\ |6\rangle \\ |7\rangle \end{pmatrix} \tag{70}$$

which again are generated by choosing appropriate phase settings at Alice's and Bob's analyzers.

Optimization of Bell inequality terms I_d— With these definitions it is now possible to find the optimal value for the parameters I_d characterizing the strength of the violation of the inequalities by the respective states, as a function of Alice's and Bob's analysis phase settings $\alpha^k_{A_i}$ and $\beta^l_{A_2}$ with indices $k, l = 1, 2$.

A numerical optimization (NMaximize function in Mathematica, allowing to determine the global maximum of an unconstrained function as derived for I_d), reveals that the maximal values to be observed for the used state analysis I_d^{Setup} compared to values when using an optimal analysis I_d^{max} correspond to:

State	2x2	2x3	2x4	2x5	2x6	2x7	2x8
I_2	**2.823**	—	—	—	—	—	—
I_3	—	**2.873**	—	—	—	—	—
I_4	—	—	**2.552**	—	—	—	—
I_5	—	—	—	**2.620**	—	—	—
I_6	—	—	—	—	1.524	—	—
I_7	—	—	—	—	—	1.895	—
I_8	—	—	—	—	1.572	**2.712**	**2.497**
I_{Max}	2.823	2.873	2.896	2.920	2.911	2.927	2.932

In this table the maximally achievable values I_d^{Setup} are compared for the different states and for the application of a d dimensional inequality on the prepared states of differing dimension. Surpassing the bound $I_d \leq 2$ allows to describe the bipartite states according to a local realistic model, allows to detect their entanglement. In all cases they are equal or lower than the maximal predicted values I_d^{max} to be obtained for an optimal analysis of the maximally entangled states (included in the lowest row). More importantly, the application of a 6 and 7 dimensional inequality on 2x6 and 2x7 dimensional states doesn't allow to surpass the bound $I_d \leq 2$, therefore not allowing to proove their entanglement (see subsequent discussion). Nevertheless, a violation of inequality I_7 is observed when it is applied on the 2x8 state, postselected at a time delay $0\Delta T$[1]. Due to these reasons only the values of the bounds I_d^{Setup} marked in red will be considered for their experimental evaluation. A list of the analysis angles optimizing these inequalities are given in the Appendix 8.1.

1 This is possible as the state space of the used 2x8 dimensional state analysis encompasses the state space of a lower dimensional state as well

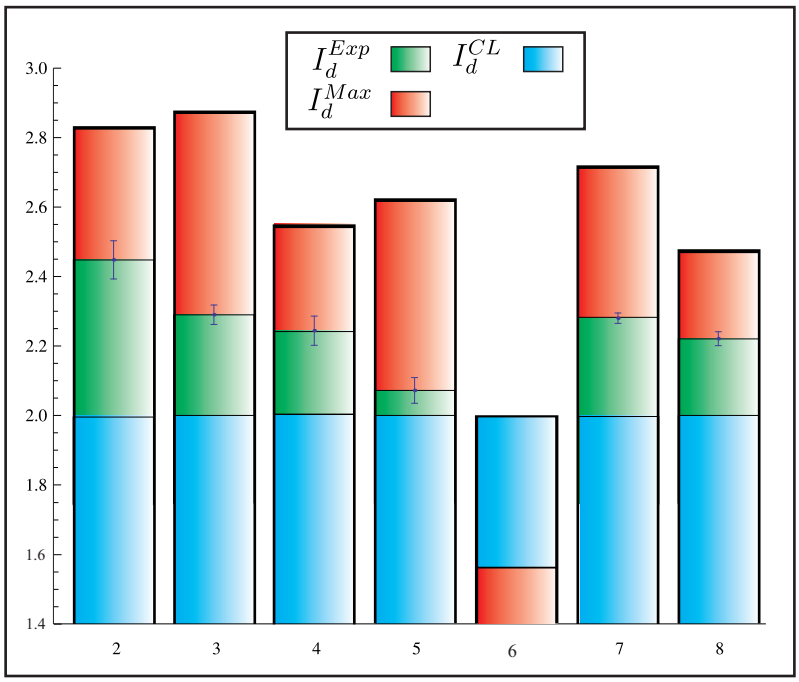

Figure 19: Comparison of the experimentally obtained values I_d^{Exp} with the theoretically predicted maximal values I_d^{Setup} for the bipartite time-energy encoded states of varying dimension 2xd analyzed in this setup. These values are shown to surpass the bounds predicted for a local realistic model $I_d^{LR} = 2$ for dimensions 2xd between 2x2 and 2x8 except for 2x6, where the analysis is not sufficient to display a violation. The violation of the bounds thus allows to detect entanglement between the two local qu*d*its.

Non-optimal violation of inequalities— The fact that a lower maximal bound I_d^{Setup} than the one expected for a maximally entangled state I_d^{max} is observed (except for the 2x2 and 2x3 dimensional states) can be attributed to the limited state space to be accessed by the respective analyzers. This is due to the fact that they provide an insufficient number of independent phase settings for that purpose. From a geometrical point of view it can be argued that the facet of the correlation polytope defined by the CGLMP inequality, constraining the set of separable states, is closer to the state analyzed with the current setup than to a state observed by the full 2xd dimensional state analysis (see [131] and [49]). The same argument can be used to explain that no violation of the inequalities $I_7 < 2$ and $I_6 < 2$ is observed when using the state analysis for a postselection at time delays $1\Delta T$ and $2\Delta T$. Here, it can be argued that for the used analysis the states cannot be shown to lie outside the correlation polytope for any of its facets, thus not allowing to detect its entanglement.

It can be argued that the non-violation of I_7 and I_6 and the observation of lower values of I_d^{Setup} than maximally possible is due to the fact that no optimal choice of the measurement basis could be found (so far restricted to using MUBs). This possibility can be excluded as no violation is observed as well if the respective measurement phase settings $\alpha_{A_i}^{O,s}$ and $\beta_{B_j}^{O,t}$ are used as independent parameters in the optimization problem. It can be shown,

nevertheless, that the optimization of I_d as a function of these additional measurement phase settings reveals maximal values at most equal to the ones observed for the choice of MUBs as the measurement basis. This motivates to further use the inequalities whose measurement basis is based on MUBs.

4.2.1 *Experimental violation of CGLMP inequalities*

It is now possible to determine I_d^{exp} for the experimentally realized time encoded states. For that purpose the experimentally determined counts $C_{k,l,s,t}$ are used to evaluate the probabilities $P_{k,l,s,t}$. For each combination of analysis angles $\{\alpha^1_{A_i}/\alpha^2_{A_i}\}$ and $\{\beta^1_{B_j}/\beta^2_{B_j}\}$ with $i,j = 1,2,3$ denoting the phases chosen in the respective interferometer arm, d^2 coincidence count rates corresponding to the d^2 possible combinations of projection measurements are evaluated. For each set of measurement settings defined in Appendix A1 it holds that $\sum_{s,t=0}^{d-1} C_{k,l,s,t} = C_{Tot}$ defines the total count rates C_{Tot} for fixed analysis settings k,l. Now, the respective probabilities are evaluated by normalizing the respective count rates to the total count rates observed according to

$$P_{k,l,s,t} = \frac{C_{k,l,s,t}}{\sum_{s,t=0}^{d-1} C_{k,l,s,t}}. \tag{71}$$

The probabilities obtained are used to evaluate the values $I_8^{Exp} = 2.191 \pm 0.020$, $I_7^{Exp} = 2.28 \pm 0.015$, $I_5^{Exp} = 2.072 \pm 0.037$, $I_4^{Exp} = 2.244 \pm 0.042$, $I_3^{Exp} = 2.29 \pm 0.028$ and $I_2 = 2.448 \pm 0.055$ (see Fig. 19). All values clearly surpass the bounds $I_d^{LR} = 2$ as defined for any local realistic model within the statistical uncertainty obtained by assuming that the observed count rates fluctuate according to Poissonian statistics. This allows to verify experimentally that the detected states with the specified dimensions are entangled.

4.2.2 *Franson loophole*

Subtle care has to be taken when a local realistic model is tested in the current experimental setup testing the coherence in the emission time degree of freedom: A postselection of coincidence counts has to be undertaken in order to test the coherence between the entangled two-photon states, and discard those which don't contribute to the entangled state (see 2.3).
In the most simple example of a 2 qubit entangled time-energy state [52], the postselected events correspond to 50% of the events to be detected. The related problem could in principle be addressed by resorting to the fair sampling assumption: The detected set of events is assumed to correspond to a set representing the whole sample of events. Here, displaying the completeness of quantum mechanics according to the definition stated in the EPR paper [44] (see 2.1.3) relies on closing the associated detection loophole.
Moreover, the loophole associated to the specific construction of unbalanced interferometers is more intricate. Here, the path information in the respective interferometer arms depends on the relative phase settings chosen. This information could be carried by a postselected photon. Additionally, this information could be associated to an hidden variable determining the chosen path. This scenario was developed in detail in [4], where it could be shown

that a local realistic model could be found in full correspondence to the quantum mechanical predictions. Therefore, for this particular configuration quantum mechanics cannot be used as the model offering a complete description of the underlying physical properties.
A more detailed discussion of the problem, as offered in [98], could be based on an argumentation used in the EPR paper. Indeed, depending on which studied properties are associated to a realistic description, different scenarios apply: If the paths traversed in the respective interferometer arms are considered as the elements of reality, indeed no violation of local realism could be shown with the used setup. In contrast, if the emission times of the photons are associated with realistic properties, a violation of local realism could be predicted by using the 2x2 dimensional interferometer setup. In this configuration a fast change in the interferometer's phase with a rate surpassing the traversal time of the photon through the interferometer would have to be undertaken. Additionally, the required critical two-photon visibilities would be considerably higher: 94.6%. Only then no local hidden variable theory would be able to predict the outcomes of the experiment.
None of these considerations (restricted so far to a 2x2 dimensional state) are applied in the current work, disabling it from displaying the departure of the observed correlations from a local realistic model.
From the viewpoint of practical implementations, the Franson loophole disables to use the present setup in a device independent configuration: In quantum communication scenarios where the transmission of a secure key relies on the violation of a Bell inequality it is desirable to show that no eavesdropper could manipulate the analysis device such as to obtain information about the encoded key. Moreover, this is exactly the case in the Franson configuration: Having access to the respective phase settings would enable him to predict the measurement outcomes and to extract the key.

4.3 FURTHER ENTANGLEMENT CRITERIA FOR QUdITS

4.3.1 *Schmidt number witness*

Schmidt decomposition and witness— An efficient way to detect entanglement is to represent a bipartite state defined in a 2xd dimensional Hilbert space in the Schmidt decomposed form [148]. For that purpose, a bipartite qu$d$it entangled state of dimension d is described as $|\Psi_d^S\rangle = \sum_{i=0}^{d-1} \lambda_i |i_A^s\rangle |i_A^s\rangle$ with $\{|i_A^s\rangle\} \in \mathcal{H}_A^d$ (and similar for Bob) representing the (Schmidt) basis of each parties qu$d$its. The Schmidt coefficients $\lambda_i = |c_{i_A^s}|^2 = |c_{i_B^s}|^2$ depend on the mode strengths $c_{i_A^s}$ and $c_{i_B^s}$ of the respective qu$d$it states encoded in each photon.
Moreover, this particular decomposition represents a singular value decomposition of pure states of the form $|\Psi_d\rangle = \sum_{i=0,j=0}^{d-1} \lambda_i |i\rangle |j\rangle$ (see 6.2 for a particular expansion of the scheme to mixed states), such that both local basis systems $\{|i\rangle\}$, $\{|j\rangle\}$ are unitarily transformed to the Schmidt bases $\{|i_A^s\rangle\}$ and $\{|i_B^s\rangle\}$, respectively. After performing this transformation, the two-particle state is called the **Schmidt decomposed** state. The Schmidt number $K_{A,B}$, corresponding to the minimum number of terms required to describe the state, is finally evaluated by making use of the partial trace over the entangled state $\rho = |\Psi_d^S\rangle\langle\Psi_d^S|$ according to

$$K_{A,B} = Tr_A[\rho] = Tr_B[\rho] = 1/\sum_i \lambda_i^2. \tag{72}$$

Entanglement can be detected by showing that the Schmidt number $K_{A,B}$ surpasses 1. Moreover, if all contributing coefficients $\lambda_i = 1/d$ are equal, a state is maximally entangled with a Schmidt number $K_{A/B} = d$ corresponding to the number of entangled modes. Therefore, the main potential of a Schmidt number witness is that it enables the detection of the number of modes contributing to an entangled state, therefore allowing to bound the dimensionality of a two-particle state (see 6.2).
Applications— Schemes for the direct evaluation of the Schmidt number of states encoded in the orbital angular momentum degree of freedom of photons could be evaluated for a SPDC photon pair source [101]. Representing states in the Schmidt decomposed form can be used to identify the correlation more likely to be big. Therefore this scheme can be used to increase the entanglement detection efficiency, as could be demonstrated experimentally for 2x2 dimensional polarization encoded quantum states [99, 100]. The Schmidt number for a selection of states encoded in this work is evaluated by the application of a Schmidt number witness in 6.2.

4.3.2 *Entanglement detection by using mutually unbiased bases (MUBs)*

Mutually unbiased bases and applications— It is also possible to apply entanglement detection schemes based on using specific sets of d dimensional observables spanned by MUBs. The characteristic used here is that once the correlation obtained for a measurement along one MUB for a given state ρ is maximal (i.e. equal ± 1), the correlation results obtained for a measurement along other uncorrelated bases are unbiased to each other, i.e. they are equal and non-zero. Hence, once a high correlation was detected, the measurement of only one additional correlation will suffice to detect the entanglement of ρ. This is described in more detail in [156] and below.
Additionally, these properties are advantageous for the tomographic reconstruction of quantum states [184, 3], as thus a full tomographic set consists of fewer measurements than for standard tomography schemes (see 5.1). Similarly, it is possible to make use of the increased security thresholds when using states encoded in MUBs for quantum key distribution [32]. There, scenarios with different attack strategies were studied. For example, the figure of merit used is the critical disturbance still allowing both parties to distill an entangled state. It could be shown that for the concrete case of an eavesdropper applying coherent attacks, the critical admixture can be parametrized as $p = (d-1)/2d$, i.e. the critical noise still enabling the detection of an eavesdropper is increased from $1/4$ for the 2 dimensional case to $1/2$ for $d \to \infty$.

Entanglement Detection— Following the scheme presented in [156] it is possible to derive bounds for efficient entanglement detection by analyzing a state in a basis spanned by MUBs $\{\mathcal{B}_k\}$ with each basis $\mathcal{B}_k = \{|i_k\rangle\} = \{|0_k\rangle, ..., |d-1_k\rangle\}$ fulfilling the relation $|\langle i_k|j_l\rangle|^2 = 1/d$.
Here, a two-qu*d*it state is prepared with two parties, Alice and Bob, analyzing each one qu*d*it. Each party's measurement is described by observables A and B encoded in the MUB basis $\mathcal{B}_k$ and for which d different outcomes $\{0, ..., d-1\}$ can be obtained. They can parametrize the

correlations observed in their measurement results by the joint probability $P_{A,B}(i,i) = \langle i_A| \otimes \langle i_B|\rho|i_A\rangle \otimes |i_B\rangle$ for a measurement along the bases $|i_A\rangle$ and $|i_B\rangle$ applied on the state ρ. A correlation function of the form $C_{A,B} = \sum_{i=0}^{d-1} P_{A,B}(i,i)$ is maximized to $C_{A,B} = 1$ if the studied state is correlated for a measurement along the bases $|i_A\rangle$ and $|i_B\rangle$. In contrast, if the state is uncorrelated an unbiased correlation measurement outcome of $C_{A,B} = 1/d$ is observed.
Measuring one correlation is not sufficient to detect entanglement for one particular pair of directions. This is due to the reason that for separable states, such as $\rho_S = \sum_{i=0}^{r} |\lambda_i|^2 |i_A^s\rangle\langle i_A^s| \otimes |i_B^s\rangle\langle i_B^s|$ the correlation measurement reveals a maximal value, in the same way as for an entangled state $|\Psi\rangle_E = \sum_{i=0}^{r} \lambda_i |i_A^s\rangle|i_B^s\rangle$ with $1 \leq r \leq d-1$.
Measurements along at least two different directions within an MUB have to be performed in order to discriminate an entangled from a separable state as only then the condition $I_2 > C_{A_1,B_1} + C_{A_2,A_2} = 1 + 1/d$ is fulfilled. Moreover, for a separable state only values $I_2 \leq C_{A_1,A_1} + C_{A_2,A_2} = 1 + 1/d$ are possible. The violation of the bound can be enhanced if further measurements along all m different MUB directions are performed leading to the bound

$$I_m = \sum_{i=1}^{m} C_{A_i,B_i} > 1 + \frac{m-1}{d}, \tag{73}$$

which is limited to $I_m \leq 1 + \frac{m-1}{d}$ for separable states. In contrast, for an entangled state a measurement along all MUBs leads to the maximal value of $I_m^{max} \leq 2$.
Here, it is possible to study the robustness of the entanglement measure with regard to the admixture of (white) noise. For general d dimensional entangled states defined as $|\Psi\rangle_d = 1/\sqrt{d} \sum_{i=0}^{d-1} |i\rangle|i\rangle$ the admixture of white noise can be parameterized as

$$\rho_I = \alpha |\Psi_d\rangle\langle\Psi_d| + \frac{1-\alpha}{d^2}\mathbb{1}. \tag{74}$$

For this type of states entanglement can be detected once the critical admixture parameter $\alpha_{Crit} = 1/(d+1)$ is surpassed, leading to a value of $\alpha_{Crit} = 0$ for $d \to \infty$. Therefore, the robustness of entanglement criteria based on MUBs is decreased with respect to the criteria derived from the violation of the CGLMP inequality (see 4.1.2), where for $d \to \infty$ the critical admixture is $\alpha_{Crit} = 0.6734$.

Application in this work— A full set of $d+1$ MUBs consists of product bases, i.e. bases which can be described as the tensor product of lower dimensional bases and entangled bases, which cannot be represented as a tensor product (see [183]). For states encoded into non-prime dimensional Hilbert spaces ($d = d_1 \cdot d_2 \cdots d_n$) partitioned into d_i dimensional states it can be shown that the maximal number of separable MUBs corresponds to the minimal dimension of all partitions.
For maximally entangled states with dimensions 2x8 as prepared in this work the used analysis can only project onto two dimensional separable bases as the Hilbert space dimension factorizes according to $8 = 2 \cdot 2 \cdot 2$. Similarly, for 2x4 dimensional states the analysis Hilbert space dimension factorizes according to $4 = 2 \cdot 2$. Moreover, for the state analysis of the 2x8 dimensional state used in this setup the state cannot be analyzed by using the 6 entangled MUBs out of the full set of 9 MUBs (see Appendix F

of [183] for an example of MUBs in 8 dimensions). This limitation can be attributed to the fact that the state analysis provides a maximum of up to 3 independent relative phases. In contrast, a minimum number of 7 phases would be required in order to analyze the state along all bases. Similar limitations apply to the bipartite states with dimensionality between 2x4 to 2x7 analyzed at the different postselection time windows, in the case of the 2x6 and 2x7 dimensional states no MUBs could be used to analyze them. Therefore, an entanglement detection scheme based on MUBs will not be used, as its entanglement detection efficiency is not optimal for the 2xd dimensional state analysis employed in this work.

4.3.3 *Entanglement witness for qudit states*

Entanglement witnesses— Detection of entanglement of quantum states can also be based on strictly geometrical arguments. Here, the detection of entanglement by using entanglement witnesses is one of the most prominent examples. It is based on the theorem that due to the convexity of the subspace of separable states an hermitian operator $\hat{\mathcal{W}}$ can be found for any entangled state $\rho_{ent} \in \mathcal{H}$ such that

$$Tr[\rho_{ent}\hat{\mathcal{W}}] < 0 \tag{75}$$

is fulfilled.

Optimization of witnesses— An analytical description of the problem is used: Using convex (closed) sets of quantum states embedded within a state space, such as the separable states, it is possible to identify Hermitian operators separating a state ρ from these separable states. These operators are denoted as entanglement witnesses.

The advantage of entanglement witnesses is that they allow to parametrize the entanglement of a state by its distance from the set of separable states. A well studied criteria suited for the detection of entanglement is based on the partial transposition $\hat{\mathcal{W}} = \mathbb{1} \otimes T$ first proposed by Horodecki et al. [71]: It can be shown that once the partial transposition is applied onto an entangled state ρ_{ent}

$$\hat{\mathcal{W}}\rho_{ent} = (\mathbb{1} \otimes T)\rho_{ent} < 0 \tag{76}$$

holds, i.e. the resulting state is negative semidefinite. The criteria has been termed as the **positive partial transpose criteria (PPT)** and provides a **necessary** and **sufficient** for the detection of entanglement of mixed states restricted to 2×2 and 2×3 dimensions.

Entanglement witness for maximally entangled d dimensional states— Further work on the identification of entanglement in general d dimensions was based on similar geometric arguments. A summary of these studies, evaluated in a broader context as for example in [86], will be presented here.

Different approaches, based on a different parameterization of the d dimensional Bloch vectors of each locally encoded state, have been developed in order to display the entanglement of two-qu$d$it entangled states as studied in this work. The generalized Gell-Mann matrices [34, 15, 175], the polarization operator basis [15] as well as the Weyl operator basis [15] have been used in order to provide a description of the studied state. Based on these, schemes have been derived aiming to expand the PPT entanglement criterion to 2xd dimensional states and to derive bounds displaying their entan-

glement ([34, 74]). Similarly, generalized Bell operators $\mathcal{B}_{ent}$ defined by the criteria $Tr[\sigma_{sep}, \mathcal{B}_{ent}] = 0$ enable to distinguish between a separable state σ_{sep} and an entangled state ρ_{ent}. Therefore, they can be used as entanglement witnesses [15]. Following the terminology used to define entanglement witnesses, Bell operators correspond to witnesses, optimized to detect the entanglement of at least one entangled state [15].
In order to apply these entanglement detection criteria on higher dimensional states, the geometric description of each local state defined in a d dimensional Hilbert space $\mathcal{H}^d$ [16] is based on its representation in a suited basis system $\{\Gamma_i\}$. It allows to parameterize any 2xd dimensional quantum state according to

$$\rho = \frac{1}{d}\mathbb{1} \otimes \mathbb{1} + n_i\Gamma_i \otimes \mathbb{1} + m_j\mathbb{1} \otimes \Gamma_j + c_{ij}\Gamma_i \otimes \Gamma_j \tag{77}$$

for complex coefficients $n_i, m_j \in \mathbb{C}$ describing the respective local states. Further on, $c_{i,j} \in \mathbb{C}$ denote the correlations to be observed between the bipartite 2xd dimensional state along this basis. It is to note that for a Schmidt decomposed state, the correlation tensor elements c_{ij} vanish expect for the diagonal elements. For example, the decomposition can be applied on a Schmidt decomposed state such as $|\Psi\rangle_d = 1/\sqrt{d}\sum_{k=0}^{d-1}|i_s\rangle|i_s\rangle$ with a white noise admixture α as

$$\rho^d = \alpha|\Psi\rangle_d\langle\Psi_d| + \frac{1-\alpha}{d^2}\mathbb{1} \tag{78}$$

for $-1/(d^2-1) \leq \alpha \leq 1$. In this case, the local correlations n_i and m_j vanish as well, allowing to describe the two-qu$d$it state by d different terms. This fact greatly simplifies the entanglement detection as the required number of correlation measurements is reduced accordingly. This corresponds to the same number of measurements required to describe the density matrix of a one-qu$d$it quantum state.
Here, the maximization over the Hilbert Schmidt measure can be further used to determine the optimal witness detecting the maximal possible entanglement of these states (see [16] for a detailed derivation). Concretely, the optimal witness is described as

$$\hat{\mathcal{W}}(\rho^d) = \frac{1}{d}\sqrt{\frac{d-1}{d+1}}\mathbb{1} \otimes \mathbb{1} - \frac{1}{2\sqrt{d^2-1}}\Lambda \tag{79}$$

when using the generalized Gell-Mann basis (GGB) expansion for arbitrary dimension d

$$\Lambda := \sum_{i<j}\Lambda_s^{jk} \otimes \Lambda_s^{jk} - \sum_{i<j}\Lambda_a^{jk} \otimes \Lambda_a^{jk} + \sum_{m=1}^{d-1}\Lambda^m \otimes \Lambda^m. \tag{80}$$

Here, a maximal bound of the Hilbert-Schmidt measure, and correspondingly a maximal violation of a generalized Bell inequality $\mathcal{B}$ corresponds to

$$\mathcal{B}(\rho_{ent}^d) = -Tr[\rho_{ent}^d, \hat{\mathcal{W}}(\rho^d)] = \frac{\sqrt{d^2-1}}{d}(\alpha - \frac{1}{d+1}) \tag{81}$$

allowing to reveal entanglement for a critical admixture of $\alpha_{crit} = 1/(d+1)$ (obtained by setting $\mathcal{B}(\rho_{ent}^d) = 0$). This result shows that for states embedded within an infinite dimensional Hilbert, two-qu$d$it entangled states are entangled for any admixture of noise α. This is the same result to be

obtained for a 2xd dimensional state analyzed by using MUBs (see 4.3.2). This entanglement detection scheme was not experimentally evaluated in this work.

5

TOMOGRAPHIC RECONSTRUCTION OF QUDIT ENTANGLED STATES

This chapter will offer a description of tomographic schemes used to reconstruct the density matrix of an experimentally prepared time-energy entangled two-qu*d*it state. It will start with a short introduction into the details of tomographic reconstruction methods (see section 5.1). Further on, it will continue with a detailed description of tomographically complete quantum tomography schemes based on the evaluation of a full set of projection measurements (section 5.2) and on the evaluation of the full correlation tensor (section 5.2.2). Subsequently, it will adress the problem that with a high probability the reconstructed density matrices are unphysical and will present strategies solving it, by resorting to convex optimization methods (section 5.3). It will be shown how this scheme allows to provide an unique reconstruction based only on an tomographically incomplete set of measurements. The first method is based on **Compressed Sensing** (section 5.4) while the second one makes use of the principle of **Correlation Complementarity** defining an **Adaptive state tomography** method (section 5.5). Finally, additional deviations in the figures of merit due to the use of constrained optimization schemes will be discussed in 5.6.

5.1 QUANTUM STATE TOMOGRAPHY

One of the fundamental problems faced with when using quantum states for applications in the field of quantum computation or cryptography is to obtain a reliable knowledge about the properties of the experimentally prepared state [127]. For that purpose a reliable knowledge about the underlying quantum states has to be acquired. Here, the application of quantum state tomography enables to fulfill this requirement. It provides an evaluation of the density matrix describing the state and can be used to estimate other measures certifying the preparation quality. For example, the entanglement of the state can be evaluated by measures such as the Uhlmann fidelity [169], the negativity [71] and the Schmidt number [145]. Similarly, its usability for quantum metrology tasks can be evaluated by corresponding measures, such as the Quantum Fischer information [87, 130].
Before describing these schemes it is important to stress out which are the limitations imposed by quantum theory for obtaining the data, based on the interaction of the ensemble of quantum particles with a measurement device: In contrast to quantum theory, classical state reconstruction (for example for the reconstruction of geological, medical or archeological structures) is simplified due to the fact that the system under study remains unchanged and can therefore be probed for different projections. This requirement does not hold in the quantum regime as the quantum state will be perturbed after applying a measurement on it. Therefore, the quantum state has to be

repeatedly prepared in order to apply the same measurement on it.
It is at this point that Born's rule [179] defines the probability $P(\Pi_i, \rho) = Tr[\Pi_i \rho]$ with which the outcome of a given projection measurement performed on a quantum state will be obtained. Here, Π_i denotes a general projection measurement and ρ the input state density matrix. It states that the probability $P(\Pi_i, \rho)$ can be determined by applying identical measurements on the ensemble of repeatedly prepared states. In this case, the resulting frequencies c_i / N normalized over the total count rate N of the ensemble allow to give an approximation of $P(\Pi_i, \rho)$ as an average over the measurement results obtained by applying the operators Π_i. Moreover, the error with which the probability $P(\Pi_i, \rho)$ is to be determined is ultimately limited by the number of measurement runs performed.
At this point, the intrinsic linearity of quantum theory allows to define the density matrix ρ as a linear combination of the measurement operators performed on it. In the most simple case, a qubit density matrix is decomposed into

$$\rho = \frac{1}{2} \sum_{i=0}^{3} \frac{P_i}{P_0} \hat{\sigma}_i, \tag{82}$$

where the Pauli operator-basis $\hat{\sigma}_i$ along the 3 directions x, y, z is chosen.
Here, a qubit is reconstructed by performing 4 different Stokes (projection) measurements [115] $P_0 = \mathcal{N}(\langle R|\rho|R\rangle + \langle L|\rho|L\rangle)$, $P_1 = \mathcal{N}(\langle R|\rho|L\rangle + \langle L|\rho|R\rangle)$, $P_2 = \mathcal{N}i(\langle R|\rho|L\rangle - \langle L|\rho|R\rangle)$ and $P_3 = \mathcal{N}(\langle R|\rho|R\rangle - \langle L|\rho|L\rangle)$ defined by using the $|0\rangle/|1\rangle$ and $|R\rangle = 1/\sqrt{2}(|0\rangle + i|1\rangle)/|L\rangle = 1/\sqrt{2}(|0\rangle - i|1\rangle)$ measurement bases. Here, $|0\rangle = (1, 0)$ and $|1\rangle = (0, 1)$ corresponds to a 2 dimensional basis.
A general reconstruction scheme is based on expressing the density matrix as a linear combination of an operator basis acting on the Hilbert space the quantum states are encoded into. Here, depending on the states reconstructed, either multi-qubit or d dimensional entangled states, different bases are chosen. For example, a full tomographic reconstruction of quantum states can be based on using a 2 dimensional Pauli-spin basis [75, 82] or using the generators of the $\mathcal{SU}(d)$ group for d dimensional Hilbert spaces [164] as well as MUB bases [3].

5.2 FULL TOMOGRAPHY

Two quantum state tomography methods based on a linear evaluation of the density matrix as a function of the obtained probabilities are treated in this work. They allow to describe the quantum states encoded into multiple qubits or into qu*d*its defined in d dimensional Hilbert spaces. The first method, based on the application of the Stokes parameterization [75] on each qubit (see 5.2.1), will be applied on the experimental data obtained from the measurement setup. The second one, based on the determination of the full correlation tensor $\hat{T}$ [82] can be used to obtain an estimation of the state with increased statistics (see 5.2.2).

5.2.1 *James tomography*

Decomposition of density matrix— The scheme proposed by James et al. [75] allows to reconstruct the density matrix of a multi-qubit quantum state directly as a function of probabilities $p_{i_1, i_2, \ldots, i_N}$ which are obtained for suit-

able projection measurements $P_{i_1,i_2,...,i_N}$. The set of projector measurements considered here, applied on each qubit's state the studied state consists of, are $J_{i_j} = \{|R\rangle\langle R|, |L\rangle\langle L|, |0\rangle\langle 0|, |P\rangle\langle P|\}$ where j denotes the index of the local qubit the projection is applied on. Trace unity is ensured by requiring trace normalization, with $\mathcal{N}$ corresponding to the normalization constant. This last requirement is fulfilled by summing up over the probabilities corresponding to the projection measurements $|R\rangle\langle R|$ (index 0) and $|L\rangle\langle L|$ (index 1) such that

$$\sum_{i_1,...,i_N=0}^{1} p_{i_1,i_2,...,i_N} = \mathcal{N} \tag{83}$$

is fulfilled.
In general, a density matrix is represented in an operator basis. Nevertheless, only the outcomes of projection measurements are experimentally accessible, so that the operator basis has to be expressed as a function of the projection measurements $P_i = |\Psi_i\rangle\langle\Psi_i|$ defined previously. Here, a general operator can be decomposed as $\hat{A}_i = \sum_i \lambda_i |\Psi_i\rangle\langle\Psi_i|$ what is possible as the corresponding eigenvalues λ_i are well defined due to the spectral decomposition theorem [124]. In this scenario, each qubit's projection measurement can be represented as an element of the operator basis $\{(\mathbb{1} + \hat{\sigma}_y), (\mathbb{1} - \hat{\sigma}_y), (\mathbb{1} + \hat{\sigma}_z), (\mathbb{1} + \hat{\sigma}_x)\}$. Accordingly, the N qubit operator basis used to analyze an N qubit state can be expressed as

$$\begin{aligned}\hat{O}^{JT}_{i_1,i_2,...,i_N} = (\mathbb{1} + (-1)^{s_{i_1}}\hat{\sigma}_{i_1})/2 \otimes (\mathbb{1} + (-1)^{s_{i_2}}\hat{\sigma}_{i_2})/2 \otimes \cdots \\ \otimes (\mathbb{1} + (-1)^{s_{i_N}}\hat{\sigma}_{i_N})/2.\end{aligned} \tag{84}$$

where the coefficients $\{s_{i_1}, ..., s_{i_N}\} \in \{0, 1\}$ are the indices for the specific choice of the projection measurement applied on the respective qubit.
Using this decomposition the coincidence probabilities $p_i = Tr[\hat{O}^{JT}_{i_1,i_2,...,i_N}\rho]$ are obtained by applying the projection measurements on the multi-qubit state ρ.
Nevertheless, it is useful to express any density matrix in a more generalized basis. For example Γ_j can be chosen with the characteristic that any density matrix ρ is decomposed into $\rho = \sum_{j=1}^{4^N} \Gamma_j r_j$ with corresponding coefficients $r_j = Tr[\Gamma_j \rho]$. Here, for example the Γ_j matrices can be chosen as the generators of the N qubit symmetry group $\mathcal{SU}(2)^{\otimes N}$. The state ρ can now be reconstructed in the newly defined basis by searching for the transformation matrix between the coefficients r_j corresponding to the basis Γ_j and the coincidence probabilities obtained by measuring in the operator basis $\hat{O}^{JT}_i$ (here, the simplification $i = i_1, i_2, ..., i_N$ is used). For that purpose, the entries of r_j are related to the measured coincidence count rates n_i according to $n_i = \mathcal{N} \sum_{i=1}^{4^N} B_{i,j} r_j$ which requires the evaluation of the $4^N \times 4^N$ dimensional transformation matrix

$$B_{i,j} = \langle\Psi_i|\Gamma_j|\Psi_i\rangle. \tag{85}$$

Here, $B_{i,j}$ is invertible only in the case that a tomographically complete set of projections $\{|\Psi_i\rangle\langle\Psi_i|\}$ is used.
This allows to determine the underlying density matrix according to

$$\rho = \frac{1}{\mathcal{N}} \sum_{i=1}^{4^N} M_i n_i \tag{86}$$

as a function of the matrices $M_i = \sum_{i=1}^{4^N} (B^{-1})_{i,j} \Gamma_j$ and the respective count rates n_i obtained for all 4^N projection measurements. Here, the normalization condition is fulfilled by the condition $\sum_i^{4^N} Tr[M_i] n_i = \mathcal{N}$.

Application on bipartite qudit entangled states— The described tomographic reconstruction scheme can be directly applied for the evaluation of the density matrix of a 2x8 qu*d*it entangled state as prepared in this work. Here, the prepared qu*d*it states are analyzed by the interferometer systems consisting of up to 3 interferometer arms. These interferometer arms used to project the incoming qu*d*its encoded into each photon into the tensor product of $|\Psi\rangle_{A_i} = 1/\sqrt{2}(|0_i\rangle_A + e^{i\alpha_{A_i}}|1_i\rangle_A)$ and $|\Psi\rangle_{B_j} = 1/\sqrt{2}(|0_j\rangle_B + e^{i\beta_{B_j}}|1_j\rangle_B)$. These are defined by the respective qubit bases $|0_{i/j}\rangle_{A/B}/|1_{i/j}\rangle_{A/B}$ encoded into the short and long paths of the respective interferometers.
For example, Alice's analysis is described as

$$|\Psi\rangle_A^8 = |\Psi\rangle_{A_1} \otimes |\Psi\rangle_{A_2} \otimes |\Psi\rangle_{A_3} = |0_1 0_2 0_3\rangle_A + |1_1 0_2 0_3\rangle_A + \cdots + |1_1 1_2 1_3\rangle_A.$$

Correspondingly, applying the analysis on both qu*d*its corresponds to their projection onto $|\Psi\rangle^8 = |\Psi\rangle_A^8 \otimes |\Psi\rangle_B^8$. For a postselection of only 8 two-photon states at the time window $0\Delta T$ the prepared two-photon states are projected onto

$$\begin{aligned}
|\Psi\rangle_8^{0\Delta T} = \\
\frac{1}{2\sqrt{2}}(|0\rangle'_A|0\rangle'_B + |1\rangle'_A|1\rangle'_B + |2\rangle'_A|2\rangle'_B + |3\rangle'_A|3\rangle'_B + |4\rangle'_A|4\rangle'_B + |5\rangle'_A|5\rangle'_B + \\
|6\rangle'_A|6\rangle'_B + |7\rangle'_A|7\rangle'_B) = \\
\frac{1}{2\sqrt{2}}(|0_1 0_2 0_3\rangle'_A|0_1 0_2 0_3\rangle'_B + |1_1 0_2 0_3\rangle'_A|1_1 0_2 0_3\rangle'_B + |0_1 1_2 0_3\rangle'_A|0_1 1_2 0_3\rangle'_B + \\
|1_1 1_2 0_3\rangle'_A|1_1 1_2 0_3\rangle'_B + |0_1 0_2 1_3\rangle'_A|0_1 0_2 1_3\rangle'_B + |1_1 0_2 1_3\rangle'_A|1_1 0_2 1_3\rangle'_B + \\
|0_1 1_2 1_3\rangle'_A|0_1 1_2 1_3\rangle'_B + |1_1 1_2 1_3\rangle'_A|1_1 1_2 1_3\rangle'_B) = \\
\frac{1}{2\sqrt{2}}(|0_1\rangle'_A|0_1\rangle'_B + |1_1\rangle'_A|1_1\rangle'_B) \otimes (|0_2\rangle'_A|0_2\rangle'_B + |1_2\rangle'_A|1_2\rangle'_B) \otimes \\
(|0_3\rangle'_A|0_3\rangle'_B + |1_3\rangle'_A|1_3\rangle'_B)
\end{aligned} \tag{87}$$

Here, in order to simplify the notation the phase acquired in each path was included into the state notation according to $|1_1\rangle'_A = e^{i\alpha_{A_1}}|1_1\rangle_A$, $|1_2\rangle'_A = e^{i\alpha_{A_2}}|1_2\rangle_A$ and $|1_3\rangle'_A = e^{i\alpha_{A_3}}|1_3\rangle_A$ and equivalently for Bob's states. Note, that in the last step of the decomposition of Eq.(87) the state is represented as the tensor product of 3 2x2 dimensional entangled states encoded into the state space of paired interferometer arms (A_1B_1, A_2B_2 and A_3B_3 interferometer pairs). This is an inherent property of the used analysis.
The prepared 2x8 dimensional two-photon state is now tomographically reconstructed in the basis $\{|0_1 0_2 0_3\rangle'_A|0_1 0_2 0_3\rangle'_B, ..., |1_1 1_2 1_3\rangle'_A|1_1 1_2 1_3\rangle'_B\}$ defined

by the used analysis described in Eq.(87). For that purpose suited projection measurements have been performed on the respective qubit state space corresponding to the different interferometer arms. For example, choosing phase settings $\alpha_{A_i} = \beta_{B_j} = 0, \pi$ allows to project each qubit on the eigenstates $|P_{i,j}\rangle = 1/\sqrt{2}(|0_i\rangle + |1_i\rangle)/|M_i\rangle = 1/\sqrt{2}(|0_i\rangle - |1_i\rangle)$ of σ_x. For $\alpha_{A_i} = \beta_{B_j} = \pm\pi/2$ a projection measurement along the eigenbasis $|R_i\rangle = 1/\sqrt{2}(|0_i\rangle + i|1_i\rangle)/|L_i\rangle = 1/\sqrt{2}(|0_i\rangle - i|1_i\rangle)$ of σ_y is implemented. In contrast, no measurement along the z direction, with eigenbasis $|0_i\rangle/|1_i\rangle$, can be directly performed with the used interferometer setup. Further details about the experimental procedure to retrieve the required data in this basis is presented in 5.2.3.

5.2.2 *Standard tomography*

Correlation tensor— The reconstruction scheme based on using a full tomographic set (see [82]) is based on the fact that any N-qubit density matrix ρ can be evaluated by the elements of the full correlation tensor $\hat{T}$ with elements

$$T_{i_1,i_2,...,i_N} = Tr[\hat{O}_i^{ST}\rho] = Tr[(\sigma_{i_1} \otimes \cdots \otimes \sigma_{i_2} \cdots \sigma_{i_N})\rho]. \tag{88}$$

Here, a measurement defined along each qubits Hilbert space is described by the following parameterization as a function of the Pauli spin matrices $\sigma_x, \sigma_y, \sigma_z$:

$$\sigma(\alpha_{A_i}, \gamma_{A_i}) = \cos\alpha_{A_i} \sin\gamma_{A_i}\sigma_x + \sin\alpha_{A_i} \sin\gamma_{A_i}\sigma_y + \cos\gamma_{A_i}\sigma_z \tag{89}$$

$$\sigma(\beta_{B_j}, \delta_{B_j}) = \cos\beta_{B_j} \sin\delta_{B_j}\sigma_x + \sin\beta_{B_j} \sin\delta_{B_j}\sigma_y + \cos\delta_{B_j}\sigma_z \tag{90}$$

The setting of α_{A_i} and α_{B_j} corresponds to a rotation of the observable along the x-y plane defined for the respective qubits Bloch sphere. A rotation along γ_{A_i} and δ_{B_j} corresponds to a measurement along the x-z measurement plane. As a function of the phases set at Alice's side, a projection onto $|0\rangle$ is achieved by choosing a phase setting $\{\alpha_{A_i} = 0, \gamma_{A_i} = 0\}$ and to $|1\rangle$ by setting $\{\alpha_{A_i} = 0, \gamma_{A_i} = \pi\}$ (for Bob's projectors accordingly).
The determination of a N qubit correlation element of $T_{i_1,i_2,...,i_N}$ along each direction $\{i_1, i_2, ..., i_N\} \in \{x, y, z\}$ is made by evaluating 2^N coincidence probabilities $p_{i_1,i_2,...,i_N}^{s_1,s_2,...,s_N}$ according to

$$T_{i_1,i_2,...,i_N} = \sum_{s_1,s_2,...,s_N=0,1} (-1)^{s_1+s_2+...+s_N} Tr[P_{i_1}^{s_1} \otimes P_{i_1}^{s_1} \cdots \otimes P_{i_N}^{s_N}\rho] = \sum_{s_1,s_2,...,s_N=0,1} (-1)^{s_1+s_2+...+s_N} p_{i_1,i_2,...,i_N}^{s_1,s_2,...,s_N}. \tag{91}$$

Here, the indices $s_i = 0$ denote the projection of each qubit into the $\{|0\rangle, |P\rangle, |R\rangle\}$ eigenstates and $s_i = 1$ a projection into $\{|1\rangle, |M\rangle, |L\rangle\}$ of the respective z,x and y Pauli spin operators. $P_{i_N}^{s_N}$ denotes the actual projection measurements on the respective qubits along the direction i_N and index s_N. The probabilities are evaluated directly out of the measured set of counts

$c^{s_1,s_2,\ldots,s_N}_{i_1,i_2,\ldots,i_N}$ by normalizing them to the total counts observed per basis according to

$$p_{i_1,i_2,\ldots,i_N} = \frac{c^{s_1,s_2,\ldots,s_N}_{i_1,i_2,\ldots,i_N}}{\sum_{s'_1,s'_2,\ldots,s'_N=0}^{1} c^{s'_1,s'_2,\ldots,s'_N}_{i_1,i_2,\ldots,i_N}}. \tag{92}$$

Decomposition of a density matrix as a function of correlation tensor elements— It is now possible to decompose the underlying N qubit density matrix ρ as a linear function of the measured elements $T_{i_1,i_2,\ldots,i_N}$ of the correlation tensor $\hat{T}$ [82] as

$$\rho = \frac{1}{2^N} \sum_{i_1,i_2,\ldots,i_N=0}^{3} T_{i_1,i_2,\ldots,i_N} \sigma_{i_1} \otimes \sigma_{i_2} \cdots \otimes \sigma_{i_N}. \tag{93}$$

Using Eqs. 91, 92 it can be directly decomposed into a linear combination of the coincidence probabilities determined from count rates according to

$$\rho = \frac{1}{2^N} \sum_{i_1,i_2,\ldots,i_N=0}^{3} \sum_{s_1,s_2,\ldots,s_N=0}^{1} p^{s_1,s_2,\ldots,s_N}_{i_1,i_2,\ldots,i_N} \prod_{j=1}^{N} (\frac{1}{3}\mathbb{1} + (-1)^{s_{i_j}} \sigma_{i_j}). \tag{94}$$

Here, the operators $\gamma^i_j = (\frac{1}{3}\mathbb{1} + (-1)^{s_{i_j}} \sigma_j)$ project onto the eigenstates of the σ_x, σ_y and σ_z operators applied on each qubit's state space. It parametrizes ρ as a function of the input probabilities $p^{a_1,a_2,\ldots,a_N}_{i_1,i_2,\ldots,i_N}$ fully determining it.
This type of tomography offers an overcomplete sample of the studied density matrix ρ, as the number of parameters effectively used to reconstruct it is on the order of 6^N. This is a factor $(1.5)^N$ higher than the total number of measurements 4^N required for a tomographically complete set as defined by the James tomography scheme in 5.2. Nevertheless, the additional number of measurements can be used to improve the statistics for the evaluation of ρ. This is ensured as the projection operators corresponding to the standard basis σ_x, σ_y and σ_z fulfill the condition $\mathbb{1} = (P^0_x + P^1_x + P^0_y + P^1_y + P^0_z + P^1_z)/3$. This advantage can be demonstrated for example for a two-qubit state. Here, a correlation tensor element T_{0x} corresponding to a measurement along $\hat{O} = \mathbb{1} \otimes \sigma_x$ is evaluated by using on average 3 times more counts. This becomes clear as the set of measurements corresponding to $(P^0_x + P^1_x) \otimes (P^0_x - P^1_x)$, $(P^0_y + P^1_y) \otimes (P^0_x - P^1_x)$ and $(P^0_z + P^1_z) \otimes (P^0_x - P^1_x)$ can be used for that purpose.
Application in this work— A high number of experiments on the entanglement of N multi-qubit entangled states have employed the described method for the reconstruction of the corresponding density matrices [83, 186]. Here, the intrinsic projection of the prepared quantum states into a qubit state by the used interferometers, enables to use this method for entangled two-qu*d*it states as well. Here, each of the measurements applied by each interferometer arm can be described as a qubit observable (see 5.2). In the concrete experimental configuration studied in this work, a set of 6 interferometer arms are used with 3 arms made available to both parties. As the logical qubits are encoded into two photons, the use of two detectors is required to observe the two-photon coincidence count rates $c^{a_{A_1},a_{A_2},a_{A_3},b_{B_1},b_{B_2},b_{B_3}}_{i_{A_1},i_{A_2},i_{A_3},i_{B_1},i_{B_2},i_{B_3}}$ between the respective outputs of the different interferometer arms.

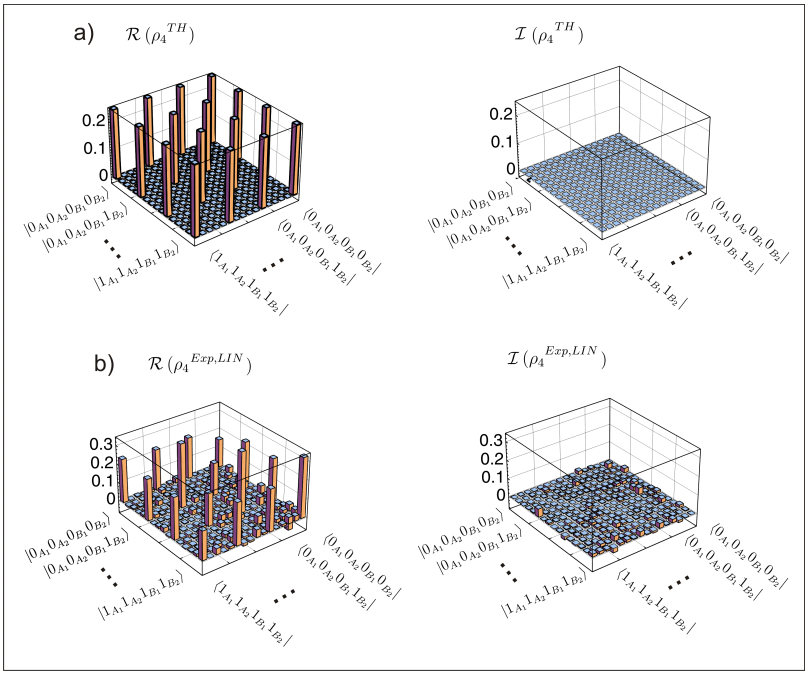

Figure 20: Tomographically reconstructed density matrix of a 2x4 dimensional state analyzed in the Hilbert space of paired interferometer arms corresponding to Alice's A_1 and A_2 and Bob's B_1 and B_2 interferometer arms: $|\Psi_4^8\rangle = 1/2(|0_1 0_2\rangle_A|0_1 0_2\rangle_B + |1_1 0_2\rangle_A|1_1 0_2\rangle_B + |0_1 1_2\rangle_A|0_1 1_2\rangle_B + |1_1 1_2\rangle_A|1_1 1_2\rangle_B) \otimes |0_3\rangle_A|0_3\rangle_B$. The theoretically predicted state is depicted in a) while the experimentally evaluated density matrix (b)) reveals a state $\rho^{Exp,LIN}$ in close correspondence to the theoretical expectations, as the fidelity of $\mathcal{F}_4^{Exp,LIN} = 0.882 \pm 0.051$ reveals.

In this work, simulations will be performed on the tomographic reconstruction of the qu*d*it states considered in this work (see 5.5 and 5.6).

5.2.3 *Experimental reconstruction using the James tomography scheme*

The James tomography scheme is favored with respect to the standard tomography scheme described above in order to reconstruct the experimentally prepared qu*d*it states of up to 2x8 dimensions. This is because it requires only the evaluation of up to $4^6 = 4096$ coincidence probabilities obtained for the full set of projection measurements, in constrast to $6^6 = 46656$ for applying the full tomography scheme.

Here, the projection of each of the 6 logical qubits on $|0\rangle$, $|P\rangle$, $|R\rangle$ and $|L\rangle$ provides such a tomographically complete set. Note that, due to current restrictions of the measurement apparatus to the *x*-*y* plane of each logical qubit, the respective coincidence count rates corresponding to a projection onto $|0\rangle$ or $|1\rangle$ have to be evaluated by blocking one path of the respective interferometer arms. This leads to an increased experimental effort, as during the blocking the stabilization feedback required to stabilize the respective phases has to be switched off and to be turned on after removing the blocking device. The phase setting set before switching off is defined

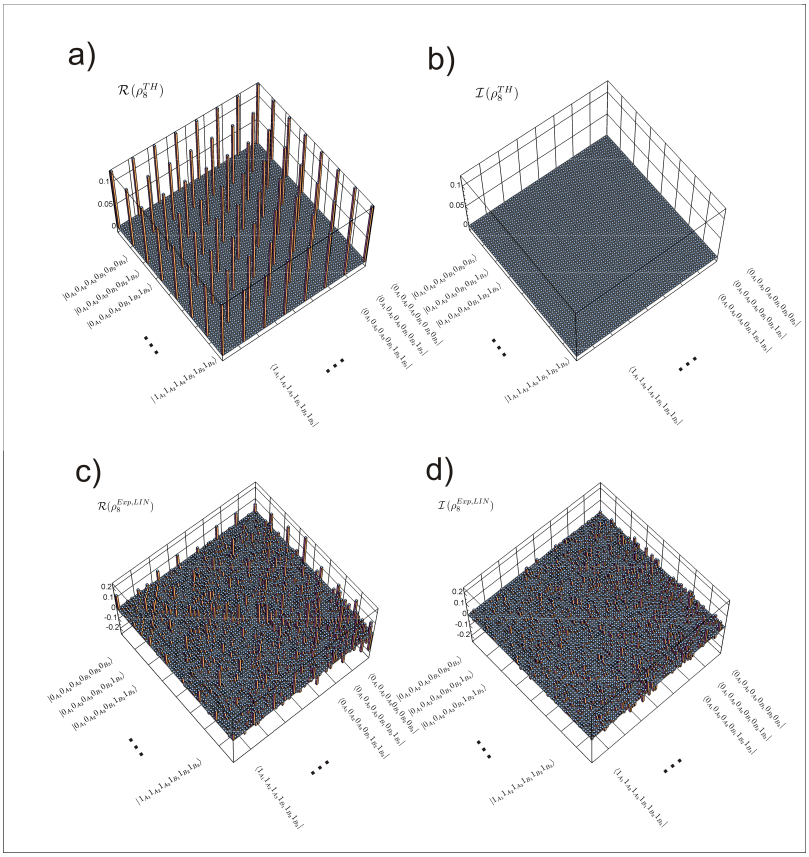

Figure 21: Tomographic reconstructed density matrices of a 2x8 dimensional state based on the tomographic decomposition according to James. Deviations from the theoretical predictions a) and b) are observed with respect to the experimentally determined density matrix as depicted in c) and d). These deviations are due to a Poissonian distribution of the acquired counts and mainly due to residual phase fluctuations in the interferometers used to analyze the time encoded states. Despite these fluctuations the evaluated fidelity corresponds to $\mathcal{F}_8^{Exp,LIN} = 0.8625 \pm 0.0121$.

by the settings of the stabilization setup, which remain constant (see section 3.3). Therefore, the phase has to be locked again to the same phase setting after switching the feedback loop on again[1].

Due to these reasons, instead of a measurement along $|0\rangle$ and $|1\rangle$ as proposed in [75], projections on $|R\rangle$ and $|L\rangle$ are chosen, allowing to define the normalization constant $\mathcal{N}$ according to Eq.(83). In this case, the blocking of only the long interferometer arm is required, while the measurements corresponding to the remaining projectors $|P\rangle$,$|R\rangle$ and $|L\rangle$ are done by a suited shift in the relative interferometer phase (see section 5.2)

Application on a 2x4 entangled state— As a first application of the scheme the linear evaluation according to James [75] is applied on a 2x4 dimensional subspace of the 2x8 dimensional state postselected in the time window $0\Delta T$. This state is analyzed by the logical qubits A_1 and A_2 at Alice's side and

1 This is additionally checked by measuring the concidence count rates after removing the blocking devices

of B_1 and B_2 at Bob's side. In this notation, the analyzed state to be reconstructed is

$$|\Psi_4^8\rangle = 1/2(|0_1 0_2\rangle_A|0_1 0_2\rangle_B + |1_1 0_2\rangle_A|1_1 0_2\rangle_B + |0_1 1_2\rangle_A|0_1 1_2\rangle_B + |1_1 1_2\rangle_A|1_1 1_2\rangle_B) \otimes |0_3\rangle_A|0_3\rangle_B. \quad (95)$$

Here, the state spanned by the Alice's and Bob's 3rd interferometer arms is projected onto $|0_3\rangle_A|0_3\rangle_B$ by blocking the respective long interferometer paths[2].
With prior measurements the analysis devices are calibrated such that all phase settings α_{A_i} and β_{B_j} are set to 0 (see 3.4.2). Typical integrated counts are in the range of ≈ 2500 per measurement time (typically 3s).
The application of the scheme requires the evaluation of 256 different coincidence probabilities for the 256 different projection measurements on $|0\rangle$, $|P\rangle$, $|R\rangle$ and $|L\rangle$ applied on each qubit. The resulting density matrix $\rho_4^{Exp,LIN}$ is depicted in Fig.20 b), which is compared with the density matrix ρ_4^{TH} (Fig.20 a)) to be observed for an ideal preparation of the state.
A figure of merit evaluating the quality of the experimentally prepared states is the Uhlmann Fidelity [124]

$$\mathcal{F}(\rho_{exp}, \sigma_{th}) = Tr[\sqrt{\sqrt{\sigma_{th}}\rho_{exp}\sqrt{\sigma_{th}}}]^2. \quad (96)$$

Here, the theoretical state which is aimed to be prepared has the 16x16 dimensional density matrix representation

$$\rho_4^{TH} = \frac{1}{4}\begin{pmatrix} 1&0&0&0&1&0&0&0&1&0&0&0&1&0&0&0&1\\ 0&0&0&0&0&0&0&0&0&0&0&0&0&0&0&0&0\\ 0&0&0&0&0&0&0&0&0&0&0&0&0&0&0&0&0\\ 0&0&0&0&0&0&0&0&0&0&0&0&0&0&0&0&0\\ 1&0&0&0&1&0&0&0&1&0&0&0&1&0&0&0&1\\ 0&0&0&0&0&0&0&0&0&0&0&0&0&0&0&0&0\\ 0&0&0&0&0&0&0&0&0&0&0&0&0&0&0&0&0\\ 0&0&0&0&0&0&0&0&0&0&0&0&0&0&0&0&0\\ 1&0&0&0&1&0&0&0&1&0&0&0&1&0&0&0&1\\ 0&0&0&0&0&0&0&0&0&0&0&0&0&0&0&0&0\\ 0&0&0&0&0&0&0&0&0&0&0&0&0&0&0&0&0\\ 0&0&0&0&0&0&0&0&0&0&0&0&0&0&0&0&0\\ 1&0&0&0&1&0&0&0&1&0&0&0&1&0&0&0&1 \end{pmatrix} \quad (97)$$

defined in a basis used to represent state $\rho = |\Psi_4^8\rangle\langle\Psi_4^8|$. With respect to this state, a fidelity of $\mathcal{F}_{Exp,LIN}^4 = 0.882 \pm 0.051$ is obtained. Also statistical errors are responsible for the observation of unphysical matrices, what causes to obtain purities above unity. This is due to negative eigenvalues in the range of up to -0.154.
Application on** 2x8 **dimensional state— In contrast, the determination of the density matrix of the analyzed 2x8 dimensional state (6 logical qubits) requires the evaluation of all $4^6 = 4096$ projection measurements performed over the full 6 qubit analysis. The density matrix has a fidelity of $\mathcal{F}_8^{Exp,LIN} = 0.863 \pm 0.012$ with respect to the theoretically predicted state. An eigenvalue decomposition reveals that it consists of an eigenstate with eigenvalue of

2 This corresponds effectively to reduce the dimension of the analyzed states from 2x8 to 2x4.

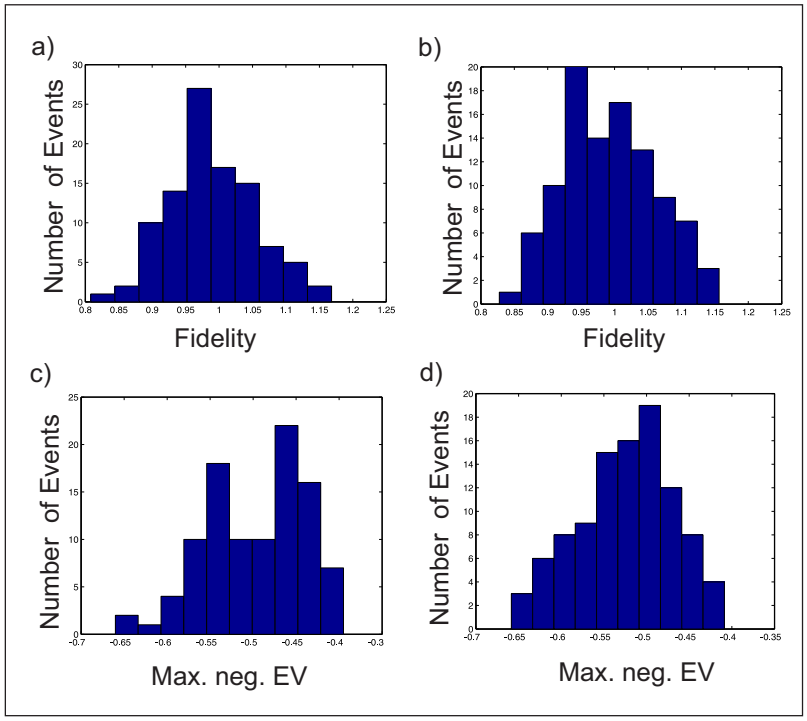

Figure 22: Simulation results for the evaluation of the fidelity and the maximal negative eigenvalues for a set of 100 density matrices simulated with additional phase noise in each of the interferometer arms and with each count rate diced according to Poissonian statistics (a) and c)). Additionally, 100 states were simulated including only phase fluctuations in the interferometers (b) and d)). In all cases the density matrices were evaluated according to the James tomography scheme. As a comparison of the observed negative eigenvalue distributions displays, the main contribution to observing unphysical, i.e. negative semidefinite density matrices, is given by the residual phase noise present in the interferometer phases.

0.933 close to the theoretical maximum of 1. Additionally, a broad and symmetric spectrum of eigenvalues spread over a range of up to $> \pm 50\%$ is observed.
A comparison of the experimentally evaluated density matrix as depicted in Fig.21 with the theoretical prediction already hints at a high contribution of noise, still small enough to allow the distinction of the 2x8 dimensional state contribution. These noise contributions can be mainly associated to residual phase noise $\Delta\alpha_{A_i}$ and $\Delta\beta_{B_i}$ present in the now 6 phases analyzing the state, as will be shown subsequently.

Negative eigenvalues— The influence of the residual interferometric phase noise for observing negative eigenvalues can best be described by completing the state analysis of the 2x8 dimensional state

$$|\Psi_8\rangle = \frac{1}{2\sqrt{2}}(|0\rangle_A|0\rangle_B + e^{i(\alpha_{A_1}+\beta_{B_1}+\Delta\alpha_{A_1}+\Delta\beta_{B_1})}|1\rangle_A|1\rangle_B + e^{i(\alpha_{A_2}+\beta_{B_2}+\Delta\alpha_{A_2}+\Delta\beta_{B_2})}|2\rangle_A|2\rangle_B + e^{i(\alpha_{A_1}+\beta_{B_1}+\alpha_{A_2}+\beta_{B_2}+\Delta\alpha_{A_1}+\Delta\beta_{B_1}+\Delta\alpha_{A_2}+\Delta\beta_{B_2})}|3\rangle_A|3\rangle_B + e^{i(\alpha_{A_3}+\beta_{B_3}+\Delta\alpha_{A_3}+\Delta\beta_{B_3})}|4\rangle_A|4\rangle_B + ... + e^{i(\alpha_{A_1}+\beta_{B_1}+\alpha_{A_2}+\beta_{B_2}+\alpha_{A_3}+\beta_{B_3}+\Delta\alpha_{A_1}+\Delta\beta_{B_1}+\Delta\alpha_{A_2}+\Delta\beta_{B_2}+\Delta\alpha_{A_3}+\Delta\beta_{B_3})}|7\rangle_A|7\rangle_B) \quad (98)$$

with the additional independent phase fluctuations $\Delta\alpha_{A_i}$ and $\Delta\beta_{B_i}$ with $i = 1, 2, 3$.
As they vary statistically for multiple preparations of the entangled states and for a fixed set of projection measurements, they contribute significantly to an additional variation of the observed coincidence count rates and to the detection of negative eigenvalues.
This last assertion is corroborated, as displayed in Fig. 22, by the simulation of the reconstruction of density matrices using the James scheme. For the simulation of 100 states a Poissonian distribution of the counts is assumed (for 2500 counts, typical for the chosen experimental scenario), with an additional Gaussian fluctuation in the phase with a standard deviation of 0.025π (corresponding to typically observed experimental values). A high average maximal negative eigenvalue of up to $\overline{EV_{Neg}}^8_{Poisson,IFPhase} = -0.524 \pm 0.056$ is observed. Similarly, simulations without the Poissonian error source show a slightly lower average value of $\overline{EV_{Neg}}^8_{NoPoisson,IFPhase} = -0.493 \pm 0.056$ (Fig. 22 d)). It follows that the main contribution to the observation of negative eigenvalues is indeed from phase noise. In contrast, the deviation in the average fidelities is minimal as displayed by $\overline{\mathcal{F}}^8_{NoPoisson} = 0.988 \pm 0.064$ (a)) and $\overline{\mathcal{F}}^8_{Poisson} = 0.992 \pm 0.068$ (b)). No simulations were performed with only Poissonian error sources. More significantly, it has to be noted that density matrices reconstructed by using the standard tomographic set yield a much lower contribution of negative eigenvalues, even with count rates affected by the additional fluctuations due to phase noise. The significance of the observation of high negative eigenvalues for the application of optimization schemes of these states will be addressed in more detail in 5.6.

5.3 CONVEX OPTIMIZATION BASED QUANTUM STATE RECONSTRUCTION

As demonstrated experimentally, estimating density matrices by the James tomography scheme has the notorious disadvantage that statistical errors in the count rates lead in general to non-positive semidefinite density matrices. This has been typically observed for similar experimental configurations based on entangled multiphoton [83, 186] or ion states [66]. It imposes restrictions on the applicability of the reconstructed density matrix ρ for determining properties of the underlying state: For example, in order to derive measures characterizing its entanglement such as the von-Neumann entropy [152].
Several optimization problems are suited to address this problem, by ensuring the resulting density matrix to fulfill positive semidefiniteness ($\rho \geq 0$). This can be done by estimating the set of probabilities $p_i(\rho) = Tr[\rho\Pi_i^q]$ for a generalized set of projection measurements Π_i^q more likely to represent the measured relative frequencies $F_i = c_i/\mathcal{N}$ under the condition $\rho \geq 0$. Here,

c_i represent the counts registered within a time interval and $\mathcal{N}$ the normalization constant. Optimization methods can be based on the application of a suited estimator function (such as free least squares) characterizing the deviation between $p_i(\rho)$ and F_i [75]. Nevertheless, they suffer from the inherent disadvantage that there is no formal proof that the optimal solution ρ^{opt} to the problem obtained with highest likelihood is indeed a global and not only a local solution. In contrast, convex optimization methods have the advantage that the obtained solution can be certified to be the global solution as well. Similarly, it allows to enhance the evaluation precision and to derive appropriate measures on the error of the estimation.
In order to implement these a more general set of linear optimization algorithms based on convex estimator functions are used. The associated research field, unified under the term of convex optimization has proven to be reliable with respect to the goal of finding and certifying the optimal global solution to an optimization problem (see [22] for a deeper insight into the field).
They are applied here for the purpose of reconstructing the density matrices of the generated quantum states as they allow to certify that the obtained density matrices are indeed the global and therefore unique solution to the optimization problem, while allowing to warrant their physicality.

5.3.1 *Convex optimization algorithm*

Estimator functions— In order to evaluate the set of probabilities $p_i(\rho)$ most likely to represent the observed frequencies F_i a series of estimator functions can be used, which themselves are convex functions (i.e. their second derivatives are non-zero). The most commonly used convex estimator functions f are called **least squares** (see [96])

$$f^{LS}(p_i(\rho)) = \sum_i w_i[F_i - p_i(\rho)]^2 \tag{99}$$

with defined weights w_i, **free weighted squares**

$$f^{FLS}(p_i(\rho)) = \sum_i [F_i - p_i(\rho)]^2 / p_i(\rho) \tag{100}$$

for the particular case in which the weights w_i are approximated by the respective probabilities as $1/p_i(\rho)$ (as used in the James tomography scheme [75]) and finally the **maximum likelihood** [73] function

$$f^{ML}(p_i(\rho)) = -\sum_i F_i log[p_i(\rho)]. \tag{101}$$

Common to all methods is that they allow to determine the optimal density matrix ρ^{opt} once the corresponding likelihood function is minimized (or maximized if the function is concave), after application of a suitable optimization algorithm. Based on these estimator functions, we will present the chosen method of a nonlinear convex optimization algorithm as described in more detail in [120]. This method allows to include additional constraints, ensuring the physicality of the obtained density matrix ($\rho \geq 0$), into the optimization problem, while being unaffected by typical additional problems restricting the applicability of similar methods: Finding a solution is intrinsically independent on providing suitable input parameters and in addition the method offers an evaluation of how far away from the global optimum

the obtained solution is. It is possible to make use of these additional advantages by resorting to the Newton optimization method (described subsequently) allowing a substantial speedup of the algorithms.
First, the density matrix ρ is represented in a suited operator basis $\hat{O}_i$ according to

$$\rho(p_i) = \frac{\mathbb{1}}{\dim(\mathcal{H})} + \sum_i p_i \hat{O}_i \tag{102}$$

where the probabilities p_i correspond to the values to be obtained after a minimization of a suited estimator function $f(\rho(p_i))$. Here, the constraint to be fulfilled is that $\rho(p_i) \geq 0$ is always true for all sets of probabilities p_i used to derive ρ. This last condition can be fulfilled by redefining the estimator function as

$$g(p_i) = -t \log\det\rho(p_i) + f(\rho(p_i)) = b_i(\rho(p_i)) + f(p_i(\rho)), \tag{103}$$

with the additional barrier term $t \log\det\rho(p_i)$. This turns the unconstrained optimization problem into a constrained one.

Here, for a small value of the penalty parameter t and for low rank states the optimized states lie exactly at the border to the set of negative semidefinite states. As this corresponds to a strong restriction of the states, the optimization problem usually is started with a value in the order of 1 and decreased down to values of 10^{-10} for which the bias in $\rho(p_i)$ attributed to the barrier term is minimal.
Algorithm— In order to evaluate the optimal value $\rho^{opt}(p_i^{opt})$, the algorithm can be started by choosing the parameter $t^0 = 1$ and the set of probabilities corresponding to the maximally mixed state $\rho^0(p_i^0) = \mathbb{1}/dim(\mathcal{H})$. Next iteration steps $n+1$ are based on decreasing the penalty parameters $t^{n+1} < t^n$ and using the set of parameters p_i^n derived from the previous step n as a starting point for evaluating the next iteration probabilities p_i^{n+1}.
An intrinsic problem associated to the nonlinear convex optimization problem is that the number of evaluations required to obtain the better approximation $\rho(p_i^{n+1})^{n+1}$ from the previous set of probabilities grows exponentially with the number of qubits the density matrix ρ consists of. One has to recall that already for 6 encoded qubits the density matrix requires the optimization of $4^6 - 1 = 4095$ and $6^6 - 1 = 46655$ variables when applied onto a tomographic set defined by James and by the standard scheme, respectively. Correspondingly, in order to ensure that $\rho^{n+1}(p_i^{n+1})$ is closer to the optimal solution with respect to the previous step it is required to use efficient schemes determining the optimal set p_i^{n+1} out of the exponentially increasing parameter space.
Numerical methods suited for nonlinear optimizations are, e.g. conjugate gradient or steepest descent, requiring the evaluation of the gradient of the estimation function $\nabla g(p_i)$. In contrast, Newton methods additionally depend on the evaluation of the Hessian matrix $\triangle g(p_i)$ [22]. In the second case, which will be the method used, the evaluation of the Hessian matrix and the calculation of its inverse is the most resource intensive step in the algorithm. Nevertheless, it provides a fast convergence to $\rho(p_i^{opt})^{opt}$ making it the chosen method here.
The Newton method allows to evaluate the next direction Δp_i^n with respect to the starting set of probabilities p_i^0 of the algorithm by approximating the estimator function up to the second order Taylor expansion as

$$g(p_i^n + \Delta p_i^n) \approx g(p_i^n) + \nabla g(p_i^n)^T \Delta p_i^n + \frac{1}{2}(\Delta p_i^n)^T \triangle g(p_i^n) \Delta p_i^n. \quad (104)$$

The resulting linear equation system has a solution

$$\Delta p_i^n = -\nabla g(p_i^n) \cdot (\triangle g(p_i^n))^{-1} \quad (105)$$

which requires the Hessian matrix $\triangle g(p_i^n)$ to be unequal 0 (and therefore invertible) as the estimator function $g(p_i^n)$ is convex. With the knowledge gained about the new direction Δp_k^n, the only parameter left is the distance by which it is necessary to advance along that direction in order to approach the optimal solution. This is done here by parametrizing the next step of the optimization as

$$p_i^{n+1} = p_i^n + s\Delta p_i^n \quad (106)$$

for which a backtracking line search method allows to obtain the optimal step length s.
Before evaluating these probabilities, concrete values for the gradient as well for the Hessian matrix have to be evaluated. Analytical expressions for these are can be formulated: First, the contribution arising from the additional barrier term $b_i^n(\rho(p_i^n)) = t \log det \rho(p_i^n)$ (first term in Eq.(103)), leads to a gradient of the form of

$$\nabla b_i^n = -Tr[(\rho^n(p_i^n))^{-1}\hat{O}_i] \quad (107)$$

and to a Hessian matrix parametrized as

$$\triangle b_{i,j}^n = -Tr[(\rho^n(p_i^n))^{-1}\hat{O}_i]Tr[(\rho^n(p_j^n))^{-1}\hat{O}_j] \quad (108)$$

This second term of the gradient of $g(p_i^n)$ in Eq.(103) is expressed in the example of a maximum likelihood estimator function (for similar derivations for free least squares estimators the reader is referred to [120]) as

$$\nabla f_i^{ML,n}(\rho(p_i)) = -\sum_k \frac{c_k}{p_k^n} Tr[\hat{O}_i P_i]. \quad (109)$$

while the corresponding Hessian matrix corresponds to

$$\triangle f_{i,j}^{ML,n}(\rho(p_i)) = -\sum_k \frac{c_k}{(p_k^n)^2} Tr[\hat{O}_i P_i]Tr[\hat{O}_j P_j] \quad (110)$$

Stopping criteria of optimization algorithm— Several algorithm steps are performed for a fixed value of the penalty term t until the gradient evaluated at a specific step falls below a defined critical value (chosen for example to be $||\nabla g(p^n)|| < 10^{-6}$). Reaching this criteria allows to approach the optimal density matrix and to decrease the penalty term defining its proximity to the set of physical states repeatedly, until the corresponding parameter reaches $t = 10^{-10}$.
The obtained optimal density matrix $\rho^{opt}(p_i^{opt})$ has the required characteristics that none of its eigenvalues are negative, while being derived from the set of probabilities being most likely in accordance with the measured relative frequencies c_i. Moreover, a fraction of the eigenvalues is most likely set exactly to 0 up to a machine precision of $10^{-8} - 10^{-10}$.

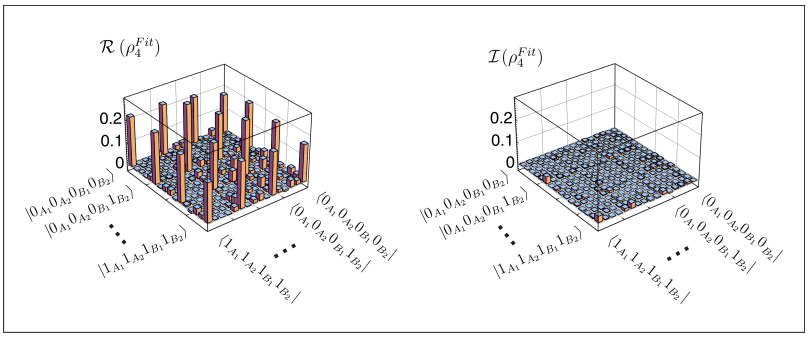

Figure 23: Real and imaginary components of the density matrix for the 2x4 dimensional state obtained by James tomography and after application of a convex optimization method. The corresponding fidelity of $\mathcal{F}_4^{CO} = 0.833$ reveals a close overlap to the theoretical expected density matrix

Furthermore, an optimization scheme based on a maximum likelihood estimator doesn't converge to the underlying density matrix when resorting to the James tomography scheme [75]. Instead, a free least squares estimator is used. A detailed explanation for this fact was not found, but could be related to the fact that a James tomography scheme based on maximum likelihood converges to the underlying state only in the case that the number of projections acquired per basis setting equals the maximal number of 6, i.e. the limit defined by the full tomography scheme (here, both estimators, free least squares and maximum likelihood can be applied).
Due to the proven suitability of a C based programming language for high performance computing and its compatibility with suited linear algebra packages (GoTo BLAS, LAPACK) this language is preferred over the encoding in programs like Matlab. Moreover, the flexibility of languages like C or Fortran90 regarding the efficient parallelization of the calculations over several central processing units (or even Graphic Processing Units) makes these languages suitable for the optimization problems treated in this work. Concretely, a speedup of the algorithms from $\approx$ 15 minutes to 1 second were obtained for a 4 qubit state when comparing codes based on Matlab and on C. This translates into a corresponding improvement from $>$ 24 hours to just $\approx$ 6 minutes for a 6 qubit state. Here, it was particularly advantageous to use highly paralellized linear algebra packages like GoTo-BLAS, for the decomposition of the Hessian matrix in its Cholesky form and for enabling to enhance the efficiency for the calculation of its inverse.

5.3.2 *Convex optimization algorithm applied on experimentally reconstructed density matrices*

The convex reconstruction algorithm presented before is useful to extract the density matrix most likely to be compatible with the measured coincidence count rates. The density matrices corresponding to 2x4 and 2x8 dimensional time encoded states are obtained by measuring each analysis qubit along the James projector basis $J_{i_j} = \{|R\rangle\langle R|, |L\rangle\langle L|, |0\rangle\langle 0|, |P\rangle\langle P|\}_{i_j}$. Here, the corresponding operator basis defined in 5.2 is applied on the 6 logical qubits distributed to both parties, Alice and Bob, in order to analyze states with up to 2x8 dimensions.

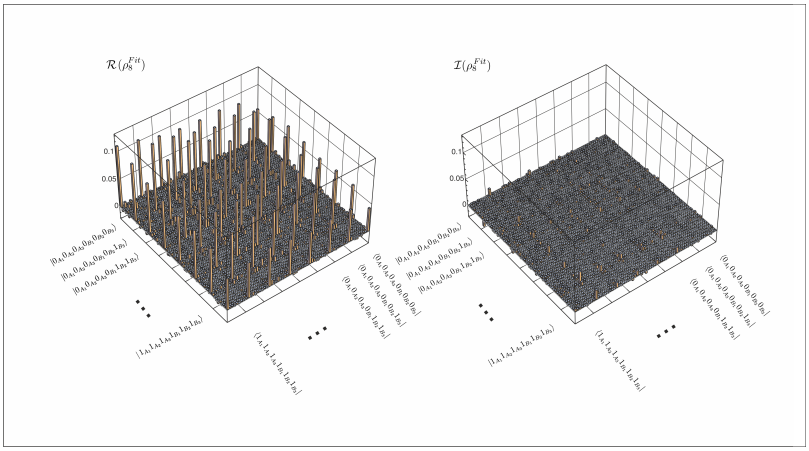

Figure 24: Tomographically reconstructed and convex optimized density matrix of a 2x8 emission time entangled state $|\Psi_8\rangle = 1/(2\sqrt{2})\sum_{i=0}^{7}|k\rangle_A|\rangle_B$ analyzed by making of Alice's and Bob's interferometer arms corresponding to a 6 logical qubit state analysis. The fidelity to the theoretically predicted state corresponds to $\mathcal{F}_8^{Exp,CO} = 0.7825 \pm 0.0121$.

First, the optimization algorithm is applied on the 2x4 dimensional state analyzed in the basis of Eq.(95). In this case the reconstructed density matrix, depicted in Fig. 23, has a spectrum of eigenvalues with only 3 non-vanishing values 0.8588, 0.1065 and 0.0265 greater than 0.02, allowing to bound its rank to 3[3]. This parameter will be relevant for the estimation of the sparsity of the reconstructed states in section 5.4.1. The fidelity obtained from the reconstruction is $\mathcal{F}_4^{Exp,CO} = 0.833 \pm 0.051$ with purity $\mathcal{P} = 0.7496$, deviating from the value estimated by linear evaluation of $\mathcal{F}_{Exp,LIN}^4 = 0.882 \pm 0.051$.
In full analogy, the application of the same scheme on the 2x8 dimensional state reveals a state close to the theoretical predictions (see Fig. 24). The evaluated fidelity of $\mathcal{F}_8^{Exp,CO} = 0.7825 \pm 0.0121$ reveals an even larger deviation by up to $\Delta\mathcal{F}_8 = 0.081$ from the values obtained by reconstructing the density matrix linearly. It is to note that for obtaining this value, an additional local filtering transformation [93, 173] was applied, as this operation preserves entanglement. This transformation increases the fidelity measure from the experimentally evaluated one of 0.7349 ± 0.0121. Here, a contribution of only 8 eigenvalues above 0.02 allows to bound the effective rank to 8. This reveals the state to be close to pure and, more importantly, physical, as the noise contributions affecting the linear evaluation were fitted to be 0 (up to the value of the t parameter at the last optimization step). It will be studied in section 5.6 whether the reason for observing lower fidelities than obtained by the linear evaluation method is due to an intrinsic bias in the reconstruction method. This effect is specially large for the James reconstruction scheme coupled with phase fluctuations in the used interferometers.

The obtained estimation of the underlying density matrices offers a detailed description of the underlying quantum states, but at a considerable

3 The choice of the eigenvalue treshhold of 0.02 is chosen as it corresponds to typically observed noise levels for the count rates obtained in the experiment

higher cost: The minimum measurement effort required scales $\propto 4^N$ with the number of logical qubits N, or correspondingly with $4^{2log_2(d)}$ of the encoded 2xd dimensions of the two-photon states. Here, the derived convex optimization scheme offers significant advantages, as it allows to apply methods requiring a lower number of measurements in order to estimate the underlying state $\rho^{opt}(p_i^{opt})$. These methods are described as compressed sensing (section 5.4) and adaptive (section 5.5) based quantum tomography schemes.

5.4 COMPRESSED SENSING BASED TOMOGRAPHY

Background— Basic research in the field of signal processing and reconstruction has led to the development of novel tomographic reconstruction schemes based on compressed sensing. A common question emerging in these scenarios is which minimal frequency is required in order to obtain a high fidelity reconstruction of a signal, consisting of a spectrum of frequencies f_i and with a maximal frequency f_{max}. This question was adressed from an informational theoretic perspective and, to the knowledge given so far, solved by Shannon and Nyquist in the form of the **Shannon-Nyquist theorem** (SNT). There, it was demonstrated that the minimal sampling frequency to be chosen is $2 \cdot f_{max}$ [153].
This theorem influenced many applications in diverse areas employing signal reconstruction techniques such as in magneto-resonance-spectroscopy (MRS), seismology, signal transmission and conversion for many years. Until it was accidentally discovered that the reconstruction of MRS signals with a much lower sampling rate than allowed by the SNT theorem was still enough to provide a high fidelity tomography, under the condition that the signal sampling is done randomly [108].
A theoretical treatment of the problem led to the demonstration that indeed one important point not addressed by the SNT sampling theorem is the sparsity of the signals studied. Indeed, most signals used in information processing scenarios are sparse, i.e. the number of non-zero coefficients allowing to describe its (Fourier-, Wavelet) decomposition is mostly low. In contrast, signals of high sparsity (i.e. maximally noisy signals) offer a low information content. The paradigm change consisted here in applying effective techniques to efficiently gain information on the highest contributing terms [1] of sparse signals. From this perspective, the signal recovery problem can be addressed by adapting the sampling rate of a signal to its information content, characterized by the number of non-zero coefficients in the decomposition used for its analysis.
A main achievement made by Tao, Candés and Romberg [29] and coworker Donoho [28, 41] was to proof that indeed it is possible to find a unique and efficient solution to the problem. It states that under these considerations the unique reconstruction of a sparse signal requires only sampling rates scaling logarithmically instead of exponentially with the number of dimensions used to describe the signal's parameter space[4]. Moreover, they showed that the optimization problems are efficiently solvable by resorting to standard computational resources.
General to these problems is the definition of the solution vector y known to consist of M entries, corresponding to a decomposition of, for example,

4 Here the maximal frequency f_{max} used to sample a signal is used to describe the signal as a vector with a dimension defined by the number of required sample points

an image in the Fourier or wavelet basis. If it is to be reconstructed from an input vector x extracted from N different measurements. Here, the studied vector x is assumed to be sparse. The corresponding linear system $\phi x = y$ defined for an MxN matrix ϕ is underdetermined once $M<N$. One of the achievements of [29] is to show that still the solution can be demonstrated to be unique and moreover to be limited only by the computation precision and the present noise, once the measurements are sampled randomly. Using these techniques, compressed sensing based algorithms could be successfully applied on noisy and non-ideally sparse samples while offering a tolerable precision, therefore allowing its practical implementation under real experimental conditions.
Based on these proofs a series of implementations in various fields could considerably profit: Efficient face recognition algorithms [76, 89] enable to recover the identity of a person even if the picture is blurred, while pattern recognition schemes could be used to identify buildings or targets by its contour shape even under non-optimal conditions of luminosity or placement of the object [40]. Further on, the possibility to develop so called sensors "single-pixel" cameras [1] based on sensors with a lower number of pixels has led to a considerable reduction in their manufacturing cost [43]. Similarly, MRI reconstruction techniques could benefit from an increase in the information bandwidth to be extracted by compressive sensing techniques. Here, for example it could be used to decrease the required high exposition times detrimental to their application on living organisms [107].
With more relevance to this work, these results could be applied on the state reconstruction schemes as required for obtaining the tomography of a quantum state efficiently [60, 59]. Here, the studies related to the efficient reconstruction problem of a vector motivate its application on matrix completion problems of a density matrix with low rank r, i.e. with a low number r of non-zero eigenvalues [27]. This second condition corresponds to the sparsity assumption about the underlying vector in the compressed sensing problem.

Application for the reconstruction of a density matrix— A direct application of these discussions to quantum state tomography was undertaken in [59, 60], where a suitable choice of a Pauli operator basis (the same basis described in 5.2.2) was chosen to parametrize the matrix instead of using each matrix element as an independent parameter. Here, the translation of the optimization problem into a convex one allows to ensure that the reconstructed state is the global optimal state in difference to similar algorithms not allowing to discard that the solution is only a local maxima.
It could be demonstrated that compressive sensing enables to reduce the number of measurements, sampled randomly out from the full set of d^2 measurements, in order to determine a (square) matrix describing the d dimensional system uniquely. In analogy, the measurement effort M is reduced to a logarithmic instead of a exponential dependence on the dimension d of the studied matrix according to

$$M \propto drlog(d)^2, \tag{111}$$

depending linearly on the rank r of the matrix.
In this work, the corresponding matrix completion problem is solved by making use of the convex optimization scheme derived in the previous section 5.3 for only a random selection Ω_s of projection measurements out of the full set Ω. Here, the optimization problem allowing to determine the

fitted density matrix σ is based on a minimization of the trace norm $Tr[\sigma]$ under the constraint that

$$Tr[\hat{O}_i\rho] = Tr[\hat{O}_i\sigma], \tag{112}$$

only by choosing measurements denoted by an index $i \in \Omega_s$ and described in the operator basis $\hat{O}_i$. This determines that the fitted matrix σ is unique and equal to the underlying state ρ once the optimization was successful. A suitable choice of the operator basis is the Pauli operator basis $\hat{O}_i$ defined in 5.2.2. Similar bases, such as the basis $\hat{J}_{i_j}$ (see 5.3.2) required for a tomographic reconstruction according to James [75], can be used accordingly.

The motivation for using the trace norm can be based on geometrical arguments: Out of the set of sampled measurements contained in Ω_s a large affine matrix space compatible with these results can be defined. The optimization task is now reduced to determining only one point out of the affine space corresponding to the underlying density matrix ρ. This can be done by reducing its geometric distance from the set of states compatible with the sampled frequencies, achieved by using least squares or maximum likelihood functions and compatible with states with a specific sparsity, by using a suited norm, such as the trace norm. Here, the assumption that the state is of low rank enables to offer a further restriction of the states compatible with the affine space of Ω_s. It is at this point that the introduction of the additional trace norm constraint into the optimization problem specifies a computationally efficient strategy for rank minimization, at least down to a rank defined by the optimization parameters. More importantly, it is possible to prove that the global minimum of the optimization defines a state σ identical to ρ and compatible with the set Ω_s, up to the precision thresholds to be fulfilled for the addition of noise.

The inclusion of these conditions into the framework defined by the convex optimization algorithm in Eq.(103) is done by replacing the estimator function by

$$g(p_i)^{CS} = f(\rho(p_i)) - t \log det\rho(p_i) + \lambda Tr[\rho], \tag{113}$$

where the additional parameter λ allows to further specify the rank of the fitted density matrix, i.e. to define the degree of admixture of full rank noise. Based upon apriori assumptions about the fraction of noise present in the system it allows to effectively tune the noise admixture of the optimized density matrix accordingly. The possibility to specify λ from a set of measurements has been addressed in literature, but no definitive solution to its derivation was achieved. Indeed, a simulation of the optimization problem for different values of λ has been done in this work, without achieving a conclusive assertion about the optimal λ to be chosen[5]. Due to that reason, it is recommended to set this parameter to 0, renouncing to provide a tuning parameter to describe the noise contributions [6]. In this case the compressed sensing optimization problem is reduced to a (convex) matrix completion problem for a tomographically incomplete set of measurements.

5 Simulations performed on 2x4 dimensional maximally entangled states (no Poissonian noise) revealed a good convergence to the underlying states for choices of the parameter $\lambda = 0.0001 - 0.5$ and for a number of projections of ≈ 32

6 Personal communication by David Gross

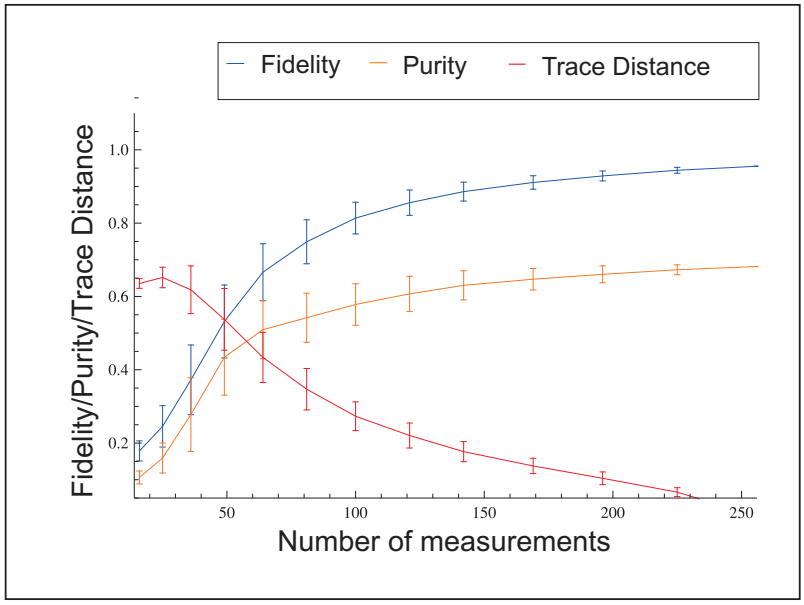

Figure 25: Convergence of parameters evaluating the reconstruction of a 2x4 dimensional two-photon entangled state using compressed sensing reconstruction techniques as a function of the number of projection measurements. Here, the used figures of merit are the fidelity, trace distance and purity of the states and are referenced to the respective density matrix obtained for the full tomographic set.

5.4.1 *Compressed sensing applied on experimental data*

Based on the preceding discussions the compressed sensing optimization scheme is applied to tomographic data obtained from experimentally prepared states. It is the purpose of this section to further corroborate the proof, derived from purely theoretical discussions, that it enables to provide a unique solution σ to the optimization problem even for a tomographically incomplete data set Ω_s. Indeed, this point can be addressed by choosing different subsets of the tomographic data for a fixed number of measurements and by comparing the resulting figures of merit, like the fidelity, trace distance and purity of the reconstructed states. As a reference for evaluating the fidelity and trace distance, it is possible to make use of the state evaluated by using the full data set. For the 2x4 dimensional state this consists of 256 and for the 2x8 state of 4096 measurements.
Figs. 25 and 26 display a convergence of the used figures of merit to the ideal values obtained for the full set of samples as a function of the number of measurements used to reconstruct the corresponding density matrices. More importantly, for the 2x4 state a number of measurements above $M_4^{Exp} \approx 144$ suffices to obtain an average fidelity above 88% of $\overline{\mathcal{F}}_4^{CS} = 0.886 \pm 0.025$ and with a maximal standard deviation of 0.025. Similarly, for the 2x8 state for more than $M_8^{Exp} \approx 1600$ measurements an average fidelity of $\overline{\mathcal{F}}_8^{CS} = 0.8867 \pm 0.021$ spread with a maximal standard deviation of only 0.021 is observed.

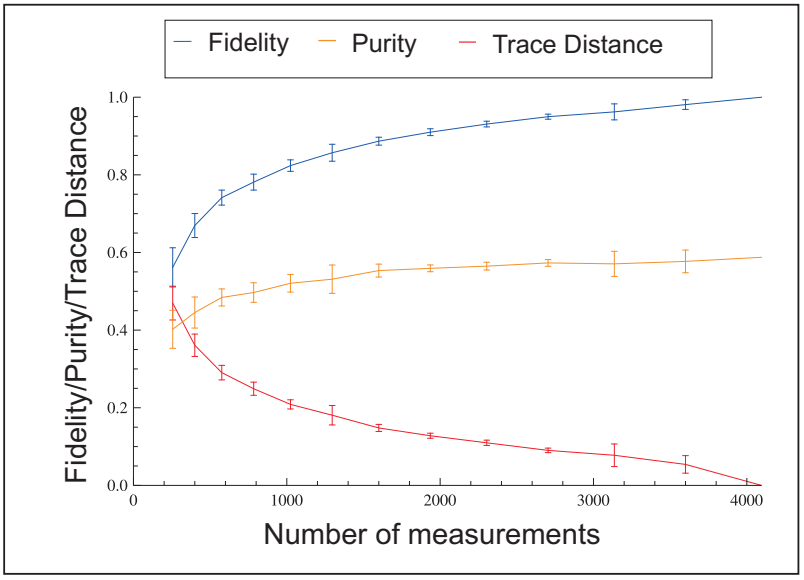

Figure 26: Convergence of parameters validating the successful reconstruction of a 2x8 dimensional two-photon entangled state using compressed sensing reconstruction techniques as a function of the number of randomly sampled measurements, as a function of the fidelity, trace distance and purity of the reconstructed states.

These results outline that the obtained density matrices correspond to near to pure states with a tolerable noise admixture enabling the efficient reconstruction of the states. The high purity of the states was certified by the fact that the convex optimized states had only 3 (out of 16) and 8 (out of 64) non-vanishing eigenvalues. The total reduction in the measurement effort is described by a factor of $\approx 256/144 = 1.778$ and of $\approx 4096/1600 = 2.56$ for the observed 2x4 and 2x8 dimensional states, respectively. In contrast, the evaluation of these results for a simulated state with fidelity 1 and no Poissonian fluctuation of the count rates reveal a convergence to the ideal figure of merit already for $M_4^{Sim} \approx 64$ and $M_8^{Sim} \approx 144$ measurements for the analyzed 4 and 8 dimensional states (not plotted).

Comparison of results with theoretical expectations— It is useful to compare these results with the results predicted by the theory: In this case, the figure of merit M, the number of required measurements, is predicted to scale according to $M \propto drlog(d)^2$ with r corresponding to the rank and d^2 to the dimension of the studied two-photon states. Here, the dimension of the reconstructed density matrices corresponds to $d = 4 \cdot 4$ and $d = 8 \cdot 8$, within which the postselected 2x4 and 2x8 dimensional states are embedded. With these values and a rank of 3 and 8, as observed for the convex optimized experimentally reconstructed states, the bounds read as $M_{d=4\cdot4}^{r=4} \approx 70$ and $M_{d=8\cdot8}^{r=8} \approx 1670$. In contrast, for rank 1 states these values correspond to $M_{n=4\cdot4}^{r=1} \approx 23$ and $M_{d=8\cdot8}^{r=1} \approx 208$. These values are in the same order of magnitude than the ones obtained from experimental ($M_4^{Exp} \approx 144$ and $M_8^{Exp} \approx 1600$) as well of simulated data ($M_4^{Sim} \approx 64$ and $M_8^{Sim} \approx 144$).

To sum up these results, it can be stated that a compressive sensing sampling scheme can be used to increase the reconstruction efficiency for low rank quantum states. Nevertheless, it is of interest to discuss if these efficien-

cies can be further increased, by making use of intrinsic properties defined by the mathematical formulation of quantum theory itself. This will be the topic discussed in the next section.

5.5 ADAPTIVE QUANTUM STATE ESTIMATION

Current tomography schemes— As displayed in the previous section, random sampling of a subset of a tomographically complete set allows to reconstruct the density matrix of quantum states uniquely. Moreover, this is only the most promising strategy to follow in the case that no apriori information is available about the studied state. Nevertheless, most low rank quantum states prepared offer inherent symmetries, which are of informational value and which can be evaluated prior performing the tomographic measurements. One of these characteristics is the permutationally invariant property [167], stating that the state is invariant under the interchange of the qubits it consists of. This is a property satisfied by most prominent states such as Dicke [181] or many GHZ [182, 21] states with wide applications in quantum information. These schemes are valuable, as they lead to only a quadratic instead of an exponential increase in the required measurements with the number of qubits N the quantum state consists of. Further on, combined with convex optimization techniques, the physicality of the resulting density matrices can be warranted [167], while the application of compressed sensing schemes on the PI subspace allows to further decrease the measurement effort [151].
Nevertheless, it is an open question to be adressed here whether alternative scheme offers an equivalent or improved speedup for states not restricted to be permutationally invariant. On the other side, it should also not require random sampling over a subset of the measurements. A useful characteristic of quantum states allowing to increase the reconstruction speedup for a broader set of states is **correlation complementarity** which is a property derived from the axiomatic foundations of quantum theory. It can be expressed in the formalism of a state decomposition based on dichotomic observables [99, 91] or on mutually unbiased bases [184].
Correlation Complementarity— It states that for a correlation measurement (corresponding to an observable A) performed on a given state ρ and for which a high expectation value close to the maximal value close to 1 is observed, there exists a large set of observables anticommuting with the observable A, whose expectation values are predicted to be very low. Here, the measurement effort can be reduced as only the observables leading to higher correlations and therefore with a higher informational value, have to be measured.
Correlation complementarity can be outlined for a two-qubit state, for which the expectation values of all 9 correlation tensor elements are denoted as $T_{ij} = Tr[\rho(\sigma_i \otimes \sigma_j)]$ for dichotomic measurements performed along the Pauli measurement basis σ_i with elements $i = x, y, z$.
The trade-off relations

$$\begin{aligned} T_{zz}^2 + T_{zx}^2 + T_{zy}^2 + T_{xz}^2 + T_{yz}^2 \leq 1 \\ T_{yy}^2 + T_{yx}^2 + T_{yz}^2 + T_{xy}^2 + T_{zy}^2 \leq 1 \\ T_{xx}^2 + T_{xy}^2 + T_{xz}^2 + T_{yx}^2 + T_{zx}^2 \leq 1 \end{aligned} \tag{114}$$

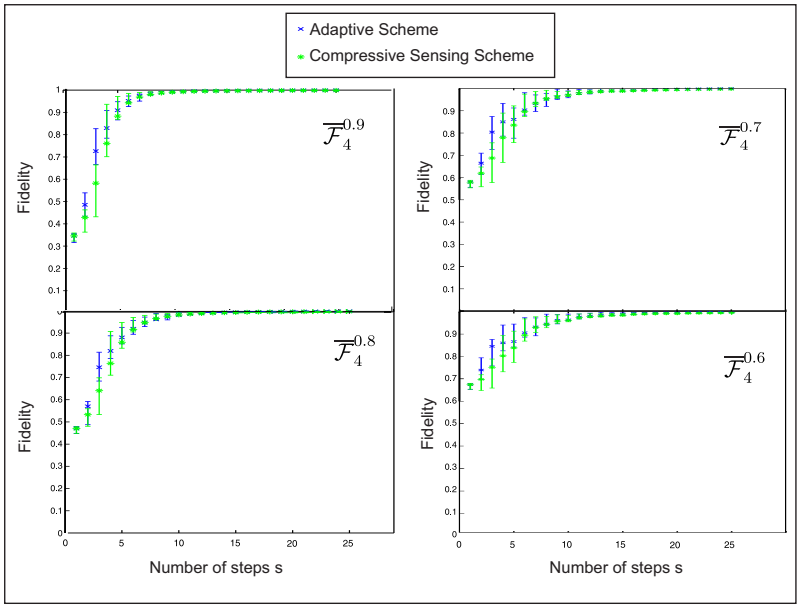

Figure 27: Efficiency of the adaptive quantum state tomography and the compressive sensing schemes applied on simulated maximally entangled states in 2x4 dimensions with varying fidelities and prepared in randomly rotated bases. The corresponding figure of merit, the fidelity with respect to the underlying state, converges to a maximum value for the different simulated states with a fidelity of 90% down to 60% with increasing number of steps s of the adaptive scheme (blue) or equivalently as a function of the randomly sampled correlation bases for the compressive sensing scheme (green). The adaptive scheme only slightly outperforms the compressed sensing scheme. Each average fidelity is plotted with the corresponding 68% confidence region.

follow directly from correlation complementarity. Here, the first condition describes that once the high correlation value $|T_{zz}| = 1$ is observed, quantum theory predicts that $|T_{zx}|$, $|T_{zy}|$, $|T_{xz}|$ and $|T_{yz}|$ corresponding to anticommuting correlations with respect to zz, are expected to be 0. From the information theoretical point of view, the measurement of $|T_{zz}| = 1$ allows to retrieve more information about the underlying quantum state than observing a low expectation value, as it directly conveys that the other correlations have to be small. In contrast, if for example $|T_{zz}| = 0$ is observed, any of the correlations in the trade-off relation of Eq.(114) can have a value between 0 and 1.

Implementation using the convex optimization scheme— The relations of Eqs.(114) are directly implemented by making use of the convex optimization framework developed in the previous sections 5.3. Here, the usage of an operator basis implemented directly in the Pauli operator basis, for which the complementarity relations hold, allows to use the relations (114). Further on, probability conservation and the positive definiteness of the resulting density matrix implies that the sum in (114) is strictly restricted to ≤ 1.

Moreover, the optimization process is shown to be **adaptive**: It makes sense to start the scheme, based upon the information retrieved from a small set

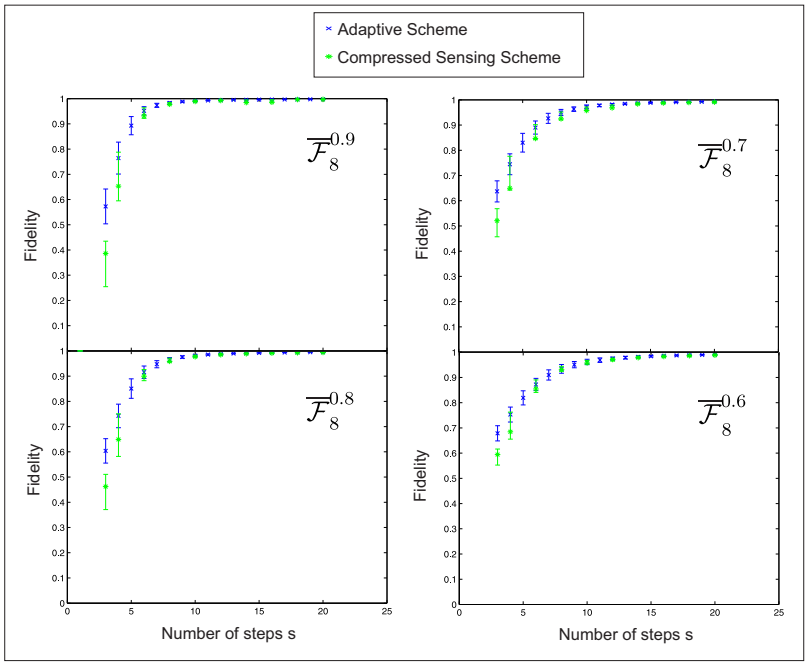

Figure 28: Efficiency of the adaptive quantum state tomography and the compressive sensing schemes applied on simulated maximally entangled states in 2x8 dimensions with varying fidelities and prepared in randomly rotated bases. The same parameters and labels as for Fig. 25 are used.

of correlation measurements, such as $B_{xx\cdots x} = \sigma_x \otimes \sigma_x \cdots \otimes \sigma_x$ and accordingly $B_{yy\cdots y}$ and $B_{zz\cdots z}$ in order to retrieve a density matrix ρ^1 by applying the convex optimization scheme. Here, the choice of correlation measurements retrieving information along all 3 Pauli spin directions of each encoded qubit is required to fulfill the criteria to be met by any matrix completion algorithm as studied here: The chosen measurement subset has to allow the retrieval of information equally over the whole parameter space of the quantum state's density matrix.

As with high probability ρ^1 won't describe the underlying quantum state, at a second step of the state reconstruction scheme it is possible to make use of correlation complementarity by choosing the direction with the next highest correlation value (excluding the correlations already considered). In order to find this direction, all correlations of ρ^1 are evaluated along all combinations of Pauli-spin bases and ordered with respect to their weight. Again, from the information theoretical point of view this correlation has the highest informational value with respect to other anticommuting correlations, more likely to lead to the observation of low correlation values. Therefore, the new correlation measurement is used together with $B_{xx\cdots x}$, $B_{yy\cdots y}$ and $B_{zz\cdots z}$ as the input for obtaining the convex optimized density matrix ρ^2. The subsequent application of this scheme allows to further increase the tomographic reconstruction efficiency, characterized by the convergence of the chosen figure of merit, such as the fidelity, to the underlying state ρ^{Th} with increasing correlation measurements.
Applications of these schemes for multiparticle qubit states of arbitrary qubit number N have been undertaken in [99, 100] for the purpose of en-

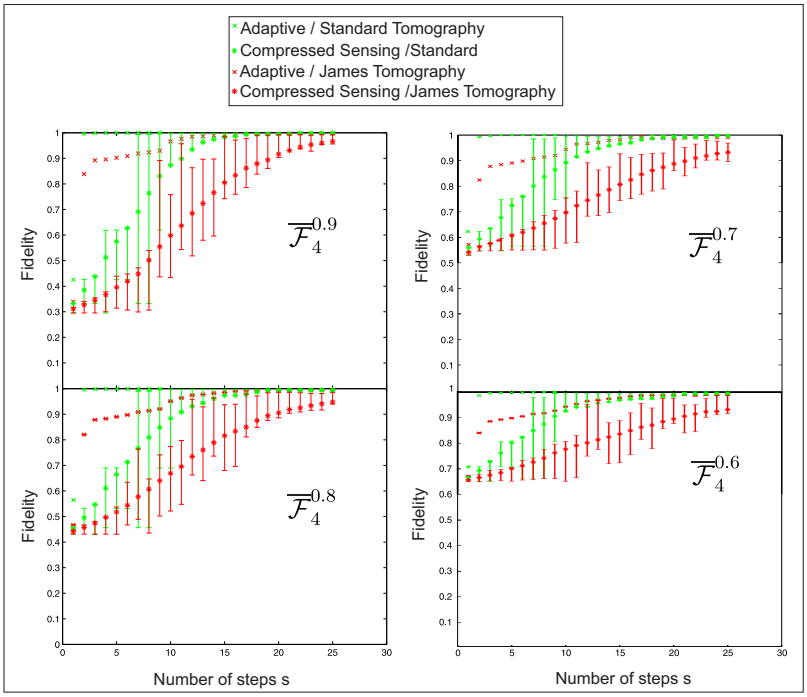

Figure 29: Average fidelities for the application of the adaptive tomographic reconstruction scheme on a simulated 2x4 dimensional maximally entangled state. It is applied on a state reconstructed by using the standard and James tomographic sets. The adaptive scheme is applied only on the input state while the compressive sensing scheme is applied on states by using up to 100 different basis sets for a fixed number of correlation measurements. The evaluated fidelities converge to the ideal fidelity of 1 with respect to a state with the corresponding target fidelity of 90% a), 80% b), 70% c) and 60% d). The adaptive scheme based on using the standard tomographic set converges faster, closely followed by the efficiency of the adaptive James tomography scheme. They clearly outperform the efficiency of schemes based on a compressed sensing sampling. The confidence regions of 68% are evaluated for the compressed based sensing method.

hancing the entanglement detection efficiency. The results have been condensed into the derivation of a decision tree enabling to determine, on the basis of previous correlation measurement results, which measurement is to be subsequently chosen.

5.5.1 *Simulation and experimental results for the adaptive tomography scheme*

Results on simulated rotated maximally entangled states— The adaptive quantum tomography scheme is first applied onto a set of simulated pure 2x4 dimensional, maximally entangled state $|\Psi\rangle = 1/2 \sum_{k=0}^{3} |k\rangle_A |k\rangle_B$.
A set of 100 states is obtained by applying a rotation of the basis of maximally entangled states such that they are distributed equally according to the Haar measure. This is done by applying unitary transformations on the states such as to obtain all pure density matrices with the same probabil-

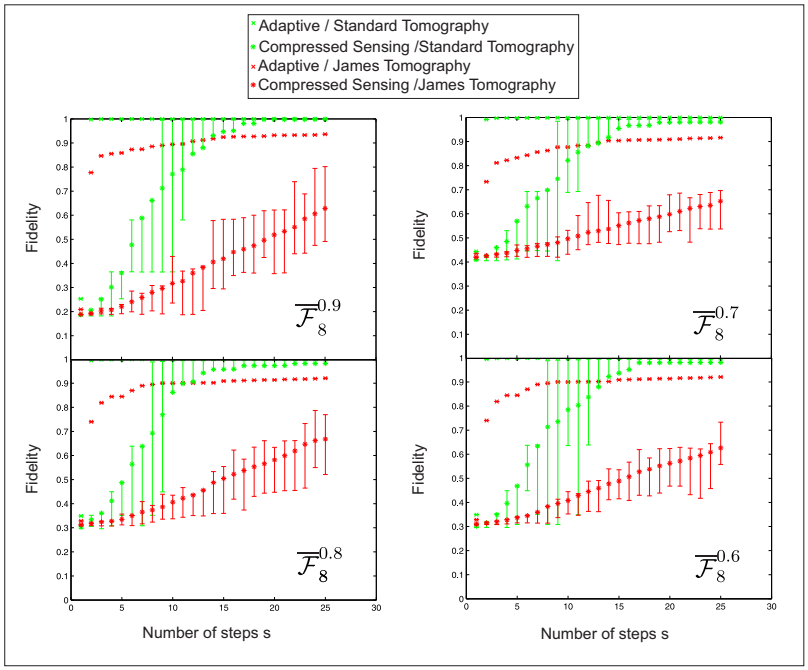

Figure 30: Simulated average fidelities for the application of the adaptive tomographic reconstruction scheme on a 2x8 dimensional maximally entangled state using identical parameters as for simulations performed on the 2x4 entangled state. Here, again the observed efficiency for an adaptive tomography scheme clearly outperforms a scheme based on compressed sensing sampling. The curves are plotted both for a scheme based on full and on James tomography.

ity [117]. In all cases the standard tomographic set is used and combined with a convex optimization based on a maximum likelihood estimator. The simulations are done for different admixtures of white noise to obtain states with target fidelities of 90%, 80%, 70% and 60%. For the obtained simulated states the average fidelities over all 100 states are plotted as a function of the step number s of the adaptive tomography scheme as depicted in Fig. 27. In parallel, a compressed sensing scheme based upon the random sampling of 30 different measurement bases to be obtained from a reduced set of s correlation bases is applied on the same rotated states. The corresponding average fidelities of the fitted density matrices over all sampling runs are plotted. Similar results are obtained for simulations with an equal choice of the parameters on a 2x8 dimensional maximally entangled and arbitrarily rotated state as depicted in Fig. 28.

As depicted in Figs. 27 and 28, the adaptive tomography scheme succeeds in average at the same step in uniquely retrieving the underlying state with respect to a compressed sensing based scheme. Here, the criteria for certifying the reconstruction success is that the obtained fidelities to the input states is $\overline{\mathcal{F}} > 98\%$. Depending on the target fidelities of the considered 2x4 (or respectively 2x8) dimensional rotated states the number of steps (correlation bases for the compressive sensing scheme) for which the reconstruction was successful increases from around 10 for a target fidelity of $\mathcal{F} = 90\%$ to 20 for a fidelity of $\mathcal{F} = 60\%$ (out of a maximum of 81 and 729 different

bases for a full tomographic set). For a reference fidelity of $\mathcal{F} = 90\%$ this results in an average reduction in the required measurements by a factor of 8 for a 2x4 dimensional state and by a factor of 72 for the 2x8 dimensional state. No James tomography reconstruction scheme was applied on the simulated data, as no arguments could be found that it could help the adaptive scheme to outperform a compressive sensing based scheme either.

Application on non-rotated maximally entangled states— Nevertheless, the framework considered for these discussions is different for typical experimental scenarios. Usually, it is well known which state is to be prepared and any considered quantum tomography scheme aims to provide a certificate that indeed this is the case for a low number of measurements. This is for example the case for states studied in this work.

The performance of both schemes is again studied on unrotated maximally entangled 2x4 and 2x8 dimensional states with varying input fidelities ranging between 90% to 60%. Here, additionally the James tomography scheme is applied by using only the corresponding subset of 4 out of the 6 projection measurements as acquired for the full tomography scheme. Concretely, for each correlation basis chosen, only the set of measurements corresponding to a projection on $\{|0\rangle, |P\rangle, |R\rangle, |L\rangle\}$ is used for that purpose (see 5.2). The number of measurements per basis is lower than for using the full set $\{|1\rangle, |0\rangle, |P\rangle, |M\rangle, |R\rangle, |L\rangle\}$ to determine one entry of the correlation tensor $\hat{T}$ in the full tomography scheme (see 5.2.2).

Results on simulated non-rotated maximally entangled states— Here, in both cases (see Fig. 29 for results on a 2x4 and 30 on a 2x8 dimensional state), a faster convergence of the state detection efficiency is observed for the adaptive scheme based on using the standard tomographic set with respect to a scheme based on James tomography. This behavior is to be expected as the corresponding number of projection measurements, used to retrieve information about the prepared quantum states, are reduced in average by a factor $(6/4)^4 = 5.06$ and $(6/4)^6 = 11.39$ with respect to the full tomography scheme. This factor is due to the reduction of the number of projection measurements per basis from 6 to 4.

More importantly, a clear enhancement in the adaptive state detection efficiency for the 2x4 dimensional state by up to 15 correlation (24) measurements with respect to the compressed sensing scheme is observed when basing it on a full and James tomography scheme for target fidelity of $\mathcal{F} = 90\%$ ($\mathcal{F} = 60\%$). Similar observations are made on the 2x8 state, where the improvement is in the range of 19 steps for a target fidelity of 90% (full tomographic set). In contrast, the convergence for the adaptive and compressive sensing James tomography scheme to the ideal values isn't reached for the chosen number of measurement bases of up to 25. Moreover, the curves saturate at a fixed value at $\approx 90\%$ within the simulated 25 steps of the scheme. A similar observation is made on the 2x4 dimensional state, where the fidelity saturates for up to 10 steps as well, before increasing to the ideal values.

Within the performed reconstruction steps, no convergence to fidelities approaching unity could be observed for the James tomography scheme on the 2x8 dimensional state. Nevertheless, the aim followed here is to display that the adaptive tomography scheme clearly outperforms a scheme based on compressed sensing, what is clearly to be extracted from the curves. For a target fidelity of $\mathcal{F} = 90\%$ and using the standard tomographic set this reduction in the measurement effort can be expressed in absolute numbers:

For compressed sensing based schemes these factors correspond to 5 and 40 and for the adaptive scheme to 27 and 400 for a simulated 2x4 and 2x8 dimensional state, respectively. Note that the efficiency of the compressed sensing scheme applied on maximally entangled states is reduced with respect to the scheme applied on maximally entangled rotated states, leading to the conclusion that compressed sensing based schemes are more successful when applied on states with an additional random measurement transformation. This observation can be interpreted in the scenario of the Random Isometry Property (RIP) [30], a property to be fulfilled by the compressed sensing based measurement scheme considered in this work. In this context, it hints at the possibility that the random sampling technique chosen here might not be optimal with regards to reducing the measurement effort.

Results on the experimentally prepared entangled states— Complementing these simulations, the efficiency of the method is evaluated as well for the experimental tomographic data obtained for the 2x4 and 2x8 dimensional states studied in the previous sections. As no tomography based on using the standard tomographic set was performed, only results on the scheme based on James tomography are provided (see 28). Nevertheless, it has to be stressed out that according to the preceding simulation results, a better convergence of the adaptive tomography scheme is predicted by using the standard tomography set.

In order to apply the compressed sensing scheme, a subset of 100 (for the case of 2x4 dimensional states) and 25 (for 2x8 dimensions) bases are randomly chosen out of the full set for a fixed step of the reconstruction.

For the 2x4 dimensional state these results reveal an increase in the detection efficiency on the order of 25 correlation measurements with respect to a scheme based on compressed sensing. This apparent improvement in the reconstruction speed with respect to the results obtained from simulated states has to be relativized by the fact that for experimental data a successful reconstruction is achieved for 30 steps while for simulated data without noise this was achieved for 14 steps. This effect can be attributed in first instance to the additional noise (Poisson distribution of counts and phase noise) present in the experimental data.

The application of the same schemes for the analyzed 2x8 dimensional state reveals again a faster convergence of the evaluated fidelities for the adaptive scheme than for the compressed sensing scheme. Nevertheless, in this case, the achieved fidelity using the adaptive scheme reaches only $\approx 87\%$ with respect to the underlying density matrix within the 200 steps of the adaptive scheme. No clear reason for this saturation was found, but could be associated to similar saturation effects as observed for the simulated data using the James tomography scheme (Fig. 30). A slower convergence of the curves to the ideal values than for the simulated states can be attributed to the additional (phase) noise contributions, as obtained for similar work [60]. Despite these restrictions a success of the reconstruction, certified by fidelities $> 85\%$, is achieved for the adaptive tomography scheme for ≈ 120 steps, while for the compressed sensing based scheme a convergence of the fidelities to the same regime couldn't be obtained within the 200 steps of the simulation. This corresponds to a reduction in the convergence speed with respect to simulations based on noiseless data as depicted in Fig. 30. Summarizing these results, an average reduction in the measurement effort by a factor of ≈ 2 is observed for the adaptive tomography scheme with respect

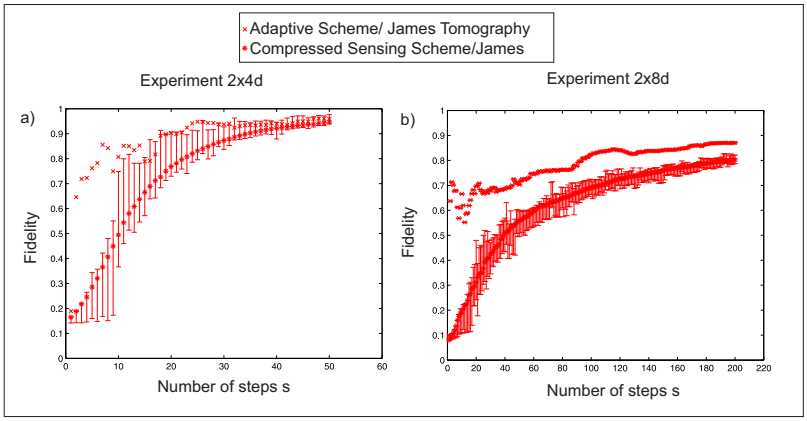

Figure 31: Average fidelities when applying the adaptive and compressed sensing based reconstruction on the experimentally realized maximally entangled 2x4 a) and 2x8 b) dimensional states. Here, the reconstruction methods are applied on a tomographic set according to the James tomography scheme. For both cases the evaluated fidelities (in the compressed sensing scheme averaged over 100 and 25 randomly sampled 2x4and 2x8 states, respectively) are plotted as a function of the number of correlation measurements used to retrieve the corresponding density matrices. Clearly, the adaptive tomography scheme is more efficient than the compressed sensing based scheme in order to retrieve the experimentally reconstructed state obtained for a tomographically complete data set.

to a compressed sensing based scheme.
The advantage of the adaptive tomography scheme over the compressed sensing scheme can be explained by the fact that the maximally entangled states display correlations close to the maximum of 1 along the chosen analysis bases. In consequence only a small number of correlations are big while a high number of correlations whose observables anti-commute with the first one are low. This can be attributed again to the fact that big correlations are of a higher informational value. As the adaptive tomography scheme detects these correlations already for a low number of steps, the state is more efficiently reconstructed, as shown for simulated and experimental data.

Conclusion— An adaptive quantum tomography scheme based on correlation complementarity is demonstrated to outperform the compressed sensing scheme for the efficient detection of the underlying quantum state for dimensions up to 2x8, if the state is maximally correlated along the used basis. For states prepared along arbitrary rotated directions, the scheme is shown in average to perform as good as the compressed sensing scheme, as demonstrated for a scheme based on full tomography.
Simulations on the statistical fluctuation of the corresponding count rates were not done in this section. As will be shown in the next section 5.6 this would lead to a bias in the corresponding figures of merit like the fidelity, when reconstructing the underlying states using constrained optimization algorithms.

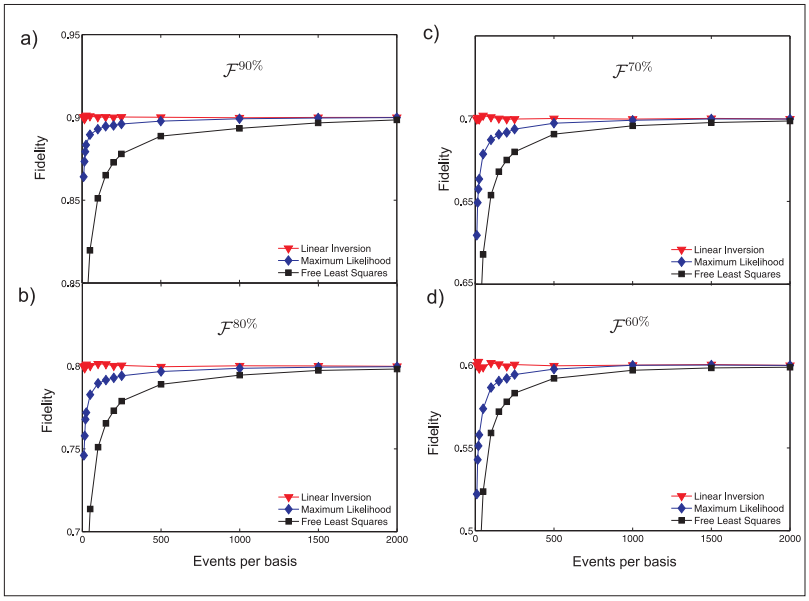

Figure 32: Average fidelities observed for a simulated tomographic experiment of a maximally entangled 2x4 dimensional state using linear inversion applied on a standard tomographic set (LIN) and convex optimization methods based on maximum likelihood (MLE) and free least squares estimators (FLS) in dependence of the used count rates per basis. Each average fidelity is plotted as a function of the total count rates per correlation basis used to reconstruct the corresponding density matrices. A clear bias is observed for low counts for all states admixed with white noise such as to obtain a target fidelity of $\mathcal{F}^{90\%,80\%,70\%,60\%}$, except for the method based on LIN. In contrast, all average fidelities asymptotically converge to the target fidelity for higher counts per basis.

5.6 BIAS IN THE FIDELITY MEASURE

A suited quantum tomography scheme, enabling to give a **unbiased** and, more importantly, a **physical** estimation of the underlying quantum state ρ, is required if reliable quantum computation or quantum information processing schemes are to be implemented. As will be seen no quantum tomography scheme known fulfill all these properties. Nevertheless, these requirements are primordial as relevant figures of merit, such as the von Neumann entropy and the Fischer Information of a state are based on using physical density matrices.

As could be observed in 5.2.3 for density matrices reconstructed by representing them directly as a linear function of the observed frequencies with a high probability they aren't physical (for 2 qubit states with an average probability of $\approx 75\%$ [75]). This method has been denoted in literature by linear inversion (LIN). In contrast, optimization schemes were developed aiming at providing the physical density most likely to be in correspondence with the observed frequencies. Formally, the problem is addressed by defining $\rho = \arg\max_{\rho \geq 0} T(\rho|f)$ where $T(\rho|f)$ corresponds to an estimator function depending on the observed frequencies f to be maximized. Here, the problem is constrained by the limitation that $\rho \geq 0$ has to be fulfilled.

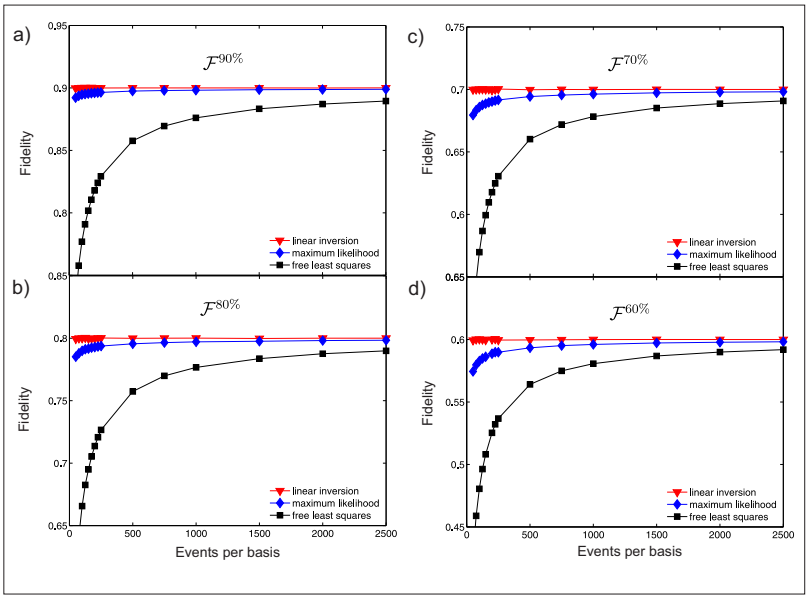

Figure 33: Average fidelities observed for a simulated tomographic experiment of a 2x8 dimensional state admixed with white noise such as to obtain a target fidelity of $\mathcal{F}^{90\%,80\%,70\%,60\%}$. The reconstruction methods applied on a standard tomographic set are based on linear inversion (LIN) and the application of convex optimization methods based on maximum likelihood (MLE) and free least squares estimators (FLS). The average fidelities obtained are plotted in dependence of the used counts per measurement basis.

It could be shown in [152], that independently of the estimator function chosen, the formulation of the optimization problem as a constrained one leads to a bias in the figures of merit extracted from the optimized density matrix. As shown exemplarily in [152], as well as in this work, simulations based on estimator functions such as maximum likelihood and weighted least squares lead to the observation of these systematic deviations in, for example, the fidelity of the reconstruction.

It is possible to display the nature of the bias by embedding the studied states within the set of physical (i.e. $\rho \geq 0$) or unphysical (i.e. $\rho < 0$) quantum states. Pure states can be embedded at the boundary separating the set of physical and unphysical states. For small admixtures of noise, i.e. for the studied quantum state remaining close to the edge, small statistical fluctuations in the associated count rates c_i used to evaluate ρ already suffice to observe variations in the eigenvalues with a magnitude surpassing the contribution of white noise, therefore with a high probability being negative. The resulting density matrix is therefore more likely to be unphysical. In contrast, for quantum states with a higher mixedness (characterized by a lower fidelity due to the admixture of white noise) it is less probable that statistical fluctuations will lead to the observation of $\rho \leq 0$.
The main purpose here is to study the effect of these statistical errors when applying the convex optimization scheme. For that purpose suited simulations are done for different total counts available per full correlation measurement basis for the full set of correlations (81 and 729 for the 2x4 and 2x8 dimensional states). The reconstruction is done on simulated states with dif-

ferent fidelities with respect to the target state. In addition, we study if the choice of the estimator, in this case maximum likelihood (ML) or free least squares (FLS) has any additional influence on the bias.

5.6.1 *Simulation results for the standard and James tomography scheme*

Simulation results for multinomial fluctuation in the count rates— Simulations are performed on 2x4 (Fig. 32) and 2x8 (Fig. 33) dimensional maximally entangled states for 500 different tomographic sets obtained by applying the standard tomography scheme. Here, the counts c_i fluctuate according to a multinomial probability distribution. The simulations reveal a strong bias in the average fidelity evaluated by FLS and ML estimators specially for low count rates. A bias is observed with respect to the maximally entangled state underlying the data for all different target fidelities of the reconstructed state between 90% down to 60% (obtained by adding a fraction of white noise to them). In contrast, the observed average fidelities converge asymptotically to the target fidelities with increasing count rates within the standard deviation obtained over all 500 simulated states. The simulations display that the density matrices reconstructed according to the linear inversion scheme (LIN), have a fidelity corresponding in average to the target fidelity for all count rates per basis.
Simulation results for fluctuation in the count rates and in the interferometer phases— Of more relevance to this work is to study the corresponding bias for additional sources of statistical noise, such as the residual phase noise present in the analysis interferometers. Here, the reconstruction is based additionally on the James tomography scheme [75] as applied on experimentally prepared states in this work. Indeed, as demonstrated in 5.2.3 the resulting density matrices are clearly unphysical, while the fidelities of the reconstructed density matrices obtained by applying a convex optimization method are clearly biased with respect to the ones obtained by a linear inversion scheme. It is possible to study here, if the experimentally observed bias corresponds to the one expected based on simulated experiments.
Fig. 34 displays the average fidelities for a set of 500 2x4 dimensional maximally entangled states each reconstructed from a different set of multinomially fluctuating count rates. These are additionally fluctuating due to phase noise simulated according to a normal distribution with a standard deviation of $\Delta\phi = 0.025\pi$. The reconstruction methods used here are based on LIN, ML, FLS and additionally on the James tomography scheme based on FLS. Clearly, an increased bias is observed for the James tomography scheme with respect to the ML and FLS reconstruction schemes applied on the standard tomographic set for all studied fidelities and all count rates.
It could be argued that a major source to the additional bias is due to the decreased number of projection measurements available for the reconstruction based on the James tomography scheme with respect to the full tomography scheme. Here, the James scheme requires to use 4 out of 6 projection measurements per qubit. Concretely, the number of projection measurements per basis is reduced by a factor $(6/4)^N = 1.5^N$ corresponding to the ratio between the projection measurements used in the standard and James tomography scheme. For 4 logical qubits (used to analyze a 2x4 dimensional state) this ratio corresponds to 5.06 and for 6 qubits (2x8 dimensions) to 11.39.
In order to compare the predictions made on density matrices between the

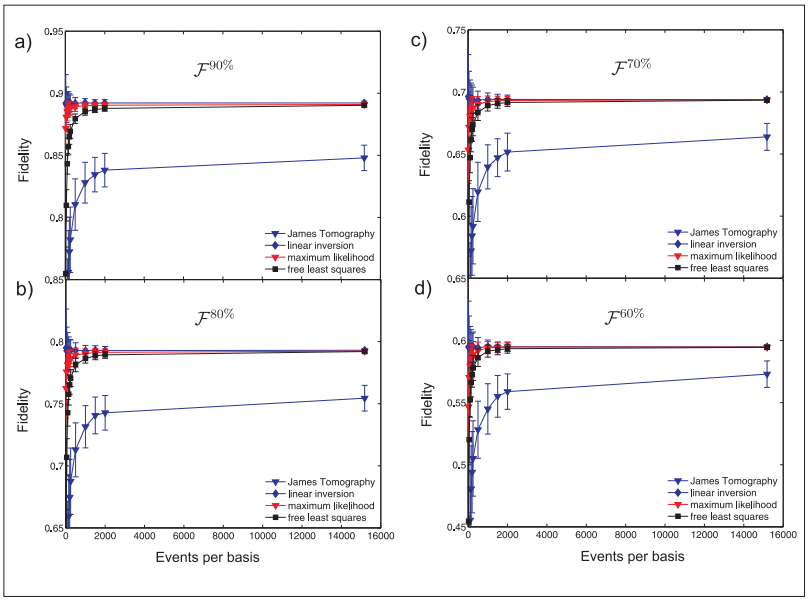

Figure 34: Average fidelities for 500 simulated experiments for a 2x4 dimensional states with a fluctuation of the count rates according to multinomial statistics and additionally, by additional phase fluctuations with a standard deviation of $\Delta\phi = 0.025\pi$ in the analysis interferometers. The reconstruction method based on linear inversion (LIN) is compared with other methods which make use of convex optimization techniques based on free-least squares and maximum likelihood estimators. All of these methods are applied using the same standard tomographic set. With more relevance to this work, these results are compared with the ones obtained by a tomographic reconstruction defined by the James tomography scheme and using a free least squares estimator. A clear bias for the last method can be observed for all considered target fidelities of $\mathcal{F}^{90\%,80\%,70\%,60\%}$ and for all simulated count rates.

ones obtained for the standard and and the James tomography scheme, the simulations are additionally performed for count rates per basis increased by the corresponding ratio. The argument for this approach is based on sample complexity [50] : In order to evaluate a density matrix with the same error bound, increasing the available number of projection measurements or the number of counts registered per projection measurement is equivalent.

Typical experimental runs allowed to retrieve up to 2500 counts per projection measurement, such that additionally simulations for count rates per basis of $2500 \cdot 5.06 = 12650$ for the 2x4 and of $2500 \cdot 11.39 = 28475$ for the 2x8 dimensional state were done. As can be seen in Fig. 32 the associated bias for the James tomography scheme for a count rate per basis of 12650 is clearly below the value obtained by using the standard tomography set for 2500 counts per basis, therefore displaying that the reduction in the fidelity in the James tomography scheme cannot be associated solely to a decrease in the available number of projection measurements. The bias can be associated accordingly to a systematic deviation attributed to the constrained

formulation of the optimization problem on a dataset affected by statistical fluctuations. This is exemplified for reconstruction schemes based on simulated density matrices with an input fidelity of 90%. The simulations corresponding to this fidelity were chosen due to the proximity of their target fidelity to the fidelity of the reconstructed states employing the linear inversion scheme studied in 5.2 and not affected by a bias. Here, the fidelities of $\mathcal{F}_4^{Exp,LIN} = 0.882 \pm 0.051$ and $\mathcal{F}_8^{Exp,LIN} = 0.863 \pm 0.012$ were observed for the experimentally prepared 2x4 and 2x8 dimensional states.

For the 2x4 dimensional maximal entangled state and a target fidelity of $\mathcal{F}^{Target} = 90\%$[7] a bias of $0.900 - 0.848 \pm 0.010\% = 0.052 \pm 0.010\%$ is observed when using the James tomography scheme for 12650 counts per basis (see Fig. 32), while the bias observed for the MLE and FLS reconstruction methods remains small. For 300 different simulations on a 2x8 dimensional state only one parametrization of $\mathcal{F}^{Target} = 90\%$ (not plotted) and count rates per basis of 28475 is used. The simulations reveal a small bias in the ML and FLS estimated fidelity, while an average value of 0.837 ± 0.006 is observed for density matrices evaluated according to the James tomography scheme, leading to a bias of $0.900 - 0.837 \pm 0.006 = 0.063 \pm 0.006$.

In contrast, the experimentally observed bias is in the range of $\mathcal{F}_4^{Exp,LIN} - \mathcal{F}_4^{Exp,CO} = 0.882 \pm 0.051 - 0.833 \pm 0.051 = 0.051 \pm 0.072$ and $\mathcal{F}_8^{Exp,LIN} - \mathcal{F}_8^{Exp,CO} = 0.863 \pm 0.012 - 0.7825 \pm 0.012 = 0.081 \pm 0.017$ for the 2x4 and 2x8 dimensional states. For the 2x4 and 2x8 dimensional states these deviations lie well within the range predicted by the theoretical simulations, while for the 2x8 state these deviations are slightly above the average values for the simulated states of 0.063 ± 0.006.

These simulations certify that the James tomography scheme is affected by an even higher bias in the evaluated fidelities than for schemes based on using the standard tomographic set when applied on a dataset affected not only by (Poissonian) fluctuations in the count rates, but by additional fluctuations due to phase noise.

In summary, the fidelity used in order to certify the suitability of experimentally realized quantum states is affected by a clear bias, if optimization schemes based on maximum likelihood or free least squares estimators, further constrained by the requirement of physical density matrices, are applied for its evaluation. This bias is not due to artifacts in the state reconstruction scheme, as certified by using a convex optimization scheme. [152] displays how to obtain lower bounds for particular nonlinear figures of merit such as the negativity, relative entropy and Fischer information directly out of data used to obtain linear inversion based density matrices. This is even more relevant as specially for these nonlinear measures the evaluation is not directly possible in case that the underlying density matrix is non-physical.

7 Choice motivated by its proximity to the fidelities evaluated by linear inversion

6

DETERMINATION OF THE DIMENSION OF QUDIT ENTANGLED STATES

In the previous chapters a complete guideline for the characterization of higher dimensional entangled states, regarding their entanglement and preparation fidelity has been provided. Nonetheless, a full description is not possible without providing measures on their dimensionality. The evaluation of the dimensionality of the prepared states is crucial for further applications for quantum information tasks. For example, determining the security thresholds for quantum key distribution schemes greatly relies on this parameter [2, 32].
It will be the main focus of this chapter to apply dimensional witnesses used to evaluate the Shannon dimensionality in 6.1 and the Schmidt number in 6.2 of the generated quantum states.

6.1 DIMENSIONAL WITNESS BASED ON THE SHANNON DIMENSION

Dimension witnesses and Shannon dimension— Different methods for the determination of the underlying dimensionality of a given quantum state have been developed and experimentally realized: The first one fulfills the requirements for a state independent detection of the underlying Hilbert space dimension, based on the evaluation of a probability polytope restricting the obtained sets of probabilities to be compatible only with states of a specific dimension [25, 68]. Further schemes based on the evaluation of dimensional witnesses using quantum contextuality [26] can be used as well to bound the dimension of the encoded quantum states [63].
In parallel to these developments, dimension detection schemes based on the determination of the average number of quantum modes emitted have been successfully implemented in [133, 134]. They are motivated by measures of the information density carried by a signal such as the Shannon entropy $S = -\sum_{i \in D} p_i log_2(p_i)$ [153]. Here, the Shannon dimension $D = \{1, 2, ..., d\}$ corresponds to the number of modes defined within a d dimensional space. Translated to the quantum scenario it allows to quantify the average number of eigenmodes contributing to a specific quantum state, i.e. the information density expressed by the number of dimensions at the disposal for encoding quantum information.
Here, the measure based on the Shannon dimensionality is maximized in the case that the number of entangled modes corresponds to the dimension of the used Hilbert space. More precisely, in this case the von-Neumann entropy (translating the Shannon entropy to the quantum scenario) of the reduced states associated to either party A or B is maximal $S_{A/B} = log_2(d)$, or equivalently, the Schmidt number corresponds to the local dimension $K_{A/B} = d$ (see 4.3.1).

It it is to remark, that dimensional witnesses such as the Schmidt number witness determines the number of modes prepared at the source of a quantum state. In contrast, the Shannon dimension witness used in this work [133, 134] detects only the number of modes accessible to the analysis device. It is possible therefore to define the Shannon dimensionality as a filtered Schmidt number. In this work the Shannon dimension is defined as the number of modes accessible to the analysis devices consisting of interferometer arms allowing to test their coherence with respect to each other (see 2.4).

Application on emission time entangled states— The Shannon dimension witness is applied onto the d dimensional emission time entangled states considered in this work: Out of a continuous range of two-photon emission time modes present within the source a superposition of d two-photon modes are detected by the analysis setup (see Fig. 2 in 2.3). Here, the entangled two-photon state prepared in the emission time modes $|i(t)\rangle_A$ and $|j(t)\rangle_B$ is described according to

$$|\Psi\rangle = \int_{-\infty}^{\infty} c_i(t)c_j(t)|i(t)\rangle_A|j(t)\rangle_B dt. \tag{115}$$

Here, the weights are distributed according to the two-photon coherence distribution function $c_i(t)c_j(t)$ with a FHWM width described by the source's coherence length (see 3.2 for experimental details). In this work, the coherence between a number of entangled two-photon states is detected by making use of an appropriate set of interferometers. In order to be able to test the coherence by the used setup, the total delays applied by these interferometers have to be orders of magnitude smaller than the coherence time of the source (see 2.3).

In this scenario, the analysis interferometers used couple to the respective time modes encoded into each photon with a strength of $\gamma_i = |\lambda_i|^2$. These weights are equal to each other for a configuration of the interferometer arms consisting of 50/50 beamsplitters. This motivates defining the eigenstates of the operators applied by the analysis devices of either party, Alice and Bob, as

$$|A(\theta_{A_i})\rangle = \sum_{i=0}^{d-1} e^{i\theta_{A_i}}\lambda_i|i\rangle_A \tag{116}$$

and

$$|B(\theta_{B_j})\rangle = \sum_{j=0}^{d-1} e^{i\theta_{B_j}}\lambda_j|j\rangle_B, \tag{117}$$

where the modes $|i\rangle_A = |i\Delta T\rangle_A$ and $|j\rangle_B = |j\Delta T\rangle_B$ correspond to the states the analysis projects the incoming time modes to, as a function of the time delays ΔT acquired at the interferometer arms. At this point the notation is simplified by using the phases θ_{A_i} and θ_{B_j}, depending on the phase settings α_{A_i} and β_{B_j} to be set at the respective interferometer arms (see 3.4.2 for a detailed description of the coincidence functions).

Both parties can detect the emitted two-photon pairs in different time windows allowing to test the coherence between a different number of two-photon emission time modes. The number of detected two-photon modes is described by the Shannon dimension d.

Determination of the Shannon dimension— The Schmidt number is defined by the respective weights c_i of the different modes prepared in the source

according to $K_{A,B} = Tr[\rho_A] = Tr[\rho_B] = 1/\sum_i c_i^2$ and is not directly accessible in this work. Only the effective Schmidt number, defined by the Shannon dimensionality

$$D = \frac{1}{\sum_i^{d-1} |\gamma_i|^2} \tag{118}$$

depending on the analyzer's coupling strength $\gamma_i = |\lambda_i|^2$ is accessible. This definition was derived and applied on experimentally prepared OAM entangled states coupling to the analysis devices in [133, 134].
Its evaluation can be performed based on coincidence counts, to be equalized to the coincidence probabilities after determining the maximal coincidence count rate. These are defined as

$$P(\theta_{A_i}, \theta_{B_j}) = |\langle A(\theta_{A_i})| \otimes \langle B(\theta_{B_j})|\Psi\rangle|^2 \tag{119}$$

This formula can be simplified to

$$P(\theta_{A_i}, \theta_{B_j}) = |\sum_{i,j=0}^{d-1} \lambda_i \lambda_j c_i c_j e^{-i(\theta_{A_i} + \theta_{B_j})}|^2 \tag{120}$$

with a summation over two different indices i, j describing the contribution of the preparation and analysis state of each separate photon. Moreover, for the regime considered here the distribution of the two-photon sources emission amplitude $A_i = c_i c_j$ are nearly constant over the regime the analyzers couple to. Here, for maximally entangled states for which the witness is optimized for, the summation indices are equalized, as the weights are equal ($c_i = c_j$). Further on, the interferometers at both analyzers are required to detect the respective modes with equal coupling $\lambda_i = \lambda_j$. If these conditions are not met, the detected Shannon dimension of the two-photon states is reduced.
In this scenario, the evaluation of the Shannon dimension (118) of the two-photon state is possible by measuring the coincidence probabilities over the full analysis phase range the analyzers have access to. Subsequently, the concrete value for the dimension is obtained by performing an integral over all phases the analysis of the respective states depends on. This is exemplified for a 2x2 dimensional state analyzed by making use of the (relative) phase settings α_{A_1} and β_{B_1}. Here, the integral over the measured coincidence probabilities corresponds to

$$\begin{aligned}
\int_0^{2\pi} P(\alpha_{A_1}, \alpha_{B_1}) d\alpha_{A_1} d\alpha_{B_1} = \\
\int_0^{2\pi} |\sum_{i=0}^{1} |c_i|^2 |\lambda_i|^2 e^{-i(\alpha_{A_i} + \beta_{B_i})}|^2 d\alpha_{A_1} d\alpha_{B_1} = \\
\int_0^{2\pi} ||c_0|^2 |\lambda_0|^2 + e^{-i(\alpha_{A_1} + \beta_{B_1})} |c_1|^2 |\lambda_1|^2|^2 d\alpha_{A_1} d\alpha_{B_1} = \\
\sum_{i=0}^{1} |\gamma_i|^2 \cdot P_{max} (2\pi)^2.
\end{aligned} \tag{121}$$

with the maximal two-photon generation probability $P_{max} = |A_i|^2 = |c_i c_i|^2$, where $|A_i|^2$ corresponds to the two-photon amplitude. Additionally, the individual interferometer coupling strengths are used to define

$\gamma_i = |\lambda_i|^2$.
Based on the equations (118) and (121), the evaluation of the average mode distribution determining the Shannon dimension is simplified to

$$D = \frac{1}{\sum_{i=0}^{1} |\gamma_i|^2} = \frac{(2\pi)^2 P_{max}}{\int_0^{2\pi} P(\alpha_{A_1}, \alpha_{B_1}) d\alpha_{A_1} d\alpha_{B_1}}. \tag{122}$$

Similar expressions for the coincidence probabilities for states with varying dimension are required to obtain the respective dimensions. Here, the only difference is that with varying dimensions the number N of independent relative phase settings required to analyze the states lead to a factor $(2\pi)^N$ instead of $(2\pi)^2$.
For example, the bipartite dimension of the 2x8 dimensional state is experimentally accessible by evaluating the following formula

$$D = \frac{1}{\sum_{i=0}^{d-1} |\gamma_i|^2} = \frac{(2\pi)^6 P_{max}}{\int_0^{2\pi} P(\alpha_{A_1}, ..., \alpha_{A_3}, \beta_{B_1}, ..., \beta_{B_3}) d\alpha_{A_1} \cdots d\alpha_{A_3} d\alpha_{B_1} \cdots d\alpha_{B_3}}, \tag{123}$$

based on an equivalent argument as used for deriving (122), with the only difference that the integration is over the 6 phases the 2x8 dimensional coincidence function depends on (see details in the next subsection).
Its evaluation can be readily applied on the experimentally prepared states, allowing to determine the dimension of the analyzed states postselected by coincidence measurements at a specific time delay.

6.1.1 *Experimental Evaluation of Shannon Dimension*

Evaluation of integral of coincidence functions— As summarized in 3.4.2, depending on the relative time delay between Alice's and Bob's photons, the 64 time modes are distributed to 15 different time windows. As the number of superposing two-photon states detected within a time window varies accordingly, the Schmidt number of the generated states lies between 1 to 8. Each two-photon state is characterized by a specific variation of the coincidence probabilities to be detected at the outputs of the respective interferometer systems. For example, for a 2x8 dimensional analysis device a variation of the coincidence probabilities according to

$$P(\alpha_{A_1}, \alpha_{A_2}, \alpha_{A_3}, \beta_{B_1}, \beta_{B_2}, \beta_{B_3})_{8d} = \cos\left(\frac{\alpha_{A_1} + \beta_{B_1}}{2}\right)^2 \cos\left(\frac{\alpha_{A_2} + \beta_{B_2}}{2}\right)^2 \cos\left(\frac{\alpha_{A_3} + \beta_{B_3}}{2}\right)^2 \tag{124}$$

is expected for an interferometer output combination $++$. Here, the application of the Shannon dimension witness enables to obtain the bipartite dimension according to

$$D = \frac{1}{|\gamma_i|^2} = \frac{(2\pi)^6 P_{max}}{\int_0^{2\pi} P(\alpha_{A_1}, \alpha_{A_2}, ..., \beta_{B_3})_{8d} d\alpha_{A_1} \alpha_{A_2} \cdots d\alpha_{B_i}} = \frac{(2\pi)^6}{8\pi^6} = 8 \tag{125}$$

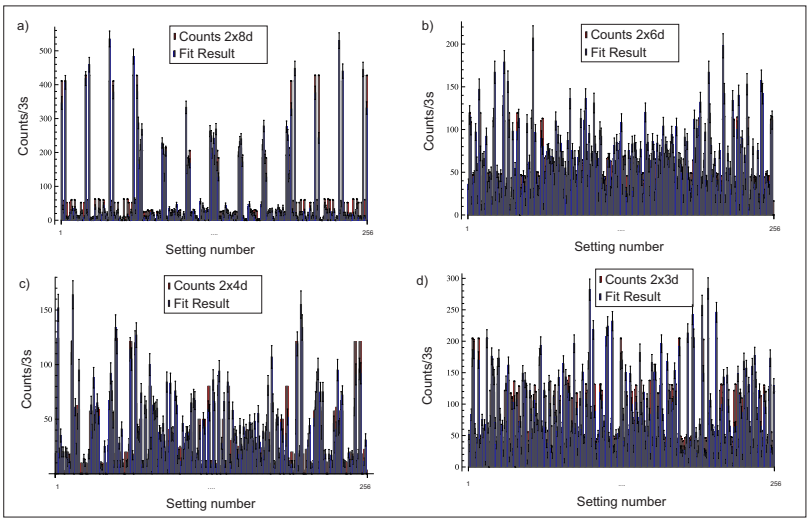

Figure 35: Coincidence count rates obtained for two-photon states of different bipartite dimension 2xd analyzed at different time delay side windows (2x8 in a), 2x6 in b), 2x4 in c) and 2x3 in d)). Here, each coincidence count rate is plotted for a specific phase setting configuration $\{\alpha_{A_i}, \beta_{B_i}\}$ for $i = 1, 2, 3$ denoting each interferometer's phase setting for a partition of each phase into 4 values $0 = 2\pi, \pi/2, \pi$ and $3\pi/2$. The respective count rates are fitted by parametrizing each fitting function according to the expected phase dependence. The fitted functions allow to obtain a measure on the bipartite Shannon dimension of each state. For states of dimension between 2x8 and 2x6 only a fraction of the count rates (in total 4096) obtained for corresponding measurement settings are displayed.

with P_{max} normalized to the maximum probability 1.
Similar calculations are used to determine the dimension of states analyzed for data collected in the different postselection time windows. In order to evaluate the corresponding integrals, the coincidence probabilities are determined at different points spaced by a phase difference of $\pi/2$. Therefore, each phase is scanned over 4 different values $\{0 = 2\pi, \pi/2, \pi$ and $3\pi/2\}$ spanning the full range between 0 and 2π. Choosing a low number of divisions div is motivated by the exponential increase $\propto (div)^N$ in the required measurement settings. Therefore, for the present analysis of a 2x8 dimensional state requiring 6 phases, the current choice leads already to $6^4 = 4096$ measurements. With decreasing dimension of the analyzed states and a lower number of required analysis phase settings this number is reduced exponentially, in the case of 2x4 dimensions down to 256 and for 2x2 down to 16 measurements.

Fitting of coincidence curves and results— The scanned probability curve has to be fitted in order to obtain a precise evaluation of the dimension with corresponding errors. For that purpose the choice of 4 divisions is shown to be sufficient, as displayed for the experimentally obtained coincidence count rates in Fig. 35. Here, the observed count rates obtained for an integration time of 3s and for a postselection time window width of only 164ps are fitted by using functions with an appropriate choice of fitting parameters and a functional dependence described by the predicted functions (41) to

(47). A numerical optimization method implemented in Mathematica (NonlinearFit) is used to retrieve the optimal values of the fitting parameters. For example, for the evaluation of the 2x8 dimensional witness a parameterization of the fit function according to

$$\begin{aligned} C^{Fit}(\alpha_{A_1}, \alpha_{A_2}, \cdots, \beta_{B_3})_{8d} = \\ A_1(1 + V_1 \cos(\frac{\alpha_{A_1} + \beta_{B_1} - \phi_1^{Offset}}{2\lambda_1})) \\ (1 + V_2 \cos(\frac{\alpha_{A_2} + \beta_{B_2} - \phi_2^{Offset}}{2\lambda_2})) \\ (1 + V_3 \cos(\frac{\alpha_{A_3} + \beta_{B_3} - \phi_2^{Offset}}{2\lambda_3})) \end{aligned} \tag{126}$$

is used, where the visibilities V_i, periods λ_i, phase offsets ϕ_i^{Offset} and amplitude A_1 for $i = 1, 2, 3$ are the independent parameters to be fitted. The integration over the obtained coincidence count rates and following normalization over the corresponding fitted maximal count rate reveals the following values for the bipartite dimension:

State	Shannon Dimension D
2x8	$7.33 \pm 0.063 > 7$
2x7	$6.42 \pm 0.076 > 6$
2x6	$5.16 \pm 0.087 > 5$
2x5	$4.201 \pm 0.045 > 4$
2x4	$3.54 \pm 0.108 > 3$
2x3	$2.416 \pm 0.057 > 2$
2x2	$1.686 \pm 0.147 > 1$

In all cases, the observed bounds surpass the values to be obtained for states with a dimension falling below the dimension to be detected by one. This shows that the detected states have the specified Shannon dimension. The corresponding errors are evaluated by parameterizing the fitted function $C^{Fit}(c_i^{opt})$ with the obtained optimal parameters c_i^{opt} and with the corresponding standard deviations Δc_i^{opt} such as to obtain the error function $\Delta C^{Fit}(c_i^{opt}) = \sqrt{\sum_i (\partial C^{Fit}(c_i)/\partial c_i|_{c_i^{opt}})^2 (\Delta c_i^{opt})^2}$. Finally, the evaluation of the integral over the same integration bounds, as used for obtaining the Shannon dimension D, is required for obtaining the total integration error.

6.2 DIMENSIONAL WITNESS BASED ON THE DETERMINATION OF THE SCHMIDT NUMBER

Schmidt number witness— The approach followed in [145] offers an alternative evaluation of the dimension of the superposing two-photon states in the form of an effective Schmidt number $K_{A,B}$, corresponding again to the Schmidt number of the state accessible to the used analysis. It is furthermore suited to provide exact bounds for evaluating the dimension even in the case of mixed states. These studies are motivated by similar studies on entanglement witnesses used for the detection of entanglement [72].
In close correspondence, the main approach followed here allows not only

to detect the entanglement but to evaluate the number of modes which are entangled with each other [162]. Moreover, the dimension detection scheme can be applied on mixed states as well:
A mixed state to be studied is represented as $\rho = \sum_i p_i |\Psi_i^{r_i}\rangle\langle\Psi_i^{r_i}|$ (under the condition $\sum_i p_i = 1$) in terms of pure states of rank r_i: $|\Psi_i^{r_i}\rangle \in \mathcal{H}_A \otimes \mathcal{H}_B$. These are defined as $|\Psi_i^{r_i}\rangle = \sum_i^{r_i} \lambda_i |e_i\rangle|f_i\rangle$ under the condition $\sum_{i=1}^{r_i} |\lambda_i|^2 = 1$. The Schmidt number k is finally determined as the minimum value of the respective maximal Schmidt ranks over all pure states according to $k = \min r_{max}$ (compare with section 4.3.1).
For the following discussions it is necessary to embed the previously defined mixed states within convex spaces S_k defining states with a specific Schmidt rank k. It allows to evaluate bounds for the derivation of the maximal Schmidt number associated to a given state ρ. Moreover, convexity allows to define that any state of Schmidt number k is embedded within the state space S_{k+1} of states with Schmidt number $k+1$.
In this framework, introducing a Schmidt number witness W_k is introduced determinining the specific bounds for a state to be embedded within the corresponding state space S_k by using specific distance measures.
Accordingly, the Schmidt number k of a state ρ can be detected if the witness W_k fulfills the condition $Tr[W_k\rho] < 0$ allowing to bound the Schmidt number of the state ρ to at least $k-1$. A central proof of [146] determines that there exists such a witness defined by a positive operator P by using

$$W = \tilde{W} - \epsilon\mathbb{1}. \tag{127}$$

An optimal choice of the parameter

$$\epsilon = \inf_{\Psi_i^{<k} \in S_{k-1}]} \langle\Psi_i^{<k}|P|\Psi_i^{<k}\rangle \tag{128}$$

is determined over all possible sets of states with Schmidt number below k.
Finding an optimal Schmidt number corresponds to an optimization process evaluating the minimal distance from the studied state from all states with Schmidt number $k-1$.
A measure fulfilling these characteristics is the Uhlmann fidelity (see Eq.(96)). It evaluates the fidelity between the experimentally estimated mixed state ρ_{exp} and any state $\rho^{<k}$ with at least rank $k-1$.
Fidelity as optimal Schmidt number witness— A particular proof for the derivation of the witness for maximally entangled states was provided by Géza Tóth [1] and is described here in full detail here due to the unavailability of published material.
Bounds for the corresponding Schmidt number witness can be derived from the description of a maximally entangled state analyzed in the Schmidt basis $|\Psi_i^{r_i}\rangle = \sum_i^{r_i} \lambda_i |e_i\rangle|f_i\rangle$. The Schmidt coefficients can be shown to be bounded by the respective Schmidt rank r_i according to

$$\sum_{i=1}^{r_i} \lambda_i \leq \sqrt{r_i}. \tag{129}$$

For a mixed state, k is defined as the maximally obtained Schmidt rank for all pure states $|\Psi_i^{r_i}\rangle$. Here, the discussion is first applied on a pure state $|\Psi^k\rangle$ with corresponding maximal Schmidt rank k and further generalized

1 Private communication

to mixed states.
When applying these studies on maximally entangled states

$$|\Psi^{max}\rangle = \frac{1}{\sqrt{d}} \sum_{m=1}^{d} |m\rangle|m\rangle \tag{130}$$

aimed to be prepared in this work, the calculation of the fidelity reveals that

$$\mathcal{F} = |\langle\Psi^{max}|\Psi^{k}\rangle|^2 = \frac{1}{d}|(\sum_{m=1}^{d}\langle m|\langle m|)(\sum_{i=1}^{k}\lambda_i|e_i\rangle|f_i\rangle)|^2 = \\ \frac{1}{d}|(\sum_{m=1}^{d}\langle m|\langle m|)(U_1\otimes U_2\sum_{i=1}^{k}\lambda_i|i\rangle|i\rangle)|^2 \leq \frac{k}{d} \tag{131}$$

holds. Here, the optimization corresponds to the determination of the optimal unitary transformations $U_1 \otimes U_2$ applied on the respective Schmidt bases of Alice and Bob. In this case, it can be shown that the maximal entangled state defined previously optimizes the measure.
Obtaining a fidelity $\mathcal{F}$ such that

$$\mathcal{F} \geq \frac{k}{d} \tag{132}$$

is fulfilled enables therefore to detect the presence of a state with at least a Schmidt number k.
The same conclusions can be derived for general mixed states ρ, due to the convexity of the set of states with a specific Schmidt rank k, for which the last expression translates into

$$\mathcal{F} = Tr[|\Psi^{max}\rangle\langle\Psi^{max}|\rho] \geq \frac{k}{d}. \tag{133}$$

6.2.1 *Experimental Evaluation of the Schmidt number witness*

Using the experimentally determined estimations of the density matrices ρ of the time-energy encoded states allows to directly evaluate the detected Schmidt number k. Here, the fidelity $\mathcal{F}$ is evaluated by applying the constrained optimization scheme described in the preceding sections.
Concretely, the free least squares estimation of the fidelity

$$\mathcal{F}^{FLS} = \langle\Psi|\rho^{FLS}|\Psi\rangle \tag{134}$$

is used, where $|\Psi\rangle$ corresponds to the maximally entangled states defined in 2x4 and 2x8 dimensions, and ρ^{FLS} the experimentally reconstructed states evaluated by using the free least squares estimator.
Here, the bounds to be surpassed for the detection of at least a Schmidt number of 3 and of 7, i.e. the presence of bipartite entangled states of a Schmidt number of 4 and 8 respectively, are $\mathcal{F}_4 \geq 75\%$ and $\mathcal{F}_8 \geq 87.5\%$.
The first bound is surpassed by the analyzed 2x4 dimensional state, as $\mathcal{F}_4^{Exp,CO} = 0.833 \pm 0.055$ was obtained by applying the convex optimization scheme. In contrast, the observed value of $\mathcal{F}_8^{Exp,CO} = 0.7825 \pm 0.012$ doesn't suffice for the detection of a Schmidt number of 8 for the 2x8 dimensional state. Instead, the same Schmidt number witness can be used to bound the dimension to be at most 7, as the corresponding threshold of

$\mathcal{F}_8^6 \geq 6/8 = 75\%$ is clearly surpassed. An equivalent result is obtained when using the fidelity calculated by applying a linear inversion scheme on the obtained data, where the obtained fidelity $\mathcal{F}_8^{Exp,CO} = 0.863 \pm 0.012$ is slightly below the bound required to detect $2x8$ dimensions.
As discussed in 5.6, a high contribution to observing a low value for the fidelities than shown for a direct application of the James tomography scheme (5.2.3) is due to a bias in the estimation method, which is particularly worsened in the case of a state reconstruction scheme based on James tomography 5.6.1 applied on a dataset affected by additional phase noise contributions. Resorting to other informationally complete tomographic sets such as the ones based on standard quantum tomography could be used to obtain a better estimation of the fidelities according to the simulation results presented in 5.6.1. Nevertheless, this comes at the considerable disadvantage of an increase in the measurement effort by a factor $(1.5)^6$. Promising alternatives based on compressed sensing (5.4) or adaptive (5.5) state estimation techniques could be followed here in order to reduce this effort.

7

CONCLUSIONS AND OUTLOOK

This work introduced and experimentally verified novel methods for enhancing the complexity of quantum states encoded into photons, useful for applications in the field of quantum information and computation. The strategy adopted here is to expand the Hilbert space dimensionality of the quantum states, denoted as qu*d*it states, encoded into the emission time degree of freedom of a pair of photons (see section 2.4). Using this degree of freedom makes it suitable for enhancing the transmission distances required for quantum communication schemes [165] with respect to the encoding into other degrees of freedom such as the orbital angular momentum or polarization, whose analysis is difficulted for a transmission over long distances. In comparison to the encoding of quantum states into multi-qubit entangled states [181], it offers an intrinsic reduction in the measurement times required for analyzing and processing the encoded quantum states.
In order to detect entanglement in the time degree a freedom, an analysis scheme is developed which is able to increase the scaling of the dimension of the entangled states encoded with respect to other related schemes (see Chapter 2 and related Publication P1 [140]). Concretely, it addresses and solves the limitations regarding the scalability [188, 165] and stability [138] of previous proposals and experiments (see section 3.2). These improvements have been achieved based on the design and test of a suited interferometer setup and on the design of an active stabilization scheme of each interferometer arm, respectively (see publication P1 [140] and section 3.3). Further on, making use of a more efficient photon pair source based on a periodically poled crystal (see section 3.1) the required measurement times could be further reduced. Using the current experimental configuration, the encoding of quantum states embedded in Hilbert spaces of up to 2x8 was experimentally demonstrated. These results encourage the encoding in Hilbert spaces with dimensions surpassing 2x16, within the current experimental constraints. Future applications could profit from a simplification of the scheme based on using waveguide based interferometers combined with a detection scheme relying on upconversion detectors (see section 3.2). This step would provide an even better scalability of the scheme to even higher dimensions, as the required time delays would be orders of magnitude lower than for the present configuration, making stabilization schemes unnecessary.
This work provides a further insight into how to characterize the encoded higher dimensional states for quantum information applications (Chapter 3). Here, the most valuable resource for these applications, entanglement, is characterized in more detail by resorting to various entanglement detection criteria (see sections 4.1 and 4.3). A scheme, based on the application of Bell-type inequalities defined for bipartite quantum states in arbitrary dimensional Hilbert spaces, is used to demonstrate the non-separability of the

two-qu*d*it states prepared (see section 4.2.1 and the publication draft P3).
Similarly, obtaining full knowledge on the density matrix of the encoded quantum states is a valuable resource for quantum information processing tasks (Chapter 4). Here, an important scheme enabling state reconstruction is based on quantum tomography. Different schemes designed to obtain unbiased and physical density matrices representing the quantum states were discussed and further applied on the experimentally obtained data. First, we used a linear decomposition of the density matrix as a function of coincidence probabilities obtained for a tomographically complete set of projection measurements (see section 5.2). Here, the main limitation of this scheme, regarding the intrinsic unphysicality of the reconstructed quantum states due to additional noise sources, was addressed. This problem was solved by applying schemes based on convex optimization techniques (see section 5.3) ensuring the physicality of the reconstructed states. The resulting convex optimized density matrices correspond to the physical density matrix most likely to represent the obtained data set, but at the cost of reduced reconstruction fidelities due to an additional bias intrinsic to the estimators used in the evaluation (see section 5.6 and related publication P5 [141]).
The convex optimization method is further used and combined with further schemes suited to reduce the measurement effort, while ensuring the high fidelity tomographic reconstruction of the states. The first scheme, based on methods motivated by the application of compressed sensing techniques on sparse signals, allows to make the measurement effort scale only logarithmically instead of exponentially with the encoded dimension (see section 5.4). The only constraint for these applications is that the underlying density matrices are required to have a low rank. This property is fulfilled by the generated states, as for experimentally realized 2x4 and 2x8 dimensional entangled states states the measurement effort is reduced by a factor of approximately 1.8 and 2.6, respectively. A further method suited to reduce the required number of measurements can be based on correlation complementarity, a property satisfied by quantum mechanical observables (see section 5.5). In a closely related scenario, the advantage of this strategy was demonstrated experimentally to reduce the number of measurements required to detect entanglement (see publications P2 and P4 [99, 100]). As demonstrated in this thesis, this property can be used as well to reduce the number of (correlation) measurements required to reconstruct the underlying quantum states with respect to a compressed sensing based scheme. Here, significant reductions in the measurement effort by a factor > 40 with respect to a full tomographic set could be predicted for simulated noiseless states. For the experimentally prepared states, affected by noise and featuring an increased rank, this effect is reduced, but still allows to observe a saving in the number of measurements by a factor of ≈ 2 with respect to a compressed sensing based scheme.
Finally, different methods were studied in more detail allowing to determine the dimension of the underlying quantum states (Chapter 5). This is of critical relevance for applications in quantum cryptography, where the dimension of the encoded states determines the security thresholds to be warranted for a secure transmission [32]. Here, two schemes, one based on the evaluation of the Shannon dimension, determining the number of analyzed entangled modes and the other one based on the application of a Schmidt number witness are applied on experimentally obtained data. They

allow the detection of the number of emission time modes encoded into a pair of photons.
These results demonstrate that the proposed scheme is well suited for preparing and analyzing emission time correlated photon pairs in dimensions of up to 2x8, allowing to foresee its scalability to even higher dimensions $\geq$ 2x16. A particular focus has been laid here on implementing the tools required to characterize their entanglement quality. Based on the fact that entanglement in high dimensional Hilbert spaces was detected with high statistical relevance, their application for (long distance) cryptography schemes using entanglement as a security certificate, is promising. Following these arguments, employing qu*d*its for these tasks enables to achieve a higher statistical relevance, as the critical noise thresholds [32] are increased and the critical detection efficiencies reduced for detecting entanglement with respect to qubits [174]. Further applications in the field of quantum computation would profit from an expansion of the scheme to time-bin encoding (section 2.4.2), as this would enable to increase the number and complexity of the information processing tasks required for these purposes [31, 97]. A central limitation still affecting their large scale application to tackle today's information processing problems. Where quantum computers could tackle currently unsolvable computation problems and quantum communication schemes could address the increasing need of certifying the security of high bandwidth data transmission.

Part III

APPENDIX

8

APPENDIX CHAPTER

8.1 ANALYSIS ANGLES FOR THE MAXIMAL VIOLATION OF THE CGLMP INEQUALITIES FOR D DIMENSIONAL QUANTUM STATES

The angles (in radian) are given in the following table and correspond to the values used to evaluate the maximum of the Bell inequality parameters I_d^{Setup} listed in Table 4.2 for MUB based preparation bases defined in section 4.2:

2x8d	Phase settings
Alice setting 1	$\alpha^1_{A_1} = 0$, $\alpha^1_{A_2} = -\frac{\pi}{2}$, $\alpha^1_{A_3} = \frac{\pi}{4}$
Alice setting 2	$\alpha^2_{A_1} = -\frac{\pi}{2}$, $\alpha^2_{A_2} = -\frac{\pi}{2}$, $\alpha^2_{A_3} = \frac{\pi}{4}$
Bob setting 1	$\beta^1_{B_1} = -\frac{\pi}{4}$, $\beta^1_{B_2} = \frac{\pi}{2}$, $\beta^1_{B_3} = -\frac{\pi}{4}$
Bob setting 2	$\beta^2_{B_1} = \frac{\pi}{4}$, $\beta^2_{B_2} = \frac{\pi}{2}$, $\beta^2_{B_3} = -\frac{\pi}{4}$

2x7d	Phase settings
Alice setting 1	$\alpha^1_{A_1} = 0.449$, $\alpha^1_{A_2} = -1.548$, $\alpha^1_{A_3} = -0.361$
Alice setting 2	$\alpha^2_{A_1} = 0$, $\alpha^2_{A_2} = 3.837$, $\alpha^2_{A_3} = 4.126$
Bob setting 1	$\beta^1_{B_1} = 2.917$, $\beta^1_{B_2} = 1.997$, $\beta^1_{B_3} = 1.259$
Bob setting 2	$\beta^2_{B_1} = -2.917$, $\beta^2_{B_2} = 2.89$, $\beta^2_{B_3} = -3.229$

2x5d	Phase settings
Alice setting 1	$\alpha^1_{A_1} = -0.928$, $\alpha^1_{A_2} = -2.158$, $\alpha^1_{A_3} = 0.142$
Alice setting 2	$\alpha^2_{A_1} = 0.662$, $\alpha^2_{A_2} = -1.219$, $\alpha^2_{A_3} = 0.651$
Bob setting 1	$\beta^1_{B_1} = -1.937$, $\beta^1_{B_2} = -1.701$, $\beta^1_{B_3} = -0.194$
Bob setting 2	$\beta^2_{B_1} = -0.609$, $\beta^2_{B_2} = -1.755$, $\beta^2_{B_3} = -1.184$

2x4d	Phase settings
Alice setting 1	$\alpha^1_{A_1} = -0.376$, $\alpha^1_{A_2} = -0.092$
Alice setting 2	$\alpha^2_{A_1} = 1.194$, $\alpha^2_{A_2} = -0.092$
Bob setting 1	$\beta^1_{B_1} = 1.162$, $\beta^1_{B_2} = 0.092$
Bob setting 2	$\beta^2_{B_1} = -0.408$, $\beta^2_{B_2} = 0.092$

2x3d	Phase settings
Alice setting 1	$\alpha^1_{A_1} = -\frac{\pi}{3}$, $\alpha^1_{A_2} = -\frac{\pi}{6}$
Alice setting 2	$\alpha^2_{A_1} = 0$, $\alpha^2_{A_2} = -\frac{\pi}{2}$
Bob setting 1	$\beta^1_{B_1} = -\frac{\pi}{2}$, $\beta^1_{B_2} = \pi$
Bob setting 2	$\beta^2_{B_1} = \frac{\pi}{6}$, $\beta^2_{B_2} = -\frac{2\pi}{3}$

2x2d	Phase settings
Alice setting 1	$\alpha^1_{A_1} = -\frac{\pi}{4}$
Alice setting 2	$\alpha^2_{A_1} = \frac{\pi}{4}$
Bob setting 1	$\beta^1_{B_1} = 0$
Bob setting 2	$\beta^2_{B_1} = \frac{\pi}{2}$

9

PUBLICATIONS

P1: [140]
D. Richart and Y. Fischer and H. Weinfurter
Experimental implementation of higher dimensional time-energy entanglement
Applied Physics B 106, 543-550, (2012) (invited publication by the German Physical Society (DFG))
Status: published (attached)
P2: [99]
Wieslaw Laskowski, Daniel Richart, Christian Schwemmer, Tomasz Paterek and Harald Weinfurter
Experimental Schmidt Decomposition and State Independent Entanglement Detection
Phys. Rev. Lett. 108, 240501 (2012)
Status: published (attached)
P3: [141]
Daniel Richart and Wieslaw Laskowski and Yvo Fischer and Harald Weinfurter
Experimental qu*d*it entanglement detection using the time-energy degree of freedom
Phys. Rev. Lett.
Status: Draft version (attached)
P4: [100]
Wieslaw Laskowski, Christian Schwemmer, Daniel Richart, Lukas Knips, Tomasz Paterek and Harald Weinfurter
Optimized state-independent entanglement detection based on a geometrical threshold criterion
Phys. Rev. A 88, 022327 (2013)
Status: published
P5: [152]
Christian Schwemmer, Lukas Knips, Daniel Richart, Harald Weinfurter, Tobias Moroder, Matthias Kleinmann and Otfried Gühne
Systematic errors in current quantum state tomography tools
Phys. Rev. Lett.
Status: In preparation

Appl Phys B (2012) 106:543–550
DOI 10.1007/s00340-011-4854-z

Applied Physics B
Lasers and Optics

Experimental implementation of higher dimensional time–energy entanglement

D. Richart · Y. Fischer · H. Weinfurter

Received: 19 September 2011 / Revised version: 11 November 2011 / Published online: 14 January 2012

Abstract Qudit entangled states have proven to offer significant advantages with respect to qubit states regarding the implementation of quantum cryptography or computation schemes. Here we propose and experimentally implement a scalable scheme for preparing and analyzing these states in the time–energy degree of freedom of two-photon pairs. Using the scheme, the entanglement of (2×4)-dimensional states is demonstrated.

1 Introduction

Entanglement is an intrinsic property of quantum mechanics which has enabled the realization of classically impossible tasks, such as the implementation of more efficient computation algorithms, provably secure cryptographic schemes and the teleportation of quantum particles. Compared with qubits, the application of qudits, i.e. states defined in a d-dimensional Hilbert space, offers interesting alternatives. For example, they allow the reduction of elementary gates, and consequently of the number of physical information carriers, necessary to perform quantum computational tasks [1]. Moreover, the number of classical bits transmitted per photon pair can be increased by resorting to high-dimensional super-dense coding schemes [2], and the fault-tolerance bounds for quantum cryptography schemes can be significantly increased, e.g. to error rates of 35% for four-dimensional encoding [3]. In this context we propose and experimentally implement a scalable scheme for preparing and analyzing high-dimensional states in the time–energy degree of freedom of entangled two-photon pairs.

This paper is structured as follows: a short introduction of the theoretical framework will be given in the following. Section 2 describes in detail the experimental setup, with a special focus on the stabilization scheme used. Finally, experimental results demonstrating entanglement between two ququats ($d = 4$) will be presented in Sect. 3.

Since the first proposal for creating time–energy correlated quantum states by Franson [4], they have been used for long-distance distribution and teleportation of entangled states [5, 6] or for the implementation of Quantum Key Distribution (QKD) schemes [7]. As described schematically in Fig. 1, a source of time–energy entangled photons can be any process that coherently emits pairs of photons. Spontaneous parametric downconversion (SPDC) driven by a source of coherent pump photons is such a process. Within the coherence time of each pump photon a continuous superposition of two-photon states $|\Psi\rangle = \int_{t'} |t\rangle|t\rangle \, \mathrm{d}t$ defined for an emission time t is created. For the analysis of the state, each photon of a pair is distributed to the two observers Alice and Bob, which are provided with unbalanced interferometers implementing the very same time delay ΔT and additional phase shifts ϕ_A and ϕ_B.

If ΔT surpasses each SPDC photon's coherence time $t_{\mathrm{c,ph}}$, the local phase shifts ϕ_A and ϕ_B will not determine the relative intensities at the outputs of the interferometers. Yet, if both parties agree to analyze coincident detections with 0 time delay, they will project the initial state $|\Psi\rangle$ onto a superposition of the two-photon states $|0\rangle_A|0\rangle_B$ (both photons arrived at the detectors along the short arm) and $|1\rangle_A|1\rangle_B$

D. Richart (✉) · Y. Fischer · H. Weinfurter
Max-Planck-Institut für Quantenoptik, Hans-Kopfermann-Str. 1, 85748 Garching, Germany
e-mail: Daniel.lrichart@mpq.mpg.de

D. Richart · Y. Fischer · H. Weinfurter
Ludwig-Maximilians-Universität, Schellingstr. 4, 80797 München, Germany

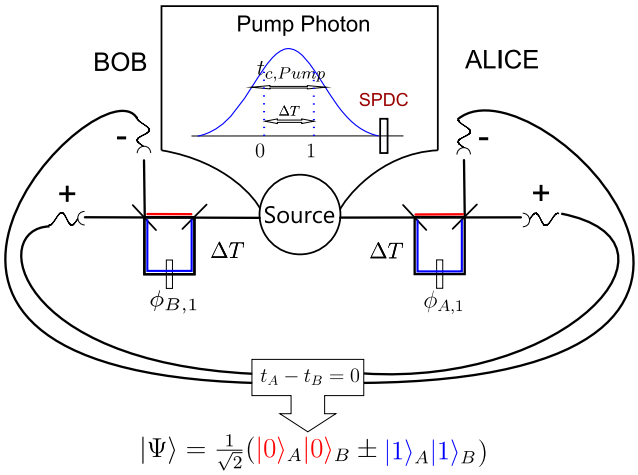

Fig. 1 Scheme for analyzing time–energy entangled two-photon states in two-dimensional Hilbert spaces. A coherent photon pair source is required to produce photon pairs within a continuous range of two-photon emission times. The parties Alice and Bob are each provided with a photon and an interferometer system. A two-dimensional entangled state can be analyzed by performing projection measurements for a time delay $t_A - t_B = 0$ between the detected photons. Each photon can be detected at any of the outputs $\pm$ of the respective interferometer system

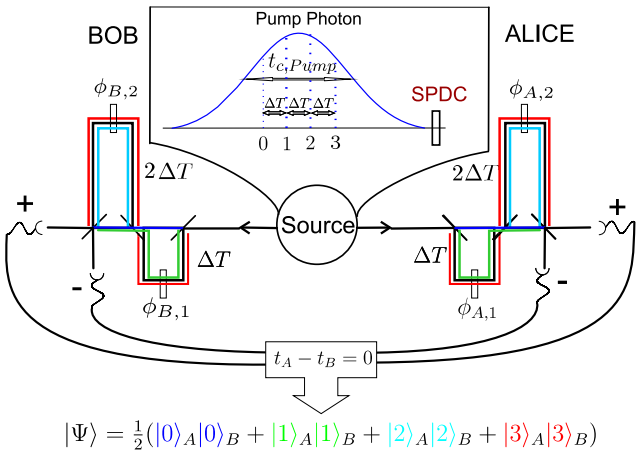

Fig. 2 Scheme for analyzing time–energy entangled two-photon states in higher dimensional Hilbert spaces. Extending the two-dimensional configuration, the parties Alice and Bob use a double-loop interferometer configuration to project onto a superposition of four two-photon detection times $|0\rangle_A|0\rangle_B$, $|1\rangle_A|1\rangle_B$, $|2\rangle_A|2\rangle_B$ and $|3\rangle_A|3\rangle_B$ of a four-dimensional entangled state

(arrival via the long arm):

$$|\Psi\rangle_{2D}^{0\Delta T} = \frac{1}{\sqrt{2}}\left(|0\rangle_A|0\rangle_B + e^{i\cdot(\phi_A+\phi_B)}|1\rangle_A|1\rangle_B\right). \quad (1)$$

They will observe a variation of the coincidence rates in dependence on the relative phases their photons acquire at their respective interferometers according to

$$C_{2D}^{0\Delta T} = \cos^2(\phi_A + \phi_B). \quad (2)$$

This behavior can only be attributed to second-order interference between the two-photon states $|0\rangle_A|0\rangle_B$ and $|1\rangle_A|1\rangle_B$, resulting in the non-classical correlations between the measurement results.

Evidently, such a scheme is not limited to only two possible arrival times. As long as the sum of the delays is sufficiently shorter than the pump coherence time, the effective dimensionality of the state is defined only by the number of delays used in the analyzers [8–10]. Figure 2 depicts how a four-dimensional state can be observed. Here a time–energy correlated state is analyzed by choosing the emission time delays (in multiples of ΔT) $|0\rangle$, $|1\rangle$, $|2\rangle$ and $|3\rangle$ within the coherence time of a pump photon as the four-dimensional computational basis. In analogy to the two-dimensional configuration, spontaneous parametric downconversion can be used to produce two-photon pairs.

They can be analyzed if one photon of a pair is sent to Alice and the other to Bob who are provided with multiple-path interferometer systems designed to project onto the four respective emission times. Here the interferometers are constructed by loops with respective delays ΔT and $2\Delta T$

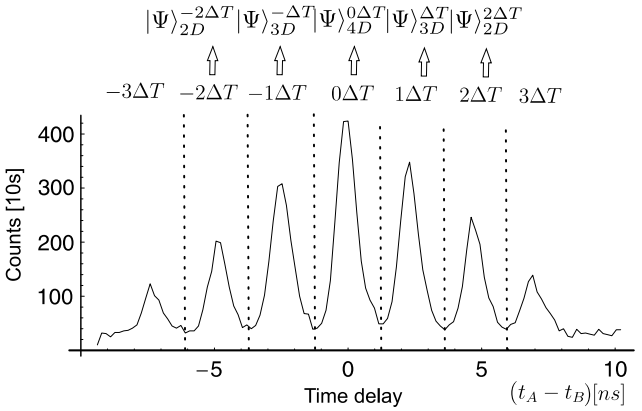

Fig. 3 Time distribution of the coincidence count rates as a function of $t_A - t_B$, Alice's and Bob's photon detection times. For a time delay of 0, coincidence count rates associated to a four-dimensional entangled state can be selected. For delays $\pm\Delta T$ and $\pm 2\Delta T$, a projection onto states with a superposition of three and two two-photon probability amplitudes is realized, displaying correlations of three- and two-dimensional entangled states, respectively. No correlations can be observed in the coincidence windows $\pm 3\Delta T$, corresponding to a projection on a one-dimensional state

such that the probabilities of a photon acquiring a time delay $i\,\Delta T$, with $i \in [0, 3]$, are equal. They allow us to project onto the two-photon states $|0\rangle_A|0\rangle_B$, $|1\rangle_A|1\rangle_B$, $|2\rangle_A|2\rangle_B$ and $|3\rangle_A|3\rangle_B$, which are indistinguishable for a detection time delay $t_A - t_B = 0$ (see Fig. 3). If the maximal time delay fulfills $3\Delta T \ll t_c$, a coherent superposition can be observed:

$$\begin{aligned}|\Psi\rangle_{4D}^{0\Delta T} = \frac{1}{2}\big(&|0\rangle_A|0\rangle_B + e^{i\cdot(\phi_{A,1}+\phi_{B,1})}|1\rangle_A|1\rangle_B \\ &+ e^{i\cdot(\phi_{A,2}+\phi_{B,2})}|2\rangle_A|2\rangle_B \\ &+ e^{i\cdot(\phi_{A,1}+\phi_{B,1}+\phi_{A,2}+\phi_{B,2})}|3\rangle_A|3\rangle_B\big). \end{aligned} \quad (3)$$

The coincidences between, say, the + output of each interferometer (Fig. 2) show a variation according to

$$C_{4\mathrm{D}}^{0\Delta T} = \frac{1}{4}\cos^2\left(\frac{\phi_{A,1}+\phi_{B,1}}{2}\right)\cos^2\left(\frac{\phi_{A,2}+\phi_{B,2}}{2}\right) \quad (4)$$

as a function of their respective relative phase settings $\phi_{A,1}$, $\phi_{A,2}$, $\phi_{B,1}$ and $\phi_{B,2}$ at the ΔT and $2\Delta T$ loops.

Similarly, both parties can agree on measuring coincidence count rates with different time delays, which allows them to project onto two-photon superpositions with a varying number of terms. Here states with the same computational basis as the four-dimensional state but with their respective coincidence functions showing an intrinsic dependence of three- and two-dimensional states are analyzed (see Fig. 3). A projection onto time delays $t_A - t_B = \pm\Delta T$ and $t_A - t_B = \pm 2\Delta T$ allows us to project onto the three- and two-dimensional maximally entangled states

$$|\Psi\rangle_{3\mathrm{D}}^{\Delta T} = \frac{1}{\sqrt{3}}\big(|1\rangle_A|0\rangle_B + \mathrm{e}^{\mathrm{i}\cdot(\phi_{A,2}+\phi_{B,1}-\phi_{A,1})}|2\rangle_A|1\rangle_B + \mathrm{e}^{\mathrm{i}\cdot(\phi_{A,2}+\phi_{B,2})}|3\rangle_A|2\rangle_B\big), \quad (5)$$

$$|\Psi\rangle_{3\mathrm{D}}^{-\Delta T} = \frac{1}{\sqrt{3}}\big(|0\rangle_A|1\rangle_B + \mathrm{e}^{\mathrm{i}\cdot(\phi_{B,2}+\phi_{A,1}-\phi_{B,1})}|1\rangle_A|2\rangle_B + \mathrm{e}^{\mathrm{i}\cdot(\phi_{A,2}+\phi_{B,2})}|2\rangle_A|3\rangle_B\big), \quad (6)$$

$$|\Psi\rangle_{2\mathrm{D}}^{2\Delta T} = \frac{1}{\sqrt{2}}\big(|2\rangle_A|0\rangle_B + \mathrm{e}^{\mathrm{i}\cdot(\phi_{A,1}+\phi_{B,1})}|3\rangle_A|1\rangle_B\big), \quad (7)$$

$$|\Psi\rangle_{2\mathrm{D}}^{-2\Delta T} = \frac{1}{\sqrt{2}}\big(|0\rangle_A|2\rangle_B + \mathrm{e}^{\mathrm{i}\cdot(\phi_{A,1}+\phi_{B,1})}|1\rangle_A|3\rangle_B\big). \quad (8)$$

For a projection onto the + outputs at the respective interferometers and normalized to the total coincidence count rates, the following rates are obtained for delays $t_A - t_B > 0$:

$$C_{3\mathrm{D}}^{\Delta T} = \frac{1}{64}\big(3 + 2\cos(\phi_{A,1} - \phi_{B,1} - \phi_{A,2}) - 2\cos(\phi_{A,2} + \phi_{B,2}) - 2\cos(\phi_{A,1} - \phi_{B,1} + \phi_{B,2})\big), \quad (9)$$

$$C_{2\mathrm{D}}^{2\Delta T} = \frac{1}{16}\big(1 - \cos(\phi_{A,1} + \phi_{B,1})\big). \quad (10)$$

In order to expand the dimensionality of the analyzed states, additional interferometer loops are required to double the previous time delays. As an advantage, the construction allows us to increase the number of analyzed emission time delays, and consequently the dimensionality exponentially $\propto 2^N$ (instead of linearly $\propto N$ for similar interferometer proposals [10]), with N the number of interferometer arms. As a drawback, the number of independent phase settings is smaller than the dimensionality of the states. Ultimately, only the pump laser coherence time and the minimal time resolution of the detection system limit the number of degrees of freedom and consequently the Hilbert space dimension as they impose constraints on the time delays ΔT to be chosen. Alternatively, one can employ time-bin encoding by using a short pump pulse and an interferometric setup for the pump laser equivalent to the analyzer ones [11] or the many mutually coherent pulses of a mode-locked laser [12] (for time-bin-entangled states an additional phase modulator between the source and the interferometers could be added. Here time-dependent phase shifts enable us to apply the phase shifts missing in (3), etc.).

2 Experimental implementation

2.1 General setup

A high-brightness SPDC photon-pair source based on a periodically poled KTP crystal is chosen to produce the entangled photons [13]. A poling period of 9.67 μm and type II degenerate phase matching are used to produce photon pairs with an efficiency of $\eta = 49{,}000\,(\mathrm{s\,mW})^{-1}$ at a central wavelength of 805.9 nm and with a bandwidth of $\Delta\lambda < 1.1$ nm (corresponding to a coherence time of ≈2 ps). The photon pairs are emitted collinearly and the H- and V-polarized photons are separated and coupled into single-mode fibers, respectively.

The implementation of the generic scheme (Fig. 2) was based on various considerations. Fused fiber couplers (FFCs) are used as beam splitters as they warrant a better spatial mode overlap between the different paths (see Fig. 4). This enables a significantly better interference visibility, while requiring only a passive temperature stabilization [5]. As a drawback, the FFCs are less suited for the near-infrared wavelength regime used here than for the Telecom wavelengths for which chromatic dispersion can be compensated routinely. Dispersion is particularly disturbing in this type of interferometer due to the different path lengths in the combined interferometers. Therefore, a hybrid interferometer configuration consisting of a fiber and a free-space path implementing the time delay is chosen, such that both arms of the interferometer share the same path length made of fiber. Polarization-mode dispersion between the different interferometer paths is less severe and is compensated by manual polarization controllers.

The minimal time delay required to distinguish between the different two-photon amplitudes in Fig. 3 depends on the timing resolution of the single photon detection devices. Recently, CMOS-based avalanche detectors (APDs) are reported to reach FWHM timing resolutions down to 50 ps [14]. However, due to the higher detection efficiency in the near infrared, we choose the standard reach-through SPAD (Perkin Elmer, AQ4C-SPCM) with a typical resolution of 500 ps. In order to make the overlap of the two-photon

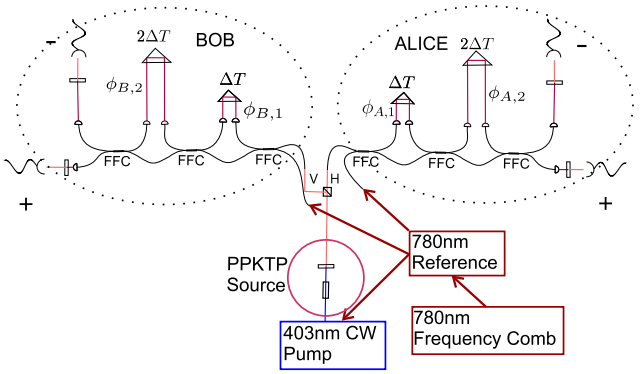

Fig. 4 Experimental setup. Photon pairs are created by pumping a periodically poled KTP crystal using parametric downconversion. The photons are separated at a polarizing beam splitter and sent to the respective interferometer systems both parties (Alice and Bob) require to analyze the shared entangled states. The interferometers are constructed by using fused fiber couplers (FFCs) as beam splitters and a free-space path to implement the required time delays. Finally, single photon avalanche detectors (APDs) are used to detect the photons at each interferometer output

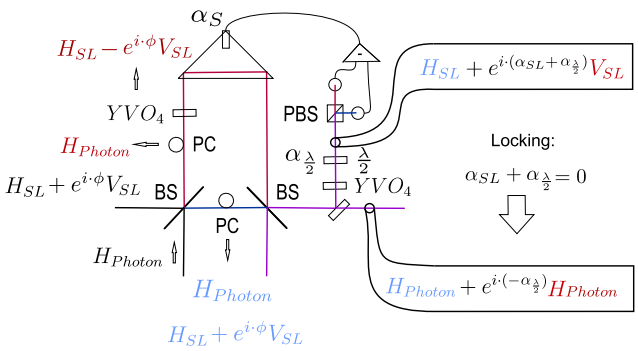

Fig. 5 Interferometer stabilization scheme using polarization multiplexing. An error signal dependent upon the interferometer phase is extracted by ensuring that the polarization transformation for a reference laser is orthogonal in both arms, while the SPDC photons share the same polarization state at the output. It can be used to drive a feedback loop adjusting the relative phase α_{SL} to a constant value while a change $\alpha_{\lambda/2}$ of the analysis $\lambda/2$ waveplate allows us to vary the relative phase acquired by the SPDC photons without any shift of the components inside the interferometer

detection signals negligible, we thus choose $\Delta T > 2.4$ ns. A computer-controlled time-correlation module with a specified resolution of 82 ps (ACAM TDC-GPX) is used for measuring the time differences between the detections at the outputs of each interferometer using four independent APDs. It is believed that further improvements in the detection efficiency and timing resolution of APDs will lead to a significant miniaturization and further scalability of the scheme. Furthermore, the minimal time delay ΔT imposes a strict lower bound for the coherence time of the SPDC pump laser. For that purpose, we use a grating-stabilized blue laser diode at 402.8 nm offering a coherence time of 2.58 µs $\gg \Delta T$.

Alice's and Bob's interferometer delays ΔT and $2\Delta T$ are equalized with respect to each other within the coherence time of their photons to enable the indistinguishability of the respective two-photon probability amplitudes. Similar adjustments are made to equalize the $2\Delta T$ delays to double those of ΔT (Fig. 4).

2.2 Interferometer stabilization

In order to warrant a stable phase relation in the interferometers over longer measurement times, a stabilization scheme compensating thermal and mechanical drifts of each interferometer has been developed.

2.2.1 Polarization-multiplexing scheme

As described before, time–energy correlated states offer an intrinsic insensitivity to the global phase acquired during the transmission of the photons to the respective analysis devices. Nevertheless, the fluctuation of the various phases of the unbalanced interferometers during the measurement time will cause a reduction or even loss of interference visibility. The variation $\Delta\phi$ of the relative phases depends on the fluctuation of the path-length difference ΔL and wavelength variation $\Delta\lambda_p$ of the pump laser. As temperature drifts and vibrations of the optical components will cause a variation of both parameters ΔL and $\Delta\lambda_p$, total path-length differences of up to 2 m require a stabilization scheme.

$\Delta\lambda_p$ is minimized by referencing the pump laser diode to a stabilized reference cavity using the Hänsch–Couillaud locking scheme. The cavity itself is stabilized by a grating-stabilized laser diode at 780 nm locked itself to a frequency-comb mode (250 kHz FWHM, 780-nm central wavelength, maser referenced) [15]. The same laser diode is used to stabilize each interferometer to a subwavelength accuracy by using polarization multiplexing (depicted in Fig. 5).

Polarization multiplexing can be used for stabilizing standard interferometers as well as for the system implemented here, for which the reference laser and photon modes spatially overlap [16]. For similar methods, fringe locking on the reference laser interference signal would limit the range over which a stable interferometer phase change is possible, and also requires the measurement of the intensities at both outputs of the respective interferometer. Instead, for polarization multiplexing it suffices to make the polarization states of the stabilization laser in both arms mutually orthogonal, while the polarization state of the SPDC photons should not be changed (in this example H). Thus, manual fiber polarization controllers (PCs) are used first for equalizing the polarizations of the SPDC photons in the respective interferometer paths. The stabilization laser is then coupled into one input of the interferometer polarized with 45°. The rotation of its polarization vector to −45° is induced along the long arm (red) using a birefringent crystal (here YVO_4)

with optical axes orientation along H. This leaves the SPDC photon's polarization H unchanged.

In this experiment, wavelengths of 780 nm and 806 nm are chosen for the stabilization laser and SPDC photons, respectively, allowing separation by a dichroic beam splitter. The polarization analysis of the stabilization laser consists of an YVO_4 crystal used to compensate for an additional phase ϕ acquired in the fibers and the dichroic beam splitter and a $\lambda/2$ waveplate before projecting onto a polarizing beam splitter (PBS) which reflects V (vertical) and transmits H (horizontal) polarized light. The polarization change by the waveplate rotation adds to the interferometer phase resulting in the error signal $E(\phi_{\mathrm{SL}}, \phi_{\frac{\lambda}{2}}) \propto \cos(\phi_{\mathrm{SL}} - 2\phi_{\lambda/2})$ extracted by measuring the difference of the intensities H/V at both outputs of the PBS (ϕ_{SL} is the relative phase difference mod 2π between the interferometer arms, and $\phi_{\lambda/2}$ is the rotation angle of the $\lambda/2$ analysis waveplate). A P–I feedback control is applied to piezoelectrically lock the phase ϕ_{SL} to 0, such that a rotation of $\phi_{\lambda/2}$ will contribute to an effective phase change $-\phi_{\lambda/2}$ acquired by the 806-nm photons. Using this method, we observe fluctuations of the error signal of each interferometer loop with $\Delta\phi_{\mathrm{SD}} \leq \pm 0.02\pi$, resulting in a relative stability of all four loops of $\Delta\phi_{\mathrm{SD}} \leq \pm 0.059\pi$ as determined from coincidence measurements over one hour (see Fig. 7).

We want to emphasize that for our method the phase-change speed is ultimately limited by typical millisecond piezoactuator response times, while the probability of fringe skipping is minimized with respect to other stabilization schemes. More importantly, no optical component is placed in the path of the photons in order to vary their phase, therefore avoiding transmission losses and mode aberrations for the SPDC photon modes.

2.2.2 *Time-multiplexing scheme for stabilization of different interferometer arms*

Figure 6 describes how the polarization-multiplexing scheme can be applied in order to extract error signals dependent on the respective phases ϕ_1 and ϕ_2 caused by the two interferometer loops ΔT and $2\Delta T$.

The H-polarized photons obtained from the SPDC source are coupled into one input, and fiber polarization controllers are placed in each path to obtain H polarization at each output of the fibers. In order to obtain independent error signals SL1 and SL2, the stabilization laser intensity is split up into two modes.

The first component (SL1) used to stabilize ΔT is coupled into the free interferometer input and extracted at the long path of the $2\Delta T$ interferometer using a dichroic beam splitter with ideal transitivity for 806 nm and a 30–70% splitting ratio for 780 nm. The error signal $E(\phi_1, \phi_{1,\frac{\lambda}{2}}) \propto$

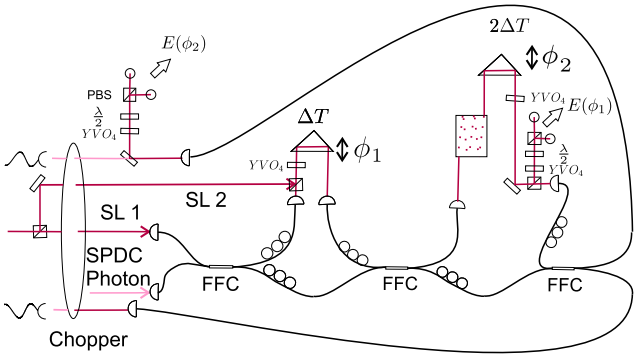

Fig. 6 Time-multiplexing scheme of stabilization laser intensities SL1 and SL2 for stabilizing of different interferometer loops independently. The electronically demultiplexed error signals depend only on the respective phase settings ϕ_1 and ϕ_2 of the delays ΔT and $2\Delta T$, allowing an independent stabilization and variation of the relative phases acquired by the photons. Here the interferometer delay $2\Delta T$ is added by using an optical delay line between two mirrors

$\cos(\phi_1 + \phi_{1,\frac{\lambda}{2}})$ can be extracted by applying the scheme described in Fig. 5. For referencing $2\Delta T$, the intensity SL2 is coupled through the free-space path of the first interferometer using a dichroic beam splitter with the same characteristics. The intensities for SL2 are extracted by interference filters after their overlap at the last beam splitter. The corresponding error signal displays a dependence only on the phase ϕ_2 acquired at the $2\Delta T$ interferometer: $E(\phi_2, \phi_{2,\frac{\lambda}{2}}) \propto \cos(\phi_2 + \phi_{2,\frac{\lambda}{2}})$. The variation of $\phi_{1,\frac{\lambda}{2}}$ and $\phi_{2,\frac{\lambda}{2}}$ allows an independent variation of the relative phases acquired by the SPDC photons in both interferometer arms.

As the stabilization light for the two loops would mutually disturb the generation of the error signals, they are time multiplexed (100-Hz frequency, offset >20 ms) by transmitting each mode through alternating blades of an optical chopper before feeding the laser light into the interferometers. For demultiplexing the respective error signals depending on the phases ϕ_1 and ϕ_2, the P–I feedback electronics are driven by analog sample-and-hold circuits triggering a feedback loop only at the times at which the respective stabilization signals are detected.

Despite the chromatic filtering between the stabilization laser and the SPDC photons, non-negligible background counts are still measured at the wavelength of 806 nm. It is believed that they can be associated with scattering processes of the stabilization laser in the fibers and other optical components. For this reason, the detection of SPDC photons and the transmission of both reference signals SL1 and SL2 are also time multiplexed with respect to each other, by transmitting the SPDC photons through a further set of blades of the same optical chopper. To minimize losses in the photon coincidence count rates, the time-averaged transmission rate of the SPDC photons is set to ≈75% while the stabilization signals share ≈25% of the time. The scheme

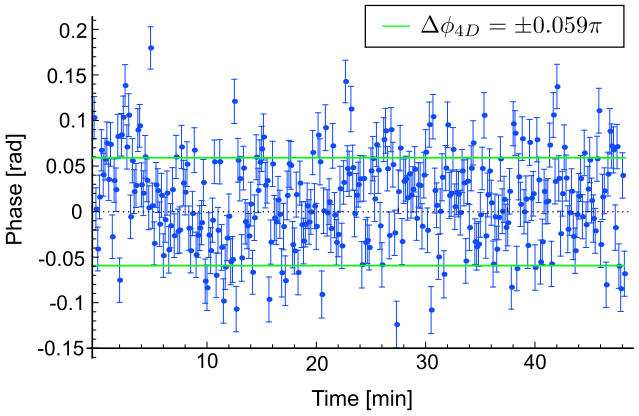

Fig. 7 Phase fluctuation of the four-dimensional coincidence rate over measurement times of up to one hour. Routinely a standard deviation of $\Delta\phi = \pm 0.059\pi$ is observed

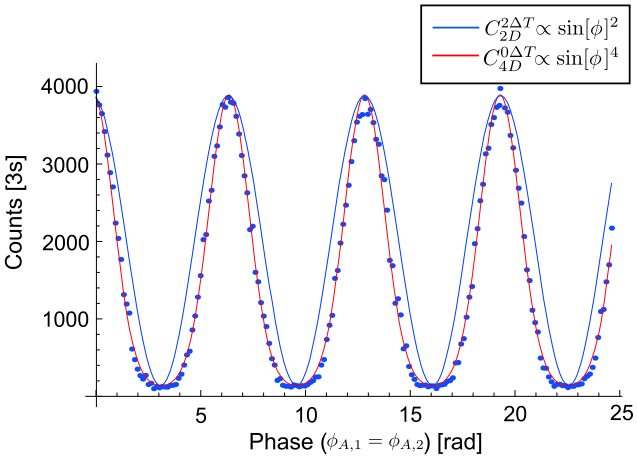

Fig. 8 Coincidence count rate variation for a simultaneous scan of phases $\phi_{A,1}$ and $\phi_{A,2}$ in both interferometer arms of Alice. The function $C_{4D}^{0\Delta T}$ is fitted to the experimental data while $C_{2D}^{2\Delta T}$ corresponds to the theoretical coincidence function for a two-dimensional state

is scalable and can be applied on additional interferometer arms used to expand the dimensionality of the analyzed states.

3 Experimental results

First, we evaluate the performance of the stabilization scheme by analyzing the time-dependent variation of the coincidence count rates for the four-dimensional state. Typical phase deviations for measurement times of up to 50 min and integration times of 10 s are displayed in Fig. 7. Average standard deviations of $\Delta\phi_{4D} = \pm 0.059\pi$ are observed, ≈3 times larger than for the single-interferometer stabilization scheme of $\Delta\phi_{PM} = \pm 0.02\pi$ described in Sect. 2.2.1, but still sufficiently small for further measurements. The main contribution to this value is due to the independent fluctuations of four interferometer phases (see (3)) and the additional phase uncertainty resulting from the short time span used for stabilization (≈8%).

In order to characterize and to evaluate the setup, first the dependence of the coincidence count rates of (4), (9) and (10) for different dimensions is tested for phases ϕ_1 and ϕ_2 for each party. An illustrative way to display the difference between two-dimensional and four-dimensional entangled states is to simultaneously scan the phases $\phi_{A,1}$ and $\phi_{A,2}$ of Alice's interferometers ($\phi_{B,1} = \phi_{B,2} = 0$). Then the coincidence functions as given in (3) and (9) simplify to $C_{4D}^{0\Delta T} \propto \cos\phi^4$ and $C_{2D}^{2\Delta T} \propto \cos\phi^2$, respectively. As illustrated in Fig. 8, the coincidence count rates clearly show an excellent overlap with the function $C_{4D}^{0\Delta T}$. As described in [17, 18] these characteristics can be used to define dimensional witnesses.

Next, we analyze the coincidence count rates observed for states of different dimensions by comparing the experimental data with the corresponding theoretical predictions. In Fig. 9 the coincidences for the $+,+$ detector combination are shown as a function of $\phi_{A,2}$ for Figs. 9(a) and 9(b) and in dependence on $\phi_{A,1}$ for (c) and (d) while keeping the respective other phases constant at 0. In (a) and (b), the fringe visibility for the four-dimensional data (blue) amounts to $V_{4D} = 0.981(8)\%$ while the corresponding value for the three-dimensional state (green) only amounts to $V_{3D} = 0.654(7)\%$ and vanishes for the two-dimensional state (red), in close correspondence with the theoretical predictions of $V_{4D,th} = 1$, $V_{3D,th} = 7/9 = 0.78$ and $V_{2D,th} = 0$ according to (3), (8) and (9). The phase difference between both coincidence count rates of $\Delta\phi = \phi_{3D} - \phi_{4D} = 1.024(2)\pi$ corresponds closely to the theoretical expected value of π. In contrast, when varying $\phi_{A,1}$ (Figs. 9c and 9d), the three-dimensional coincidence function remains constant at 1/9 of the maximal probability, while the two-dimensional coincidence count rate displays a visibility of $V_{2D} = 0.919(11)\%$, in clear correspondence with the theoretical expectations ($V_{2D,th} = 1$). Again, the phase difference $\Delta\phi = \phi_{2D} - \phi_{4D} = 1.013(2)\pi$ displays the good reproducibility of the interferometer setup. The periods of all curves show a deviation of less than ≈4% with respect to the ideal value. A contribution of accidental coincidence count rates in the range of 1% of the maximal count rates of the four-dimensional state is observed, resulting in a negligible reduction of its interference visibility. For the two-dimensional state, the count rates are reduced by a factor of four as compared to the four-dimensional state (see (9)); the same background causes a significantly lower signal/noise ratio and a higher reduction of the visibility.

A figure of merit for the suitability of the setup for preparing higher dimensional time–energy entanglement is

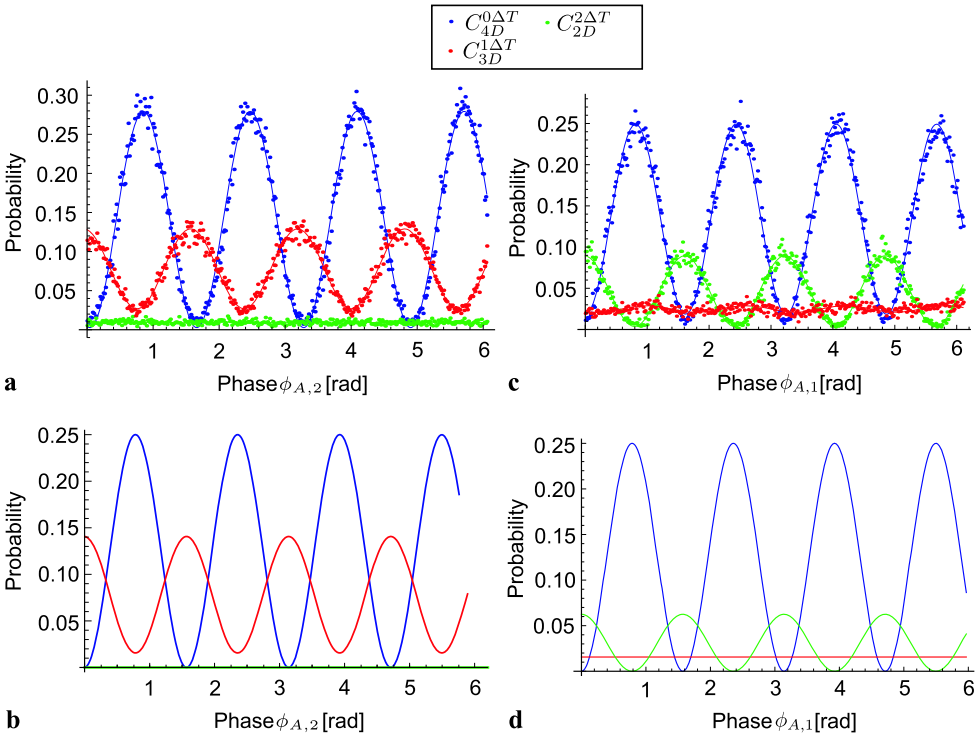

Fig. 9 Experimental and theoretical coincidence probabilities for four-dimensional, three-dimensional and two-dimensional states as a function of $\phi_{A,2}$ (**a** and **b**) and $\phi_{A,1}$ (**c** and **d**)

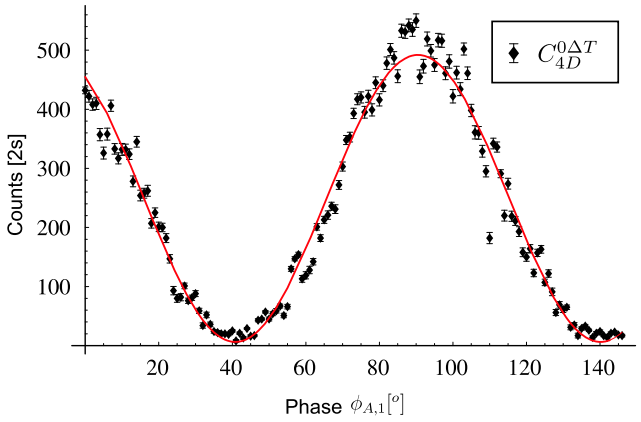

Fig. 10 Coincidence count rate of the four-dimensional entangled state scanned as a function of the phase $\phi_{A,1}$ of Alice's short interferometer

the interference visibility of the coincidence curves. Following the considerations given in [19], a Bell inequality can be defined [18], which is violated only by (2×4)-dimensional entangled states. Here the bound $I \leq 2$ can be translated into a minimal fringe visibility of $V_c = 78.4\%$ to allow a violation of local realism for the state space spanned by our interferometer system. The experimentally determined visibility (Fig. 10) of $V_{exp} = 0.975(16)\%$ surpasses the bound by 12 standard deviations, offering the potential for a violation of higher dimensional Bell inequalities [18].

4 Conclusion

We introduced an experimental scheme which is suited for the preparation and analysis of four-dimensional entangled photons. The experimental results exhibit high visibilities and are in good agreement with the described theoretical predictions, enabling the expansion of the scheme to entangled states of even higher dimensions. From the viewpoint of fundamental research, they offer the opportunity for studying the increased non-classicality of high-dimensional states as characterized by the violation of Bell tests [18, 20] or allow studies of the non-contextual nature of quantum mechanics [21–23]. With increasing dimensionality of the encoded states, the application of mutually unbiased bases allows us to increase the security bounds of quantum cryptography schemes [20] while minimizing the experimental effort for full state determination [24] with respect to standard tomographic techniques. It is thus of high relevance to utilize the benefits of the scheme demonstrated here and to further increase the dimensionality of qudit states.

Acknowledgements We would like to thank Witlef Wieczorek, Nikolai Kiesel, and Wieslaw Laskowski for helpful discussions. We acknowledge the support by the DFG-Cluster of Excellence MAP and an exchange program by DAAD.

References

1. B.P. Lanyon, M. Barbieri, M.P. Almeida, T. Jennewein, T.C. Ralph, K.J. Resch, G.J. Pryde, J.L. O'Brien, A. Gilchrist, A.G. White, Nat. Phys. **5**, 134 (2009)

Experimental Schmidt Decomposition and State Independent Entanglement Detection

Wiesław Laskowski,[1,2,3] Daniel Richart,[2,3] Christian Schwemmer,[2,3] Tomasz Paterek,[4] and Harald Weinfurter[2,3]
[1]*Institute of Theoretical Physics and Astrophysics, University of Gdańsk, PL-80-952 Gdańsk, Poland*
[2]*Max-Planck-Institut für Quantenoptik, Hans-Kopfermann-Strasse 1, D-85748 Garching, Germany*
[3]*Department für Physik, Ludwig-Maximilians-Universität, D-80797 München, Germany*
[4]*Centre for Quantum Technologies, National University of Singapore, 3 Science Drive 2, 117543 Singapore, Singapore*
(Received 17 November 2011; revised manuscript received 6 April 2012; published 11 June 2012)

We introduce an experimental procedure for the detection of quantum entanglement of an unknown quantum state with a small number of measurements. The method requires neither *a priori* knowledge of the state nor a shared reference frame between the observers and can thus be regarded as a perfectly state-independent entanglement witness. The scheme starts with local measurements, possibly supplemented with suitable filtering, which essentially establishes the Schmidt decomposition for pure states. Alternatively we develop a decision tree that reveals entanglement within few steps. These methods are illustrated and verified experimentally for various entangled states of two and three qubits.

DOI: 10.1103/PhysRevLett.108.240501 PACS numbers: 03.67.Mn, 03.65.Ta, 03.67.Bg, 42.50.Ex

Introduction.—Entanglement is the distinguishing feature of quantum mechanics and it is the most important resource for quantum information processing [1,2]. For any experiment it is thus of utmost importance to easily reveal entanglement, ideally with as little effort as possible. Common methods suffer from disadvantages. On the one hand, employing the Peres–Horodecki criterion [3,4] or evaluating entanglement measures, one can identify entanglement in arbitrary states; however, it requires full state tomography. On the other hand, various entanglement witnesses [4–10] can be determined with much fewer measurements, but they give conclusive answers only if the state under investigation is close to the witness state; i.e., they require *a priori* knowledge.

Recently, it has been shown that the existence of entanglement can be inferred from analyzing correlations among the measurement results on the subsystems of a quantum state. The properly weighted sum of correlations will overcome characteristic thresholds only if the state is entangled [11]. Here we further develop this approach to obtain a simple and practical method to detect entanglement of all pure states and some mixed states by measuring only a small number of correlations. Since the method is adaptive, it does not require *a priori* knowledge of the state nor a shared reference frame between the possibly remote observers, and thus it greatly simplifies the practical application. We describe two schemes. The first one essentially can be seen as a direct implementation of Schmidt decomposition, which identifies the maximal correlation directly. For bipartite pure systems, this approach can be divided conceptually into two stages: (i) calibration that establishes the experimental Schmidt decomposition [12,13] of a pure state by local measurements and suitable filtering and (ii) two correlation measurements to verify the entanglement criterion. The second scheme shows how to use a decision tree to obtain a rapid violation of the threshold, thereby identifying entanglement.

Entanglement criterion.—For a two-qubit quantum state ρ, Alice and Bob observe correlations between their local Pauli measurements σ_k and σ_l, respectively. They are defined as the expectation values of the product of the two measurements, $T_{kl} = \mathrm{Tr}[\rho(\sigma_k \otimes \sigma_l)]$, with the so-called correlation tensor elements $T_{kl} \in [1, -1]$. The local values T_{k0} (T_{0l}), with σ_0 being the identity operator, form the local Bloch vector of Alice (Bob). Using these measurements, a sufficient condition for entanglement can be formulated as [11,14]:

$$\sum_{k,l=x,y,z} T_{kl}^2 > 1 \Rightarrow \rho \text{ is entangled.} \tag{1}$$

For pure states this is also a necessary condition, while for mixed states care has to be taken. For mixed states, the likelihood of detecting the entanglement decreases with purity [15]. An extension of (1) can generally identify entanglement of an arbitrary mixed state, however, then losing the state independence [11,16]. Note two important facts. First, Eq. (1) can be seen as a state-independent entanglement witness, derived without any specific family of entangled states in mind. Second, to test whether the state is entangled, it is sufficient to break the threshold; i.e., it is neither required to measure all correlations nor to compute the density matrix [17]. Rather, it is now the goal to find strategies that minimize the number of correlation measurements. We show how this can be done by a particularly designed decision tree, or by identifying a Schmidt decomposition from local results and filtering when necessary.

Schmidt decomposition.—Consider pure two-qubit states. Any such state has a Schmidt decomposition

$$|\psi_S\rangle = \cos\theta|a\rangle|b\rangle + \sin\theta|a_\perp\rangle|b_\perp\rangle, \quad \theta \in \left[0, \frac{\pi}{4}\right], \tag{2}$$

where the coefficients are real and the local bases $\{|a\rangle, |a_\perp\rangle\}$ and $\{|b\rangle, |b_\perp\rangle\}$ are called the Schmidt bases. Once the bases are known, Alice constructs her local measurements $\sigma_{z'} = |a\rangle\langle a| - |a_\perp\rangle\langle a_\perp|$ and $\sigma_{y'} = i|a_\perp\rangle\langle a| - i|a\rangle\langle a_\perp|$, and so does Bob in analogy. They can now detect entanglement with only two correlation measurements because $T^2_{z'z'} + T^2_{y'y'} = 1 + \sin^2 2\theta > 1$ for all pure entangled states. Note, the laboratories are not required to share a common reference frame.

In order to extract the Schmidt bases from experimental data, one starts with local measurements, determining the local Bloch vectors $\vec{\alpha}(\vec{\beta})$ of Alice (Bob). (Those vectors are related to the correlation tensor coefficients via $\alpha_i = T_{i0}/\sqrt{T^2_{x0} + T^2_{y0} + T^2_{z0}}$.) We consider two cases. First, suppose that a pure state has nonvanishing local Bloch vectors. Their directions define the Schmidt bases of Alice and Bob up to a global phase ϕ. Writing these bases in the computational basis

$$\begin{aligned} |a\rangle &= \cos\xi_A|0\rangle + e^{i\varphi_A}\sin\xi_A|1\rangle, \\ |a_\perp\rangle &= \sin\xi_A|0\rangle - e^{i\varphi_A}\cos\xi_A|1\rangle, \\ |b\rangle &= \cos\xi_B|0\rangle + e^{i\varphi_B}\sin\xi_B|1\rangle, \\ |b_\perp\rangle &= e^{i\phi}(\sin\xi_B|0\rangle - e^{i\varphi_B}\cos\xi_B|1\rangle), \end{aligned} \tag{3}$$

we see that the required coefficients can be inferred directly from the local Bloch vectors, $\vec{\alpha} = (\sin 2\xi_A \cos\varphi_A, \sin 2\xi_A \sin\varphi_A, \cos 2\xi_A)$ on Alice's side, and similarly for Bob. The global phase of $|b_\perp\rangle$ shows up as the relative phase in the decomposition (2); i.e., $|\psi_S\rangle = \cos\theta|a\rangle|b\rangle + \sin\theta e^{i\phi}|a_\perp\rangle|\tilde{b}_\perp\rangle$ (with $|b_\perp\rangle = e^{i\phi}|\tilde{b}_\perp\rangle$). It can be determined, for example, from the T_{yy} correlation as $\cos\phi = T_{yy}/\sqrt{1 - T^2_{x0} - T^2_{y0} - T^2_{z0}}$. If Bob would use the basis $\{|b\rangle, |\tilde{b}_\perp\rangle\}$ to build his observables $\sigma_{z''}$ and $\sigma_{y''}$, the corresponding correlations $T_{y'y''} = \sin 2\theta \cos\phi$ would vanish for $\cos\phi = 0$ and the two measurements $T_{z'z''}$ and $T_{y'y''}$ would not suffice to detect entanglement. In such a case, however, the other two correlations, $T_{x'y''}$ and $T_{y'x''}$, are nonzero, and can be used to reveal entanglement. Therefore, the determination of ϕ in the calibration is not essential if one accepts possibly one more correlation measurement.

Second, in the case of vanishing local Bloch vectors, the pure state under consideration $|\psi_m\rangle$ is maximally entangled and admits infinitely many Schmidt decompositions. In order to truly prove entanglement, Bob can thus freely choose some basis, say computational basis, for which the state will now be of the form $|\psi_m\rangle = \frac{1}{\sqrt{2}} \times (|a\rangle|0\rangle + |a_\perp\rangle|1\rangle)$. The basis of Alice can be found after *filtering* by Bob in his Schmidt basis: $F = |0\rangle\langle 0| + \varepsilon|1\rangle\langle 1|$. (For an actual implementation, see the experimental section.) When Bob informs Alice that his detector behind the filter clicked, the initial state becomes

$$(\mathbb{1} \otimes F)|\psi_m\rangle \to \frac{1}{\sqrt{1+\varepsilon^2}}(|a\rangle|0\rangle + \varepsilon|a_\perp\rangle|1\rangle). \tag{4}$$

Note that, due to filtering, a nonvanishing local Bloch vector emerges for Alice. Thus, the respective Schmidt basis can be found with the method described above and used for the evaluation of $T^2_{z'z} + T^2_{y'y}$.

Decision tree.—Our second algorithm for entanglement detection does not even require calibration and also applies directly to mixed states. Alice and Bob choose three orthogonal local directions x, y, and z independently from each other and agree to only measure correlations along these directions. In Fig. 1 we show exemplarily which correlations should be measured in order to detect entanglement in a small number of steps. Starting with a measurement of T_{zz}, one continues along the solid (or dotted) arrow if the correlation is higher (or lower) than some threshold value (e.g., 1/2 in Fig. 1). The tree is based on the principle of correlation complementarity [19–22]: in quantum mechanics there exist trade-offs for the knowledge of dichotomic observables with corresponding anticommuting operators. For this reason, if the correlation $|T_{zz}|$ is big, correlations $|T_{zx}|$, $|T_{zy}|$, $|T_{xz}|$, and $|T_{yz}|$ have to be small, because their corresponding operators anticommute with the operator $\sigma_z \otimes \sigma_z$. Therefore, the next significant correlations have to lie in the xy plane of the correlation tensor, and thus the tree continues with a measurement of the T_{yy} correlation. This concept can be

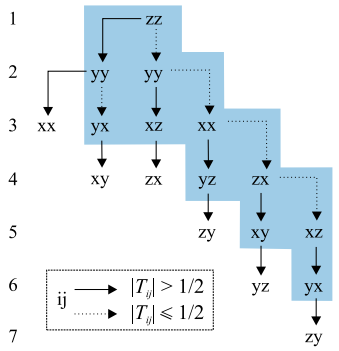

FIG. 1 (color online). The decision tree for efficient two-qubit entanglement detection. No shared reference frame is required between Alice and Bob; i.e., they choose their local x, y, z directions randomly and independently, which effectively gives rise to a basis $\{x_A, y_A, z_A\}$ for Alice and $\{x_B, y_B, z_B\}$ for Bob (not detailed in the figure or the main text). The scheme starts with measuring T_{zz} and follows at each step along the dashed arrow if the modulus of correlation is less than $\frac{1}{2}$ and otherwise along the continuous arrow. The algorithm succeeds as soon as $\sum T^2_{ij} > 1$. The measurements in the blue shaded area suffice to detect all maximally entangled pure states with Schmidt-base vectors along x,y, or z.

generalized to multiqubit states. A decision tree for three qubits is given in the Supplemental Material [15]. The number of detected states grows with the number of steps through the decision tree. Since condition (1) is similar to the purity of a state, the scheme succeeds faster the more pure a state is (see Supplemental Material [15] for detailed analysis). Varying the threshold value does not lead to any significant changes in the statistic of detected states.

Finally, we connect both methods discussed here for the analysis of multiqubit states. A numerical simulation for pure states reveals that the correlation measurement along local Bloch vectors gives correlations close to the maximal correlations in more than 80% of cases. Therefore, these local directions give an excellent starting point for the decision tree.

Experiment.—For the demonstration of these new simple analysis methods we first use two photon-polarization entangled states. In the following, we will thus replace the computational basis states by horizontal ($|0\rangle \rightarrow |H\rangle$) and vertical ($|1\rangle \rightarrow |V\rangle$) linear polarization, respectively. The photon source (Fig. 2) is based on the process of spontaneous parametric down-conversion (SPDC), using a pair of crossed type I cut β-barium-borate (BBO) crystals pumped by a cw laser diode at a wavelength of $\lambda_{\text{pump}} = 402$ nm, with linear polarization of 45°. It emits pairs of horizontally and vertically polarized photons that superpose to the state $|\Psi\rangle = \frac{1}{\sqrt{2}}(|H\rangle|H\rangle + e^{i\delta}|V\rangle|V\rangle)$ [23]. The spectral bandwidth of the photons is reduced to 5 nm using interference filters, and two spatial emission modes are selected by coupling the photon pairs into two separate single-mode fibers.

For the purpose of preparing any pure two-qubit state, the polarization of each photon can be rotated individually by a set of quarter- (QWP) and half-wave plates (HWP) in each mode. By tilting an yttrium vanadate crystal (YVO_4) in front of the BBOs, the relative phase δ among the photon pairs can be set. Additionally, the state can be made asymmetric by removing a portion of vertically polarized light in one spatial mode with a Brewster plate

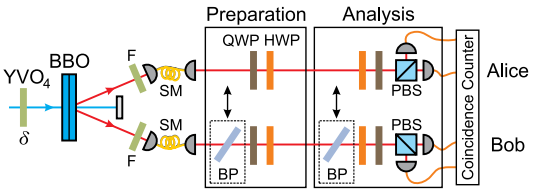

FIG. 2 (color online). Scheme of the experimental setup. The state $|\Psi\rangle = \frac{1}{\sqrt{2}}(|H\rangle|H\rangle + e^{i\delta}|V\rangle|V\rangle)$ is created by type I SPDC process. An yttrium vanadate crystal (YVO_4) is used to manipulate the phase δ of the prepared state. For preparation and analysis of the state, half- (HWP) and quarter-wave plates (QWP) are employed. Brewster plates (BP) can be introduced to make the state asymmetric and to perform the filter operation, respectively.

(BP). In the last step of the experiment, the polarization of each photon is analyzed with additional quarter- and half-wave plates and projection on $|H\rangle$ and $|V\rangle$ using a polarizing beam splitter (PBS). The local filtering of a maximally entangled state can be accomplished by placing a Brewster plate in front of the analysis wave plates. This Brewster plate reflects with a certain probability vertically polarized photons and, together with detection of a photon behind the Brewster plate, implements the filtering operation (4). Finally, the photons are detected by fiber-coupled single-photon detectors connected to a coincidence logic.

Experimental Schmidt decomposition.—Let us consider the state shown in Fig. 3(a). The protocol starts with Alice and Bob locally measuring the polarization of the photons, enabling them to individually determine the local Bloch vectors. For high efficiencies, which are possible in experiments with atoms or ions, the local measurements can indeed be done independently [24]. If nonvanishing local Bloch vectors can be identified, one can proceed to the next

a) Initial state

A \ B	1	X	Y	Z
1		-0.042	0.025	0.127
X	0.093	0.028	-0.773	0.523
Y	-0.007	-0.922	0.018	0.029
Z	0.173	0.006	0.514	0.768

b) Filtering

A \ B	1	X	Y	Z
1		0.000	0.040	0.334
X	0.188	0.008	-0.707	0.526
Y	-0.034	-0.849	0.088	-0.039
Z	0.336	-0.012	0.491	0.817

c) Schmidt decompostion

A \ B	1	X´	Y´	Z´
1		0.038	0.079	0.119
X´	0.060	0.930	-0.186	-0.093
Y´	-0.094	-0.145	-0.864	0.144
Z´	0.172	0.116	0.141	0.922

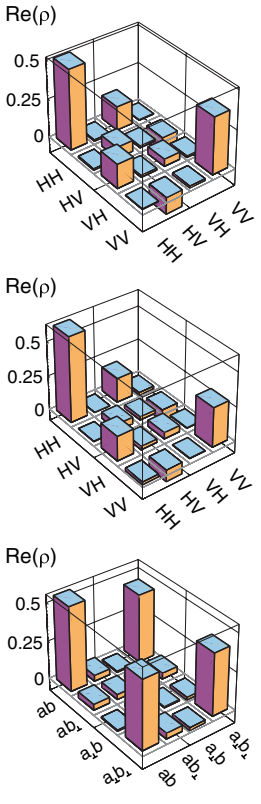

FIG. 3 (color online). Demonstration of Schmidt decomposition of a maximally entangled state prepared in unknown bases. The correlation tensor and corresponding density matrix are depicted for (a) the unknown state, (b) the state after applying local filtering, and (c) the state analyzed in the Schmidt bases. It is important to note that only the blue shaded elements of the correlation tensors will be measured, as this suffices to prove entanglement. The full correlation tensors and the corresponding states are only shown for completeness and didactic reasons.

step. For the example here, the local expectation values are close to zero and filtering has to be applied. By using a Brewster plate in front of Bob's analysis wave plate, local Bloch vectors emerge as long as the filtering operation is successful [Fig. 3(b)] [25]. In this case, we obtain $T_{0l} = (0.000, 0.040, 0.334)$ and $T_{k0} = (0.188, -0.034, 0.336)$.

In the next step, Alice and Bob use their local Bloch vectors to realign their analyzers to the new local Schmidt bases $\{|a\rangle, |a_\perp\rangle\}$ and $\{|b\rangle, |\tilde{b}_\perp\rangle\}$, respectively. This process diagonalizes the correlation tensor, as depicted in Fig. 3(c). Therefore, it is only necessary to measure $T_{z'z''} = 0.922 \pm 0.015$ and $T_{y'y''} = -0.864 \pm 0.015$ to prove entanglement, since $T^2_{z'z''} + T^2_{y'y''} = 1.597 \pm 0.038 > 1$. Hence, 2×3 *local* measurements are needed in the first step of the algorithm, three combined measurements are needed for filtering if necessary, and finally only two correlation measurements have to be performed for entanglement detection.

Application of the decision tree.—In order to demonstrate the application of the decision tree, we will apply it to three states. For the first state $\frac{1}{\sqrt{2}}(|H\rangle|H\rangle + |V\rangle|V\rangle)$, whose correlation tensor is depicted in Fig. 4(a), the decision tree (Fig. 1) starts with the measurement of the correlation $T_{zz} = 0.980 \pm 0.015$ and continues with $T_{yy} = -0.949 \pm 0.015$. These two measurements already prove entanglement since $T^2_{zz} + T^2_{yy} = 1.869 \pm 0.041 > 1$. For a second state, $\frac{1}{\sqrt{2}}(|R\rangle|R\rangle + i|L\rangle|L\rangle)$, we obtain a correlation of $T_{zz} = -0.056 \pm 0.015$, close to zero [Fig. 4(b)]. Consequently, the next steps according to our algorithm (Fig. 1) are to determine the correlation $T_{yy} = 0.978 \pm 0.015$, followed by $T_{xz} = -0.959 \pm 0.015$, with their squares adding up to a value of $1.879 \pm 0.041 > 1$ and hence proving entanglement. As a last example, we consider the initial state of Fig. 3. According to our decision tree, we need to measure $T_{zz} = 0.768 \pm 0.015$, $T_{yy} = 0.018 \pm 0.015$, and $T_{yx} = -0.922 \pm 0.015$, thus giving a value of $1.440 \pm 0.036 > 1$ and proving entanglement with only three steps.

a) HH+VV

A \ B	1	X	Y	Z
1	-0.114	0.024	0.051	
X	-0.101	0.969	-0.023	0.059
Y	-0.023	-0.013	-0.949	-0.061
Z	0.071	-0.073	-0.008	0.984

b) RR+iLL

A \ B	1	X	Y	Z
1	0.028	0.005	-0.057	
X	0.044	-0.017	-0.110	-0.959
Y	0.022	-0.014	0.978	-0.067
Z	-0.018	-0.954	-0.036	-0.056

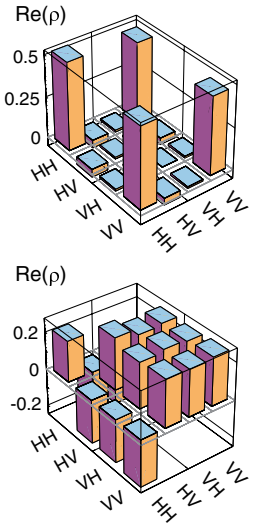

FIG. 4 (color online). Correlation tensors and density matrices of the experimental realization of two different states. The imaginary parts of the density matrices are negligible and therefore skipped. Using the decision tree, only the blue shaded correlations have to be measured for detecting entanglement. The errors of the correlations are <0.015 for (a) and <0.023 for (b).

Many qubits.—For the demonstration of multiqubit entanglement detection, we use two three-photon, polarization-entangled states: the W state [26] and the G state [27] (Fig. 5). In order to observe these states, a collinear type II SPDC source is used together with a linear setup to prepare the four-photon Dicke state $D^{(2)}_4$ [28,29]. Once the first photon is measured to be vertically polarized, the other three photons are projected into the W state. Similarly, the three-photon G state is obtained if the first photon is measured to be $+45°$ polarized.

The protocol for entanglement detection starts with observers locally measuring the polarization of the photons, enabling them to individually determine the local Bloch vectors. For the G state we obtain $T_{i00} = (0.636, -0.008, -0.015)$, $T_{0j0} = (0.623, -0.092, 0.010)$, and $T_{00k} = (0.636, 0.070, 0.022)$. The local Bloch vectors suggest that the correlation T_{xxx} is big. Therefore, the decision tree starts with the measurement of $T_{xxx} = 0.904 \pm 0.025$ and continues with $T_{xzz} = -0.578 \pm 0.025$ (see Fig. 2 in the Supplemental Material [15]). These two measurements already prove entanglement because $T^2_{xxx} + T^2_{xzz} = 1.152 \pm 0.038 > 1$. For the W state, the local Bloch vectors $T_{i00} = (0.016, -0.070, 0.318)$, $T_{0j0} = (-0.010, -0.073, 0.308)$, and $T_{00k} = (-0.011, -0.0547, 0.319)$ suggest that now the correlation T_{zzz} is big. Indeed, we observe $T_{zzz} = -0.882 \pm 0.025$. The decision tree is the same as above but with local axes renamed as follows: $x \to z \to y \to x$. Therefore, the second measurement has to be T_{zyy}. With $T_{zyy} = 0.571 \pm 0.025$, we again prove entanglement as $T^2_{xxx} + T^2_{zyy} = 1.104 \pm 0.037 > 1$.

Conclusions.—We discussed and experimentally implemented two methods for fast entanglement detection for states about which we have no *a priori* knowledge. They are well suited for quantum communication schemes as the parties do not have to share a common reference frame, making the scheme insensitive to a rotation of the qubits during their transmission to the distant laboratories.

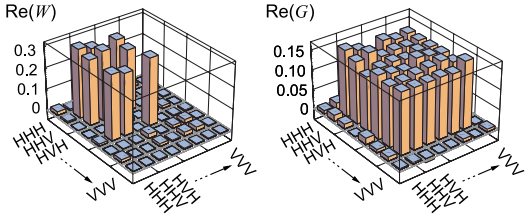

FIG. 5 (color online). Density matrices of the experimental realization of the G and W state. The corresponding fidelities are equal to 92.23% and 89.84%.

The two methods use a particularly simple and practical entanglement identifier [11]. One of them can be seen as experimental Schmidt decomposition and the other establishes a sequence of correlation measurements, leading to entanglement detection in a small number of steps.

We thank M. Żukowski for stimulating discussions. This work is supported by the EU project QESSENCE, the DAAD/MNiSW, the DFG-Cluster of Excellence MAP, and by the National Research Foundation and Ministry of Education in Singapore. W. L. is supported by the MNiSW Grant No. N202 208538 and by the Foundation for Polish Science. CS thanks QCCC of the Elite Network of Bavaria for support.

[1] M. A. Nielsen and I. Chuang, *Quantum Computation and Quantum Information* (Cambridge University Press, Cambridge, 2000).
[2] R. Horodecki, P. Horodecki, M. Horodecki, and K. Horodecki, Rev. Mod. Phys. **81**, 865 (2009).
[3] A. Peres, Phys. Rev. Lett. **77**, 1413 (1996).
[4] M. Horodecki, P. Horodecki, and R. Horodecki, Phys. Lett. A **223**, 1 (1996).
[5] M. Bourennane, M. Eibl, C. Kurtsiefer, S. Gaertner, H. Weinfurter, O. Gühne, P. Hyllus, D. Bruß, M. Lewenstein, and A. Sanpera, Phys. Rev. Lett. **92**, 087902 (2004).
[6] B. M. Terhal, Phys. Lett. A **271**, 319 (2000).
[7] M. Lewenstein, B. Kraus, J. I. Cirac, and P. Horodecki, Phys. Rev. A **62**, 052310 (2000).
[8] D. Bruss, J. I. Cirac, P. Horodecki, F. Hulpke, B. Kraus, M. Lewenstein, and A. Sanpera, J. Mod. Opt. **49**, 1399 (2002).
[9] O. Gühne and P. Hyllus, Int. J. Theor. Phys. **42**, 1001 (2003).
[10] O. Gühne and G. Toth, Phys. Rep. **474**, 1 (2009).
[11] P. Badziąg, Č. Brukner, W. Laskowski, T. Paterek, and M. Żukowski, Phys. Rev. Lett. **100**, 140403 (2008).
[12] E. Schmidt, Math. Ann. **63**, 433 (1907).
[13] A. Peres, *Quantum Theory: Concepts and Methods* (Kluwer Academic, Dordrecht, 1995).
[14] R. Horodecki, P. Horodecki, and M. Horodecki, Phys. Lett. A **210**, 377 (1996).
[15] See Supplemental Material at http://link.aps.org/supplemental/10.1103/PhysRevLett.108.240501 for more details on the efficiency of the method based on the decision tree for pure and mixed states of two qubits and an algorithm that constructs the tree for many qubits.
[16] W. Laskowski, M. Markiewicz, T. Paterek, and M. Żukowski, Phys. Rev. A **84**, 062305 (2011).
[17] Although the effort to evaluate (1) generally scales as the one for full state tomography, we can directly evaluate the criterion from raw data without any further numerics required to reconstruct a physical density matrix [18].
[18] D. F. V. James, P. G. Kwiat, W. J. Munro, and A. G. White, Phys. Rev. A **64**, 052312 (2001).
[19] P. Kurzyński, T. Paterek, R. Ramanathan, W. Laskowski, and D. Kaszlikowski, Phys. Rev. Lett. **106**, 180402 (2011).
[20] G. Toth and O. Gühne, Phys. Rev. A **72**, 022340 (2005).
[21] S. Wehner and A. Winter, J. Math. Phys. (N.Y.) **49**, 062105 (2008).
[22] S. Wehner and A. Winter, New J. Phys. **12**, 025009 (2010).
[23] P. G. Kwiat, E. Waks, A. G. White, I. Appelbaum, and P. H. Eberhard, Phys. Rev. A **60**, R773 (1999).
[24] Due to the low efficiency of the SPDC setup we have to use coincidence counts here. Using only the single counts, the local Bloch vector of Alice is slightly different. In this example we obtain $T_{0l} = (-0.073, -0.091, -0.059)$ and $T_{k0} = (0.031, 0.041, 0.037)$.
[25] This in consequence means, that for the filtering Alice and Bob have to communicate with each other and hence this measurement is *not* local.
[26] $|W\rangle = (|HHV\rangle + |HVH\rangle + |VHH\rangle)/\sqrt{3}$; W. Dür, G. Vidal, and J. I. Cirac, Phys. Rev. A **62**, 062314 (2000).
[27] $|G\rangle = (|W\rangle + |\bar{W}\rangle)/\sqrt{2}$, where $|\bar{W}\rangle = (|VVH\rangle + |HVV\rangle + |VHV\rangle)/\sqrt{3}$; A. Sen(De), U. Sen, and M. Żukowski, Phys. Rev. A **68**, 032309 (2003).
[28] $|D_4^{(2)}\rangle = (|HHVV\rangle + |HVHV\rangle + |VHHV\rangle + |HVVH\rangle + |VHVH\rangle + |VVHH\rangle)/\sqrt{6}$; R. Krischek, C. Schwemmer, W. Wieczorek, H. Weinfurter, P. Hyllus, L. Pezze, and A. Smerzi, Phys. Rev. Lett. **107**, 080504 (2011).
[29] N. Kiesel, C. Schmid, G. Toth, E. Solano, and H. Weinfurter, Phys. Rev. Lett. **98**, 063604 (2007).

Experimental qu$d$it entanglement detection using the time-energy degree of freedom (Draft version)

Daniel Richart,[1,2] Wiesław Laskowski,[3,1,2] Yvo Fischer,[1,2] and Harald Weinfurter[1,2]

[1] *Max-Planck-Institut für Quantenoptik, Hans-Kopfermann-Strasse 1, D-85748 Garching, Germany*
[2] *Department für Physik, Ludwig-Maximilians-Universität, D-80797 München, Germany*
[3] *Institute of Theoretical Physics and Astrophysics, University of Gdańsk, PL-80-952 Gdańsk, Poland*

We present experimental results on the preparation and detection of entangled two-photon qu$d$it states including scenarios in which no information about each qu$d$it reference frame is shared. The used scheme is scalable for dimensions of $d \leq 8$ and is suitable for the long distance transmission of entangled states.

PACS numbers: 03.67.Mn

Introduction— Pioneering efforts in the field of Quantum Information Processing and Communication such as Quantum Computation, Teleportation and Crytography had been restricted to physical systems defined in a 2 dimensional Hilbert space. As a matter of fact however, physical quantum systems as defined for atomic states, are intrinsically encoded in qu$d$it, i.e. d-level states. Therefore, in order to harness their full potential for quantum information processes, it is necessary to charaterize scalable schemes for their preparation and to define appropriate measures to characterize their entanglement. Research on their properties revealed that qu$d$it states offer significant advantages with respect to qubit states: Schemes of superdense coding [1] have enabled to increase the information density usable for quantum communication tasks while studies on the security of QKD schemes have demonstrated the lower error susceptibility for protocols based on qu$d$it states [2, 3]. Critical to quantum communication purposes is the lower critical detection efficiency required to close the detection loophole [4]. Similarly, quantum computation schemes based on qu$d$its require a lower number of physical information carriers with respect to qubit states in order to implement any arbitrary gate [5].

Schemes for the realization of qu$d$its have been experimentally realized using superconducting circuits [6], the orbital angular momentum [7, 8] of photon pairs or the entanglement in several degrees of freedom to create hyperentangled states [9, 10]. So far, an important drawback for their application for long distance quantum crytography is the rotation of their polarization state and the requirement of an adaptive optics compensation scheme in order to compensate for a rotation in the angular momentum and the polarization [11].

An alternative scheme not affected by these restrictions is to use time- energy [12] encoding into the relative detection times of two-photon pairs in order to create d dimensional bipartite entangled states [13]. In contrast to previous implementations [14, 15] limited by the linear increase in the dimension with the number of linear optical components, here we resort to a scheme scaling exponentially, as described in more detail in [16].

This paper provides a description of the experimental scheme used to create scalable qu$d$it states and presents methods for their characterization. Concretely, we present results on an entanglement [17] and a combined entanglement and dimensional witness [18, 19] used respectively to charaterize the entanglement and to determine the dimension of the states prepared. Similar approaches based on the definition of device independent inequalities were derived and experimentally verified in [20, 21].

Experimental Scheme— In the scheme depicted in Fig. 1. the emission times 0,...,7 of a pump photon are taken into detailed study. At any of these times the photon can undergo the process of spontaneous parametric downconversion (SPDC) such that a photon pair can be created with equal probability. Indeed, a continuous superposition of two-photon emission times can be defined within the coherence time of the pump photon, but the effective dimensionality of the analyzed states will depend only on the number of modes coupling to the the analyzers the two parties, Alice and Bob, are provided with. By making use of a series of unbalanced interferometers they can implement different delays of ΔT, $2\Delta T$ and $4\Delta T$ and a relative phase shift ϕ_1, ϕ_2 and ϕ_3 depending on the path taken by their respective photon at each interferometer loop. Depending on the number of time delays acquired by the respective photons, the states can be spanned by an up to 8 dimensional basis defined by the eight time delays $|0\rangle$, $|1\rangle$,...,$|7\rangle$ in units of ΔT.

Both parties place single photon detectors at the outputs + and − of their respective interferometer systems and perform coincidence measurements. They observe a distribution of the coincidences along 15 different time windows (see Fig. 2). Under the condition the time delays acquired by each party overlap within the photon's coherence time, 8 two-photon probabilities superpose to a state in the time window $0\Delta T$, while the number of superposing two-photon states decreases with the separation from the central time window. Depending on the time window chosen, the Hilbert space spanned by the

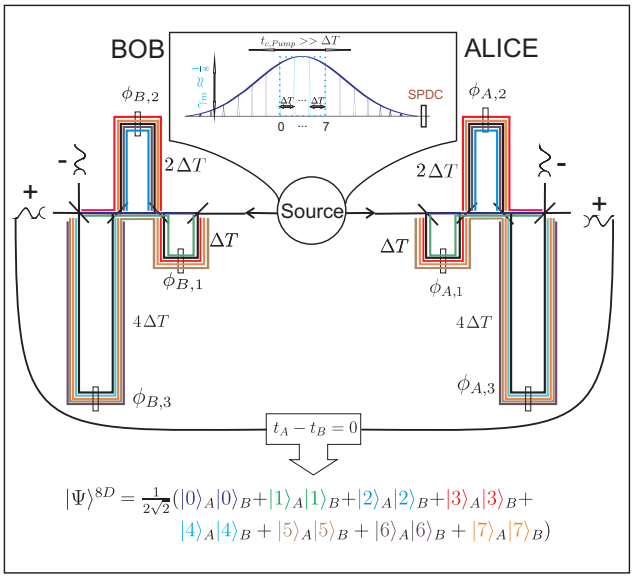

Figure 1. Experimental scheme used to observe time-energy entangled two-photon states in a 8 dimensional Hilbert space. Both parties, Alice and Bob, each share a photon of a qu$d$it entangled state created by spontaneous parametric downconversion (SPDC) using a periodically poled KTP crystal. Entangled qu$d$it two-photon states encoded in the time degree of freedom are created with a Schmidt number inherently limited by the coherence time of the pump photon source. They are analyzed by a triple loop interferometer configuration implementing the time delays ΔT, $2\Delta T$ and $4\Delta T$. A coincidence measurement between the detectors placed at their respective outputs corresponds to a projection to a superposition state of 8 two-photon detection times $|0\rangle_A|0\rangle_B$, $|1\rangle_A|1\rangle_B$,..., and $|7\rangle_A|7\rangle_B$.

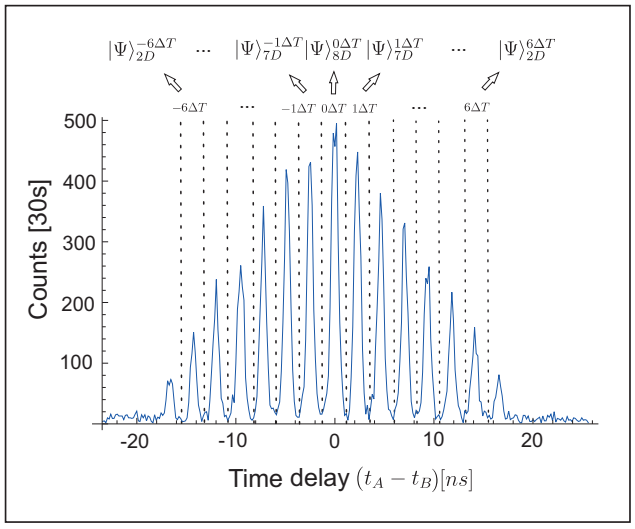

Figure 2. Distribution of the coincidence counts into 15 different time windows in dependence of Alice's and Bob's relative photon detection times. A projection onto states of different dimension d is performed if both parties agree to perform their time-delay measurements on a specific time delay. For example, for a time delay of 0, $\pm\Delta T$ and $\pm 2\Delta T$ they analyze a 2x8d, 2x7d down to 2x1 dimensional entangled two-photon state, respectively.

two-photon states is therefore 2×8, 2×7, 2×6 and down to 2×1 dimensional respectively. The states can be written as the maximally entangled states

$$|\Psi\rangle_d = \frac{1}{\sqrt{d}} \sum_{k=0}^{d-1} (|k\rangle_A |k\rangle_B). \tag{1}$$

It is important to note, that no variations in the single photon probabilities are observed as a function of the interferometer phases due to interference of photons with themselves, as the time delay introduced surpasses the coherence time of the photons by many orders of magnitude.

Entanglement detection— A Bell type inequality suited for proving entanglement of states defined in higher dimensional Hilbert spaces was defined in [17] (CGLMP inequality). It can be used to detect entanglement, as long as its classical bounds $I_d \leq 2$ defined for any local hidden variable theory for $d \geq 2$ are surpassed. For that purpose, appropriate preparation bases have to be chosen for the bipartite qu$d$it entangled states as encoded in this work. In this work, we choose one set of maximally unbiased bases (MUBs) [22], which can be prepared by choosing suited offset phase settings $\phi^{O,s}_{A_i}$ and $\phi^{O,t}_{B_i}$ used by both parties to define their d different measurement results:

$$|a^s\rangle_A = \frac{1}{\sqrt{d}} \sum_{m=0}^{d-1} e^{(i\frac{k}{d}(\phi^k_{A_i} + \phi^{O,s}_{A_i}))} |m\rangle_A \tag{2}$$

$$|b^t\rangle_B = \frac{1}{\sqrt{d}} \sum_{n=0}^{d-1} e^{(i\frac{k}{d}(\phi^l_{B_j} + \phi^{O,t}_{B_j}))} |n\rangle_B \tag{3}$$

Both parties require to choose between 2 analysis phase settings $\{\phi^k_{A,1}, \phi^k_{A,2}\}$ and $\{\phi^l_{B,1}, \phi^l_{B,2}\}$ for $k, l \in [0, 1]$. A coincidence measurement on the $8d$ state corresponds to the measurement of

$$\begin{aligned} C_{k,l,s,t} = Tr[\rho_{8d}.(|a^s\rangle \otimes |b^t\rangle)(\langle a^s| \otimes \langle b^t|)] = \\ \cos\left(\phi^k_{A_1} + \phi^l_{B_1} + \phi^{O,s}_{A_1} + \phi^{O,t}_{B_1}\right)^2 \\ \times \cos\left(\phi^k_{A_2} + \phi^l_{B_2} + \phi^{O,s}_{A_2} + \phi^{O,t}_{B_2}\right)^2 \\ \times \cos\left(\phi^k_{A_3} + \phi^l_{B_3} + \phi^{O,s}_{A_3} + \phi^{O,t}_{B_3}\right)^2 \end{aligned} \tag{4}$$

In order to determine the analysis angles required to surpass the bound $I_d \geq 2$ for all d dimensional states defined in (1), a numerical optimization over all

analysis angles is applied. For the 2x8d state and a 8d preparation basis the bound is $I^8_{8,QM} \approx 2.473 > 2$, while for the test of an inequality for 7dimensions on the 8d state reveals a violation of $I^8_{7,QM} \approx 2.715 > 2$. Similarly, $I^5_{5,QM} \approx 2.62 > 2$ is obtained for the encoded 5d state, while no violation of the corresponding inequalities $I^7_{7,QM} = 1.895 < 2$ and $I^6_{6,QM} = 1.524 < 2$ was found when applied on the 2x7 and 2x6 dimensional states. Finally, for 2x4d, 2x3d and 2x2d states, a violation of $I^4_{4,QM} \approx 2.552 > 2$, $I^3_{3,QM} \approx 2.87 > 2$ can be defined for the encoded 4 and 3d states. For the 2x2d the bound $I^{2d}_{2,QM} = 2 \cdot \sqrt{2} > 2$ obtained is equivalent to the bound given by the CHSH inequality [23].
It is to note that a higher maximal violation (see Fig. 4) and, respectively, the violation of the inequalities for the 7 and 6 dimensional states, requires the addition of independent analyzer phases such that their number equal each photon's state dimension. This requirement can be met by resorting to time-bin encoding as described in [13, 16].

Experimental Results—The evaluation of the CGLMP inequality terms $I_d \geq 2$ for d dimensional states requires the measurement of $4d^2$ coincidence probabilities. For experimentally observed count rates of up to $\approx 200 - 300/s$ for a postselection window of 164ps for the 2x8 dimensional state, an integration time of 3s is sufficient. We observe the violation of the bounds as $I^{Exp}_8 = 2.191 \pm 0.02$, $I^{Exp}_7 = 2.28 \pm 0.015$, $I^{Exp}_5 = 2.072 \pm 0.037$, $I^{Exp}_4 = 2.244 \pm 0.042$, $I^{Exp}_3 = 2.29 \pm 0.028$ and $I_2 = 2.448 \pm 0.055$ with good statistical relevance. This certifies that entangled states defined in Hilbert spaces of up to 8 are observed.

Dimensional witness— Crucial for many quantum information tasks is not only the determination of entanglement, but the determination of the dimension of unknown states, as it is critical in order to choose the optimal quantum communication protocol and to determine the tolerable error rates. In this scenario, the approach followed in [19, 24] is useful as it allows to determine the Shannon dimension of bipartite entangled states.Here, the Shannon dimension describes a bound for the dimension of the Hilbert space the analysis devices have access to. In this work, the analysis tests the coherence between a specific number of two-photon emission-time modes out of the continuous range of modes emitted by the source, superposing to the entangled state

$$|\Psi\rangle = \int_{-\infty}^{\infty} c_i(t) c_j(t) |i(t)\rangle_A |j(t)\rangle_B dt. \tag{5}$$

Here, the emission time modes $|i(t)\rangle_A$ and $|j(t)\rangle_B$ are associated to the photons distributed to either Alice's or Bob's analysis devices and the two-photon amplitude $A(t)$ is described by the function $A(t) = c_i(t)c_j(t)$. Its

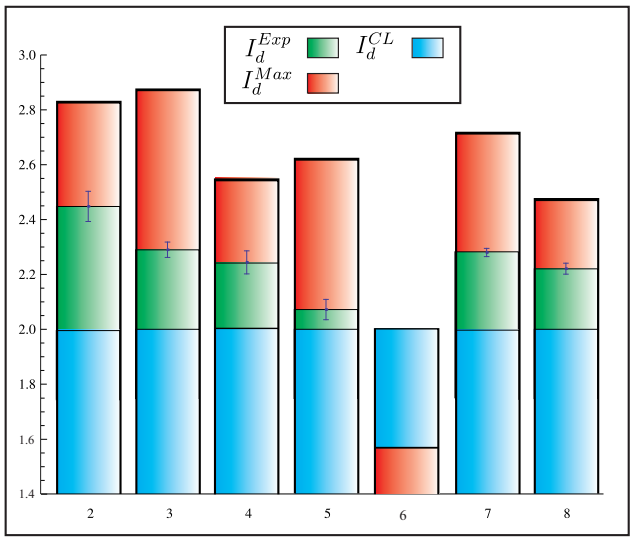

Figure 3. Experimental results for the evaluation of the CGLMP inequality parameter I_d. The experimentally determined values I_d^{Exp} surpass the classical bound $I_d^{CL} \geq 2$ and are limited by the maximally determined bounds I_d^{Max} for the states prepared, except for a test of the inequality for 6 dimensions.

FWHM distribution is restricted by the coherence time of the pump photon, and restricts the applicability of the scheme to the case that the maximal time delays analyzed doesn't surpass this bound.
The used analyzers consist of unbalanced interferometers coupling to the emission-time modes of the photons with the respective weights $\gamma_i = |\lambda_i|^2$. They project them onto the states $|i\rangle_A = |i\Delta T\rangle_A$ and $|j\rangle_B = |j\Delta T\rangle_B$ at Alice's and Bob's location, as a function of the applied time delays ΔT. This leads to the definition of the operators applied by the analysis devices of either party, Alice and Bob, as

$$|A(\phi_{A_i})\rangle = \sum_{i=0}^{d-1} e^{i\phi_{A_i}} \lambda_i |i\rangle_A \tag{6}$$

and

$$|B(\phi_{B_j})\rangle = \sum_{j=0}^{d-1} e^{i\phi_{B_j}} \lambda_j |j\rangle_B. \tag{7}$$

Depending on the postselection time window chosen for the analysis of the two-photon states, the coherence between a different number of two-photon modes is tested. Both parties are now able to detect the two-photon Shannon dimension of each state by resorting to its definition as

$$D = \frac{1}{\sum_i^{d-1} |\gamma_i|^2}, \tag{8}$$

depending only on the two-photon coupling strengths $\gamma_i = |\lambda_i|^2$.
As shown first with the example of a 2x2 dimensional state, its evaluation can be reduced by calculating the coincidence probabilities

$$P(\phi_{A_i}, \phi_{B_j}) = |\langle A(\phi_{A_i})| \otimes \langle B(\phi_{B_j})|\Psi\rangle|^2, \quad (9)$$

leading to

$$P(\phi_{A_i}, \phi_{B_j}) = |\sum_{i,j=0}^{d-1} \lambda_i \lambda_j c_i c_j e^{-i(\phi_{A_i}+\phi_{B_j})}|^2. \quad (10)$$

Here, the evaluation is simplified for the maximally entangled states the witness is optimized for, for which the summation indices are equalized ($c_i = c_j$), while a similar condition $\lambda_i = \lambda_j$ is ensured by choosing interferometer arms with equal coupling to the respective time modes. Deviations from these conditions lead to a reduction in the detected two-photon dimensions.
Finally, the two-photon dimension can be determined by performing the integral over the coincidence probability over all phases the used analysis has access to. This can be derived by observing that

$$\begin{gathered}\int_0^{2\pi} P(\phi_{A_1}, \phi_{B_1}) d\phi_{A_1} d\phi_{B_1} = \\ \int_0^{2\pi} |\sum_{i=0}^{1} |c_i|^2 |\lambda_i|^2 e^{-i(\phi_{A_1}+\phi_{B_i})}|^2 d\phi_{A_1} d\phi_{B_1} = \\ \int_0^{2\pi} ||c_0|^2|\lambda_0|^2 + e^{-i(\phi_{A_1}+\phi_{B_1})}|c_1|^2|\lambda_1|^2|^2 d\phi_{A_1} d\phi_{B_1} = \\ \sum_{i=0}^{1} |\gamma_i|^2 \cdot P_{max} (2\pi)^2, \end{gathered} \quad (11)$$

which combined with Eq. 8 allows to represent the Shannon dimension as a function of

$$D = \frac{1}{\sum_{i=0}^{1} |\gamma_i|^2} = \frac{(2\pi)^2 P_{max}}{\int_0^{2\pi} P(\phi_{A_1}, \phi_{B_1}) d\phi_{A_1} d\phi_{B_1}}. \quad (12)$$

In this notation, the maximal two-photon probability $P_{max} = |A_i|^2 = |c_i c_i|^2$ was introduced.
The scheme can be expanded for the determination of the Shannon dimension of the different prepared states, with the difference that it requires the evaluation of the additional interferometer phases the corresponding probabilities depend on. The definition of the Shannon dimension is therefore generalized to

$$D = \frac{(2\pi)^N P_{max}}{\int_0^{2\pi} P(\phi_{A_1}, ..., \phi_{B_{\frac{N}{2}}}) d\phi_{A_1} \cdots d\phi_{B_{\frac{N}{2}}}}. \quad (13)$$

Experimental Evaluation— In order to evaluate the integral over all phase settings the analysis devices depends on experimentally determined probabilities, each phase is scanned at 4 different values $\{0 = 2\pi, \pi/2, \pi$ and $3\pi/2\}$. For the evaluation of the dimensional witness for the 2x8 dimensional state, whose full analysis depends on 6 phases, up to $4^6 = 4096$ different measurements are performed, while this number is reduced to 256 and 16 for the 2x4 and 2x2 dimensional states, respectively. Again, a choice of integration times of 3s and a postselection window of 164ps is sufficient to obtain results with sufficient statistics. Finally, the detected Shannon dimension is calculated by integrating over the fitted probability functions derived from the experimental data.
The experimentally obtained values are summarized in the following table:

State	Shannon Dimension D
2x8	$7.33 \pm 0.063 > 7$
2x7	$6.42 \pm 0.076 > 6$
2x6	$5.16 \pm 0.087 > 5$
2x5	$4.201 \pm 0.045 > 4$
2x4	$3.54 \pm 0.108 > 3$
2x3	$2.416 \pm 0.057 > 2$
2x2	$1.686 \pm 0.147 > 1$

It describes, that for all experimentally prepared two-photon states a Shannon dimension higher than the next lower dimension is detected. This allows to certify the suitability of the Shannon dimensional witness for energy-time entangled states.
Conclusions—We have demonstrated the experimental application of entanglement and dimension witnesses on a scalable source for entangled higher dimensional qu$d$it states of dimension up to 2x8. This proves the suitability of the scheme for further applications of quantum communication and computation tasks, as proposed and experimentally demonstrated for bipartite states in [25] and [26]. In this work, the encoding into the emission-time degree of freedom offers important advantages with respect to the implementation of long distance quantum communication scenarios: The encoded state is not sensitive to polarization mode dispersion nor to deformations of the spatial mode. Also, the tested scheme offers promising alternatives to address the limited scalability of similar methods using photonic entanglement, such as multi-photon entangled states, which are affected by orders of magnitude lower detection efficiencies.
This work is supported by the DFG-Cluster of Excellence MAP and the DAAD/MNiSW project.

[1] J. T. Barreiro, T.-C. Wei, and P. G. Kwiat, Nature Physics **4**, 282 (2008).
[2] G. M. Nikolopoulos and G. Alber, Physical Review A

(Atomic, Molecular, and Optical Physics) **72**, 032320 (2005).
[3] D. Kaszlikowski, P. Gnaciski, M. Zukowski, W. Miklaszewski, and A. Zeilinger, Phys. Rev. Lett. **85**, 4418 (2000).
[4] T. Vértesi, S. Pironio, and N. Brunner, Phys. Rev. Lett. **104**, 060401 (2010).
[5] B. P. Lanyon, M. Barbieri, M. P. Almeida, T. Jennewein, T. C. Ralph, K. J. Resch, G. J. Pryde, J. L. OBrien, A. Gilchrist, and A. G. White, Nature Physics **5**, 134 (2009).
[6] M. Neeley, M. Ansmann, R. C. Bialczaka, M. Hofheinz, E. Lucero, A. D. O'Connell, D. Sank, H. Wang, J. Wenner, A. N. Cleland, M. R. Geller, and J. M. Martinis, Science **325**, 722 (2009).
[7] A. Mair, A. Vaziri, and A. Zeilinger, Nature **412**, 313 (2001).
[8] A. Dada, J. Lesch, G. Buller, M. J. Padgett, and E. Andersson, Nature Physics **7**, 677 (2011).
[9] J. T. Barreiro, N. K. Langford, N. A. Peters, and P. G. Kwiat, Physical Review Letters **95**, 260501 (2005).
[10] G. Vallone, G. Donati, N. Bruno, A. Chiuri, and P. Mataloni, Phys. Rev. A **81**, 050302 (2010).
[11] B.-J. Pors, C. Monken, E. Eliel, and J. Woerdman, Optics Express **19**, 6671 (2011).
[12] J. D. Franson, Phys. Rev. Lett. **62**, 2205 (1989).
[13] I. Marcikic, H. de Riedmatten, W. Tittel, H. Zbinden, M. Legré, and N. Gisin, Phys. Rev. Lett. **93**, 180502 (2004).
[14] M. Zukowski, A. Zeilinger, and M. A. Horne, Phys. Rev. A **55**, 2564 (1997).
[15] R. T. Thew, A. Acin, H. Zbinden, and N. Gisin, Physical Review Letters **93**, 010503 (2004).
[16] D. Richart, Y. Fischer, and H. Weinfurter, Applied Physics B **106**, 543 (2012).
[17] D. Collins, N. Gisin, N. Linden, S. Massar, and Popescu, Phys. Rev. Lett. **88**, 040404 (2002).
[18] P. Badzia, C. Brukner, W. Laskowski, T. Paterek, and M. Zukowski, Phys. Rev. Lett. **100**, 140403 (2008).
[19] J. B. Pors, S. S. R. Oemrawsingh, A. Aiello, M. P. van Exter, E. R. Eliel, G. W. 't Hooft, and J. P. Woerdman, Phys. Rev. Lett. **101**, 120502 (2008).
[20] N. Brunner, S. Pironio, A. Acin, N. Gisin, A. A. Méthot, and V. Scarani, Phys. Rev. Lett. **100**, 210503 (2008).
[21] M. Hendrych, R. Gallego, M. Micuda, N. Brunner, A. Acin, and J. P. Torres, Nature Physics **8**, 588591 (2012).
[22] M. Wiesniak, T. Paterek, and A. Zeilinger, New Journal of Physics **13**, 053047 (2011).
[23] J. F. Clauser and M. A. Horne, Phys. Rev. D **10**, 526 (1974).
[24] B.-J. Pors, F. Miatto, G. W. t Hooft, E. R. Eliel, and J. P. Woerdman, Journal of Optics **13**, 064008 (2011).
[25] S. Etcheverry, G. Canas, E. S. Gomez, W. A. T. Nogueira, C. Saavedra, G. B. Xavier, and G. Lima, Nature Scientific Reports **3**, 2316 (2013).
[26] G. Vallone, G. Donati, R. Ceccarelli, and P. Mataloni, Phys. Rev. A **81**, 052301 (2010).

BIBLIOGRAPHY

[1] What is happening in the mathematical sciences –compressed sensing makes every pixel count. *American Mathematical Society*, pages http://www.ams.org/samplings/math–history/hap7–pixel.pdf, 2007.

[2] A. Acin, N. Gisin, and L. Masanes. From Bell's theorem to secure quantum key distribution. *Phys. Rev. Lett.*, 97:120405, Sep 2006.

[3] R. B. A. Adamson and A. M. Steinberg. Improving quantum state estimation with mutually unbiased bases. *Phys. Rev. Lett.*, 105(3):030406, Jul 2010.

[4] S. Aerts, P. Kwiat, J.-A. Larsson, and M. Zukowski. Two-photon Franson-type experiments and local realism. *Physical Review Letters*, 83:2872–2875, 1999.

[5] I. Afek, O. Ambar, and Y. Silberberg. High-NOON states by mixing quantum and classical light. *Science*, 328:879–881, 2010.

[6] I. Afek, A. Natan, O. Ambar, and Y. Silberberg. Quantum state measurements using multipixel photon detectors. *Phys. Rev. A*, 79:043830, Apr 2009.

[7] I. Ali-Khan, C. J. Broadbent, and J. C. Howell. Large-alphabet quantum key distribution using energy-time entangled bipartite states. *Physical Review Letters*, 98(6):060503, 2007.

[8] J. Alnis, A. Matveev, N. Kolachevsky, T. Udem, and T. W. Haensch. Subhertz linewidth diode lasers by stabilization to vibrationally and thermally compensated ultralow-expansion glass Fabry-pérot cavities. *Phys. Rev. A*, 77:053809, May 2008.

[9] A. Aspect, P. Grangier, and G. Roger. Experimental tests of realistic local theories via Bell's theorem. *Phys. Rev. Lett.*, 47(7):460–463, Aug 1981.

[10] A. Aspect, P. Grangier, and G. Roger. Experimental realization of Einstein-Podolsky-Rosen-Bohm Gedankenexperiment: A new violation of Bell's inequalities. *Phys. Rev. Lett.*, 49(2):91–94, Jul 1982.

[11] A. Banerjee, D. Das, and V. Natarajan. Precise frequency measurements of atomic transitions by use of a rb-stabilized resonator. *Optics Letters*, 17:1579–1581, 2003.

[12] J. T. Barreiro, T.-C. Wei, and P. G. Kwiat. Beating the channel capacity limit for linear photonic superdense coding. *Nature Physics*, 4:282–286, 2008.

[13] J. Bell. On the Einstein Podolski Rosen paradox. *Physics*, 195, 1964.

[14] J. Bell. *Speakable and Unspeakable in Quantum Mechanics: Collected Papers on Quantum Philosophy*. Cambridge University Press, 1990.

[15] R. A. Bertlmann, K. Durstberger, B. C. Hiesmayr, and P. Krammer. Optimal entanglement witnesses for qubits and qutrits. *Phys. Rev. A*, 72:052331, Nov 2005.

[16] R. A. Bertlmann and P. Krammer. Bloch vectors for qudits and geometry of entanglement. *arXiv/quant-ph*, page 0706.1743v1, 2007.

[17] I. Bloch. Quantum coherence and entanglement with ultracold atoms in optical lattices. *Nature*, 453:1016–1022, 2008.

[18] D. Bohm. A suggested interpretation of the quantum theory in terms of "hidden" variables. i. *Phys. Rev.*, 85(2):166–179, Jan 1952.

[19] D. Bohm. A suggested interpretation of the quantum theory in terms of "hidden" variables. ii. *Phys. Rev.*, 85(2):180–193, Jan 1952.

[20] N. Bohr. The quantum postulate and the recent development of atomic theory. *Nature*, 121:580–590, 1928.

[21] D. Bouwmeester, J.-W. Pan, M. Daniell, H. Weinfurter, and A. Zeilinger. Observation of three-photon Greenberger-Horne-Zeilinger entanglement. *Phys. Rev. Lett.*, 82:1345–1349, Feb 1999.

[22] S. Boyd and L. Vandenberghe. *Convex Optimization*. Cambridge University Press, 2004.

[23] T. Brougham, V. Kostak, I. Jex, E. Andersson, and T. Kiss. Entanglement preparation using symmetric multiports. *European Journal of Physics D*, 61:231–236, 2011.

[24] C. Brukner, M. Zukowski, J.-W. Pan, and A. Zeilinger. Bell's inequalities and quantum communication complexity. *Phys. Rev. Lett.*, 92:127901, Mar 2004.

[25] N. Brunner, S. Pironio, A. Acin, N. Gisin, A. A. Methot, and V. Scarani. Testing the dimension of hilbert spaces. *Phys. Rev. Lett.*, 100:210503, May 2008.

[26] A. Cabello, J. M. Estebaranz, and G. G. Alcaine. Bell-Kochen-Specker theorem: A proof with 18 vectors. *Phys.Lett. A*, 212:183, 1996.

[27] E. J. Candes and Y. Plan. Matrix completion with noise. *Arxiv: quant-ph*, page arXiv:0903.3131v1.

[28] E. J. Candes, J. Romberg, and T. Tao. Robust uncertainty principles: Exact signal reconstruction from highly incomplete frequency information. *IEEE TRANSACTIONS ON INFORMATION THEORY*, 52:489–509, 2006.

[29] E. J. Candes, J. K. Romberg, and T. Tao. Stable signal recovery from incomplete and inaccurate measurements. *Communications on Pure and Applied Mathematics*, 59:1207–1223, 2006.

[30] E. J. Candes and T. Tao. Decoding by linear programming. *IEEE Trans. Inf. Th., 51(12): 4203-4215*, 2005.

[31] R. Ceccarelli, G. Vallone, F. De Martini, P. Mataloni, and A. Cabello. Experimental entanglement and nonlocality of a two-photon six-qubit cluster state. *Phys. Rev. Lett.*, 103:160401, Oct 2009.

[32] N. J. Cerf, M. Bourennane, A. Karlsson, and N. Gisin. Security of quantum key distribution using d-level systems. *Phys. Rev. Lett.*, 88(12):127902, Mar 2002.

[33] J. K. Chin, D. E. Miller, Y. Liu, C. Stan, W. Setiawan, Sanner, K. Xu, and W. Ketterle. Evidence for superfluidity of ultracold fermions in an optical lattice. *Nature*, 443:961–964, 2006.

[34] D. Chruciski and A. Rutkowski. Entanglement witnesses for d x d systems and new classes of entangled qudit states. *European Journal of Physics D*, 62:273–277, 2011.

[35] J. I. Cirac and P. Zoller. Quantum computations with cold trapped ions. *Phys. Rev. Lett.*, 74:4091–4094, May 1995.

[36] J. F. Clauser and M. A. Horne. Experimental consequences of objective local theories. *Phys. Rev. D*, 10(2):526–535, Jul 1974.

[37] J. F. Clauser, M. A. Horne, A. Shimony, and R. A. Holt. Proposed experiment to test local hidden-variable theories. *Phys. Rev. Lett.*, 23(15):880–884, Oct 1969.

[38] D. Collins, N. Gisin, N. Linden, S. Massar, and Popescu. Bell inequalities for arbitrarily high-dimensional systems. *Phys. Rev. Lett.*, 88:040404, 2002.

[39] A. Dada, J. Lesch, G. Buller, M. J. Padgett, and E. Andersson. Experimental high dimensional two-photon entanglement and violations of generalized Bell inequalities. *Nature Physics*, 7:677–680, 2011.

[40] M. A. Davenport, M. F. Duarte, M. B. Wakin, J. N. Laska, D. Takhar, and K. F. K. R. G. Baraniuk. The smashed filter for compressive classification and target recognition. *Proc. SPIE Computational Imaging V, San Jose, California*, 2007.

[41] D. Donoho. Compressed sensing. *IEEE Transactions on Information Theory*, 52:1289–1306, 2006.

[42] J. P. Dowling and G. J. Milburn. Quantum technology: the second quantum revolution. *Phil. Trans. R. Soc. Lond. A*, 361:doi: 10.1098/rsta.2003.1227, 2003.

[43] M. F. Duarte, M. A. Davenport, D. Takhar, J. N. Laska, T. Sun, K. F. Kelly, and R. G. Baraniuk. Single-pixel imaging via compressive sampling. *IEEE SIGNAL PROCESSING MAGAZINE*, 83, 2008.

[44] A. Einstein, B. Podolsky, and N. Rosen. Can quantum-mechanical description of physical reality be considered complete? *Phys. Rev.*, 47(10):777–780, May 1935.

[45] A. Ekert and R. Jozsa. Quantum computation and Shor's factoring algorithm. *Rev. Mod. Phys.*, 68:733–753, Jul 1996.

[46] S. Etcheverry, G. Canas, E. S. Gomez, W. A. T. Nogueira, C. Saavedra, G. B. Xavier, and G. Lima. Quantum key distribution session with 16-dimensional photonic states. *Nature Scientific Reports*, 3:2316, 2013.

[47] A. Fedrizzi, T. Herbst, A. Poppe, T. Jennewein, and A. Zeilinger. A wavelength-tunable fiber-coupled source of narrowband entangled photons. *Opt. Express*, 15(23):15377–15386, Nov 2007.

[48] R. Fickler, R. Lapkiewicz, W. N. Plick, M. Krenn, C. Schaeff, S. Ramelow, and A. Zeilinger. Quantum entanglement of high angular momenta. *Science*, 338:640–643, 2012.

[49] Y. Fischer. Interferometry in higher-dimensional Hilbert spaces. Master's thesis, LMU Muenchen/ MPI fuer Quantenoptik, 2011.

[50] S. T. Flammia, D. Gross, Y.-K. Liu, and J. Eisert. Quantum tomography via compressed sensing: Error bounds, sample complexity, and efficient estimators. *New Journal of Physics*, page 095022, 2012.

[51] P. A. Franken, A. E. Hill, C. W. Peters, and G. Weinreich. Generation of optical harmonics. *Phys. Rev. Lett.*, 7:118–119, Aug 1961.

[52] J. D. Franson. Bell inequality for position and time. *Phys. Rev. Lett.*, 62(19):2205–2208, May 1989.

[53] S. J. Freedman and J. F. Clauser. Experimental test of local hidden-variable theories. *Phys. Rev. Lett.*, 28:938–941, Apr 1972.

[54] M. Gell-Mann. The symmetry group of the vector and axial vector currents. *Science*, 1:563, 1964.

[55] M. Ghioni, A. Gulinatti, I. Rech, F. Zappa, and S. Cova. Progress in silicon single-photon avalanche diodes. *EEE J. Sel. Top. Quant.*, 13:852–862, 2007.

[56] V. Giovannetti, S. Lloyd, and L. Maccone. Quantum metrology. *Phys. Rev. Lett.*, 96:010401, Jan 2006.

[57] V. Giovannetti, S. Lloyd, and L. Maccone. Advances in quantum metrology. *Nature Photonics*, 5:222–229, 2011.

[58] N. Gisin, G. Ribordy, W. Tittel, and H. Zbinden. Quantum Cryptography. *Rev. Mod. Phys.*, 74:145–195, Mar 2002.

[59] D. Gross. Recovering low-rank matrices from few coefficients in any basis. *IEEE TRANSACTIONS ON INFORMATION THEORY*, 57:1518–1566, 2011.

[60] D. Gross, Y.-K. Liu, S. T. Flammia, S. Becker, and J. Eisert. Quantum state tomography via compressed sensing. *Phys. Rev. Lett.*, 105:150401, Oct 2010.

[61] L. K. Grover. Quantum mechanics helps in searching for a needle in a haystack. *Phys. Rev. Lett.*, 79:325–328, Jul 1997.

[62] O. Guehne and G. Toth. Entanglement detection. *Physics Reports*, 474:1–75, 2009.

[63] O. Gühne, C. Budroni, A. Cabello, M. Kleinmann, and J.-A. Larsson. Bounding the quantum dimension with contextuality. *quant-ph*, page arXiv:1302.2266, 2013.

[64] S. Gulde, M. Riebe, G. P. T. Lancaster, C. Becher, J. Eschner, H. Häffner, F. Schmidt-Kaler, I. L. Chuang, and R. Blatt. Implementation of the Deutsch-Jozsa algorithm on an ion-trap quantum computer. *Nature 421, 48-50 (2 January 2003)*, 421:48–50, 2003.

[65] U. Gustafsson, G. Somesfalean, J. Alnis, and S. Svanberg. Frequency-modulation spectroscopy with blue diode lasers. *Applied Optics*, 21:3774–3780, 2000.

[66] H. Häffner, W. Haensel, C. F. Roos, J. Benhelm, D. C. al kar, M. Chwalla, Koerber, D. Rapol, M. Riebe, P. O. Schmidt, C. Becher, O. Guehne, W. Duer, and R. Blatt. Scalable multiparticle entanglement of trapped ions. *Nature*, 438:643–646, 2005.

[67] H. Häffner, C. Roos, and R. Blatt. Quantum computing with trapped ions. *Physics Reports*, 469:155–203, 2008.

[68] M. Hendrych, R. Gallego, M. Micuda, N. Brunner, A. Acìn, and J. P. Torres. Experimental estimation of the dimension of classical and quantum systems. *Nature Physics*, 8:588–591, 2012.

[69] S. Hermelin, S. Takada, M. Yamamoto, S. Tarucha, A. D. Wieck, L. Saminadayar, C. Bürle, and T. Meunier. Electrons surfing on a sound wave as a platform for quantum optics with flying electrons. *Nature*, 477:435–438, 2011.

[70] R. Holzwarth, T. Udem, T. W. Hänsch, J. C. Knight, W. J. Wadsworth, and P. S. J. Russell. Optical frequency synthesizer for precision spectroscopy. *Phys. Rev. Lett.*, 85:2264–2267, Sep 2000.

[71] M. Horodecki, P. Horodecki, and R. Horodecki. Separability of mixed states: necessary and sufficient conditions. *Physics Letters A*, 223:1–8, 1996.

[72] R. Horodecki, P. Horodecki, M. Horodecki, and K. Horodecki. Quantum entanglement. *Rev. Mod. Phys.*, 81:865–942, Jun 2009.

[73] Z. Hradil. Quantum-state estimation. *Phys. Rev. A*, 55:R1561–R1564, Mar 1997.

[74] M. A. Jafarizadeh and N. Behzadi. Constructing entanglement witness via real skew-symmetric operators. *European Journal of Physics D*, 55:729–744, 2009.

[75] D. F. V. James, P. G. Kwiat, W. J. Munro, and A. G. White. Measurement of qubits. *Phys. Rev. A*, 64:052312, Oct 2001.

[76] K. Jia, T.-H. Chan, and Y. Ma. Robust and practical face recognition via structured sparsity. *European Conference on Computer Vision (ECCV)*, 2012.

[77] K. Johan, Aström, and R. M. Murray. *Feedback Systems–An introduction to Scientists and Engineers*. Princeton University Press, 2008.

[78] D. Kaszlikowski, K. chang, D. Oi, L. Kwek, and C. Oh. Quantum cryptography based on Bell inequalities for three-dimensional systems. *ArXiv:quant-ph/o20617ov1*, 2002.

[79] D. Kaszlikowski, P. Gnaciski, M. Zukowski, W. Miklaszewski, and A. Zeilinger. Violations of local realism by two entangled n-dimensional systems are stronger than for two qubits. *Phys. Rev. Lett.*, 85(21):4418–4421, Nov 2000.

[80] D. Kaszlikowski, L. C. Kwek, J.-L. Chen, M. Zukowski, and C. H. Oh. Clauser-Horne inequality for three-state systems. *Phys. Rev. A*, 65:032118, Feb 2002.

[81] I. A. Khan and J. C. Howell. Experimental demonstration of high two-photon time-energy entanglement. *Physical Review A*, 73(3):031801, 2006.

[82] N. Kiesel. *Experiments on Multiphoton Entanglement*. LMU München, 2007.

[83] N. Kiesel, C. Schmid, G. Toth, E. Solano, and H. Weinfurter. Experimental observation of four-photon entangled dicke state with high fidelity. *Physical Review Letters*, 98(6):063604, 2007.

[84] E. Knill, R. Laflamme, and G. Milburn. A scheme for efficient quantum computation with linear optics. *Nature*, 409:46–52, 2001.

[85] P. Kok, W. J. Munro, K. Nemoto, T. C. Ralph, J. P. Dowling, and G. J. Milburn. Linear optical quantum computing with photonic qubits. *Rev. Mod. Phys.*, 79:135–174, Jan 2007.

[86] P. Krammer. *Entanglement beyond two qubits: geometry and entanglement witnesses*. Universitaet Wien, 2009.

[87] R. Krischek, C. Schwemmer, W. Wieczorek, H. Weinfurter, P. Hyllus, L. Pezze, and A. Smerzi. Useful multiparticle entanglement and sub-shot-noise sensitivity in experimental phase estimation. *Phys. Rev. Lett.*, 107:080504, Aug 2011.

[88] R. Krischek, W. Wieczorek, A. Ozawa, N. Kiesel, P. Michelberger, T. Udem, and H. Weinfurter. Ultraviolet enhancement cavity for ultrafast nonlinear optics and high-rate multiphoton entanglement experiments. *Nature Photonics*, 4:170–173, 2010.

[89] K. L. Kroeker. Face recognition breakthrough. *Communications of the ACM*, page doi:10.1145/1536616.1536623, 2009.

[90] C. Kurtsiefer, S. Mayer, P. Zarda, and H. Weinfurter. Stable solid-state source of single photons. *Phys. Rev. Lett.*, 85:290–293, Jul 2000.

[91] P. Kurzynski, T. Paterek, R. Ramanathan, W. Laskowski, and D. Kaszlikowski. Correlation complementarity yields bell monogamy relations. *Phys. Rev. Lett.*, 106:180402, May 2011.

[92] O. Kuzucu, F. N. C. Wong, S. Kurimura, and S. Tovstonog. Time-resolved single-photon detection by femtosecond upconversion. *Optics Letters*, 33:2257–2259, 2008.

[93] P. G. Kwiat, S. Barraza-Lopez, A. Stefanov, N. E. entanglement distillation, and 'hidden' non locality. Experimental entanglement distillation and 'hidden' non-locality. *Nature 409*, 2001.

[94] P. G. Kwiat, K. Mattle, H. Weinfurter, A. Zeilinger, A. V. Sergienko, and Y. Shih. New high-intensity source of polarization-entangled photon pairs. *Phys.Rev.Lett.*, 75:4337–41, 1995.

[95] P. G. Kwiat, E. Waks, A. G. White, I. Appelbaum, and P. H. Eberhard. Ultrabright source of polarization-entangled photons. *Phys. Rev. A*, 60:R773–R776, Aug 1999.

[96] N. K. Langford. *Encoding, manipulating and measuring quantum information in optics– Ph.D. thesis*. School of Physical Sciences, University of Queensland, 2007.

[97] B. P. Lanyon, M. Barbieri, M. P. Almeida, T. Jennewein, T. C. Ralph, K. J. Resch, G. J. Pryde, J. L. OBrien, A. Gilchrist, and A. G. White. Simplifying quantum logic using higher-dimensional Hilbert spaces. *Nature Physics*, 5:134–140, 2009.

[98] J.-A. Larsson. Energy time entanglement, elements of reality, and local realism. *AIP Conference Proceedings*, 1232:115–127, 2009.

[99] W. Laskowski, D. Richart, C. Schwemmer, L. Knips, T. Paterek, and H. Weinfurter. Experimental Schmidt decomposition and state independent entanglement detection. *Phys. Rev. Lett*, 108:240501, 2012.

[100] W. Laskowski, D. Richart, C. Schwemmer, L. Knips, T. Paterek, and H. Weinfurter. Optimized state-independent entanglement detection based on a geometrical threshold criterion. *Phys. Rev. A*, 88:022327, 2013.

[101] C. K. Law and J. H. Eberly. Analysis and interpretation of high transverse entanglement in optical parametric down conversion. *Phys. Rev. Lett.*, 92:127903, Mar 2004.

[102] K. C. Lee, M. R. Sprague, B. J. Sussman, J. Nunn, N. K. Langford, X.-M. Jin, T. Champion, P. Michelberger, K. F. Reim, D. England, D. Jaksch, and I. A. Walmsley. Entangling macroscopic diamonds at room temperature. *Science*, 334:1253–1256, 2011.

[103] J. Liang, S. M. Hendrickson, and T. B. Pittman. Role of pump coherence in two-photon interferometry. *Phys. Rev. A*, 83:033812, Mar 2011.

[104] G. Lima, G. Vallone, A. Chiuri, A. Cabello, and P. Mataloni. Experimental Bell-inequality violation without the postselection loophole. *Phys. Rev. A*, 81:040101, Apr 2010.

[105] D. Loss and D. P. DiVincenzo. Quantum computation with quantum dots. *Phys. Rev. A*, 57:120–126, Jan 1998.

[106] B. Lounis and W. E. Moerner. Single photons on demand from a single molecule at room temperature. *Nature*, 407:491–493, 2000.

[107] M. Lustig. *SPARSE MRI–Dissertation*. STANFORD UNIVERSITY, 2008.

[108] M. Lustig, D. Donoho, and J. M. Pauly. Sparse mri: The application of compressed sensing for rapid MR imaging. *Magnetic Resonance in Medicine*, 58:1182–1195, 2007.

[109] A. Mair, A. Vaziri, G. Weihs, and A. Zeilinger. Entanglement of the orbital angular momentum states of photons. *Nature*, 412:313–316, 2001.

[110] I. Marcikic, H. de Riedmatten, W. Tittel, H. Zbinden, M. Legre, and N. Gisin. Distribution of time-bin entangled qubits over 50 km of optical fiber. *Phys. Rev. Lett.*, 93(18):180502, Oct 2004.

[111] M. Mariantoni, H. Wang, T. Yamamoto, M. Neeley, R. C. Bialczak, Y. Chen, M. Lenande, E. Lucero, A. D. O'Connell, D. Sank, M. Weides, J. Wenner, Y. Yin, J. Zhao, A. N. Korotkov, A. N. Cleland, and J. M. Martinis. Implementing the quantum von Neumann architecture with superconducting circuits. *Science*, 334:61–65, 2011.

[112] E. Martin-Lopez, A. Laing, T. Lawson, R. Alvarez, X.-Q. Zhou, and J. L. O'Brien. Experimental realization of Shor's quantum factoring algorithm using qubit recycling. *Nature Photonics*, 6:773–776, 2012.

[113] L. Masanes. Tight Bell inequality for d-outcome measurements correlations. *Quantum Information and Computation*, 3:345, 2002.

[114] S. Massar. Nonlocality, closing the detection loophole, and communication complexity. *Phys. Rev. A*, 65:032121, Mar 2002.

[115] W. H. McMaster. Polarization and the Stokes parameters. *American Journal of Physics*, 22:351, 1954.

[116] N. D. Mermin. What's wrong with these elements of reality? *Physics Today*, 43:6, June 1990.

[117] F. Mezzadri. How to generate random matrices from the classical compact groups. *NOTICES of the AMS*, 54:592–604, 2007.

[118] P. Michler, A. Kiraz, C. Becher, W. V. Schoenfeld, P. M. Petroff, L. Zhang, E. Hu, and A. Imamoglu. A quantum dot single-photon turnstile device. *Science*, 290:2282–2285, 2000.

[119] T. Monz, P. Schindler, J. T. Barreiro, M. Chwalla, D. Nigg, W. A. Coish, M. Harlander, W. Hänsel, M. Hennrich, and R. Blatt. 14-qubit entanglement: Creation and coherence. *Phys. Rev. Lett.*, 106:130506, Mar 2011.

[120] T. Moroder, P. Hyllus, G. Toth, C. Schwemmer, A. Niggebaum, S. Gaile, O. Guehne, and H. Weinfurter. Permutationally invariant state reconstruction. *New Journal Physics*, 14:105001, 2012.

[121] M. Neeley, R. C. Bialczak, M. Lenander, E. Lucero, M. Mariantoni, A. D. O'Connell, D. Sank, H. Wang, M. Weides, J. Wenner, Y. Yin, T. Yamamoto, A. N. Cleland, and J. M. Martinis. Generation of three-qubit entangled states using superconducting phase qubits. *Nature*, 467:570ï£¡573, 2010.

[122] C. Negrevergne, T. S. Mahesh, C. A. Ryan, M. Ditty, F. Cyr-Racine, W. Power, N. Boulant, T. Havel, D. G. Cory, and R. Laflamme. Benchmarking quantum control methods on a 12-qubit system. *Phys. Rev. Lett.*, 96:170501, May 2006.

[123] P. Neumann, N. Mizuochi, F. Rempp, P. Hemmer, H. Watanabe, S. Yamasaki, V. Jacques, T. Gaebel, F. Jelezko, and J. Wrachtrup. Multipartite entanglement among single spins in diamond. *Science*, 320:1326–1329, 2008.

[124] M. A. Nielsen and I. Chuang. *Quantum Computation and Quantum Information*. Cambridge University Press, 2000.

[125] I. Osborne and R. Coontz. Quantum wonderland. *Science*, 319:1201, 2008.

[126] J.-W. Pan, Z.-B. Chen, C.-Y. Lu, H. Weinfurter, A. Zeilinger, and M. Zukowski. Multiphoton entanglement and interferometry. *Rev. Mod. Phys.*, 84:777–838, May 2012.

[127] M. Paris and J. Rehacek. *Quantum State Estimation*. Springer, 2004.

[128] M. Pelton, P. Marsden, D. Ljunggren, M. Tengner, A. Karlsson, A. Fragemann, C. Canalias, and F. Laurell. Bright, single-spatial-mode source of frequency non-degenerate, polarization-entangled photon pairs using periodically poled KTP. *Optics Express*, 12:3573–3580, 2004.

[129] W. Pernice, C. Schuck, O. Minaeva, M. Li, G. Goltsman, A. Sergienko, and H. Tang. High-speed and high-efficiency travelling wave single-photon detectors embedded in nanophotonic circuits. *Nature Communications*, 3:1325, 2012.

[130] D. Petz. Covariance and Fisher information in quantum mechanics. *Journal of Physics A: Mathematical and General*, 35:929, 2002.

[131] I. Pitowsky. *Quantum Probability and Quantum Logic* . Springer, Berlin / Heidelberg,, 1989.

[132] A. Politi, M. J. Cryan, J. G. Rarity, S. Yu, and J. L. O'Brien. Silica-on-silicon waveguide quantum circuits. *Science*, 320:646–649, 2008.

[133] B. Pors, S. S. R. Oemrawsingh, A. Aiello, M. P. van Exter, E. R. Eliel, G. W. 't Hooft, and J. P. Woerdman. Shannon dimensionality of quantum channels and its application to photon entanglement. *Phys. Rev. Lett.*, 101:120502, Sep 2008.

[134] B.-J. Pors, F. Miatto, G. W. 't Hooft, E. R. Eliel, and J. P. Woerdman. High-dimensional entanglement with orbital-angular-momentum states of light. *Journal of Optics*, 13(6):064008, 2011.

[135] B.-J. Pors, C. Monken, E. Eliel, and J. Woerdman. Transport of orbital angular momentum entanglement through a turbulent atmosphere. *Optics Express*, 19:6671–6683, 2011.

[136] K. Predehl, G. Grosche, S. M. F. Raupach, S. Droste, O. Terra, J. Alnis, T. Legero, T. W. Hänsch, T. Udem, R. Holzwarth, and H. Schnatz. A 920-kilometer optical fiber link for frequency metrology at the 19th decimal place. *Science*, 336:441–444, 2012.

[137] R. Prevedel, P. Walther, F. Tiefenbacher, P. Böhi, R. Kaltenbaek, T. Jennewein, and A. Zeilinger. High-speed linear optics quantum computing using active feed-forward. *Nature*, 445:65–69, 2007.

[138] M. Reck. *Quantum Interferometry with Multiports: Entangled Photons in Optical Fibers*. PhD thesis, University of Innsbruck, 1996.

[139] L. Ricci, M. Weidemuller, T. Esslinger, A. Hemmerich, C. Zimmermann, V. Vuletic, W. Konig, and T. Hänsch. A compact grating-stabilized diode laser system for atomic physics. *Optics Communications*, 117:541–549, 1995.

[140] D. Richart, Y. Fischer, and H. Weinfurter. Experimental implementation of higher dimensional time-energy entanglement. *Applied Physics B*, 106:543–550, 2012.

[141] D. Richart, W. Laskowski, Y. Fischer, and H. Weinfurter. Experimental qudit entanglement detection using the time-energy degree of freedom.

[142] D. L. Richart. Entanglement of higher dimensional Hilbert spaces. Master's thesis, Technische Universität München, 2008.

[143] M. Rosticher, F. R. Ladan, J. P. Maneval, S. N. Dorenbos, T. Zijlstra, T. M. Klapwijk, V. Zwiller, A. Lupacu, , and G. Nogues. A high efficiency superconducting nanowire single electron detector. *Appl. Phys. Lett.*, 97:183106, 2010.

[144] B. Saleh and M. Teich. *Fundamentals of Photonics*. John Wiley & Sons, 1991.

[145] A. Sanpera, D. Bruss, and M. Lewenstein. Schmidt-number witnesses and bound entanglement. *Phys. Rev. A*, 63:050301, Apr 2001.

[146] A. Sanpera, D. Bruss, and M. Lewenstein. Schmidt-number witnesses and bound entanglement. *Phys. Rev. A*, 63:050301, Apr 2001.

[147] L. Sansoni, F. Sciarrino, G. Vallone, P. Mataloni, A. Crespi, R. Ramponi, and R. Osellame. Polarization entangled state measurement on a chip. *Phys. Rev. Lett.*, 105:200503, Nov 2010.

[148] E. Schmidt. Zur Theorie der linearen und nichtlinearen Integralgleichungen. *Math. Ann.*, 63:433–457, 1907.

[149] E. Schrödinger. Die gegenwärtige Situation in der Quantenmechanik. *Naturwissenschaften*, 48:807–812, 1935.

[150] O. Schulz, R. Steinhübl, M. Weber, B.-G. Englert, C. Kurtsiefer, and H. Weinfurter. Ascertaining the values of σ_x, σ_y, and σ_z of a polarization qubit. *Phys. Rev. Lett.*, 90(17):177901, Apr 2003.

[151] C. Schwemmer. Experimental comparison of efficient tomography schemes for a six-qubit state. *Physical Review Letters*, 2014.

[152] C. Schwemmer, L. Knips, D. Richart, H. Weinfurter, T. M. M. Kleinmann, and O. Gühne. Systematic errors in current quantum state tomography tools.

[153] C. Shannon. A mathematical theory of communication. *Bell System Technical Journal*, 27:379–423, 1948.

[154] P. W. Shor. Polynomial-time algorithms for prime factorization and discrete logarithms on a quantum computer. *SIAM J. Comput.*, 26(5):1484–1509, Oct. 1997.

[155] C. Spengler. Geometrical aspects of qudits concerning Bell inequalities. Master's thesis, Universität Wien, 2008.

[156] C. Spengler, M. Huber, S. Brierley, T. Adaktylos, and B. C. Hiesmayr. Entanglement detection via mutually unbiased bases. *Phys. Rev. A*, 86:022311, Aug 2012.

[157] S.Tanzilli, H. Riedmatten, W.Tittel, H. Zbinden, P. Baldi, M. de Micheli, D. Ostrowsky, and N. Gisin. PPLN waveguide for quantum communication. *The European Journal of Physics D*, 18:155–160, 2002.

[158] F. Steinlechner, P. Trojek, M. Jofre, H. Weier, D. Perez, T. Jennewein, R. Ursin, J. Rarity, M. W. Mitchell, J. P. Torres, H. Weinfurter, and V. Pruneri. A high-brightness source of polarization-entangled photons optimized for applications in free space. *Optics Express*, 20:9640–9649, 2012.

[159] F. Stellari. High-speed CMOS circuit testing by 50 ps time-resolved luminescence measurements. *IEEE Transactions on Electron Devices*, 48:12, 2001.

[160] D. V. Strekalov, T. B. Pittman, A. V. Sergienko, Y. H. Shih, and P. G. Kwiat. Postselection-free energy-time entanglement. *Phys. Rev. A*, 54(1):R1–R4, Jul 1996.

[161] H. Takesue and K. Inoue. Generation of polarization-entangled photon pairs and violation of Bell's inequality using spontaneous four-wave mixing in a fiber loop. *Phys. Rev. A*, 70:031802, Sep 2004.

[162] B. M. Terhal and P. Horodecki. Schmidt number for density matrices. *Phys. Rev. A*, 61:040301, Mar 2000.

[163] R. T. Thew, A. Acin, H. Zbinden, and N. Gisin. Bell-type test of energy-time entangled qutrits. *Physical Review Letters*, 93(1):010503, 2004.

[164] R. T. Thew, K. Nemoto, A. G. White, and W. J. Munro. Qudit quantum-state tomography. *Phys. Rev. A*, 66:012303, Jul 2002.

[165] W. Tittel, J. Brendel, B. Gisin, T. Herzog, H. Zbinden, and N. Gisin. Experimental demonstration of quantum correlations over more than 10 km. *Phys. Rev. A*, 57(5):3229–3232, May 1998.

[166] W. Tittel, J. Brendel, N. Gisin, and H. Zbinden. Long-distance Bell-type tests using energy-time entangled photons. *Phys. Rev. A*, 59(6):4150–4163, Jun 1999.

[167] G. Tóth, W. Wieczorek, D. Gross, R. Krischek, C. Schwemmer, and H. Weinfurter. Permutationally invariant quantum tomography. *Phys. Rev. Lett.*, 105:250403, Dec 2010.

[168] P. Trojek. *Efficient Generation of Photonic Entanglement and Multiparty Quantum Communication*. PhD thesis, Ludwig Maximilian Universität München, 2007.

[169] A. Uhlmann. Transition probabilities in the state space of a *-algebra. *Rep. Math. Phys.*, 9:273–279, 1976.

[170] R. Ursin, F. Tiefenbacher, T. Schmitt-Manderbach, H. Weier, T. Scheidl, M. Lindenthal, B. Blausteiner, T. Jennewein, J. Perdigues, P. Trojek, B. Oemer, M. Fürst, M. Meyenburg, J. Rarity, Z. Sodnik, C. Barbieri, H. Weinfurter, and A. Zeilinger. Entanglement-based quantum communication over 144 km. *Nature Physics*, 3:481 – 486, 2007.

[171] G. Vallone, G. Donati, N. Bruno, A. Chiuri, and P. Mataloni. Experimental realization of the Deutsch-Jozsa algorithm with a six-qubit cluster state. *Phys. Rev. A*, 81:050302, May 2010.

[172] L. M. K. Vandersypen, M. Steffen, G. Breyta, C. S. Yannoni, M. H. Sherwood, and I. L. Chuang. Experimental realization of Shor's quantum factoring algorithm using nuclear magnetic resonance. *Nature*, 414:883–887, 2001.

[173] F. Verstraete, J. Dehaene, and B. DeMoor. Local filtering operations on two qubits. *Phys. Rev. A*, 64:010101, Jun 2001.

[174] T. Vértesi, S. Pironio, and N. Brunner. Closing the detection loophole in bell experiments using qudits. *Phys. Rev. Lett.*, 104:060401, Feb 2010.

[175] J. I. D. Vicente. Separability criteria based on the bloch representation of density matrices. *Quantum Information & Computation*, 7:624–638, 2007.

[176] S. P. Walborn, D. S. Lemelle, M. P. Almeida, and P. H. S. Ribeiro. Quantum key distribution with higher-order alphabets using spatially encoded qudits. *Phys. Rev. Lett.*, 96:090501, Mar 2006.

[177] P. Walther, K. J. Resch, T. Rudolph, E. Schenck, H. Weinfurter, V. Vedral, M. Aspelmeyer, and A. Zeilinger. Experimental one-way quantum computing. *Nature*, 434:169–176, 2005.

[178] R. F. Werner. Quantum states with einstein-podolsky-rosen correlations admitting a hidden-variable model. *Phys. Rev. A*, 40:4277–4281, Oct 1989.

[179] J. A. Wheeler and W. H. Zurek. *Quantum theory and measurement –On the quantum mechanics of collisions*. Princeton University Press, 1983.

[180] W. Wieczorek. *Multi-Photon Entanglement– Experimental Observation, Characterization, and Application of up to Six-Photon Entangled States*. Ludwig Maximilians Universität München, 2009.

[181] W. Wieczorek, R. Krischek, N. Kiesel, P. Michelberger, G. Tóth, and H. Weinfurter. Experimental entanglement of a six-photon symmetric dicke state. *Phys. Rev. Lett.*, 103:020504, Jul 2009.

[182] W. Wieczorek, C. Schmid, N. Kiesel, R. Pohlner, O. Gühne, and H. Weinfurter. Experimental observation of an entire family of four-photon entangled states. *Phys. Rev. Lett.*, 101:010503, Jul 2008.

[183] M. Wiesniak, T. Paterek, and A. Zeilinger. Entanglement in mutually unbiased bases. *New Journal of Physics*, 13:053047, 2011.

[184] W. Wooters and B. D. Fields. Optimal state determination by mutually unbiased measurements. *Annals of Physics*, 191:363–381, 1989.

[185] W. K. Wooters. Quantum mechanics without probability amplitudes. *Foundations of Physics*, 16:4, 1986.

[186] X.-C. Yao, T.-X. Wang, P. Xu, H. L. andGe Sheng Pan, X.-H. Bao, C.-Z. Peng, C.-Y. Lu, Y.-A. Chen, and J.-W. Pan. Observation of eight-photon entanglement. *Nature Photonics*, 6:225–228, 2012.

[187] J. Ye and S. T. Cundiff, editors. *Femtosecond Optical Frequency Comb: Principle, Operation, and Applications*. Kluwer Academic Publishers / Springer, 2004.

[188] M. Zukowski, A. Zeilinger, and M. A. Horne. Realizable higher-dimensional two-particle entanglements via multiport beam splitters. *Phys. Rev. A*, 55(4):2564–2579, Apr 1997.

10

ACKNOWLEDGMENTS

First, I would like to thank Prof. Weinfurter for the possibility to perform this PhD thesis in his group. Specially, with regards to the flexibility to try out different solutions and strategies, and to correspondingly make errors. A quite important strategy in any scientific endeavour. Thanks go as well to the group gathered together, making the discussion on different aspects of a problem possible. In this respect, many thanks go to Christian Schwemmer, Lukas Knips and Yvo Fischer for making the long and tedious work on the different projects, we had the opportunity to share, more fun. Even if that meant working until the last U-Bahn was circulating. And for the many shots of self-destilled liqueur, on the afterwork meetings. On similar lines many thanks go to Witlef Wieczorek, Pavel Trojek, Nikolai Kiesel and Christian Schmid for always having open ears to share their knowledge on many of the problems encountered in this thesis. Thanks as well for the nice co-working atmosphere to Alexander Niggebaum and Patrick Michelberger. Along the same line, I acknowledge the help as well of the Cryptography team composed of Martin Fürst, Markus Rau and Sebastian Nauerth without whose help tackling hardware problems would have become more tedious. Many thanks as well to Wenjamin Rosenfeld, Markus Weber, Michael Krug, Florian Henkel, Daniel Burchhardt, Kai Redeker and Julian Hofmann, for their always good and positive co-working attitude. Last but not least, I am grateful to Daniel Schlenk for these coffee hours and for handling much of the necessary administrative work and to Gwenaelle Vest and Lars Liebermeister for joining the coffee discussions.

Thanks as well to the many people who we had the luck to join in our cooperation programs. Thanks to Wieslaw Laskowski and Marek Zukowski from the university of Gdansk for giving us the possibility to research at the core questions of quantum mechanics. Thanks as well to Geza Toth from the university of Bilbao and Tobias Moroder, Matthias Kleinmann and Ottfried Gühne from the University of Siegen without who many of the questions adressed in this work would have remained unsolved. And finally, thanks to David Gross from the University of Freiburg for enabling us to participate in the fast growing research community around compressed sensing. Many thanks to my grandfather, who was true about that one has to finish what one begins. And specially to the many friends maybe not understanding anything what I was doing but still having understanding when experiments were compelling me to disappear for some time.